DISSERTATION

submitted to the
Combined Faculties for the Natural Sciences and Mathematics
of the Ruperto-Carola University of Heidelberg, Germany
for the degree of
Doctor of Natural Sciences

Put forward by
Bernd Hezel
born in Schramberg, Germany

Oral examination: July 21, 2010

Interaction-induced stabilization of ultracold Rydberg atoms in a Ioffe-Pritchard trap

Wechselwirkungs-induzierte Stabilisierung von ultrakalten Rydberg-Atomen in einer Ioffe-Pritchard Falle — Gegenstand dieser Arbeit ist eine theoretische Untersuchung der Quanteneigenschaften hoch angeregter Atome in inhomogenen magnetischen Feldkonfigurationen. Wir untersuchen wie die extreme Größe von Rydberg-Atomen deren Kopplung an steile magnetische Gradienten beeinflusst und zeigen dass Rydberg-Atome in elektronischen Zuständen mit langer Lebensdauer in einen sehr kleinen Raumbereich hinein gefangen werden können. Diese starke Einsperrung erlaubt die Erzeugung eines eindimensionalen Rydberg-Gases das gegen Selbstionisation durch eine dipolare Abstoßung zwischen den Atomen stabilisiert wird, die von einem äußeren elektrischen Feld generiert werden kann. Diese stark anisotrope dipolare Wechselwirkung ermöglicht außerdem eine gut kontrollierbare Gleichgewichtskonfiguration zweier Rydberg-Atome in der Falle, wobei der Abstand der Atome durch die Stärke des elektrischen Feldes verändert werden kann.

Interaction-induced stabilization of ultracold Rydberg atoms in a Ioffe-Pritchard trap — Subject of this thesis is a theoretical investigation of the quantum properties of highly excited atoms in an inhomogeneous magnetic field configuration. It is demonstrated how the large size of the Rydberg atoms alters the coupling to strong magnetic gradients. We find that Rydberg atoms can be tightly trapped in long-lived electronic states. This confinement permits the creation of a one-dimensional Rydberg gas stabilized against auto-ionization by a dipolar repulsion between the atoms, which is generated imposing a homogeneous electric field. This strongly anisotropic interaction is also responsible for a well controllable equilibrium configuration of two Rydberg atoms in the trap whose distance can be changed by tuning the electric field.

Contents

Contents

Introduction

The success story of ultracold atomic gases began with the development of powerful experimental cooling techniques [1] that allow to probe the nanokelvin regime and that have made the preparation of ultracold ground state atom samples laboratory routine. The advantages of ultracold dilute gases are manifold. Cooling, trapping and manipulation rely on lasers and electro-magnetic fields and such gases are hence comfortable to work with. Their diluteness entails lengths scales that are optically imageable, sometimes even in situ. Most importantly, however, the reduction of thermal energy in the gas is exciting because it makes the dynamics completely determined by the external potential and the interaction between the atoms. The potential for the atomic motion is provided by external electric, magnetic, or optical fields, which allow for a vast variety of potential landscapes, and the interaction between the atoms can also be tailored almost arbitrarily. The scattering length can, for instance, be changed in the vicinity of a Feshbach resonance by simply tuning the strength of a magnetic or an electric field [2], to obtain attractive, repulsive or even vanishing interaction, i.e. an ideal gas.

Initial research concentrated on weakly interacting gases. The long predicted [3,4] Bose-Einstein condensation (BEC), a phase transition for non-interacting atoms, was experimentally implemented in the mid nineties [5,6]. It is associated with the condensation of atoms into the state of lowest energy as a consequence of quantum statistical effects. Many experiments elucidated the coherent matter wave features and superfluid properties of such condensates [7–9]. This regime is also appealing from a theoretical point of view due to the fact that inter-atomic distances are typically much larger than the scattering length a, which characterizes the strength of the interaction, and it is therefore possible to calculate properties of the gas reliably from the knowledge of two-body scattering at low energies. To interpret the mentioned features it therefore suffices to employ mean field descriptions, like the Gross-Pitaevskii equation in case of bosons [10–13].

Research has turned toward strongly interacting systems which make a theoretical description more difficult but also allow for novel ground states with collective properties of the many-body system [14]. In spite of the diluteness of ultracold atomic gases (they are five to six orders of magnitude less dense than the air that surrounds us), they have the potential to model condensed matter systems along the lines of the quantum simulator originally suggested by Feynman [15]. Famous examples for their versatility are the demonstration of the Mott-Insulator to superfluid phase-transition [16], the BEC-Bardeen-Cooper-Schrieffer crossover in a gas of ^{6}Li [17], or the Kosterlitz-Thouless phase transition studied within a two-dimensional Bose-Einstein condensate [18].

Most experiments to date have been carried out with ground state atoms, so that interactions are point-like and life times are long. Recently, a growing interest in ultracold gases with atoms that are highly excited can be observed [19–22]. Their attractiveness arises from the extraordinary properties of such Rydberg atoms which have an electron in a state with a very high principal quantum number. The large displacement of the valence electron and

the atomic core is responsible for the massively enhanced response to external fields and, therewith, for their enormous polarizability. Rydberg atoms possess large dipole moments and, despite being electronically highly excited, they can possess lifetimes of the order of milliseconds or even more (a more detailed description of Rydberg atom properties can be found in Chapter 1). Due to the susceptibility with respect to external fields and due to the long range interaction, Rydberg atom ensembles are intriguing many-body systems with rich excitations and decay channels. In the extreme case the Rydberg atoms in the gas may ionize each other leading to an ultracold Rydberg plasma [23].

In Rydberg gas experiments a laser beam typically excites a sub-ensemble of ultracold ground state atoms to the desired excited states. Since the ultra-slow motion of the atoms can be ignored on short timescales, Rydberg-Rydberg interactions dominate the system and we encounter a so-called frozen Rydberg gas [24] which behaves in many ways more like a solid than a gas. The strength of the interaction can be varied by tuning external fields and by selecting specific atomic states. Instead of binary collisions, many-body interactions among the static atoms become important. It has been found, for instance, that the strong interaction gives rise to a non-linear excitation behavior: Rydberg atoms strongly inhibit excitation of their neighbors entailing a state dependent local excitation blockade [25–29], which on its part results in a collective excitation of many atoms [30–32]. This can turn Rydberg atom ensembles into possible candidates for quantum information processing schemes [33–37]. The large size of Rydberg atoms can also give rise to bonding interactions between Rydberg and ground state atoms. The scattering-induced attractive interaction binds the ground-state atom to the Rydberg atom at a well-localized position within the Rydberg electron wavefunction and thereby yields giant molecules that can have internuclear separations of several thousand Bohr radii [38–41]. The spectroscopic characterization of such exotic molecular states, named trilobite and butterfly states on account of their particular electronic density, has succeeded recently [19].

Most of the experiments with Rydberg atoms still involve a whole gas of Rydberg atoms. They can therefore unavoidably only investigate effective and averaged properties since individual atoms are typically not resolved. It is hence of great interest to study only a small number of Rydberg atoms [37], that are preferably individually controllable, and arrangeable with respect to one another. It is furthermore necessary to stabilize these Rydberg atom configurations against autoionization. In this thesis we provide candidate solutions to these problems.

A precondition for enabling such processing of Rydberg atoms is the availability of tools to control their quantum behavior and properties. An essential step in this respect is the trapping of electronically highly excited atoms. Several works have focused on trapping Rydberg atoms, based on electric [42], optical [43], or strong magnetic fields [44]. Due to the high level density and the strong spectral fluctuations with spatially varying fields, trapping or manipulation in general is a delicate task. This is particularly the case when both, the center of mass and the internal motion are of quantum nature, and the inhomogeneous external fields lead to an inherent coupling of these motions.

First experimental evidence for trapped Rydberg gases has been found by Choi and co-workers [44, 45]. The authors use strong bias fields to trap "guiding center" drift atoms for up to 200 ms. Quantum mechanical studies of highly excited atoms in magnetic quadrupole fields demonstrated the existence of e.g. intriguing spin polarization patterns and magnetic field-induced electric dipole moments [46, 47]. These investigations were based on the as-

sumption of an infinitely heavy nucleus. A description of the coupled center of mass and electronic dynamics has been presented in Refs. [48, 49]: Trapping has been achieved for quantum states with sufficiently large total, i.e. electronic and center of mass, angular momentum. Pictorially speaking this addresses atoms that circle around the point of zero field at a sufficiently large distance. When excited from ultracold atomic samples, however, Rydberg atoms are usually prepared in states with small or vanishing center of mass angular momentum and a three-dimensional quadrupole trap can hence not provide stable confinement.

Overcoming the drawback of the three-dimensional quadrupole configuration and enabling the trapping of a Rydberg atom that is ultracold, i.e. with very small center of mass kinetic energy, is possible considering a magnetic field configuration that, unlike the quadrupole trap, does not have a point of zero magnetic field. A Ioffe-Pritchard trap features a homogenous offset field, that removes the degeneracy of the trapped and anti-trapped states at the origin, and thereby inhibits unwanted spin flips. Addressing the regime of inherently coupled center of mass and electronic dynamics, we first provide a thorough investigation of how the large size of Rydberg atoms affects their coupling to strongly inhomogeneous magnetic fields. The main objective of this work is to arrange and stabilize Rydberg atom ensembles. A first approach to achieve this is to exploit the results from the above analysis to constrain the atoms motion into one dimension. A stabilization can then be achieved by means of an external electric field that entails a dipolar repulsion between the Rydberg atoms. A more elaborate approach to the formulated goal for only two atoms involves an additional longitudinal confinement and provides a clean and well controllable system of interacting Rydberg atoms.

As already mentioned above we start with a short introduction to Rydberg atoms and their fascinating properties in *Chapter 1*. We particularly draw our attention to the allure of circular Rydberg atoms and review methods to excite such semi-classical states. In *Chapter 2* we lay the foundation for the following chapters by deriving a Hamiltonian that models a highly excited alkali atom as a two-body system and includes the coupling of the electronic and center of mass dynamics. Some of the coupling terms in the Hamiltonian can be eliminated using a unitary transformation. The remaining couplings are dealt with by adiabatically separating the center of mass and electronic dynamics assuming the latter to adapt instantaneously to the local magnetic field while the atom is moving slowly through the external field. An analysis of the energy scales shows that every n-manifold can be considered separately. As it is not in general possible to solve the Schrödinger equation analytically we have to find a numerical approach to the problem, too. This is done in *Chapter 3* where we introduce the variational method that maps the Schrödinger equation to an ordinary algebraic eigenvalue problem. The corresponding matrix representation of the Hamiltonian has to be diagonalized to solve the problem and we consequentially describe an adequate basis. In *Chapter 4* we solve the electronic Schrödinger equation for fixed center of mass positions to obtain adiabatic electronic energy surfaces that serve as potentials for the center of mass motion. The solutions can be obtained analytically in the limit of large ratios of homogeneous field and field gradient by rotating the Hamiltonian into the direction of the local magnetic field. For the opposite limit numerical solutions are obtained. We classify the shapes of the adiabatic surfaces for different parameter regimes and find that the uppermost surface, that belongs to the electronic state with the longest lifetime, perfectly qualifies for the confinement of the atom. The analysis of the fully quan-

tized compound center of mass and electronic states shows that very tight confinement of the center of mass motion in two dimensions is achievable while the electronic structure is barely changed compared to the field free case. This paves the way for generating a one-dimensional ultracold Rydberg gas described in *Chapter 5*. Specifically, we propose a modified Ioffe-Pritchard trap, a magneto-electric trap, in which the atoms possess an oriented electric dipole moment. The resulting dipole-dipole interaction in conjunction with the transversal confinement is demonstrated to give rise to an effectively one-dimensional ultracold quantum Rydberg gas with a macroscopic interparticle distance. We derive analytical expressions for the required linear density of Rydberg atoms below which a one-dimensional Rydberg gas is expected to form. The lifetime of the Rydberg atoms is long enough to probe the dynamics of the interacting gas, which means that this system is complementary to the well-studied frozen Rydberg gases. This is only one of the reasons to also confine the atoms in the translationally symmetric longitudinal direction of the trap in *Chapter 6*. For a macroscopic Ioffe-Pritchard trap it can be generated by slightly changing its geometry. For the miniaturized form of a Ioffe-Pritchard configuration on an atom chip [50, 51] the longitudinal confinement is inherent to the geometry of the wire generating the magnetic field [52]. *Chapter 7* deals with the electric dipole moment expectation value of a Rydberg atom in these environments. We find that the inhomogeneous magnetic field breaks the parity symmetry of the electric eigenfunctions. It is therefore responsible for a permanent electric dipole moment that is perpendicular to the local magnetic field axis. The application of an electric field has similar consequences. For moderate field strengths the resulting induced electric dipole moments are perpendicular to the direction of the local magnetic field as well. In *Chapter 8* we derive an expression for the interaction energy of two Rydberg atoms by expanding the Coulomb interaction between the charges of different atoms. Assuming the distance of the atoms to be much larger than the extension of their electronic wave functions, we can expand the expression in reciprocal powers of the atomic distance. We find the leading order term to be the dipolar interaction operator, as expected, which is subsequently represented in single-atom electronic eigenstates. We also investigate the transition matrix elements of the dipole-dipole interaction operator to other surfaces and the closely related second order contributions to the interaction of the atoms which give a quality measure for the used basis. In the final *Chapter 9* all the insights gained in the previous chapters are knitted together to describe two interacting Rydberg atoms in a three-dimensionally confining Ioffe-Pritchard trap. The balance of longitudinal confinement and dipolar repulsion, paired with the steep transversal confinement, stabilizes the atoms into an equilibrium position on the longitudinal axis. The atomic distance in this stable configuration is tuneable over a large range by the electric field, while the center of mass states are barely changed. Finally we describe different experimental schemes for exciting two atoms into this well controllable configuration.

The last chapter concludes with a summary and prospects of further research.

1 Rydberg atoms

Atoms with an electron in a state with high principal quantum number n are called Rydberg atoms. Such highly excited atoms have been studied since over a century. They since gave inspiration to the semiclassical quantum mechanics of Niels Bohr [53] and they assisted with the understanding of the quantum mechanical description of the structured vacuum [54,55]. They have been an important radiation source for astronomers [56] and they have provided information about the thermodynamic properties in astrophysical and laboratory plasmas [57, 58], to name just some areas of application. In the future they will most probably constitute quantum simulators that can reproduce any other many-particle quantum system with short-range interactions [22].

Rydberg atoms possess remarkable properties. Although being electronically highly excited, they can possess lifetimes of the order of milliseconds. Moreover, due to the large displacement of the valence electron and the atomic core, they are highly susceptible to electric fields and, therefore, easily polarizable. The interest in Rydberg atoms has grown immensely in recent years since the development of tunable lasers and of powerful experimental cooling techniques have made Rydberg systems readily available. Their extreme properties would be impossible to generate in other systems and they have thus become the testing (play-)ground for a plethora of quantum mechanical problems.

1.1 Rydberg atom properties

When people tried to understand the atomic spectral data measured in the late nineteenth century it was evident from the hydrogen spectrum that there must be a mathematical expression connecting the spectral lines. Johann Balmer developed a formula that described the wavelengths of the visible series of atomic hydrogen which was generalized shortly after by Janne Rydberg to include all levels and also alkali atoms [59]. He formulated the expression for the wave numbers of the observed series,

$$\nu_{nl} = \nu_{\infty l} - \frac{Ry}{(n - \delta_l)^2} \ ,$$
(1.1)

henceforth known as Rydberg formula. The constants $\nu_{\infty l}$ and δ_l are the limits and the quantum defects of the spectral series. The Rydberg constant Ry is universal because it can describe (via the expression (1.1)) not only the wave numbers of different series of the same atom, but also those of different species.

It was Niels Bohr that could phenomenologically interpret this Rydberg formula by connecting the principal quantum number n and the angular momentum quantum number l to the electronic structure of the atom. Bohr's model is based on an electron moving classically in discrete circular orbits around an ionic core, with the size of these orbits increasing with the square of the principal quantum number, which is responsible for the enormous extension, and the binding energy decreasing as $1/n^2$. In other words, the valence electron in a

Table 1.1: Selected properties of Rydberg atoms and their principal dependence on n. For alkali atoms the principal quantum number n has to be substituted by the effective principal quantum number $n^\star = n - \delta_l$. Adapted from [60].

property	dependence
binding energy	n^{-2}
energy between adjacent states	n^{-3}
orbital radius	n^2
geometric cross section	n^4
dipole moment $\langle nd|er|nf\rangle$	n^2
polarizability	n^7
radiative lifetime	n^3
radiative lifetime of circular states	n^5
fine structure interval	n^{-3}

Rydberg atom is in a large loosely bound orbit. He also connected Ry to atomic quantities,

$$Ry = \frac{1}{2}\frac{Z^2 e^4 m}{(4\pi\epsilon_0)^2} \ , \tag{1.2}$$

where Z is the nuclear charge in units of e, ϵ_0 is the vacuum permittivity, $\hbar$ is Planck's constant and m is the electron mass. While being superseded by the quantum mechanical description, Bohr's model can explain most of the properties of Rydberg atoms predicting at least the right scaling with the principal quantum number n. The n dependences of some Rydberg atom properties are tabulated in Tab. 1.1. The scaling laws apply to hydrogen. For alkali atoms, the principal quantum number n has to be replaced by the effective quantum number $n^\star = n - \delta_l$ involving the quantum defects δ_l that account for the finite size of the rest-ion consisting of the atoms nucleus and the remaining electrons. In case of alkali atoms these electrons form a closed spherically symmetric shell and shield the core so that the Rydberg electron sees a core charge $Z = 1$, as in hydrogen. This shielding is not perfect for small l since the electronic wave function penetrates the ionic core. The resulting discrimination of the energy levels is illustrated in Fig. 1.1 where we compare the level schemes of rubidium and hydrogen.

The physics of high angular momentum states is evidently very different from low l states. To exemplify this we consider the spontaneous decay rates. They are given by the Einstein A coefficients for the decay from the nl state to the lower lying $n'l'$ state which are proportional to the cubed energy differences and to the squared dipole matrix elements,

$$A_{fi} \propto E_{if}^3 |\boldsymbol{r}_{fi}|^2 \ . \tag{1.3}$$

The energy difference is $E_{if} = E_i - E_f$ and the dipole matrix element reads $\boldsymbol{r}_{fi} = \langle f|\boldsymbol{r}|i\rangle$. The decay rate of the excited state is the sum of the A coefficients to all final states, and the lifetime τ is its inverse,

$$1/\tau = \sum_f A_{fi} \ . \tag{1.4}$$
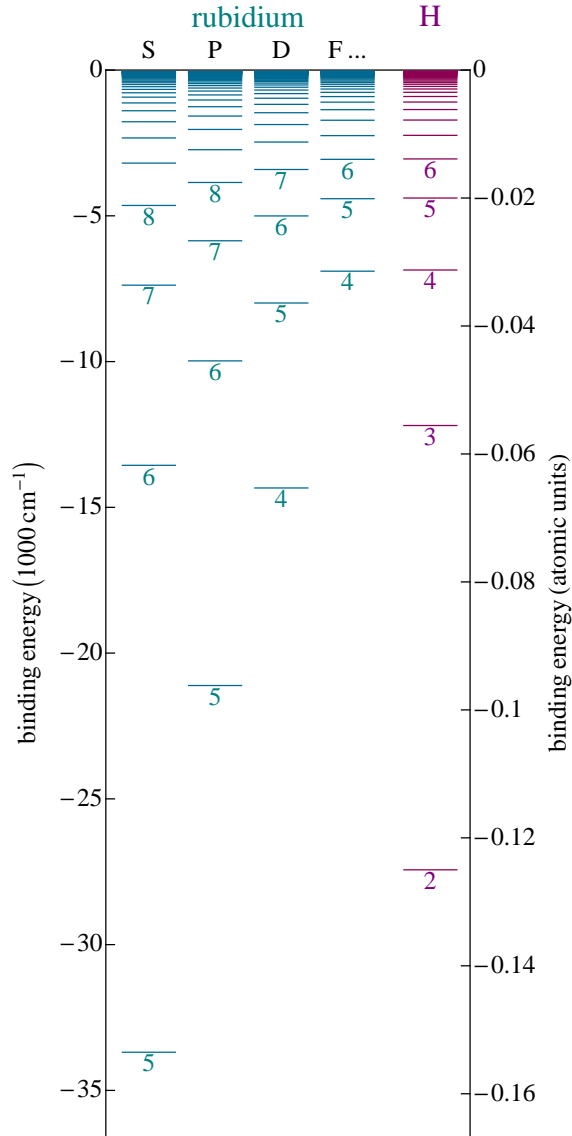
Figure 1.1: Energy levels of rubidium and hydrogen. The degeneracy of the energies levels for different angular momenta in hydrogen is lifted for alkali atoms like rubidium due to the different quantum defects δ_l which come from the finite size of the ionic core. The principal quantum number n is indicated under the levels. For angular momentum quantum numbers $l \gtrsim 3$ (i.e. starting from F) the binding energies hardly differ from the hydrogenic ones since the corresponding quantum defects are practically zero. The energies are calculated with Eq. (1.1) for large n, they are extracted from the NIST-database for small n [61].

Since A_{fi} is proportional to the cubed energy separations, spontaneous decays with the highest frequencies dominate the decay rate and therefore dominate its dependence on n. Due to the dipole selection rules only transitions that satisfy $l' = l - 1$ are allowed to first order. Low l states therefore decay into the lowest $l - 1$ state with a small principal quantum number $n > l$ and large binding energy (compare the Fig. 1.1). The frequency of these transitions become independent of n for $n \to \infty$ since the energy of the initial state hardly changes for large n. The A coefficients then only depend on the squared dipole matrix element which in case of largely differing radial wave functions is proportional to n^{-3} and we find

$$\tau_{\text{low } l} \propto n^3 \ . \tag{1.5}$$

This reasoning does not apply for large l states since the final state, that must satisfy $l' = l - 1$, cannot have a small principal quantum number because it is always $n > l - 1$. In the extreme case, $l = n - 1$, there is only one decay channel left, namely to the final state with the quantum numbers $n' = n - 1$, $l' = n - 2$. The energy difference between adjacent n-states is very small, $E_{if} \sim n^3$. The dipole matrix element, in contrast, is very large since the radial wave functions greatly overlap, $\langle n - 1, n - 2 | \boldsymbol{r} | n, n - 1 \rangle \sim n^2$. We find

$$\tau_{\text{high } l} \propto (n^{-3})^3 \cdot (n^2)^2 = n^5 \ . \tag{1.6}$$

High angular momentum states, and in particular circular Rydberg states with maximal orbital and magnetic quantum numbers, $l = m_l = n - 1$, not only feature such long radiative lifetimes, they also prove to be the states with the highest anisotropy, and their behavior is closest to a classical localized electronic motion in a circular orbit like in Bohr's picture. Circular Rydberg atoms have therefore found numerous applications and they also play a major role in this thesis. We describe different ways of creating circular Rydberg atoms in the next section.

1.2 Creation of circular Rydberg states

Rydberg states with maximum angular momentum (l) and magnetic (m_l) quantum numbers are called *circular*, or more precisely *oriented-circular-orbit* Rydberg states (in comparison to *aligned-circular-orbit* states if $|m_l|$ is maximal and m_l can hence be also maximally negative). They have the most remarkable properties among Rydberg states. Their electron density is peaked along a circle that corresponds to a Bohr orbit and circular states are hence semiclassical objects situated at the frontier of classical and quantum mechanics. From this particular shape of the orbital, highly anisotropic collision cross sections and a highly anisotropic behavior with respect to external perturbations are expected [62]. Circular Rydberg states possess the largest magnetic moments, the are subject to the smallest (quadratic) Stark effect in contrary to a huge (linear) Stark effect for ordinary Rydberg atoms. They can only decay into the nearest less-excited circular state which makes them useful approximations to two-level systems in cavities. This single decay channel is also responsible for the longest radiative lifetimes in a given n-manifold ($\tau \sim n^5 \cdot 10^{-10}$ s), as has been explained in the previous section.

The preparation of circular Rydberg states has been delayed for a long time due to the difficulty of transferring a large number of angular momentum units into an atom. Since optical sequential excitation with photons of different color is out of reach experimentally,

the methods of preparation either tune the transitions such that only a monochromatic source is sufficient or they try to circumvent the dipole selection rule $\Delta l = 1$.

We will review the different schemes for creating circular Rydberg atoms that have been proposed and applied starting with the *adiabatic microwave transfer method* of Hulet and Kleppner. We then describe the *adiabatic crossed-fields method* proposed by Delande and Gay and the *adiabatic RF field method* proposed by Molander et al.. We close by elucidating that the latter are formally equivalent and present a way to get the best of both methods.

Adiabatic rapid passages in a changing electric field

Using the adiabatic microwave transfer method (also called *adiabatic rapid passage* technique), Hulet and Kleppner produced Li oriented circular states [63]. More precisely, the excited states are Stark states with the parabolic quantum numbers $n_1 = 0$, $n_2 = 0$ and $|m| = n - 1$. After a laser excitation to the lowest level of the n Stark manifold in an electric field the method employs this field (Stark effect $\sim |m|$) to control a sequence of adiabatic rapid passages through single photon resonances. This method is limited to atoms with a regular Stark structure, namely the light alkali and alkaline-earth atoms, and to moderate principal quantum numbers ($n \approx 25$).

These shortcomings are overcome by a modified adiabatic rapid passage preparation technique for rubidium described by Nussenzveig et al. [64] which only prepares oriented circular states, meaning $m_l = +l$. A Stark switching method is used to reach the initial state of the adiabatic rapid passage process, $|n = 50, m = 3, n_1 = 0\rangle$. The following circularization with a RF field while slowly decreasing the electric field strength is completed within 5 μs. It ends up in the $|m = 49, n_1 = 0\rangle$ circular state.

Crossed-field method

The adiabatic crossed-fields method was first described by Delande et al. [65], and it was first realized by Hare et al. [66]. Atoms are excited to the highest energy Stark state in a strong electric field $\boldsymbol{F}$. This field is then switched off adiabatically in the presence of a constant magnetic field $\boldsymbol{B}$ perpendicular to $\boldsymbol{F}$. By continuity of the energy level in the combined electro-magnetic manifold down to zero electric field, the atoms are finally left in the highest level of the Zeeman manifold which is the circular state with $m = n - 1$. The scheme does not involve a series of adiabatic rapid passages as the energy levels are always equally spaced. The advantages of the technique are consequentially less stringent conditions for adiabaticity than in the rapid passage type schemes described above. A magnetic field is needed (≈ 10 G) instead of one or several microwave sources.

The method exploits the SO(4) symmetry of hydrogen which is responsible for the degeneracy of the n^2 sublevels of the n-manifold. Both the orbital angular momentum $\boldsymbol{L}$ and the Runge-Lenz vector $\boldsymbol{A}_L$ are constants of motion. In the presence of both an electric and a magnetic field, the problem is neither separable in the parabolic representation nor in the spherical representation. However, for electric and magnetic fields small enough, that second-order effects can be neglected, the z-components of $\boldsymbol{L}$ and $\boldsymbol{A}_L$ are conserved and a common basis can be found, as was pointed out by Pauli [67, 68]. The energetically uppermost state of this basis is the circular state in the Zeeman limit (i.e. when the coupling to the magnetic field dominates the coupling to the electric field). The key to the
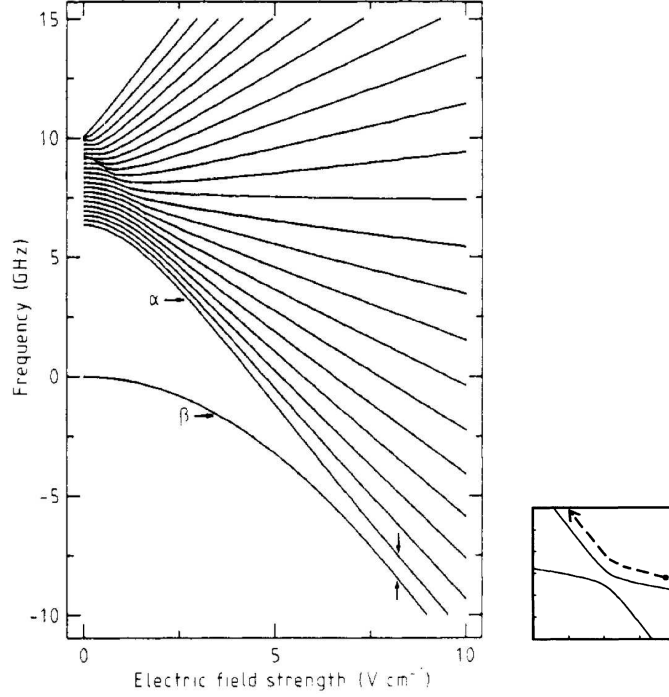
Figure 1.2: Eigenvalues of the RF-dressed Rydberg states in the frame rotating with the RF as a function of the field strength. α is the adiabatic continuation of the zero field circular state, whereas β is the dressed state adiabatically linked to the d state. At the field strength where the avoided crossing occurs (indicated by the vertical arrows) the optical excitation from the $l = 0$ takes place. An adiabatic RF turn off converts the dressed state into the circular state. The plot on the right schematically illustrates where the laser excitation takes place (indicated by a point) and how the adiabatic passage through the avoided crossing takes place when the field is slowly reduced (dotted arrow). Plots are taken from [69, 70].

crossed-fields method is that this state is accessible to laser excitation from low-lying states for dominating electric field since it is a $m = 0$ state in the Stark limit.

adiabatic RF field technique

Another method to selectively prepare the oriented circular states is the adiabatic RF field method proposed by Molander et al. [69] and, in a slightly modified form, applied by Cheng et al. [70]. It is based on a radio-frequency (RF) field that dresses the atom for the optical excitation. The dressed states are linear combinations of many different angular momentum states, but every one of them continuously becomes an angular momentum eigenstate as the RF field is turned off adiabatically. The dressed eigenvalues of the Rydberg states (in a frame rotating at the frequency of the field) are shown as a function of the RF field strength in Fig. 1.2.

The RF field only couples aligned states, $l = m_l$, since it is circularly polarized and $m = 0$ transitions can be disregarded. Due to the large quantum defect of S and P states, the RF field does not mix those states with the rest of the manifold. The field has to supply $n - 3$ units of angular momentum to go from the d to the circular state and its frequency

is therefore chosen near this $n - 3$ multi-photon resonance. It has to be far enough from resonance that the separation of the dressed states is sufficiently large to allow the optical excitation of only the desired state and to allow for adiabatic turnoff.

The dressed state marked with an α in Fig. 1.2, which is the adiabatic continuation of the zero field circular state, undergoes an avoided crossing with the dressed state β which is linked to the d state. The different energetic distance of the latter is due to the quantum defect for $l = 2$ which vanishes for states with higher l. At the field strength for which this avoided crossing occurs (indicated by the arrows in Fig. 1.2), the Rydberg atom is excited into the dressed state α by a resonantly enhanced two-photon absorption using a P state as an intermediate state. This can either happen by a pulsed or a continuous wave optical excitation.

An experimental implementation of this idea, see Ref. [70], uses a microwave field instead of the RF source and features minimal optical selectivity requirements and efficient and rapid transfer to the circular state.

We note that the crossed-field and the adiabatic-RF-field techniques are formally equivalent. This is show by Chen et al. [71] who point out that the RF field becomes static in the rotating coordinate system whereas the rotational motion is equivalent to a magnetic field according to the Larmor theorem. The switching of the RF field in the adiabatic RF field method is hence the counterpart of the electric field switching in the crossed-field method. In combining the advantages of both techniques the authors suggest a complementary method using an RF field and a static electric field.

2 Ultracold Rydberg atoms in a Ioffe-Pritchard trap

In a highly anisotropic magnetic field configuration like that of a Ioffe-Pritchard trap the strength of the magnetic field can vary significantly over the extension of a Rydberg atom. The large size of Rydberg atoms can therefore modify the way they couple to the magnetic field compared to the coupling of ground state atoms. We incorporate the large extension of the atoms into our description by modeling a Rydberg atom by two particles, a valence electron and an ionic core. This is particularly appropriate for alkali atoms that are commonly used in Rydberg experiments. We include into our model the coupling of the electronic and the center of mass motion of the atom and hence do not resort to the infinitely heavy mass approximation. While the inclusion of the fine-structure and quantum defects can be readily done, it turns out not to be necessary for high angular momentum electronic states on which we will be focusing on. The derivation of the Hamiltonian for a highly excited atom in a Ioffe-Pritchard field configuration lays the foundation for the following chapters.

In particular we proceed as follows. In Section 2.1 we introduce the two-body approach into the minimal coupling Hamiltonian. We adopt relative and center of mass coordinates and use a unitary transformation to simplify the coupling terms. We narrow our considerations to the Ioffe-Pritchard field configuration in Section 2.2 before we analyze the symmetries of the Hamiltonian in Section 2.3. We project the Hamiltonian to a hydrogenic manifold of a single principal quantum number n and scale it to eliminate distracting parameter dependencies of the couplings. In Section 2.4 we eventually deal with the remaining couplings by adiabatically separating the relative and the center of mass dynamics that take place on very different time scales.

Most of the results presented here and in Chapter 4 are published in Refs. [72, 73].

2.1 Two-body Hamiltonian for an alkali Rydberg atom in a magnetic field

The large distance of the highly excited valence electron (particle 1) from the remaining closed-shell ionic core of an alkali Rydberg atom (particle 2) renders it possible to model the mutual interaction by an effective potential which is assumed to depend only on the distance of the two particles. For alkali atoms, in particular, whose cores possess zero total angular momentum and zero total spin, the only essential difference to the Coulombic case is due to the finite size of the core. In any case, the effective potential $V(r)$ only noticeably differs from the pure Coulomb potential at small distances r. States of high *electronic* angular momenta l, on which we focus in this thesis, almost exclusively probe the Coulombic tail of this potential.

The coupling of the charged particles to the external magnetic field is introduced via

the minimal coupling, $\boldsymbol{p} \rightarrow \boldsymbol{p} - q\boldsymbol{A}$, where q is the charge of the particle and $\boldsymbol{A}$ is a vector potential belonging to the magnetic field $\boldsymbol{B}$. Including the coupling of the magnetic moments to the external field ($\boldsymbol{\mu}_1$ and $\boldsymbol{\mu}_2$ originate from the electronic and nuclear spin, respectively), our initial Hamiltonian reads

$$
\begin{aligned}
H_{init} \quad = \quad & \frac{1}{2M_1}\left(\boldsymbol{p}_1 - q_1\boldsymbol{A}(\boldsymbol{r}_1)\right)^2 + \frac{1}{2M_2}(\boldsymbol{p}_2 - q_2\boldsymbol{A}(\boldsymbol{r}_2))^2 \\
& +V(|\boldsymbol{r}_1 - \boldsymbol{r}_2|) - \boldsymbol{\mu}_1 \cdot \boldsymbol{B}(\boldsymbol{r}_1) - \boldsymbol{\mu}_2 \cdot \boldsymbol{B}(\boldsymbol{r}_2) \, .
\end{aligned} \tag{2.1}
$$

We use atomic units, detailed in the appendix, except when stated otherwise. We do not take into account spin-orbit-coupling and relativistic mass changes. The difference in energy shift for adjacent, large angular momentum states ($l, l \pm 1$) due to these relativistic corrections is $\Delta W_{FS} = \alpha^2/2n^5$ [74], where α is the fine structure constant, and therefore negligible for Rydberg states. At $n = 30$ we find the correction $\Delta W_{FS} = 1.1 \times 10^{-12}$ a.u.. To give an idea of the scope of this approximation we anticipate a result from Chapter 4: The energy gap between two adjacent high-l electronic states is approximately $\Delta E = B/2$. Demanding $\Delta W_{FS}/\Delta E \ll 1$ results in constraining the Ioffe field strength B to be much larger than 5 mG (for $n = 50$ B must be a lot larger than 0.4 mG).

Before we focus on the Ioffe-Pritchard configuration we first examine a general field $\boldsymbol{B}$ composed of a constant term $\boldsymbol{B}_c$, a linear term $\boldsymbol{B}_l$ and higher order terms, $\boldsymbol{B} = \sum \boldsymbol{B}_i$. The vector potential shall satisfy the Coulomb gauge. The squared terms can then be simplified taking advantage of the vanishing commutator $[\boldsymbol{A}(\boldsymbol{r}_1), \boldsymbol{p}_1]$ to obtain $(\boldsymbol{p}_1 - q\boldsymbol{A}(\boldsymbol{r}_1))^2 = \boldsymbol{p}_1^2 - 2q\boldsymbol{A}(\boldsymbol{r}_1) \cdot \boldsymbol{p}_1 + q^2\boldsymbol{A}(\boldsymbol{r}_1)^2$. In the so-called symmetric gauge the vector potential of a constant magnetic field is given by $\boldsymbol{A}_c(\boldsymbol{r}_1) = 1/2\,\boldsymbol{B}_c \times \boldsymbol{r}_1$. The analogon for a linear field is $\boldsymbol{A}_l(\boldsymbol{r}_1) = 1/3\boldsymbol{B}_l(\boldsymbol{r}_1)\times\boldsymbol{r}_1$. It can be proven that the vector potential of an arbitrary magnetic field can be expanded in a corresponding form [75] permitting a representation of the vector potential as a cross product $\boldsymbol{A}(\boldsymbol{r}_1) = \sum_i \boldsymbol{A}_i(\boldsymbol{r}_1) = \tilde{\boldsymbol{B}}(\boldsymbol{r}_1) \times \boldsymbol{r}_1$, where $\tilde{\boldsymbol{B}}(\boldsymbol{r}_1) = \sum g_i\boldsymbol{B}_i(\boldsymbol{r}_1)$ and $i \in \{c, l, \dots\}$ denotes the order of the corresponding terms of $\boldsymbol{A}$ and $\boldsymbol{B}$ with respect to spacial coordinates. g_i are the coefficients $\frac{1}{2}$, $\frac{1}{3}$ etc. The particular form of this potential and the vanishing divergence of magnetic fields admit the simplification

$$
\boldsymbol{A}(\boldsymbol{r}_1) \cdot \boldsymbol{p}_1 = (\boldsymbol{r}_1 \times \boldsymbol{p}_1) \cdot \tilde{\boldsymbol{B}}(\boldsymbol{r}_1) = \boldsymbol{L}_1 \cdot \tilde{\boldsymbol{B}}(\boldsymbol{r}_1) \quad , \tag{2.2}
$$

where we exemplarily defined the angular momentum of particle 1, $\boldsymbol{L}_1 = \boldsymbol{r}_1 \times \boldsymbol{p}_1$.

Since the interaction potential depends only on the distance of the two particles, it is natural to introduce relative and center of mass coordinates, $\boldsymbol{r}_1 = \boldsymbol{R} + (M_2/M)\boldsymbol{r}$ and $\boldsymbol{r}_2 = \boldsymbol{R} - (M_1/M)\boldsymbol{r}$ with the total mass $M = M_1 + M_2$. If no external field was present, the new coordinates would decouple the internal degrees of freedom from the external center of mass ones. Yet even a homogeneous magnetic field couples the relative and the center of mass motion [76, 77]. For neutral systems in static homogeneous magnetic fields, however, a so-called *pseudoseparation* can be performed providing us with an effective Hamiltonian for the relative motion, that depends on the center of mass motion only parametrically via the eigenvalues of the pseudomomentum [77–80] which is associated with the center of mass motion. Such a procedure is not available in the present case of a more general

inhomogeneous field. In the new coordinate system the Hamiltonian (2.1) becomes

$$H = H_0 + \boldsymbol{L}_1 \tilde{\boldsymbol{B}}(\boldsymbol{R} + \frac{M_2}{M}\boldsymbol{r}) - \boldsymbol{L}_2 \tilde{\boldsymbol{B}}(\boldsymbol{R} - \frac{M_1}{M}\boldsymbol{r})$$
$$- \boldsymbol{\mu}_1 \boldsymbol{B}(\boldsymbol{R} + \frac{M_2}{M}\boldsymbol{r}) - \boldsymbol{\mu}_2 \boldsymbol{B}(\boldsymbol{R} - \frac{M_1}{M}\boldsymbol{r}) + \mathcal{O}(\boldsymbol{A}^2) \ , \quad (2.3)$$

where the angular momenta of the particles read

$$\boldsymbol{L}_1 = (M_1/M)\boldsymbol{L}_R + (M_2/M)\boldsymbol{L}_r + \boldsymbol{R} \times \boldsymbol{p} + (m/M)\boldsymbol{r} \times \boldsymbol{P}$$
$$\boldsymbol{L}_2 = (M_2/M)\boldsymbol{L}_R + (M_1/M)\boldsymbol{L}_r - \boldsymbol{R} \times \boldsymbol{p} - (m/M)\boldsymbol{r} \times \boldsymbol{P}$$

(see also Ref. [49]), and the terms that do not depend on the field are summarized to $H_0 = \frac{\boldsymbol{p}^2}{2m} + \frac{\boldsymbol{P}^2}{2M} + V(\boldsymbol{r})$. Here, $\boldsymbol{L}_r = \boldsymbol{r} \times \boldsymbol{p}$, $\boldsymbol{L}_R = \boldsymbol{R} \times \boldsymbol{P}$, and the reduced mass $m = M_1 M_2 / M$ have been introduced.

To simplify the Hamiltonian we apply the unitary transformation

$$U = \exp\left\{ \frac{i}{2} \boldsymbol{B}_c \times \boldsymbol{r} \cdot \boldsymbol{R} \right\} \qquad (2.4)$$

that reduces the complexity of the terms coupling relative and center of mass dynamics generated by the homogeneous field component. The transformation only alters terms involving momentum operators, any operator commuting with both coordinate operators $\boldsymbol{R}$ and $\boldsymbol{r}$ is invariant under the action of U. We use the Baker-Campbell-Hausdorff formula

$$e^V W e^{-V} = \sum_{m=0}^{\infty} \frac{1}{m!} W_m \qquad (2.5)$$

with V and W being linear operators, $e^V := \sum_{k=0}^{\infty} \frac{1}{k!} V^k$ and $W_m = [V, W]_m := [V, [V, W]_{m-1}]$, $W_0 := W$. The kinetic energy operators transform as follows:

$$U^\dagger \boldsymbol{p}^2 U = U^\dagger \boldsymbol{p} U U^\dagger \boldsymbol{p} U = (\boldsymbol{p} - \frac{1}{2}(\boldsymbol{B}_c \times \boldsymbol{R}))^2 = \boldsymbol{p}^2 - (\boldsymbol{B}_c \times \boldsymbol{R}) \cdot \boldsymbol{p} + \mathcal{O}(B_c^2 R^2) \ ,$$

$$U^\dagger \boldsymbol{P}^2 U = U^\dagger \boldsymbol{P} U U^\dagger \boldsymbol{P} U = (\boldsymbol{P} + \frac{1}{2}(\boldsymbol{B}_c \times \boldsymbol{r}))^2 = \boldsymbol{P}^2 + (\boldsymbol{B}_c \times \boldsymbol{r}) \cdot \boldsymbol{P} + \mathcal{O}(B_c^2 r^2) \ . \qquad (2.6)$$

The terms quadratic in $\boldsymbol{B}_c$ are suppressed as long as $\frac{1}{4}(\boldsymbol{B}_c \times \boldsymbol{R})^2 \ll (\boldsymbol{B}_c \times \boldsymbol{R}) \cdot \boldsymbol{p}$ which is equivalent to

$$|X|, |Y| \ll \frac{4}{Bn} \ . \qquad (2.7)$$

The transformed field-free Hamiltonian H_0 therefore reads

$$U^\dagger H_0 U = H_0 + \frac{1}{2}\boldsymbol{B}_c \left(-\frac{1}{m}\boldsymbol{R} \times \boldsymbol{p} + \frac{1}{M}\boldsymbol{r} \times \boldsymbol{P} \right) + \mathcal{O}(B_c^2 R^2, B_c^2 r^2) \ . \qquad (2.8)$$

The term coming from the linear magnetic field, $\boldsymbol{A}_l(\boldsymbol{R} + \boldsymbol{r}) \cdot \boldsymbol{p}$, is invariant under the action of U since the only differential operator involved is p_z. The exponent of the transformation U does not include z and the crucial commutator therefore vanishes. The transformation of the remaining terms generates exclusively additional terms, that are quadratic with respect

to the magnetic field. They are specified for the case of a Ioffe-Pritchard field configuration in Eq. (6.3) and a condition for their neglect similar to (2.7) is formulated in Eq. (6.4).

We now exploit the fact that the mass of the ionic core is much larger than the mass of the valence electron. Only magnetic field dependent terms of the order of the inverse light mass $1/M_1 \approx 1/m$ ($M_1 = 1$ in atomic units) are being kept. Since we are dealing with ultracold atoms it is even $\langle \boldsymbol{P}/M \rangle \ll \langle \boldsymbol{p}/m \rangle$, which allows us to neglect the center of mass momentum dependent terms emerging from (2.1) after the introduction of the coordinates $\boldsymbol{r}$ and $\boldsymbol{R}$. We arrive at the Hamiltonian

$$
\begin{aligned}
U^\dagger H U =& \frac{\boldsymbol{P}^2}{2M} + \frac{\boldsymbol{p}^2}{2} + U^\dagger V(\boldsymbol{r}) U + \frac{1}{2}\, \boldsymbol{L_r} \cdot \boldsymbol{B}_c \\
& + \boldsymbol{A}_l(\boldsymbol{R}+\boldsymbol{r}) \cdot \boldsymbol{p} + (\boldsymbol{L_r} + \boldsymbol{R} \times \boldsymbol{p}) \cdot \tilde{\boldsymbol{B}}_n(\boldsymbol{R}+\boldsymbol{r}) \\
& - \boldsymbol{\mu}_1 \cdot \boldsymbol{B}(\boldsymbol{R}+\boldsymbol{r}) - \boldsymbol{\mu}_2 \cdot \boldsymbol{B}(\boldsymbol{R}) \,.
\end{aligned}
\tag{2.9}
$$

The diamagnetic terms in the Hamiltonian (2.1) which are proportional to $\boldsymbol{A}^2$ (and herewith proportional to $\boldsymbol{B}^2$, see Eq. (2.2)) have been neglected: Due to the unitary transformation U, $\boldsymbol{R}$-dependent terms that are quadratic in the Ioffe field strength B do not occur and only an electronic term $B^2(x^2 + y^2)/8$ remains whose typical energy contribution amounts to $B^2 n^4/8 \approx 10^5 B^2$ for $n = 30$. Besides we obtain a term quadratic in the field gradient G. The term quadratic in the Ioffe field is negligible in comparison with the dominant shift due to the linear Zeeman term as long as B is significantly smaller than 10^4 Gauss which is guaranteed in our case. Moreover, the center of mass coordinate dependence of this diamagnetic term is much weaker than the center of mass coordinate dependence of the terms linear in the field gradient. The term quadratic in the field gradient can be neglected in comparison with the corresponding linear term. Up to now we did not use the explicit form of the Ioffe-Pritchard field configuration (in anticipation of the special field configuration we leave the term containing $\boldsymbol{A}_l$ in (2.9) in its original form.)

2.2 Ioffe-Pritchard field configuration

Two widely spread magnetic field configurations that exhibit a local field minimum and serve as key ingredients for the trapping of weak-field seeking atoms are the three-dimensional quadrupole and the Ioffe-Pritchard configuration. The Ioffe-Pritchard configuration resolves the problem of particle loss due to spin flip at the point of zero field by means of an additional constant magnetic field. A macroscopic realization uses four parallel current carrying Ioffe bars which generate the quadrupole field. Encompassing Helmholtz coils create the additional constant field and potentially the longitudinal confinement depending on the geometry. There are many alternative layouts, the field of a clover-leaf trap, for example, features the same expansion around the origin [81]. On a microscopic scale the Ioffe-Pritchard trap has been implemented on atom chips by a Z-shaped wire [50, 52].

The vector potential and the magnetic field of the macroscopic Ioffe-Pritchard trap read

$$\boldsymbol{A} = \underbrace{\frac{B}{2} \begin{pmatrix} -y \\ x \\ 0 \end{pmatrix}}_{=\boldsymbol{A}_c} + \underbrace{G \begin{pmatrix} 0 \\ 0 \\ xy \end{pmatrix}}_{=\boldsymbol{A}_l} + \boldsymbol{A}_q , \tag{2.10}$$

$$\boldsymbol{B} = \underbrace{B \begin{pmatrix} 0 \\ 0 \\ 1 \end{pmatrix}}_{=\boldsymbol{B}_c} + \underbrace{G \begin{pmatrix} x \\ -y \\ 0 \end{pmatrix}}_{=\boldsymbol{B}_l} + \boldsymbol{B}_q . \tag{2.11}$$

where $\boldsymbol{A}_q = \frac{Q}{4}(x^2 + y^2 - 4z^2)(y\mathbf{e}_x - x\mathbf{e}_y)$ and $\boldsymbol{B}_q = Q(-2xz\mathbf{e}_x - 2yz\mathbf{e}_y + (-x^2 - y^2 + 2z^2)\mathbf{e}_z)$. $\boldsymbol{B}_c$ is the constant field created by the Helmholtz coils with B being the Ioffe field strength. $\boldsymbol{B}_l$ originates from the Ioffe bars and depends on the field gradient G. $\boldsymbol{B}_q$ designates the quadratic term generated by the Helmholtz coils whose magnitude, compared to the first Helmholtz term, can be varied by changing the geometry of the trap, $Q = B\tilde{Q} = B \cdot \frac{3}{2}(4D^2 - R^2)/(R^2 + D^2)^2$, where R is the radius of the Helmholtz coils, and $2D$ is their distance from each other. For a more detailed discussion of the geometry parameter see Section 6.1.

If we now insert the special Ioffe-Pritchard field configuration using Eqs. (2.10) and (2.11) into the transformed Hamiltonian (2.9) we obtain

$$\begin{aligned} H_{IP} = & H_A + \boldsymbol{P}^2/2M + BL_z/2 + G(x + X)(y + Y)p_z \\ & + Q/4\big[((x + X)p_y - (y + Y)p_x) \\ & \qquad \cdot ((x + X)^2 + (y + Y - 2(z + Z))(y + Y + 2(z + Z)))\big] \\ & - \boldsymbol{\mu}_1 \cdot \boldsymbol{B}(\boldsymbol{R} + \boldsymbol{r}) - \boldsymbol{\mu}_2 \cdot \boldsymbol{B}(\boldsymbol{R}) , \end{aligned} \tag{2.12}$$

where $H_A = \boldsymbol{p}^2/2 - 1/r$ is the operator for a field-free atom. The well known Zeeman term $BL_z/2$ comes from the uniform Ioffe field generated by the Helmholtz coils. The following term, involving the field gradient G, arises from the linear field generated by the Ioffe bars and couples the relative and center of mass dynamics. The part in the squared brackets originates from the quadratic term, again created by the coils. It is the only one that depends on the Z coordinate and we will see below that it vanishes for a certain ratio of radius and distance of the current-carrying coils (Helmholtz configuration). The last term couples the spin of particle 2 to the magnetic field. Since the electronic spins of closed shells combine to zero, the spin of particle two is the *nuclear* spin only. Even though $\boldsymbol{\mu}_2$ is smaller than $\boldsymbol{\mu}_1$ by a factor of m_e/m_p, we will still keep the term $-\boldsymbol{\mu}_2 \cdot \boldsymbol{B}$ since it is the only one containing the nuclear spin and it is therefore essential for a proper symmetry analysis.

2.3 Symmetries, scaling, and the approximation of a single *n*-manifold

Our Hamiltonian is invariant under a number of symmetry transformations U_S that are composed of the elementary operations listed in Tab. 2.1. The parity operations P_j, $j \in$

Table 2.1: Symmetry operation nomenclature. P_j, $\hat{S}_j$, and $\hat{\Sigma}_j$ are exemplified by $j = x$, but hold of course also for $j = y, z$.

operator		operation
P_x	x parity	$x \to -x,\ X \to -X$
$\hat{S}_x$	electronic spin x operator	$S_y \to -S_y,\ S_z \to -S_z$
$\hat{\Sigma}_x$	nuclear spin x operator	$\Sigma_y \to -\Sigma_y,\ \Sigma_z \to -\Sigma_z$
I_{xy}	coordinate exchange	$x \leftrightarrow y,\ X \leftrightarrow Y$
S_{xy}	electronic spin component exchange	$S_x \to -S_y,\ S_y \to S_x$
Σ_{xy}	nuclear spin component exchange	$\Sigma_x \to -\Sigma_y,\ \Sigma_y \to \Sigma_x$
T	conventional time reversal	$A \to A^*$

$\{x, y, z\}$, are defined by their action on the spatial laboratory coordinates of the particles which translates one-to-one to center of mass and relative coordinates. In order to exchange the x and y components of the electronic spin we introduce the operator

$$S_{xy} = \begin{pmatrix} -i & 0 \\ 0 & 1 \end{pmatrix},$$

where $S_{xy}S_{xy}^* = 1$. T represents the conventional time reversal operator for spinless particles which, in the spatial representation, corresponds to complex conjugation. Our unitary symmetries are

$$P_x P_y \hat{S}_z \hat{\Sigma}_z \tag{2.13a}$$

$$P_y P_z I_{xy} S_{xy} \Sigma_{xy} \tag{2.13b}$$

$$P_x P_z I_{xy} S_{xy}^* \Sigma_{xy}^* . \tag{2.13c}$$

The Hamiltonian is also left invariant under the anti-unitary symmetry transformation

$$TP_y. \tag{2.14}$$

By consecutively applying the latter operator and the unitary operators (2.13a), (2.13b) and (2.13c) it is possible to create further anti-unitary symmetries:

$$TP_x \hat{S}_z \hat{\Sigma}_z \tag{2.15a}$$

$$TP_z I_{xy} S_{xy} \Sigma_{xy} \tag{2.15b}$$

$$TP_x P_y P_z I_{xy} S_{xy}^* \Sigma_{xy}^*. \tag{2.15c}$$

Paying regard to the fact that $S_{xy}^2 = -\hat{S}_z$ and $\Sigma_{xy}^2 = -\hat{\Sigma}_z$ and that T neither commutes with $\hat{S}_y$ nor with S_{xy} and Σ_{xy}, one finds that the operators (2.13a-2.15c) form a symmetry group.

If no Ioffe field is present ($B = 0$), eight additional symmetries can be found leaving the Hamiltonian invariant. For an effective one particle approach (and the corresponding one particle symmetries) this situation has been discussed in Ref. [82].

As indicated before, the quadratic magnetic field term $\boldsymbol{B}_q$ can be tuned by changing the trap geometry and can provide confinement in longitudinal (Z-)direction. In the following, however, we consider a trap in Helmholtz configuration where $2D = R$ and $\boldsymbol{B}_q$ is zero. In this case the term in the squared brackets of the Hamiltonian (2.12) drops out and the Z coordinate is cyclic. The corresponding conjugated momentum P_z is consequently conserved and the longitudinal motion is integrated by simply employing plane waves $|k_Z\rangle = \exp\{iZk_Z\}$. Even for non-Helmholtz configurations of the trap the term can be negligible. The constraints for this approximation to be valid can be obtained by comparing the above-mentioned term in squared brackets with the Zeeman term, $BL_z/2$. Estimating $\langle x \rangle \approx n^2$, $\langle xp_y \rangle \approx \langle yp_x \rangle \approx n$, and using $|Q| \lesssim B/(D^2 + R^2)$ we find

$$D^2 + R^2 \gg n^4 \qquad \text{and} \qquad (2.16)$$

$$\sqrt[3]{n(D^2 + R^2)} \gg |X|, |Y| \, , \qquad (2.17)$$

where D and R characterize the trap geometry. For one Rydberg atom around the trap center Eqs. (2.16) and (2.17) are easily fulfilled. We are then left with the Hamiltonian

$$H = H_A + (P_x^2 + P_y^2)/2 + H_e \, , \qquad (2.18)$$

where the electronic Hamiltonian reads

$$H_e = BL_z/2 + G(x + X)(y + Y)p_z - \boldsymbol{\mu}_1 \cdot \boldsymbol{B}(\boldsymbol{R} + \boldsymbol{r}) \, . \qquad (2.19)$$

For all laboratory fields one finds the magnetic field strength B and the magnetic field gradient G to be a lot smaller than 1. Our Hamiltonian (2.12) is thus dominated by H_A. The energies of the field-free spectrum $E_A^n = -1/2n^2$ are n^2-fold degenerate. We can assume the Ioffe-Pritchard field not to couple adjacent n-manifolds as long as the energetic distance of adjacent field-free energies is a lot larger than the coupling energy of the atom to the field, $|E_A^n - E_A^{n\pm1}|/E_{Zee} \gg 1$. The resulting constraints $B \ll n^{-4}$, $G \ll n^{-6}$ and $GR \ll n^{-4}$ yield $B \ll 2900$ G, $G \ll 6 \cdot 10^6$ T/m for $n = 30$ and $R \ll 2.9$ mm if we additionally assume the field gradient G to be as large as 100 T/m. In our parameter regime each n-manifold can therefore be considered separately. We thus project the full Hamiltonian on the hydrogenic eigenfunctions $|\alpha\rangle = |n, l, m_l, m_s\rangle$, $H_A|\alpha\rangle = E_A^n|\alpha\rangle$, with fixed principal quantum number n, that cover an entire n-manifold. l denotes the orbital angular momentum quantum number, m_l the one of its z component L_z and m_s stands for the quantum number of the electronic spin.

Working in a single n-manifold we can reformulate the term in the Hamiltonian (2.18) involving the field gradient G into a more compact form. We first consider the commutator $[yz, H_A] = [yz, \boldsymbol{p}^2]/2 = i(yp_z + zp_y)$. This yields

$$\langle\alpha|yp_z|\alpha'\rangle + \langle\alpha|zp_y|\alpha'\rangle = -i\langle\alpha|[yz, H_A]|\alpha'\rangle = 0 \, , \qquad (2.20)$$

since $|\alpha\rangle$ and $|\alpha'\rangle$ are eigenkets to the same eigenvalue E_n. Establishing the relation to the orbital angular momentum operator via $yp_z = L_x + zp_y$ results in

$$(\langle\alpha|yp_z|\alpha'\rangle) = \frac{1}{2}(\langle\alpha|L_x|\alpha'\rangle) \, . \qquad (2.21)$$

The same procedure can be applied to xp_z leading to

$$(\langle\alpha|xp_z|\alpha'\rangle) = -\frac{1}{2}(\langle\alpha|L_y|\alpha'\rangle) \,. \tag{2.22}$$

Furthermore $\langle\alpha|XYp_z|\alpha'\rangle = 0$ since $p_z \sim [H_A, z]$, and eventually we can write

$$G(x + X)(y + Y)p_z = G(xyp_z + XL_x/2 - YL_y/2) \,, \tag{2.23}$$

where we omitted the bracketing alphas, but keep in mind that the above identity holds in a single n-manifold only. The electronic term xyp_z can also be expressed with angular momentum operators within one n-manifold. The required commutator and the alternative formulation can be found in Eqs. (7.5) and (7.6), respectively.

In order to remove the separate dependencies on the field parameters B, G, and on the mass M from the coupling terms, we introduce scaled center of mass coordinates, $\mathbf{R} \to \gamma^{-\frac{1}{3}}\mathbf{R}$, with $\gamma = GM$, and simultaneously we introduce the energy unit $\epsilon = \gamma^{\frac{2}{3}}/M$. Introducing the effective magnetic field

$$\boldsymbol{G}(X,Y) = \begin{pmatrix} X \\ -Y \\ \zeta \end{pmatrix}, \quad \zeta = B/\epsilon \,, \tag{2.24}$$

and omitting the constant energy offset E_A^n, the Hamiltonian within a single n-manifold can be given the advantageous form

$$\mathcal{H} = \frac{P_x^2 + P_y^2}{2} + \boldsymbol{\mu} \cdot \boldsymbol{G}(X,Y) + \gamma^{\frac{1}{3}}(xyp_z + xS_x - yS_y). \tag{2.25}$$

The first term is the center of mass kinetic energy. $\boldsymbol{\mu}$ is the $2n^2$-dimensional matrix representation of the total magnetic moment of the electron, $\frac{1}{2}(\boldsymbol{L_r} + 2\boldsymbol{S})$, and the second term in (2.25) describes its coupling to the effective magnetic field $\boldsymbol{G}$. The latter results from the original field $\boldsymbol{B}_c + \boldsymbol{B}_l$ in Eq. (2.11) taking into account the corresponding coordinate and energy scaling factors. S_i are the components of the electronic spin, $\boldsymbol{S} = -\boldsymbol{\mu}_1$. The nuclear spin term $-\boldsymbol{\mu}_2 \cdot \boldsymbol{B}(\boldsymbol{R})$ has been omitted since it is several orders of magnitude smaller than the electronic one.

2.4 Adiabatic separation of relative and center of mass dynamics

The large difference of the particles masses and velocities in our two body system makes it plausible to adiabatically separate the electronic and the center of mass motion. The corresponding time scales differ substantially even for large principal quantum numbers n. However, it is a priori not guaranteed that the adiabatic approach is meaningful. The high level density around Rydberg states can entail non-adiabatic couplings around avoided crossings of energy levels and therewith invalidate the approach. The procedure is reminiscent of the Born-Oppenheimer ansatz in molecular systems and is based on the idea that the slow change of the heavy particle's position allows the electron to adapt instantaneously

to the inhomogeneous field. The electronic energy of the system can thus be considered as a function of the position of the heavy particle.

The adiabatic approximation is introduced by subtracting the center of mass kinetic energy, $\mathcal{T} = (P_x^2 + P_y^2)/2$, from the total Hamiltonian (2.25). The remaining electronic Hamiltonian for fixed center of mass reads

$$\mathcal{H}_e = \boldsymbol{\mu} \cdot \boldsymbol{G}(X,Y) + \gamma^{\frac{1}{3}}(xyp_z + xS_x - yS_y) \ . \tag{2.26}$$

The electronic wave function φ_κ depends parametrically on $\boldsymbol{R}$ and the total atomic wavefunction can be written as

$$|\Psi(\boldsymbol{r},\boldsymbol{R})\rangle = |\varphi_\kappa(\boldsymbol{r};\boldsymbol{R})\rangle \otimes |\psi_\nu(\boldsymbol{R})\rangle \ , \tag{2.27}$$

where $\psi_\nu(\boldsymbol{R})$ is the center of mass wave function. The internal problem posed by the stationary, electronic Schrödinger equation,

$$\mathcal{H}_e |\varphi_\kappa(\boldsymbol{r};\boldsymbol{R})\rangle = E_\kappa(X,Y) |\varphi_\kappa(\boldsymbol{r};\boldsymbol{R})\rangle \ , \tag{2.28}$$

is solved for the adiabatic electronic potential energy surfaces $E_\kappa(X,Y)$, that serve as a potential for the center of mass dynamics. Within this approximation, the equation of motion for the center of mass wave function reads

$$(\mathcal{T} + E_\kappa(X,Y)) |\psi_\nu(\boldsymbol{R})\rangle = \epsilon_\nu |\psi_\nu(\boldsymbol{R})\rangle \ . \tag{2.29}$$

The spatially dependent transformation $\mathcal{U}(X,Y)$, that diagonalizes the matrix representation $\mathcal{H}_e$ of the electronic Hamiltonian, is composed of the vector representations of the electronic eigenfunctions, $\boldsymbol{\mathcal{U}}_\kappa = (\mathcal{U}_{\kappa\alpha}) = (\langle \alpha | \varphi_\kappa(\boldsymbol{r};\boldsymbol{R})\rangle)$. Since $\mathcal{U}$ depends on the center of mass coordinates, the transformed kinetic energy involves non-adiabatic couplings $\Delta\mathcal{T}$,

$$\mathcal{U}^\dagger \mathcal{H} \mathcal{U} = \mathcal{U}^\dagger \mathcal{H}_e \mathcal{U} + \mathcal{U}^\dagger \mathcal{T} \mathcal{U} = E_\kappa(X,Y) + \mathcal{T} + \Delta\mathcal{T} \ , \tag{2.30}$$

that have been neglected in the adiabatic approximation of Eq. (2.29),

$$\Delta\mathcal{T} = -1/2 \cdot (\mathcal{U}^\dagger(\partial_X^2 \mathcal{U}) + \mathcal{U}^\dagger(\partial_Y^2 \mathcal{U}) + 2\mathcal{U}^\dagger(\partial_X \mathcal{U})\partial_X + 2\mathcal{U}^\dagger(\partial_Y \mathcal{U})\partial_Y) \ . \tag{2.31}$$

They can be calculated explicitly as soon as the electronic adiabatic eigenfunctions have been computed. Non-adiabatic contributions can be neglected if the conditions

$$|\frac{\langle \varphi_{\kappa\prime}|(\partial_X \mathcal{H})|\varphi_\kappa\rangle}{E_{\kappa\prime} - E_\kappa}| \ll 1 \ , \quad |\frac{\langle \varphi_{\kappa\prime}|(\partial_Y \mathcal{H})|\varphi_\kappa\rangle}{E_{\kappa\prime} - E_\kappa}| \ll 1 \ , \tag{2.32}$$

$$|\frac{\langle \varphi_{\kappa\prime}|(\partial_X^2 \mathcal{H})|\varphi_\kappa\rangle}{E_{\kappa\prime} - E_\kappa}| \ll 1 \ , \quad |\frac{\langle \varphi_{\kappa\prime}|(\partial_Y^2 \mathcal{H})|\varphi_\kappa\rangle}{E_{\kappa\prime} - E_\kappa}| \ll 1 \tag{2.33}$$

are fulfilled. The energy denominator in (2.32) and (2.33) indicates that one can expect non-adiabatic couplings to become relevant between the adiabatic energy surfaces when they come very close in energy, i.e. in the vicinity of avoided crossings.

Recalling the results of the symmetry analysis, it can be demonstrated that the energy surfaces E_κ exhibit three mirror symmetries. Within the adiabatic approximation, X and Y are mere parameters in the electronic Schrödinger equation. Symmetry operations applied

to the electronic Hamiltonian thereby only act onto the electronic subspace. If we apply the corresponding restricted symmetry operation $U_P = P_x P_y \hat{S}_z \hat{\Sigma}_z$ (2.13a), that was already shown to leave the full Ioffe-Pritchard Hamiltonian (2.12) invariant, to the electronic Hamiltonian H_e (2.19), we find

$$U_P^\dagger H_e(\boldsymbol{r}; X, Y) U_P = H_e(\boldsymbol{r}; -X, -Y) \,. \tag{2.34}$$

Since unitarily equivalent observables, A and $U^\dagger A U$, possess the same eigenvalue spectrum, we find the energy surfaces to be inversion symmetric with respect to the origin in the X-Y plane. The symmetry operator $U_Y = T P_y$, and the operator that is composed of U_Y and U_P, namely $U_X = T P_x \hat{S}_z \hat{\Sigma}_z$ (see (2.14) and (2.15a)), mirror the energy surfaces at the axes,

$$U_Y^\dagger H_e(\boldsymbol{r}; X, Y) U_Y = H_e(\boldsymbol{r}; X, -Y) \,, \tag{2.35}$$

$$U_X^\dagger H_e(\boldsymbol{r}; X, Y) U_X = H_e(\boldsymbol{r}; -X, Y) \,. \tag{2.36}$$

The electronic problem (2.28), with the core fixed at an arbitrary position, is three-dimensional. No symmetry arguments can be exploited to reduce the dimensionality of the problem. In order to solve it, we employ the variational method, which maps the stationary Schrödinger equation onto an ordinary algebraic eigenvalue problem. Since the matrix representation of the electronic Hamiltonian is sparsely occupied, an Arnoldi decomposition is used as is described in the following chapter. Both, this decomposition and the surfaces mirror symmetries, help to reduce the computational cost of solving the electronic Schrödinger equation.

3 Numerical approach

In the preceding chapter we developed the Hamiltonian for a Rydberg atom in a Ioffe-Pritchard trap. The stationary states of this quantum mechanical problem are found solving the stationary Schrödinger equation

$$H|\Psi_i\rangle = E_i|\Psi_i\rangle \ . \tag{3.1}$$

For special cases the solutions of this equation can be found analytically, as will be demonstrated in Sec. 4.1. The resulting analytical expressions for the wave functions are enormously helpful to understand the underlying physics of the problem [83]. In order to expand this understanding to cases that only slightly differ from the analytically solvable ones, approximate analytical solutions can be provided by a perturbative approach. For arbitrary situations, however, i.e. for arbitrary structure of the Hamiltonian, one has to resort on numerical methods for solving the Schrödinger equation (3.1).

In this chapter we describe the necessary methods and concepts that form the basis of the numerical treatment of the quantum mechanical system. We start with introducing the variational principle in Section 3.1. It maps the stationary Schrödinger equation onto an ordinary algebraic eigenvalue problem and therefore allows to find ground and excited state energies with, in principle, arbitrary accuracy. In Section 3.2 we describe the representation of the Hamiltonian in a basis set that is well suited to our physical system. The resulting Hamiltonian matrix is of large dimension and sparsely occupied. We therefore present the Arnoldi decomposition in Section 3.3 that is particularly appropriate to solve such large scale and structured eigenvalue problems.

3.1 Variational method

A powerful tool to find numerical solutions of the eigenvalue equation $\mathcal{O}\phi = \omega\phi$ is the variational method that is presented in this section. Since the stationary Schrödinger equation is such an eigenvalue equation the method has become a standard technique in quantum mechanics. It is based on the variational principle which states that the expectation value of a Hamiltonian calculated using any trial wave function is never lower than the ground state energy. A similar statement for excited states can be deduced with the aid of the Hylleraas-Undheim theorem. Our presentation is based on the description by Szabó and Osterlund [84].

Given an arbitrary normalized state $|\Phi\rangle$, the expectation value of the Hamiltonian in this state is an upper bound of the exact ground state energy E_0,

$$\langle\Phi|H|\Phi\rangle \geq E_0 \ . \tag{3.2}$$

The trial function $|\Phi\rangle$ is constructed employing a set of basis functions $\{|\beta\rangle\}$ that shall be orthonormalized, $\langle\beta|\beta'\rangle = \delta_{\beta\beta'}$. Due to the completeness of the basis set, $\sum_\beta |\beta\rangle\langle\beta| = 1$,

one can expand the trial wave function into

$$|\Phi\rangle = \sum_{\beta} |\beta\rangle\langle\beta|\Phi\rangle = \sum_{\beta} c_{\beta}|\beta\rangle \; . \tag{3.3}$$

It depends linearly on the expansion coefficients c_{β} that will serve as variational parameters. It is shown in the following that finding the optimal parameters c_{β} can be reduced to an algebraic eigenvalue equation and thus to diagonalizing a matrix.

The Hamiltonian H in this basis reads $\mathcal{H} = (\mathcal{H}_{\beta\beta'}) = (\langle\beta|H|\beta'\rangle)$ and the expectation value of H in the trial wave function is

$$\langle H\rangle = \langle\Phi|H|\Phi\rangle = \sum_{\beta\beta'} c_{\beta}^* c_{\beta'} \; \langle\beta|H|\beta'\rangle = \sum_{\beta\beta'} c_{\beta}^* \mathcal{H}_{\beta\beta'} c_{\beta'} = \boldsymbol{c}^{\dagger}\mathcal{H}\boldsymbol{c} \; , \tag{3.4}$$

where $\boldsymbol{c}$ is the column vector of the expansion coefficients c_{β}. They have to fulfill the condition

$$\boldsymbol{c}^{\dagger}\boldsymbol{c} = \sum_{\beta\beta'} c_{\beta}^* c_{\beta'} \; \delta_{\beta,\beta'} = \sum_{\beta\beta'} c_{\beta}^* c_{\beta'} \; \langle\beta|\beta'\rangle = \langle\Phi|\Phi\rangle = 1 \; , \tag{3.5}$$

as the trial function $|\Phi\rangle$ was chosen to be normalized.

According to the variational principle, the expectation value $\langle\Phi|H|\Phi\rangle$ has to be minimized in order to find the energy that is closest to the exact value. An elegant way to minimize a function subject to a constraint is using *Lagrangian multipliers*. The optimal set of expansion coefficients (c_{β}) can thus be found minimizing the expression

$$G = \sum_{\beta\beta'} c_{\beta}^* \mathcal{H}_{\beta\beta'} c_{\beta'} - \varepsilon \left(\sum_{\beta\beta'} c_{\beta}^* c_{\beta'} - 1 \right) , \tag{3.6}$$

where the Lagrangian multiplier ε prefixes the term that accounts for the constraint that $|\Phi\rangle$ shall be normalized, Eq. (3.5). Setting the derivatives of G with respect to c_{β}^* to zero yields the following set of equations for the optimal components,

$$\frac{\partial G}{\partial c_{\beta}^*} = \sum_{\beta'} (\mathcal{H}_{\beta\beta'} - \varepsilon) c_{\beta'} = 0 \quad \Leftrightarrow \quad \mathcal{H}\boldsymbol{c} = \varepsilon\boldsymbol{c} \; , \tag{3.7}$$

which is the algebraic eigenvalue problem we set out to find. It can be solved to yield as many orthonormal eigenvectors $\boldsymbol{c}$ and eigenvalues ε as there are basis functions, of course. The Lagrangian multipliers ε are the expectation values of the Hamiltonian with respect to the trial wave function $|\Phi\rangle$,

$$\langle\Phi'|H|\Phi\rangle = \boldsymbol{c}'^{\dagger}\mathcal{H}\boldsymbol{c} = \varepsilon\boldsymbol{c}'^{\dagger}\boldsymbol{c} = \varepsilon\delta_{\Phi,\Phi'} \; . \tag{3.8}$$

The smallest eigenvalue ε_0 is the best approximation to the ground state energy E_0 that is obtainable in the set of the employed basis functions $\{|\beta_i\rangle\}$. The equation $\varepsilon_0 = E_0$ holds (cf. (3.2)) if the trial wave function is identical to the eigenfunction of H, $|\Psi_0\rangle$. In general this can only happen employing all basis functions $|\beta\rangle$, i.e. allowing for all coefficients c_{β} in (3.3) to be nonzero.

One can furthermore find that ε_i is an upper bound to the energy of the ith excited state of H, that is

$$E_i \leq \varepsilon_i \quad \text{for all } i \; , \tag{3.9}$$

if the energies E_i and the approximated eigenvalues ε_i are arranged in ascending order. This is the *Hylleraas-Undheim theorem* [85]. It includes the statement that all approximate eigenvalues obtained by diagonalizing $\mathcal{H}$ in a subspace can only become smaller (and therefore become better estimates for E_i) when the subspace is enlarged, i.e. when more basis functions $|\beta_i\rangle$ are used. In practice, the variational method is equivalent to solving the stationary Schrödinger equation in a subspace. Numerically exact results can be obtained by enlarging the basis set until the energies converge.

3.2 Representation in hydrogenic eigenfunctions

The variational approach maps the stationary Schrödinger equation onto an ordinary algebraic eigenvalue problem. To solve the Schrödinger equation we hence have to diagonalize the matrix Hamiltonian $\mathcal{H}$ in (3.7). In general, any set of functions that forms a basis of the considered Hilbert space is valid. It is impossible, however, to diagonalize infinitely dimensional matrices numerically. Since we hence have to limit the number of basis functions, it is advantageous for obtaining good results within tolerable time, to choose basis functions that closely resemble the true expected wave functions. This is possible in case of Rydberg atoms since their wave functions are very similar to the hydrogenic eigenfunctions. This is even true in external magnetic and electric fields as long as the Coulomb interaction between the core and the electron is a lot stronger than the coupling of the electron to the external fields. We thus represent the electronic Hamiltonian in Eq. (2.28) in hydrogenic eigenfunctions and restrict the basis to one n-manifold which is justified in Section 2.3.

The radial part of the hydrogenic basis functions $R_{n,l}(\boldsymbol{r})$ reads [86]

$$R_{n,l}(\boldsymbol{r}) = \frac{1}{n}\left(\frac{(n-l-1)!}{(n+l)!}\right)^{\frac{1}{2}}\left(\frac{2r}{n}\right)^{l+1}L_{n-l-1}^{2l+1}\left(\frac{2r}{n}\right)e^{-\frac{r}{n}}\ ,\tag{3.10}$$

where L_ν^α symbolize the *generalized Laguerre polynomials*,

$$L_\nu^\alpha(x) = \frac{e^x x^{-\alpha}}{\nu!}\frac{d^\nu}{dx^\nu}(e^{-x}x^{\nu+\alpha})\ .\tag{3.11}$$

The angular part of the hydrogenic eigenfunctions is given by the *spherical harmonics* Y_l^m [87],

$$Y_l^m(\theta,\phi) = (-1)^m\sqrt{\frac{(2l+1)}{4\pi}\frac{(l-m)!}{(l+m)!}}\ P_l^m(\cos\theta)\ e^{im\phi}\quad (m\geq 0)\ ,\tag{3.12}$$

where P_l^m symbolize the *associated Legendre functions*,

$$P_l^m(x) = (1-x^2)^{\frac{m}{2}}\frac{d^m}{dx^m}P_l(x)\ ,\quad \text{with } P_l(x) = \frac{1}{2^l l!}\frac{d^l}{dx^l}(x^2-1)^l\ .\tag{3.13}$$

The spherical harmonics Y_l^m are the eigenstates of the angular momentum operators $\boldsymbol{L_r^2}$ and L_z,

$$\boldsymbol{L_r^2}Y_l^m = l(l+1)Y_l^m\ ,\ L_zY_l^m = mY_l^m\ ,\tag{3.14}$$

and they fulfill the orthonormality relation

$$\int Y_l^{m*}(\Omega)Y_{l'}^{m'}(\Omega)d\Omega = \int_0^\pi\sin\theta d\theta\int_0^{2\pi}d\phi Y_l^{m*}(\theta,\phi)Y_{l'}^{m'}(\theta,\phi) = \delta_{l,l'}\delta_{m,m'}\ .\tag{3.15}$$

3 Numerical approach

The spherical harmonics for negative azimuthal quantum numbers are obtained via

$$Y_l^{-m}(\theta, \phi) = (-1)^m (Y_l^m(\theta, \phi))^* . \tag{3.16}$$

The eigenfunctions of the electronic Hamiltonian H_e are two component spinors. The basis of the corresponding spin space is composed of the orthonormal spinors $|\uparrow\rangle$ and $|\downarrow\rangle$ that are defined via

$$S_z|\uparrow\rangle = \frac{1}{2}|\uparrow\rangle \quad \text{and} \quad S_z|\downarrow\rangle = -\frac{1}{2}|\downarrow\rangle , \tag{3.17}$$

where the Z-axis is chosen as the quantization axis. In the corresponding matrix representation, where S_z is diagonal, the spinors $|\uparrow\rangle$ and $|\downarrow\rangle$ are given by

$$|\uparrow\rangle = \begin{pmatrix} 1 \\ 0 \end{pmatrix} \quad \text{and} \quad |\downarrow\rangle = \begin{pmatrix} 0 \\ 1 \end{pmatrix} , \tag{3.18}$$

and we can write the matrix representation of the spin operators as $\boldsymbol{S} = \boldsymbol{\sigma}/2$. The components of $\boldsymbol{\sigma}$ are the Pauli matrices,

$$\sigma_x = \begin{pmatrix} 0 & 1 \\ 1 & 0 \end{pmatrix}, \quad \sigma_y = \begin{pmatrix} 0 & -i \\ i & 0 \end{pmatrix}, \quad \sigma_z = \begin{pmatrix} 1 & 0 \\ 0 & -1 \end{pmatrix} . \tag{3.19}$$

The total Hilbert space is the tensor product of the Hilbert spaces assigned to the wave functions $R_{n,l}$ and Y_l^m and of the spin space h_S, and the basis vectors are given by

$$|\alpha\rangle = |n, l, m_l, m_s\rangle = |R_{n,l}\rangle \otimes |Y_l^m\rangle \otimes |\updownarrow\rangle . \tag{3.20}$$

The total basis $\{|n, l, m_l, m_s\rangle\}$ is orthonormal and the trial wave function can be expanded to

$$|\Phi\rangle = \sum_{l, m_l, m_s} c_{nlm_l m_s} |n, l, m_l, m_s\rangle , \tag{3.21}$$

where we do not sum over n since we can neglect the inter-n-manifold mixing.

The elements of the matrix $\mathcal{H}$ that represent the electronic Hamiltonian in the chosen basis read

$$\mathcal{H}_{\alpha\alpha'} = \langle\alpha|H|\alpha'\rangle = \langle n, l, m_l, m_s|\mathcal{H}|n, l', m_l', m_s'\rangle . \tag{3.22}$$

If we can restrict our considerations to a single n-manifold, then $\mathcal{H}$ has the dimension $2n^2 \times 2n^2$. Since our basis system is given in the spherical coordinates r, θ and ϕ, it is favorable to transform the electronic Hamiltonian into these coordinates, too. Its terms are then products of operators of the form $u(r)$, $v(\theta, \phi)$, and $w(S)$, and the matrix elements can be written as the product of the individual matrix elements of these operators,

$$\langle n, l, m_l, m_s|u(r)\, v(\theta, \phi)\, w(S)|n, l', m_l', m_s'\rangle$$
$$= \langle R_{n,l}|u(r)|R_{n',l'}\rangle \, \langle Y_l^m|v(\theta)|Y_{l'}^{m'}\rangle \, \langle\updownarrow |w(S)|\updownarrow'\rangle . \tag{3.23}$$

3.3 Arnoldi decomposition

The matrix representation $\mathcal{H}$ of the electronic Hamiltonian, that enters the eigenvalue problem (3.7), is of large dimension but sparsely occupied. Direct methods to solve the problem are therefore inappropriate. A method that is particularly suited to find numerical solutions of such large structured eigenvalue problems is the Arnoldi decomposition. It significantly reduces the dimension of the problem which can then be solved with comparatively little computational cost. The numerical implementation is based on routines provided by the Arpack and the SuperLU software packages.

We briefly outline the idea of the Arnoldi method [88]. The Arnoldi decomposition of a matrix A yields a matrix of lower dimension, H_k, whose eigenvalues approximate those of A. The eigenvalue problem of H_k can efficiently be solved by direct methods, in contrast to the original problem. If $A \in \mathbb{C}^{n \times n}$ then a relation of the form

$$AV_k = V_k H_k + \boldsymbol{f}_k \boldsymbol{e}_k^T \tag{3.24}$$

exists where $V_k \in \mathbb{C}^{n \times k}$ has orthonormal columns and $V_k^T \boldsymbol{f}_k = 0$. $H_k \in \mathbb{C}^{k \times k}$ is an upper Hessenberg matrix. This is called the *k-step Arnoldi factorization* of A [88]. If A is Hermitian, then H_k is real, symmetric, and tridiagonal. It is the orthogonal projection of A onto the so-called *Krylov subspace* that consists of the sequence of vectors produced by the power method,

$$\mathcal{K}_k := \mathrm{span}\{\boldsymbol{v}, A\boldsymbol{v}, A^2\boldsymbol{v}, \ldots, A^{k-1}\boldsymbol{v}\} \,, \tag{3.25}$$

for any nonzero vector $\boldsymbol{v} \in \mathbb{C}^n$. If a vector $\boldsymbol{y}$ fulfills $H_k \boldsymbol{y} = \theta \boldsymbol{y}$, then $\boldsymbol{x} = V_k \boldsymbol{y}$ satisfies

$$||A\boldsymbol{x} - \theta\boldsymbol{x}|| = ||(AV_k - V_k H_k)\boldsymbol{y}|| = |\beta_k \boldsymbol{e}_k^T \boldsymbol{y}| \,. \tag{3.26}$$

The pair $(\boldsymbol{x}, \theta)$ is an approximate solution of the eigenvalue problem of A, called *Ritz pair*. The quality of the approximation is measured with the so-called *Ritz estimate* $|\beta_k \boldsymbol{e}_k^T \boldsymbol{y}|$ on the right hand side of (3.26). It decreases when the dimension k of the Krylov subspace is increased. The Ritz pair $(\boldsymbol{x}, \theta)$ is considered converged as soon as the Ritz estimate drops under an adjustable value (machine precision in our case). The remaining problem is to diagonalize the k-dimensional Hessenberg matrix H_k. This can be done using standard algorithms.

An unfortunate aspect of the Arnoldi process is that one cannot know how many steps will be required to converge the Ritz values. This is particularly true if wide ranged eigenvalues are clustered. The often intractable storage problems, that come along with the original Arnoldi method, are bypassed using the implicitly restarted Arnoldi method for which the storage of a large amount of basis vectors is no longer necessary. The method is implemented in the Arpack collection [88] whose routines only ask for a means to solve linear systems of equations $AX = B$. The user is free to utilize any solver and any convenient data structure for the matrix representation. The SuperLU package [89] accomplishes this task by a triangular factorization of the matrix A into a unit lower triangular matrix L ($L_{ii} = 1$) and a upper triangular matrix U. The matrices are thereby stored in an efficient data structure called *Harwell-Boeing format*. It only stores nonzero matrix elements and is thus well suited for sparse matrices. We additionally use a *shift-and-invert* spectral transformation to be able to converge eigenvalues in whatever region of the spectrum.

4 Electronic potential energy surfaces

In this section we analytically and numerically solve the electronic Schrödinger equation formulated in (2.28) to find the electronic adiabatic energy surfaces E_κ. Their properties are analyzed for different regimes of Ioffe field strengths and field gradients. These two parameters shape the surfaces E_κ that act as potentials for the center of mass dynamics. We inspect the electronic Hamiltonian to unravel the influence of the individual terms for different parameter regimes.

The characteristic length scale of the center of mass dynamics is of the order of one in scaled atomic units. It is therefore adequate to compare the magnitudes of the different parts of the electronic Hamiltonian (2.26) in order to estimate their impact on the center of mass motion, putting X and Y equal to one. The first part, $\boldsymbol{\mu} \cdot \boldsymbol{G}(X, Y)$, consists of the coupling terms $X(\frac{1}{2}L_x + S_x) - Y(\frac{1}{2}L_y + S_y)$, that are then of the order of $\langle L_i \rangle \approx n$ for high angular momentum states, and of the Zeeman term $\zeta(\frac{1}{2}L_z + S_z)$, which can be as large as ζn. The finite size part, $\gamma^{1/3}(xyp_z + xS_x - yS_y)$, is quadratic in the relative coordinates which makes it particularly important for high principal quantum numbers n. If we consider the expectation values of the relative coordinates to be of the order of n^2, and $\langle yp_z \rangle \approx \langle L_x \rangle \approx n$, the overall magnitude can be estimated to $\gamma^{1/3}n^3$. In a nutshell, we have the relative orders of magnitude

$$1 , \quad \zeta \quad \text{and} \quad \gamma^{\frac{1}{3}} n^2 , \tag{4.1}$$

for the respective terms in the electronic Hamiltonian $\mathcal{H}_e$. Due to the special form of $\mathcal{H}_e$, changing the magnetic field parameters B and G while keeping their ratio $B/G = \zeta/\gamma^{1/3}$ (and n) constant results in a mere scaling of the center of mass coordinates. We provide typical examples for values of the quantities (4.1) in Tab. 4.1.

In Section 4.1 we consider the case in which the Ioffe field is large compared with the gradient field. In a region around the trap center we can then neglect the finite size term and solve the electronic problem analytically. In a second step in Section 4.2 we investigate the effect of the finite size term on the electronic surfaces for large field gradients. We furthermore characterize the electronic wave function that corresponds to the energetically uppermost solution. The final part of the chapter, Sec. 4.3, deals with the center of mass dynamics in the potential surfaces obtained in the first sections.

4.1 Analytical solution of the electronic problem

To understand the impact of the Ioffe field strength B on the adiabatic energy surfaces, we isolate its effect by suppressing other influences. This can be done by choosing a relatively low field gradient G and/or a small principal quantum number n (see Tab. 4.1). The factor $\gamma^{\frac{1}{3}} n^2$ becomes small, and the finite size term (the last term in Eq. (2.26)) will hardly provide

4 Electronic potential energy surfaces

Table 4.1: Explicit values for $\gamma^{1/3}n^2 = (GM)^{1/3}n^2$ and $\zeta = BM^{1/3}G^{-2/3}$ for ^{87}Rb in atomic units. The first block lists $\gamma^{1/3}n^2$ for different values of the field gradient G and for different principal quantum numbers n. The second block lists ζ for different field gradients and for different field strengths B.

G [T/m]		0.01	0.1	1	10	100	1000	10000
	n							
$\gamma^{\frac{1}{3}}n^2$	3	0.001	0.001	0.003	0.006	0.014	0.030	0.064
	10	0.007	0.015	0.033	0.071	0.153	0.329	0.709
	30	0.064	0.138	0.296	0.638	1.375	2.963	6.383
	50	0.177	0.382	0.823	1.773	3.820	8.229	17.729
	80	0.454	0.978	2.107	4.539	9.778	21.067	45.387
	B [Gauss]							
ζ	0.01	134.0	28.87	6.220	1.340	0.289	0.062	0.013
	0.1	1340	288.7	62.20	13.40	2.887	0.622	0.134
	1	13402	2887	622.0	134.0	28.87	6.220	1.340
	10	134015	28873	6220	1340	288.7	62.20	13.40

any contribution. Within this regime, that we focus on in this section, approximate analytical expressions for the electronic adiabatic energy surfaces can be derived. We diagonalize the approximate electronic Hamiltonian

$$\tilde{H}_e = \frac{1}{2}(\boldsymbol{L} + 2\boldsymbol{S}) \cdot \boldsymbol{G} \tag{4.2}$$

by applying the spatially dependent unitary transformation

$$U_D(X,Y) = e^{i\phi(L_z+S_z)}e^{i\beta(L_y+S_y)} \, , \tag{4.3}$$

with

$$\tan\phi = \frac{Y}{X} \, , \quad \cos\beta = \frac{\gamma^{-2/3}M_2B}{|\boldsymbol{G}(X,Y)|} \, , \quad \text{and} \quad \sin\beta = -\frac{\sqrt{X^2+Y^2}}{|\boldsymbol{G}(X,Y)|} \, . \tag{4.4}$$

For the transformed approximate electronic Hamiltonian we find

$$U_D^\dagger \tilde{H}_e U_D = \frac{1}{2}(L_z + 2S_z)|\boldsymbol{G}(X,Y)| \, . \tag{4.5}$$

The spatially dependent transformation U_D locally rotates the magnetic moment of the electron, which includes its spin and its angular momentum, such that it is parallel to the local direction of the magnetic field. The operators L_z and S_z are not identical to the ones before having applied the transformation (4.3), they are rather related to the local quantization axis defined by the local magnetic field direction.

The adiabatic potential surfaces evaluate to

$$\begin{aligned} E_\kappa(X,Y) &= \frac{1}{2}(m_l + 2m_s)|\boldsymbol{G}(X,Y)| \\ &= \frac{1}{2}(m_l + 2m_s)\sqrt{X^2 + Y^2 + \zeta^2} \, . \end{aligned} \tag{4.6}$$
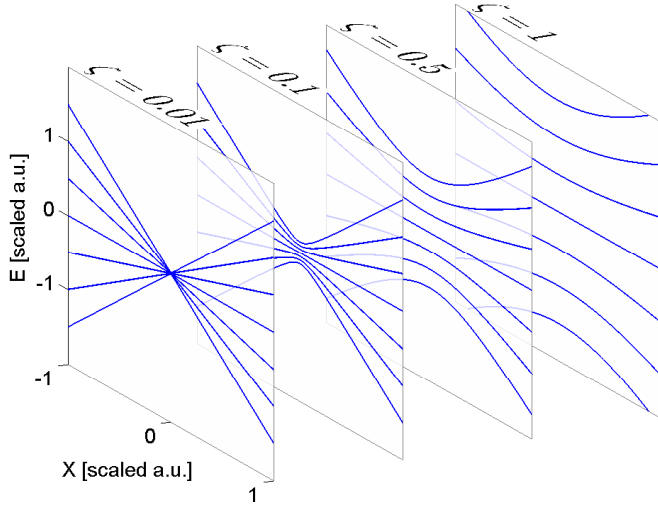
Figure 4.1: Sections along the X-axis through the electronic adiabatic energy surfaces of an entire $n = 3$ manifold. The field gradient is fixed at $G = 1$ Tesla/m in order to suppress the influence of the last term in H_e (2.26). From left to right, $\zeta = BM\gamma^{-2/3}$ increases due to an increasing Ioffe field.

The possible combinations of m_l and m_s yield $2n+1$ energy surfaces. The surfaces highest and lowest in energy correspond to circular states, ($|m_l| = l_{max} = n - 1$, $m_l + 2m_s = \pm n$), and they are the only non-degenerate ones. For the other surfaces ($|m_l + 2m_s| < n$), the multiplicity of ($m_l + 2m_s$), and with that the degree of degeneracy of the corresponding surfaces, is given by $2n - |m_l + 2m_s + 1| - |m_l + 2m_s - 1|$. Starting from the highest energy surface, the levels of degeneracy thus are 1, 2, 4, 6, ...

The approximate surfaces E_κ (4.6) are rotationally symmetric around the Z-axis. An expansion around this axis ($\rho = \sqrt{X^2 + Y^2} \ll \zeta$) yields a harmonic potential,

$$E_\kappa(\rho) \approx (\zeta + \frac{1}{2\zeta}\rho^2) \cdot \frac{1}{2}(m_l + 2m_s) \,, \tag{4.7}$$

while we find a linear behavior,

$$E_\kappa(\rho) \approx \frac{\rho}{2} \cdot (m_l + 2m_s) \,, \tag{4.8}$$

when the center of mass is far from the Z-axis ($\rho \gg \zeta$).

For reasons of illustration we demonstrate the behavior of the adiabatic surfaces with increasing Ioffe field by means of an artificial example where other, previously neglected interactions might actually be more important. Fig. 4.1 shows sections through all the surfaces for $n = 3$. This principal quantum number has been chosen in order to keep the sections simple while displaying the entire n-manifold. We employ ^{87}Rb parameters in this expository example although the electronic ground state of its outermost electron is 5s. The sections have been calculated for the field gradient $G = 1$ T/m and for different field strengths B using the total electronic Hamiltonian (2.26). These parameters yield $\gamma^{1/3}n^2 = 0.003$, and values for ζ ranging from 0.01 to 1. The surfaces in the different graphs of Fig. 4.1 indeed validate the approximate expression (4.6): We find $2n + 1$ degenerate surfaces and the harmonic behavior around the Z-axis, i.e. for $|X| \ll \zeta$, gives way to a linear increase for $|X| \gg \zeta$. The energetic distances and lengths in the different graphs are comparable, since the scaling factor for the center of mass coordinates $\gamma = GM$ has not been changed. We can conclude that increasing the Ioffe field strength B separates the surfaces from each other.
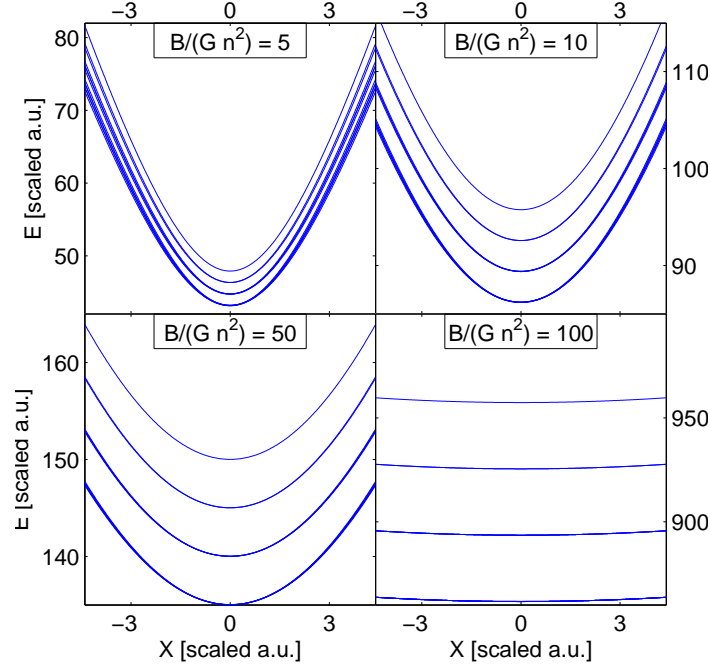
Figure 4.2: Sections along the X-axis through the uppermost 21 surfaces of the $n = 30$ manifold of ^{87}Rb for increasing ratios $B/(Gn^2)$. The field gradient is fixed at $G = 10$ T/m while the Ioffe field is increased from top left to bottom right. ($B = 24$ mG, $B = 48$ mG, $B = 0.24$ G, $B = 0.48$ G). For small ratios $B/(Gn^2)$ the influence of the second term in (2.26) is not completely suppressed as can be seen from the lifted degeneracies in the upper subfigures.

The data presented in Fig. 4.2 have been computed for the $n = 30$ manifold. In order to keep the last term in (2.26) small, the field gradient has been set to $G = 0.1$ T/m ($\rightarrow \gamma^{1/3}n^2 = 0.14$). The uppermost 21 energy surfaces are shown for different values of the magnetic field strength B. Similar to the $n = 3$ case, one can see the harmonic behavior around the origin. The surfaces' minimal distance becomes larger for increasing ζ. Since ζ and $\gamma^{1/3}n^2$ are of the same order of magnitude in upper left sub-figure, the contribution of the finite size term lifting the degeneracy of the curves is visible.

The energetic distance of the approximate surfaces described by Eq. (4.6) increases with larger distances from the Z-axis, ρ, and with larger ζ. The minimum energetic gap between two adjacent surfaces is at the origin and reads

$$|E_\kappa(O) - E_{\kappa \pm 1}(O)| = \frac{B}{2}M\gamma^{-\frac{2}{3}} = \frac{\zeta}{2} \ . \tag{4.9}$$

The parameter ζ (an hence the field strength B) is the tool to control the energetic distance between the adiabatic surfaces. Increasing ζ, one can thus also minimize the non-adiabatic couplings $\Delta\mathcal{T}$ (2.31) discussed in Sect. 2.4, since they scale with the reciprocal energetic distance of the surfaces.

To check the range of validity of our approximation, the minimal energetic distance between the two uppermost adiabatic surfaces in the $n = 30$ manifold is calculated for different parameters, subtracting the full 2D surfaces from each other, that are obtained

Table 4.2: Minimal distance ΔE of the two uppermost surfaces of the $n = 30$ manifold. Δ denotes the discrepancy between ΔE and the approximate predicted value for the distance, $\frac{\zeta}{2}$, according to Eq. (4.9).

B [G]	ζ	G [T/m]	$\gamma^{1/3}n^2$	ΔE	Δ [%]
0.01	0.288	100	1.375	0	
0.1	2.89	100	1.375	1.291	15.193
1	28.87	100	1.375	14.421	1.476
0.01	1.340	10	0.638	0.600	11.101
0.1	13.40	10	0.638	6.694	0.103
1	134.0	10	0.638	67.006	0.002
10	1340	10	0.638	670.07	0.001
0.01	6.220	1	0.296	3.107	0.104
0.1	62.20	1	0.296	31.101	0.001
1	622.0	1	0.296	311.022	0.000

using the full electronic Hamiltonian (2.26). One finds the minimal distance to be located at the origin, as expected. Δ in Tab. 4.2 denotes the relative deviation between the predicted (Eq. (4.9)) and the computed value in percent. It is small for large Ioffe field strengths B and low field gradients G. Then we have $\zeta \gg \gamma^{1/3}n^2$, the finite size term in the electronic Hamiltonian is negligible and our approximation that leads to (4.9) is justifiable.

4.2 High gradients

A more complicated picture of the surfaces' properties arises when the field gradients become larger. The last term in the electronic Hamiltonian, that accounts for effects due to the finite size of the atom,

$$\gamma^{\frac{1}{3}}\left(xyp_z + xS_x - yS_y\right) , \tag{4.10}$$

is no longer small compared to the other terms in equation (2.26). This results in modulations of the adiabatic surfaces we already spotted in the previous section. They lift the degeneracy that was found in the limit of small gradients.

The finite size term Eq. (4.10) in the electronic Hamiltonian depends on relative coordinates only. Due to this lack of center of mass dependence one is tempted to argue that this term could be treated as a mere energy offset to the adiabatic electronic potentials and that it does not contribute to the shape of these potentials. Yet this would only be the case if the Hamiltonian in question would only feature pure relative and pure center of mass terms. It is a major characteristic of the Rydberg Hamiltonian (2.25), however, to couple electronic and center of mass dynamics. For this reason purely relative terms implicitly create an $\boldsymbol{R}$-dependent effect on the wave function, and with that on the energy as well.

In order to isolate the effect of the term (4.10) on the adiabatic surfaces, we vary the scaling factor $\gamma = GM$ by changing the field gradient G, while keeping $\zeta = BM^{1/3}G^{-2/3}$ constant. It is, for example, reasonable to demand $\zeta = 5$ and to adjust the Ioffe field strength B to meet this condition. Fig. 4.3 demonstrates the increasing influence of the interaction (4.10) when G is increased. The spectra are computed for the $n = 30$ manifold
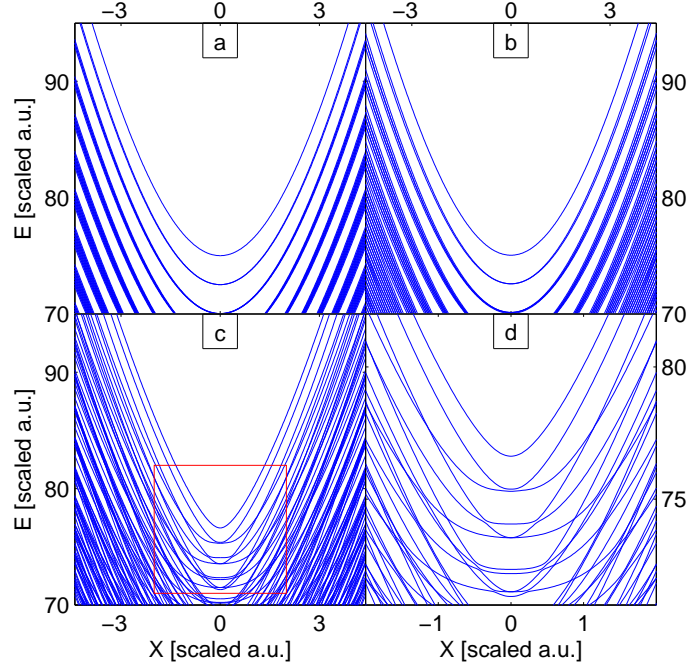
Figure 4.3: Sections $(Y = 0)$ through the adiabatic potential energy surfaces belonging to the $n = 30$ manifold of ^{87}Rb for decreasing ratios $B/(Gn^2) = \zeta/(\gamma^{1/3}n^2)$. The influence of the Zeeman term in $\mathcal{H}_e$ (2.26) is fixed $(\zeta = 5)$ while $\gamma^{1/3}n^2$ increases. (a) $B/(Gn^2) = 10 \leftrightarrow B = 22.9$ mG, $G = 4.81$ T/m; (b) $B/(Gn^2) = 5 \leftrightarrow B = 91.6$ mG, $G = 38.5$ T/m; (c) $B/(Gn^2) = 1 \leftrightarrow B = 2.29$ G, $G = 4807$ T/m; (d) draws the indicated region in (c) to a larger scale.

of ^{87}Rb, $\zeta = 5$, while G is varied from 4.8 to 4800 T/m. For small field gradients ((a), $B/(Gn^2) = 10$), the surfaces approach the shapes predicted in the limit addressed in the previous Section (4.1): The adiabatic surfaces with the same value of the magnetic moment $(m_l + 2m_s)/2$ are approximately degenerate around $\rho = 0$. The uppermost energy surface is the only non-degenerate one and to the corresponding eigenstate the quantum numbers $m_l = n - 1$ and $m_s = 1/2$ can still be assigned. An increasing field gradient lifts the degeneracy and groups of curves can be observed ((b), $B/(Gn^2) = 5$). The energetic distance between these groups stays tunable by the bias field strength, as we elucidated above (see Eq. (4.9)). For even higher field gradients, the different parts of the electronic Hamiltonian are of comparable size and finite size effects substantially alter the shape of the energy surfaces ((c), (d), $B/(Gn^2) = 1$). Avoided level crossings appear and non-adiabatic transitions are likely to occur. The uppermost energy surface, however, proves to be very robust when the field gradient is varied. It is energetically well-isolated from the other adiabatic surfaces. Its distance to the surface, that is formed by the second highest eigenvalue, only decreases significantly when the ratio $B/(Gn^2)$ approaches one ((c), (d)). This holds true for the entire X-Y-plane. Inspecting the full uppermost surface one furthermore finds the azimuthal symmetry, that is found for large ratios $B/(Gn^2)$ (see Sect. 4.1), to be approximately conserved.

Another example for the complicated structure of the adiabatic electronic energy surfaces
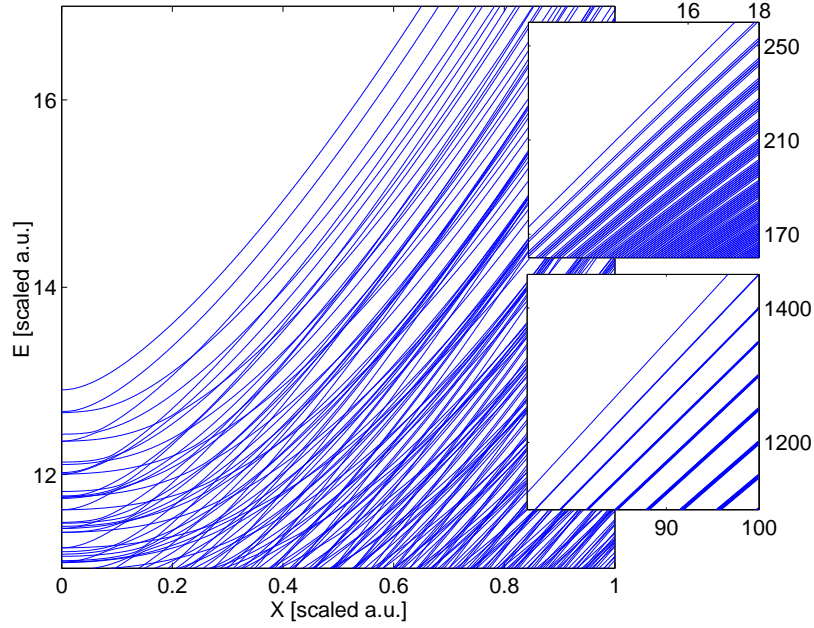
Figure 4.4: Section through the $n = 30$ manifold for a field strength of 0.01 Gauss and a field gradient of 20 T/m (^{87}Rb). A large number of avoided crossings can be observed. The uppermost curve, however, stays isolated from the other curves. The insets show the linear behavior of the surfaces far away from the Z-axis.

is shown in Fig. 4.4. The data are calculated for an extremely small Ioffe field strength of 0.01 G and a field gradient of 20 T/m. For these parameters, the contributions of all terms in the electronic Hamiltonian are of the same order of magnitude around $X = 1$. One immediately notices the large number of avoided crossings between the surfaces. The uppermost curve however remains isolated from the rest of the curves. Far away from the trap center, i.e. for large $\rho = \sqrt{X^2 + Y^2}$, the coupling term in (2.26), $X(\frac{1}{2}L_x + S_x) - Y(\frac{1}{2}L_y + S_y)$, becomes dominant. A Zeeman like splitting of the surfaces emerges, visible in the smaller graphs on the right.

Electronic Wave Functions

To characterize the electronic wave function $\varphi_\kappa(\boldsymbol{r}; \boldsymbol{R})$, that corresponds to the energy eigen-values constituting the uppermost adiabatic surface, we analyze its radial extension, angular momentum and spin. The electronic wave function depends parametrically on the center of mass position and is, in general, distorted compared to the field-free case by the external magnetic field. This is reflected in the expectation value $\langle r \rangle_e(\boldsymbol{R}) = \langle \varphi_\kappa(\boldsymbol{r}; \boldsymbol{R})|r|\varphi_\kappa(\boldsymbol{r}; \boldsymbol{R})\rangle$ which is shown in Fig. 4.5 for different ratios $B/(Gn^2)$. The limits of the graphs with respect to X and Y correspond to thirty characteristic lengths of the center of mass motion. While keeping $G = 100$ T/m, B is increased for the different plots from left to right. For the small-est ratio under consideration ($B/Gn^2 < 1$, left plot in Fig. 4.5), a pronounced maximum of the expectation value $\langle r \rangle_e$ can be observed at the trap center. This maximum breaks up into four maxima arranged along the diagonals when the ratio is increased ($B/Gn^2 > 1$,
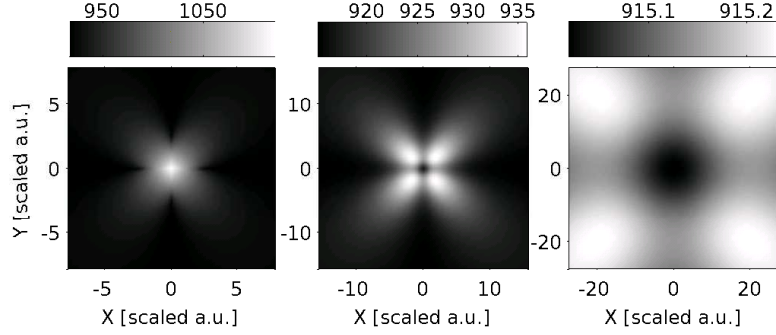
Figure 4.5: Expectation value $\langle r \rangle_\varphi$ of the wave functions that correspond to the uppermost electronic energy surface for $G = 100$ T/m ($n = 30$, ^{87}Rb). B is varied yielding different values for the ratio $\zeta/\gamma^{1/3}n^2 = B/Gn^2$: 0.01 G $\to B/Gn^2 = 0.21$ a.u. (left plot), 0.1 G $\to B/Gn^2 = 2.1$ (middle), 1 G $\to B/Gn^2 = 21$ (right). The depicted ranges of X and Y correspond to 30 characteristic lengths of the center of mass motion in scaled units.

middle plot), while the amplitude of the spatial variation of $\langle r \rangle_e$ decreases. For an even higher value of B ($B/Gn^2 \gg 1$, right plot), only a marginal deviation from the hydrogenic field-free value for the highest possible angular momentum quantum number remains (for $n = 30$ one finds $\langle r \rangle_{\text{hydrogen}}(n = 30, l = 29) = 915$). In the region of local homogeneity, where the magnetic field does not vary significantly over the extension of the electronic cloud (i.e. far from the Z-axis), the expectation value approaches the field-free value in all subfigures that are shown in Fig. 4.5. In accordance with the abovementioned scaling property of the electronic Hamiltonian $\mathcal{H}_e$, changing the field parameters while keeping the ratio B/Gn^2 unaltered only modifies the scale of the center of mass coordinates, whereas the shape of the bright regions and the energy range of the eigenvalues are not changed.

We now study the angular momentum and its orientation. It is to be expected that for dominating Ioffe field, i.e. for large ratios $B/(Gn^2)$, the expectation value of the angular momentum, $\langle \boldsymbol{L_r} \rangle = (\langle L_x \rangle, \langle L_y \rangle, \langle L_z \rangle)$, is oriented in the Ioffe-field direction (Z-axis). Since the Ioffe field in any case dominates around the origin, $\langle L_x \rangle$ and $\langle L_y \rangle$ are expected to vanish at $(X, Y) = (0, 0)$ while $\langle L_z \rangle$ becomes maximal. This behavior can be observed in Fig. 4.6 where $\langle L_i \rangle$ are displayed (a,b,c) for $B = 0.1$ G and $G = 100$ T/m. These parameters yield $B/(Gn^2) = 2.1$. The alignment of $\langle \boldsymbol{L_r} \rangle$ and the local field direction $\boldsymbol{G}(X, Y)$ is found to be very good in the entire X-Y-plane (the maximum angle between the two is smaller than $3.6°$). In subplot (d) we provide the spatial behavior of the projection of $\langle \boldsymbol{L_r} \rangle$ onto this local field axis, $\Pi = \langle \boldsymbol{L_r} \rangle \cdot \boldsymbol{G}(\boldsymbol{R})/|\boldsymbol{G}(\boldsymbol{R})|$. In the local homogeneity limit, Π approaches the maximal value for $\langle L_z \rangle$, namely $m_{l,max} = n - 1$. In the same manner the expectation value $\langle \boldsymbol{L}^2 \rangle$, which is displayed in subplot (e), converges to the maximal value, $l_{max}(l_{max} + 1) = n(n - 1)$. Far from the Z-axis, the uppermost surface hence corresponds to the circular state $|m_{l,max}, l_{max}\rangle$. The deviation of Π and $\langle \boldsymbol{L}^2 \rangle$ from the maximal values close to the Z-axis reflect the admixture of states with lower quantum numbers m and l to the state of the uppermost surface.

Increasing the applied Ioffe field by a factor of 10 ($\to B/(Gn^2) = 21$), decreases the angle between $\langle \boldsymbol{L_r} \rangle$ and $\boldsymbol{G}(X, Y)$ by a factor of 10^2, i.e. a quasi perfect alignment is found. As can be seen in Fig. 4.7, the projection Π now only deviates marginally from $m_{l,max}$.
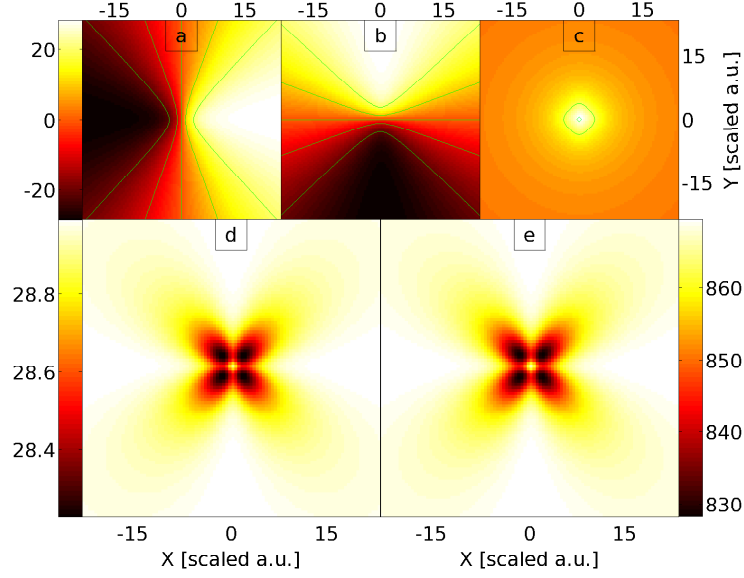
Figure 4.6: (Color online) Expectation values $\langle L_x \rangle$, $\langle L_y \rangle$ and $\langle L_z \rangle$ (a,b,c, respectively) for a ratio $B/(Gn^2) = 2.1$ (Ioffe field $B = 0.1$ G, gradient $G = 100$ T/m, ^{87}Rb, n=30). In (d) the projection Π of $\langle \boldsymbol{L_r} \rangle$ onto the local magnetic field direction $\boldsymbol{G}$ is displayed. It is close to the field-free maximum value for the angular momentum projection, $m_{l,max} = n - 1$. Subplot (e) shows the spatial behavior of $\langle \boldsymbol{L}^2 \rangle$. The range of X and Y corresponds to 30 times the characteristic length of the center of mass motion.

Figure 4.7: Spatial dependence of the projection Π of $\langle \boldsymbol{L_r} \rangle$ onto the local field axis for $B = 1$ G (all other parameters are the same as in Fig. 4.6). For this ratio, $B/(Gn^2) = 21$, the deviations from the maximal value $m_{l,max} = n - 1$ are marginal. (Equally, $\langle \boldsymbol{L}^2 \rangle \approx l_{max}(l_{max} + 1)$, not shown.)

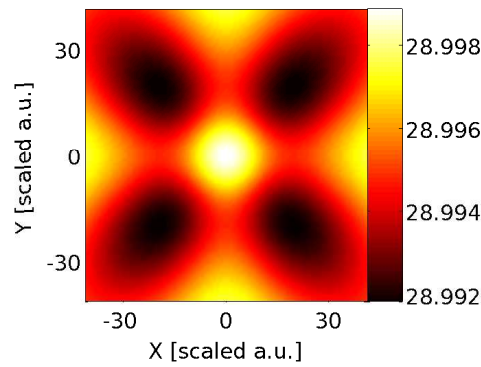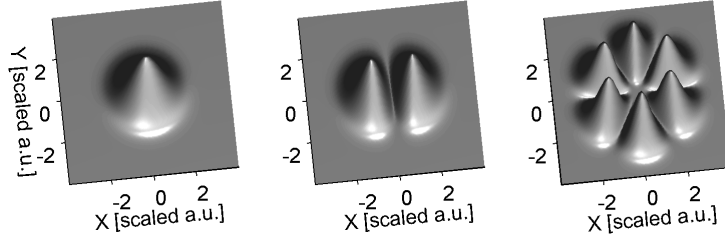**Figure 4.8:** Probability densities of the ground state and the first and tenth excited states of the center of mass motion in the uppermost adiabatic potential surface of the $n = 30$ manifold of ^{87}Rb (from left to right). The Ioffe field strength is set to $B = 0.1$ G and the field gradient is $G = 10$ T/m.

Consequently, also $\langle \boldsymbol{L}^2 \rangle$ exhibits only minor deviations from its maximum value in the whole X-Y-plane. For high ratios $B/(Gn^2)$, the admixture of other states is therefore very small and one can in a very good approximation assume the electronic state in the uppermost surface to be the circular state $|m_{l,max}, l_{max}\rangle$ for any center of mass position. Similar observations can be made considering the respective expectation values for the spin. For the parameters in Fig. 4.7 the projection of $\langle \boldsymbol{S} \rangle$ onto $\boldsymbol{G}$ differs less than 10^{-4} from the expected value $1/2$. The expectation values of the examined electronic observables hence converge to the field-free values for increasing ratios $B/(Gn^2)$.

Our findings indicate that the electronic structure of the atom is barely changed in the limit of large ratios $B/(Gn^2)$. The radiative lifetimes can hence be expected to differ only slightly from the field-free ones [49].

4.3 Quantized center of mass motion

The energetically uppermost adiabatic electronic energy surface is the most appropriate to achieve confinement. It does not suffer a significant deformation when the field gradient is increased and it stays well isolated from lower surfaces for a wide range of parameters. Large energetic distances to adjacent surfaces suppress the non-adiabatic couplings formulated in Eqs. (2.32) and (2.33).

In order to obtain the quantized center of mass states we therefore solve the Schrödinger equation (2.29) for the center of mass motion in the uppermost surface E_{2n^2} by discretizing the Hamiltonian on a grid. The wave function for the fully quantized state is hence composed of the eigenfunction $|\varphi_\kappa(\boldsymbol{r}; \boldsymbol{R})\rangle$ of the electronic Hamiltonian in equation (2.28), the wave function for the center of mass motion in the X-Y plane, $|\psi_\nu(\boldsymbol{R})\rangle$, and the plain wave in Z direction,

$$|\Psi(\boldsymbol{r}, \boldsymbol{R})\rangle = |\varphi_\kappa(\boldsymbol{r}; \boldsymbol{R})\rangle \otimes |\psi_\nu(\boldsymbol{R})\rangle \otimes |k_Z\rangle . \qquad (4.11)$$

In Fig. 4.8 the probability densities of the ground state and two excited states of the center of mass motion in the uppermost surface of the $n = 30$ manifold of ^{87}Rb are displayed. These densities reflect the spatial symmetries of the electronic Hamiltonian $\mathcal{H}_e$ (2.26) and consequently those of the electronic energy surface. They are computed for a Ioffe field strength $B = 0.1$ G and a field gradient of $G = 10$ T/m, which yields $\zeta = 13.4$ and $\zeta/\gamma^{\frac{1}{3}}n^2 = B/Gn^2 = 21$. According to the discussion in Sec. 4.1, the electronic surface
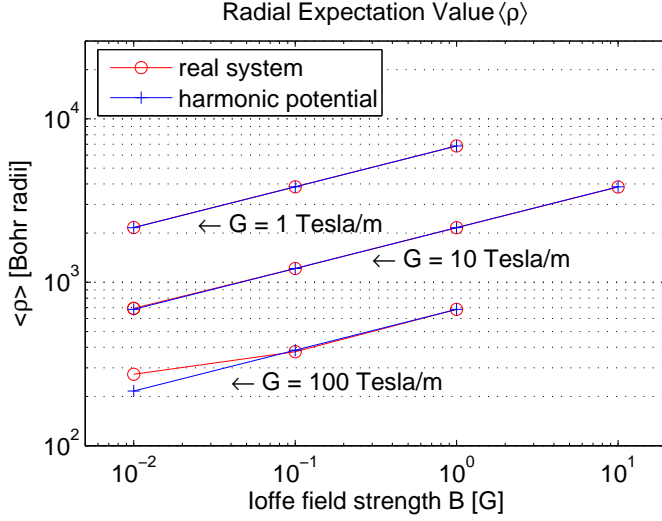
Radial Expectation Value $\langle\rho\rangle$

Figure 4.9: Double logarithmic plot of the expectation value $\langle\rho\rangle$ for the center of mass ground state (circles, ∘) in the uppermost adiabatic energy surface ($n = 30$, ^{87}Rb). The corresponding expectation values for the center of mass wave function in a perfectly harmonic potential are depicted for comparison (+).

then exhibits a harmonic behavior around the origin, and the system resembles the two dimensional isotropic harmonic oscillator in the potential $E_h(X, Y) = (\zeta + \rho^2/2\zeta) \cdot n/4$ (cf. Eq. (4.7), $m_l = n - 1$). The first two probability densities (from left to right) in Fig. 4.8 explicitly demonstrate the analogy to the harmonic oscillator. Although not immediately identifiable as an eigenstate of the two-dimensional harmonic oscillator, the state on the right is the tenth excited eigenstate. Its nodal structure does not come from a Cartesian product of one-dimensional harmonic oscillator eigenfunctions but from a combination of two-dimensional eigenfunctions in the corresponding degenerate subspace.

The energies of the center of mass wave functions in the approximate potential $E_h(X, Y)$ read

$$\epsilon_{h,\nu} = (N_1 + N_2 + 1)\,\omega\,, \quad N_1, N_2 = 0, 1, 2 \ldots\,, \tag{4.12}$$

where $\omega^2 = n/2\zeta$. They are in very good agreement with the exact results in the regime where the finite size term of the electronic Hamiltonian, Eq. (4.10), is negligible. Within this approximation, the energy level spacing scales with the inverse square root of ζ,

$$\Delta\epsilon_{h,\nu} = \omega \sim 1/\sqrt{\zeta}\,, \tag{4.13}$$

whereas the energetic distance of adjacent surfaces scales linearly with ζ, see Eq. (4.9).

To describe the properties of the compound quantized state, we analyze the extension of the center of mass motion, which can be measured by the expectation value

$$\langle\rho\rangle = \langle\psi_\nu(\boldsymbol{R})|\,\sqrt{X^2 + Y^2}\,|\psi_\nu(\boldsymbol{R})\rangle\,, \tag{4.14}$$

and the mean distance of the core and the electron $\langle r \rangle$. Fig. 4.9 presents the numerically computed radial expectation value $\langle\rho\rangle$ in Bohr radii for the center of mass ground state in the uppermost energy surface for different parameter sets of the magnetic field. For comparison, the expectation value of the center of mass state in a perfectly harmonic potential, $\langle\rho\rangle_h = \frac{\sqrt{\pi}}{2}x_0 \sim \zeta^{1/4}$, is also depicted. The characteristic length of the center of mass motion is

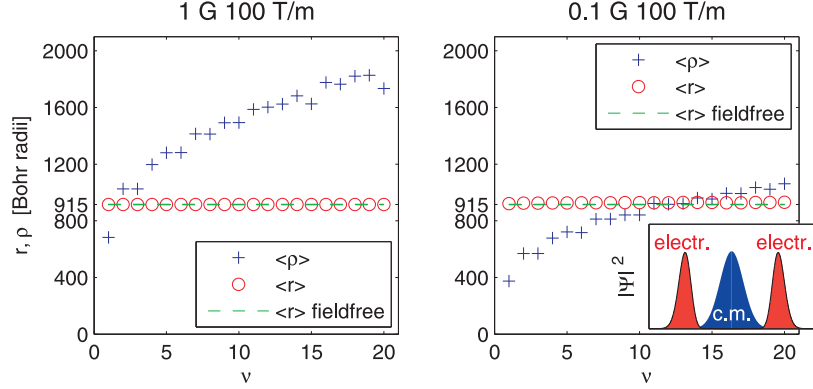$$x_0 = 1/\sqrt{\omega} = \sqrt[4]{2\zeta/n}\,. \tag{4.15}$$

39

Figure 4.10: Comparison of the mean extension of the center of mass wave function, $\langle \rho \rangle$, and the mean distance of the core and the electron, $\langle r \rangle$, for the $n = 30$ manifold of ^{87}Rb.

Due to the rescaling of the center of mass coordinates with $\gamma^{-1/3}$ in Sec. 2.2 this is of the order of 1 for a wide range of parameter sets $\{B, G, n\}$ in scaled atomic units (for explicit values of ζ see Tab. 4.1). The expectation values for the real system, $\langle \rho \rangle$, deviate from the straight line formed by $\langle \rho \rangle_h$, as the ratio B/G becomes very small. Hence, the trapping potential is harmonic even for large ratios G/B and very tightly confining harmonic traps for highly excited atoms can be obtained ($B = 0.1$ G and $G = 100$ T, for instance, give rise to a transversal trap frequency of approximately 1.4 MHz).

The mean distance of the Rydberg electron from the core is calculated weighting $\langle r \rangle_e(X, Y)$ with the probability density of the center of mass wave function,

$$\langle r \rangle = \langle \psi_\nu(\boldsymbol{R})| \ \langle \varphi_\kappa(\boldsymbol{r}; \boldsymbol{R})| \ r \ |\varphi_\kappa(\boldsymbol{r}; \boldsymbol{R})\rangle \ |\psi_\nu(\boldsymbol{R})\rangle \ . \tag{4.16}$$

It is depicted in Fig. 4.10, along with $\langle \rho \rangle$, versus the degree of excitation of the center of mass motion ν. Due to the very tight confinement, $\langle \rho \rangle$ and $\langle r \rangle$ are of comparable size! For a Ioffe field strength of $B = 0.1$ G and a field gradient of $G = 100$ T/m, for instance, the ratio of $\langle \rho \rangle$ and $\langle r \rangle$ for the ground state ($\nu = 1$) is as small as $\langle \rho \rangle / \langle r \rangle = 0.4$. The extension of the center of mass wave function is thus smaller than the extension of the electronic cloud. The expectation value $\langle r \rangle$ for the electron, on the other hand, remains nearly constant as the degree of excitation increases, and it barely differs from the corresponding field-free value (dashed line in Fig. (4.10)). As indicated previously, we find the electron to be in the circular state with $m_l = n - 1$, which features the smallest mean square deviation of the nucleus-electron separation $\langle r^2 \rangle - \langle r \rangle^2 = n^2(2n + 1)/4$. It is therefore possible, that the center of mass and the electronic wave function do not even overlap which is indicated in the inset of the upper right plot in Fig. 4.10 for $\nu = 1$. This novel regime opens up the possibility to control Rydberg atoms in the quantum regime and paves the way to study many-body effects in low-dimensional ultracold Rydberg gases [16]. We lay the foundations for creating such a gas in the following section.

5 One-dimensional Rydberg gas in a magneto-electric trap

The properties of many-atom systems are defined to a great extend by their order and reducing the dimension of the system can profoundly affect that order. This gives rise to often completely different physics and provides the attraction of studying low-dimensional systems.

The long-range order in a three-dimensional system at low temperatures can for instance get lost in two dimensions due to thermal fluctuations [18] which prevents a two-dimensional system from condensing into a BEC at finite temperature. More specifically, the mean field Gross-Pitaevskii description fails and has to be replaced by a Berezinskii-Kosterlitz-Thouless theory in two-dimensional systems which associates the occurring phase transition with a topological order. In one-dimensional bosonic systems the mean field theory has to be substituted by the approach of Lieb and Liniger who were the first to solve the system of arbitrary many interacting bosons in one dimension using Bethe's ansatz [90]. It can describe the limit of an infinitely strong inter-particle interaction strength in which a so-called Tonks-Girardeau gas emerges [91]. In such a gas the bosons behave like spin-less non-interacting fermions piled up in the single-particle eigenstates of the one-dimensional potential. Experimentally, this has been realized in a ^{87}Rb Bose-Einstein condensate of very low density in a tight optical potential using an optical lattice to manipulate the atoms' effective mass [92].

Since the dimensionality of a system is reduced by strongly confining the atomic motion in one or several directions it yields discrete energy levels for the center of mass motion in these directions as described previously in our example in Chapter 4.3. This structure can be exploited to modify the scattering along the unconfined direction [93] and a further low-dimensional effect, so-called confinement-induced resonances, can be observed [94].

Besides gases of ground state atoms, particularly Rydberg gases represent excellent systems to study the influence of a strong inter-particle interaction on the dynamics of many-particle ensembles. Due to the large displacement of the ionic core and the valence electron, Rydberg atoms can develop a large electric dipole moment leading to a strong and long-ranged dipole-dipole interaction among them. However, unlike ground state atoms, Rydberg atoms suffer from radiative decay and the mutual interaction time is hence limited by the lifetime of the electronically excited state.

Circular Rydberg atoms in a Ioffe-Pritchard configuration are the perfect answer in respect of the above requirements demanded from the system. As described in the preceding chapters of this thesis they provide both, very strongly confined center of mass states due to the strongly enhanced coupling to the magnetic field, and the possibility of very strong interaction among the atoms. And in addition to that, circular Rydberg states can exhibit lifetimes of several milliseconds. Here we use the Ioffe-Pritchard configuration as an ideal starting point in order to 'prepare' and study a one-dimensional Rydberg gas. Specifically,

we propose a modified Ioffe-Pritchard trap, a magneto-electric trap, which offers confining potential energy surfaces for the atomic center of mass motion in which the atoms possess an oriented permanent electric dipole moment. In Section 5.1 we first incorporate the coupling to the electric field into the description of the system. In Section 5.2 we then describe the modified electronic surfaces and the emerging electric dipole moments. In Section 5.3 we estimate below which Rydberg atom density a one-dimensional Rydberg gas is expected to form. In Section 5.4 we show that the coupling of radial and longitudinal dynamics is negligible for a vast range of parameters before we shortly dwell on the possible experimental realization of the gas in the closing Section 5.5.

Most of the results presented in this chapter are published in Ref. [95].

5.1 Hamiltonian with additional external electric field

In this section we derive the Hamiltonian for an ultracold Rydberg atom in a Ioffe-Pritchard trap that is superimposed by a homogeneous electric field transversal to the translationally symmetric axis. Proceeding along the lines of Chapter 2, we again employ a two-body approach in order to model an alkali metal atom in a Rydberg state. We assume the single valence electron and the ionic core to interact via a pure Coulomb potential. While the inclusion of the fine-structure and quantum defects can be readily done, it turns out not to be necessary for high angular momentum electronic states in the regime we are focusing on. The Ioffe-Pritchard field configuration is given by Eq. (2.10) and (2.11) where we assume the quadratic term, that is responsible for the longitudinal confinement, to be zero, $Q = 0$. To make it vanish, the coils of the trap can be placed at a distance of twice their radius from each other.

In case of a neutral two-body system the electric field interaction couples only to the relative coordinate,

$$H_F = q_i \phi(\boldsymbol{r}_i) = e\boldsymbol{F} \cdot \boldsymbol{r}_1 - e\boldsymbol{F} \cdot \boldsymbol{r}_2 = \boldsymbol{F} \cdot \boldsymbol{r} . \tag{5.1}$$

Here $\boldsymbol{r}_1$ and $\boldsymbol{r}_2$ are the positions of the valence electron and the core, respectively, and $\boldsymbol{r}$ is the relative coordinate in accordance with the naming introduced in Sec. 2.1. The unitary transformation $U = \exp\left\{\frac{i}{2}\boldsymbol{B}_c \times \boldsymbol{r} \cdot \boldsymbol{R}\right\}$, applied in Sec. 2.1 to simplify the coupling of relative and center of mass motion, does not affect H_F. We choose the electric field to point in the X-direction, $\boldsymbol{F} = F\boldsymbol{e}_X$, and the Hamiltonian describing the Rydberg atom becomes

$$H = H_A + \boldsymbol{A}_c(\boldsymbol{r}) \cdot \boldsymbol{p} + \frac{\boldsymbol{P}^2}{2M} - \boldsymbol{\mu}_2 \cdot \boldsymbol{B}(\boldsymbol{R}) + Fx - \boldsymbol{\mu}_1 \cdot \boldsymbol{B}(\boldsymbol{R} + \boldsymbol{r}) + \boldsymbol{A}_l(\boldsymbol{R} + \boldsymbol{r}) \cdot \boldsymbol{p}. \tag{5.2}$$

Here, $H_A = \frac{\boldsymbol{p}^2}{2} - \frac{1}{r}$ is the hydrogen Hamiltonian. The second term denotes the energy of the electron in the homogeneous Ioffe field due to its orbital motion. The following two terms describe the motion of a point-like particle possessing the magnetic moment $\boldsymbol{\mu}_2$ in the presence of the field $\boldsymbol{B}$. The magnetic moments are connected to the electronic spin $\boldsymbol{S}$ and the nuclear spin $\boldsymbol{\Sigma}$ according to $\boldsymbol{\mu}_1 = -\boldsymbol{S}$ and $\boldsymbol{\mu}_2 = -\frac{g_2}{2M_c}\boldsymbol{\Sigma}$, with g_2 being the nuclear g-factor. We neglect the term involving $\boldsymbol{\mu}_2$ in the following due to the large nuclear mass. The electric field interaction gives rise to the fifth term. The last two terms of H are spin-field and motion-induced terms coupling the electronic and center of mass dynamics. We focus on a parameter regime which allows us to neglect the diamagnetic interactions as is thoroughly discussed in Section 2.1.

In order to find the stationary states of the Hamiltonian (5.2), we assume that neither the magnetic nor the electric field causes couplings between electronic states with different principal quantum number n. The parameter range in which this approximation is valid is determined in Section 2.3 for the magnetic contributions, see the discussion after Eq. (2.19). The condition to be satisfied in order for the electric field not to couple adjacent n-manifolds is found comparing $\mathcal{H}_F$ with the Zeeman term $\boldsymbol{\mu} \cdot \boldsymbol{B}(\boldsymbol{R})$ and reads

$$F_x \ll B/n \ , \tag{5.3}$$

see also the discussion of the electric field Hamiltonian in Section 7.2. If the above conditions are met we can consider each n-manifold separately and may represent the Hamiltonian (5.2) in the space of the $2n^2$ states which span the n-manifold under investigation.

Both the Ioffe-Pritchard field for vanishing Q and the homogeneous electric field are translationally symmetric in the longitudinal axis. The center of mass motion along Z can therefore be separated from the transversal motion in X and Y. More specifically, since P_z commutes with the Hamiltonian the longitudinal motion can be integrated by employing plane waves $|k_Z\rangle = \exp\{iZk_Z\}$. As indicated above, we only consider the action of all operators in a single n-manifold and can thus simplify the Hamiltonian incorporating the relations (2.20), (2.21) and (2.22), which exploit the degeneracy of the hydrogen-manifold for zero fields. Additionally, if we omit the constant energy offset E_n we eventually arrive at the Hamiltonian[1]

$$\mathcal{H} = \frac{P_x^2 + P_y^2}{2M} + \boldsymbol{\mu} \cdot \boldsymbol{B}(\boldsymbol{R}) + G(xyp_z + xS_x - yS_y) + \mathcal{H}_F \ , \tag{5.4}$$

cf. the working Hamiltonian (2.25) in Section 2.3. This Hamiltonian governs the transversal center of mass as well as the electronic dynamics. The symbols $\boldsymbol{\mu}$ and $\mathcal{H}_F$ are the $2n^2$-dimensional matrix representations of the operator $\frac{1}{2}(\boldsymbol{L} + 2\boldsymbol{S})$ and of the electric field interaction $H_F = Fx$, respectively.

5.2 Energy surfaces and electronic properties

The difference in the time scales of relative and center of mass dynamics allows us to employ an adiabatic approach in order to solve the Schrödinger equation that corresponds to the Hamiltonian (5.4). The adiabatic separation is introduced and justified in Section 2.4. In the limit of vanishing center of mass kinetic energy we apply a unitary transformation $U(X,Y)$ which diagonalizes the remaining Hamiltonian, i.e.,

$$U^\dagger(X,Y)(\boldsymbol{\mu} \cdot \boldsymbol{B}(\boldsymbol{R}) + G(xyp_z + xS_x - yS_y) + \mathcal{H}_F)U(X,Y) = E_\kappa(X,Y) \ . \tag{5.5}$$

Since $U(X,Y)$ depends on the center of mass coordinates, the transformed kinetic energy term involves non-adiabatic (off-diagonal) coupling terms $\Delta\mathcal{T}$, Eq. (2.31), which are suppressed by the splitting of adjacent energy surfaces ($\sim 1/B$), see Eqs. (2.32) and (2.33). They can be neglected in our parameter regime and we are led to a set of $2n^2$ decoupled differential equations governing the adiabatic center of mass motion within the individual

---

[1]In contrast to the working Hamiltonian (2.25) in Section 2, we did not scale the Hamiltonian here.

two-dimensional energy surfaces $E_\kappa(X, Y)$, i.e., the surfaces $E_\kappa(X, Y)$ serve as potentials for the center of mass motion of the atom.

We first find approximate analytical solutions of the eigenvalue equation (5.5) in the limit of small magnetic field gradient and small electric field strength by following the approach chosen in Section 4.1: In this case the Zeeman term $\boldsymbol{\mu}\cdot\boldsymbol{B}(\boldsymbol{R})$ is dominant and we diagonalize it by applying the unitary transformation

$$U = \exp(-i\alpha(L_x + S_x)) \cdot \exp(-i\beta(L_y + S_y)) \tag{5.6}$$

with

$$\tan\alpha = \frac{-GY}{\sqrt{B^2 + G^2 X^2}} \;, \quad \tan\beta = \frac{-GX}{B} \;. \tag{5.7}$$

The transformation U rotates the Z-axis into the local magnetic field direction where α and β denote the rotation angles. It does not affect the field-free Hamiltonian H_A. The resulting adiabatic electronic energy surfaces,

$$E_\kappa(X, Y) \approx \left(\frac{m_l}{2} + m_s\right)|\boldsymbol{B}| \;, \tag{5.8}$$

exhibit a quadratic behavior in $\rho = \sqrt{X^2 + Y^2}$ around the Z-axis and a linear increase for large ρ, see Eqs. (4.6), (4.7) and (4.8), respectively. At the origin the surfaces with different factors $\left(\frac{m_l}{2} + m_s\right)$ are separated by the energy $B/2$.

We are going to focus our considerations on the uppermost electronic surface in the following. The latter is most appropriate for confining the atoms since it is the only non-degenerate surface and it is energetically well isolated from other surfaces, see Chapter 4. In the abovementioned limit of small G and F it is constituted almost exclusively by the state with the largest angular momentum projection quantum number $m_l = n - 1$, $|\text{circ}\rangle = |n, n-1, n-1, 1/2\rangle$, which is called *circular* state. Since $|\text{circ}\rangle$ is a parity eigenstate, the atoms exhibit almost no electric dipole moment in this case.

In the analytical approach to find approximate solutions of the eigenvalue equation (5.5) we have neglected the finite size term and the electric field term. As long as the contribution of the Zeeman term is significantly larger, their influence on $E_\kappa(X, Y)$ can be calculated using perturbation theory. A thorough analysis of the effects of these perturbations is the subject of Chapter 7. In the parameter regime we consider here, the contribution of the finite size term $G(xyp_z + xS_x - yS_y)$ is negligible in comparison with the contribution of H_F and we therefore only consider the influence of the electric field here.

Due to the coupling to the electric field, the electronic state constituting the uppermost energy surface is no longer the pure circular state. Anticipating the results from Section 7.2, that are obtained with second order perturbation theory in H_F, we find that the electric field yields an admixture of the state $|3\rangle = |n, n-2, n-2, 1/2\rangle$ to the energetically uppermost surface within a single n-manifold of the hydrogenic basis, see Eq. (7.40). This entails the modified energy

$$E_{|\text{circ}\rangle} + E_F = \frac{n}{2}|\boldsymbol{B}| + \frac{9}{4}F_x^2 n^2(n-1)\frac{B^2 + G^2 Y^2}{B^2 + G^2 Y^2 + G^2 X^2} \;, \tag{5.9}$$

see Eq. (7.44). From the angular dependency of the extra energy originating from the admixture, E_F, we can see that it is constant for $X = 0$, whereas for for $Y = 0$ it decreases
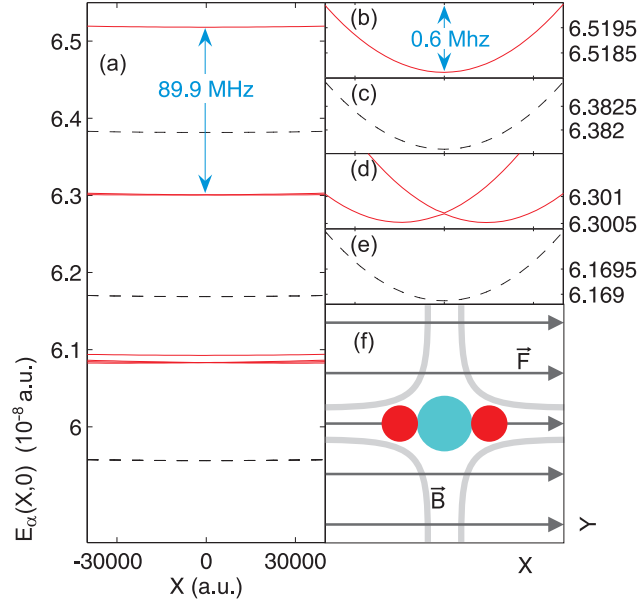
Figure 5.1: Potential energy surfaces of the center of mass motion of a ^{87}Rb atom ($n = 30$) in an IP trap with $B = 10\,\mathrm{G}$, $G = 10\,\mathrm{Tm^{-1}}$. Dashed lines: $F = 0$, solid lines: $F = 5.14\,\mathrm{Vm^{-1}}$. An overview of the seven energetically highest potential curves is shown in panel (a). Magnified views of the uppermost (b,c) and next lower ones (d,e) are also provided. The range of the X-coordinate, corresponding to 2.1μm, is the same for each subfigure (a)-(e). The characteristic length of the center of mass dynamics is $\omega^{-1/2} \approx 1200$ a.u. ≈ 65 nm. The total field configuration is sketched in panel (f) where the disks depict the locations of the minima of the uppermost (big disk) and the two adjacent lower-lying (small disks) center of mass surfaces. The magnetic field lines are indicated in gray while the electric field is sketched by black arrows.

with X^2 around the Z-axis, $E_F \sim 1 - (G/B)^2 X^2 + \mathcal{O}(GX/B)^4$. For parameters that yield small ratios G/B, the coupling to the electric field therefore yields an energetic contribution to the uppermost adiabatic surface that is essentially constant close to the longitudinal axis.

Since the states $|\mathrm{circ}\rangle$ and $|3\rangle$ have opposite parity, the admixture is also responsible for a finite dipole moment of the atom. Up to first order in F/B we find the expression

$$\boldsymbol{d}_F(\boldsymbol{R}) = \frac{9}{2}\frac{F}{|\boldsymbol{B}|}n^2(n-1) \cdot \left(\cos\beta \begin{pmatrix} \cos\beta \\ 0 \\ \sin\beta \end{pmatrix} + \sin\alpha\sin\beta \begin{pmatrix} \sin\alpha\sin\beta \\ \cos\alpha \\ -\sin\alpha\cos\beta \end{pmatrix} \right)$$

$$= \frac{9}{2}\frac{F}{|\boldsymbol{B}|}n^2(n-1) \cdot \frac{1}{\boldsymbol{B}^2} \begin{pmatrix} B^2 + G^2 Y^2 \\ G^2 XY \\ BGX \end{pmatrix} , \qquad (5.10)$$

see Eq. (7.46), which on the longitudinal axis points in the direction of the electric field,

$$\boldsymbol{d}_F(0,0,Z) = \frac{9}{2}\frac{F}{B}n^2(n-1)\boldsymbol{e}_z . \qquad (5.11)$$

In order to substantiate these analytical results (and to examine their predictions for parameters that lie at the border of the range of validity of the perturbative treatment) we
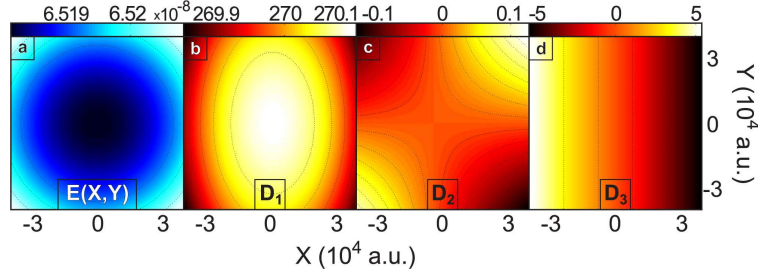
Figure 5.2: (a) Uppermost electronic potential surface for the center of mass motion of ^{87}Rb in the $n = 30$ multiplet and the parameters used in Fig. 5.1. (b-d) Components of the electronic dipole moment $\boldsymbol{d}_F(\boldsymbol{R})$ in atomic units. One recognizes the clear alignment of the electric dipole moment along the electric field vector. The numerically calculated values of $\boldsymbol{d}_F(\boldsymbol{R})$, that are shown in the plots, are to good accuracy reproduced by Eq. (5.10).

solve the internal eigenvalue equation (5.5) numerically with methods described in Chapter 3. In Fig. 5.1 we present numerically computed intersections along the X-direction of the potential surfaces E_κ for $B = 10$ G, $G = 10\,\mathrm{Tm}^{-1}$ and $n = 30$ in case of ^{87}Rb. For zero electric field strength (dashed lines), the potential curves are organized in groups which are energetically well-separated by a gap of $B/2 = 87.9$ MHz. The uppermost surface is non-degenerate and provides an approximately harmonic confinement with a trap frequency of $\omega = G\sqrt{n/(2BM)} = 13.9\,\mathrm{kHz}$ corresponding to $0.1\,\mu$K. The two adjacent lower surfaces are degenerate and also approximately harmonic. The adiabatic surfaces for vanishing electric field are discussed in detail in the preceding Chapter 4. As soon as an electric field is applied, all surfaces are shifted considerably in energy. This is visible from the solid curves in Fig. 5.1 for which an electric field of strength $F = 10^{-11}$a.u. $= 5.14\,\mathrm{Vm}^{-1}$ is applied. The shapes of the potentials are barely affected by the electric field such that Rydberg states which were trapped in a pure Ioffe-Pritchard configuration remain also confined in the magneto-electric trap. This can be expected from the perturbative result (5.9) for the uppermost energy surface. As already indicated, the additional energy due to the coupling to the electric field only weakly depends on the center of mass coordinates for small ratios G/B. Moreover, adding the electric field leads to non-trivial effects: The second and third surface, which were almost degenerate in the absence of the electric field, are now shifted in opposite ways along the X-direction, i.e., they are centered at different spatial positions. All surfaces that are shown provide a harmonic confinement with a trap frequency ω also in the Y-direction. We remark that the chosen parameter set lies well within the regime where our approximations hold (even if the influence of the electric field cannot be treated perturbatively anymore) and does not generate an extreme constellation: An even stronger confinement can be achieved without invalidating the applied approximations as can be seen in Section 4.3.

The plots in Fig. 5.2 present numerical data for the uppermost potential surface and the three components of the electric dipole expectation value $\boldsymbol{d}_F(\boldsymbol{R})$ for the same parameters as in Fig. 5.1. It can be clearly seen that a permanent dipole moment is established whose dominant contribution points along the electric field vector. As can be seen from the corresponding analytical expression for the dipole moment, Eq. (5.10), $\boldsymbol{d}_F(\boldsymbol{R})$ scales proportional to the third power of the principal quantum number and can therefore gain a significant

magnitude even if the ratio F/B is small. Good agreement of Eq. (5.10) with the calculated data presented in Fig. 5.2 is found, e.g., in the vicinity of the minimum of the potential surface ($X = Y = 0$) we find an exact value of $d_x = 270$, whereas the expression (5.10) yields 276. For the remaining components Eq. (5.10) yields zero at the origin whereas we numerically find the values 10^{-10} and -0.02 for the y- and the z-component, respectively. For smaller ratios of F/B, even better agreement can be achieved.

5.3 One dimensional atom chain

Due to the dependence on the angles α and β, the dipole moment depends weakly on the quantum state of the center of mass motion. However, since the field configuration is translationally symmetric, the electric dipole moment is independent of the Z-position of the Rydberg atoms in the trap. We now consider two transversally confined atoms in the same trap at the longitudinal positions Z_A and Z_B. Considering the orientation of the dipole moments of the atoms close to the longitudinal axis, and assuming that $|Z_A - Z_B|$ is large compared to the transversal oscillator length of the trap, we can approximate their dipole-dipole interaction by

$$V_{\mathrm{dd}}(\boldsymbol{R}_A, \boldsymbol{R}_B) \approx \frac{\boldsymbol{d}(\boldsymbol{R}_A) \cdot \boldsymbol{d}(\boldsymbol{R}_B)}{|Z_A - Z_B|^3} \; . \tag{5.12}$$

We get the approximate expression (5.12) from more general expressions derived in Chapter 8 where we thoroughly investigate the interaction of two Rydberg atoms. Using this approximation one can estimate the interaction energy of one atom being part of an infinite atomic chain with an inter-particle spacing a. One finds

$$E_{\mathrm{int}} = \frac{2}{a^3} \boldsymbol{d}^2(0) \sum_{k=1}^{\infty} k^{-3} = \frac{81}{2} \frac{\zeta(3)}{2} \frac{1}{a^3} \frac{F^2}{B^2} n^4 (n-1)^2 \tag{5.13}$$

with the Riemann zeta function, $\zeta(x)$. Here we have approximated $\boldsymbol{d}^2(\boldsymbol{R}) \approx \boldsymbol{d}^2(0)$ since the dipole moment barely varies in the vicinity of $X = Y = 0$. If the interaction energy E_{int} is smaller than the transversal trap frequency ω, we can assume that the interacting atoms remain in the transversal ground state: This is considered the one-dimensional regime. The linear density below which a one-dimensional Rydberg gas, illustrated in Fig. 5.3, is expected to form is then given by

$$N_{\mathrm{1D}} = \frac{\sqrt{B}}{3} \left(3 \sqrt{\frac{M}{2}} \frac{F^2}{G} \zeta(3) \, n^{7/2} (n-1)^2 \right)^{-1/3} . \tag{5.14}$$

Above this density, excited transversal center of mass states might be populated resulting in a quasi one-dimensional Rydberg gas with similar properties. For our parameter set, we obtain a minimal interparticle spacing $a = 43 \, \mu$m; hence a chain of 1 mm in length contains 23 particles. This density can be further increased by either increasing the magnetic field gradient and/or decreasing the electric field strength: At $B = 10 \, \mathrm{G}$, $G = 100 \, \mathrm{Tm}^{-1}$, and $F = 0.514 \, \mathrm{Vm}^{-1}$ a chain of the same length would contain 230 Rydberg atoms.

Figure 5.3: Ultracold Rydberg atoms in a magnetic guide subject to dipolar repulsion form a one-dimensional structured gas. The red arrows symbolize the atoms' electric dipole moments induced by the electric field in X-direction and the yellow tube indicates the strong transversal magnetic confinement.
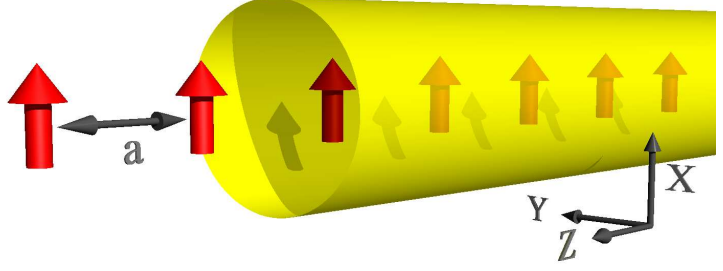
5.4 Coupling of radial and longitudinal dynamics

The transversal dependence of the electric dipole moments of the atoms can in principle couple the longitudinal with the transversal center of mass dynamics. To quantify this coupling we consider the two-atom basis

$$\{|IJ\rangle\} := \{|\psi_I^A(\boldsymbol{R}_A)\rangle \otimes |\varphi(\boldsymbol{r}_A; \boldsymbol{R}_A)\rangle \otimes |\psi_J^B(\boldsymbol{R}_B)\rangle \otimes |\varphi(\boldsymbol{r}_B; \boldsymbol{R}_B)\rangle\} \tag{5.15}$$

where I and J number the single-atom center of mass wave functions ψ of atom A and atom B, respectively. The electronic states φ do not have an index here since we assume that they are the same for both atoms. The representation of the dipole-dipole interaction Hamiltonian,

$$V_{\mathrm{dd}} = R_{AB}^{-3}(\boldsymbol{d}_A.\boldsymbol{d}_B - 3(\boldsymbol{d}_A.\hat{\boldsymbol{R}}_{AB})(\boldsymbol{d}_B.\hat{\boldsymbol{R}}_{AB})) \ , \tag{5.16}$$

becomes diagonal in this two-atom representation if we assume that the electric dipole moments of the atoms, and with it the dipole-dipole interaction operator V_{dd}, does not depend on the center of mass position. It is then

$$\langle IJ|V_{\mathrm{dd}}|I'J'\rangle = \langle I|I'\rangle\langle J|J'\rangle\langle\varphi|V_{\mathrm{dd}}|\varphi\rangle \sim \delta_{I,I'}\delta_{J,J'} \tag{5.17}$$

since the center of mass eigenfunctions to different eigenvalues are orthogonal.

If we include the transversal dependence of the electric dipole moments into our considerations the matrix elements read

$$\begin{aligned}
\langle IJ|V_{\mathrm{dd}}|I'J'\rangle =& \langle IJ|R_{AB}^{-3}(\boldsymbol{d}_A.\boldsymbol{d}_B - 3(\boldsymbol{d}_A.\hat{\boldsymbol{R}}_{AB})(\boldsymbol{d}_B.\hat{\boldsymbol{R}}_{AB}))|I'J'\rangle \\
\approx& R_{AB}^{-3}\left(\boldsymbol{D}_{II'}\boldsymbol{D}_{JJ'} - 3D_{II',z}D_{JJ',z}\right) \ .
\end{aligned} \tag{5.18}$$

The symbols $\boldsymbol{D}$ abbreviate $\boldsymbol{D}_{KK'} = \langle\psi_K|\boldsymbol{d}|\psi'_K\rangle$ with $\boldsymbol{d}(X,Y) = \langle\varphi|\boldsymbol{r}|\varphi\rangle(X,Y)$. In the last step of equation (5.18) we assumed $|X_I|, |Y_I| \ll R_{AB}$ which entails $\hat{\boldsymbol{R}}_{AB} \approx (0,0,1)$. This approximation holds for large distances of the Rydberg atoms and strong transversal confinements.

In order to quantify the coupling we must thus compute $\boldsymbol{D}_{KK'}$. Due to the harmonic nature of the trapping potential around the Z-axis we can assume $|\psi_K\rangle$ to be two-dimensional harmonic oscillator eigenstates

$$\langle X,Y|\psi_{\mathrm{2DHO},n_1,n_2}\rangle = (2^{n_1+n_2}n_1!n_2!X_0Y_0\pi)^{-1/2}H_{n_1}\left(\frac{X}{X_0}\right)H_{n_2}\left(\frac{Y}{Y_0}\right)e^{-\frac{1}{2}\left(\frac{X^2}{X_0^2}+\frac{Y^2}{Y_0^2}\right)} \ , \tag{5.19}$$

Table 5.1: As long as the parameter C, Eq. (5.22), is small the radial variations of the electric dipole moments do not couple longitudinal and radial center of mass dynamics.

C	$G = 0.1\,\mathrm{Tm}^{-1}$	$G = 1\,\mathrm{Tm}^{-1}$	$G = 10\,\mathrm{Tm}^{-1}$	$G = 100\,\mathrm{Tm}^{-1}$
$B = 0.1\,\mathrm{G}$	5×10^{-5}	5×10^{-4}	5×10^{-3}	0.05
$B = 1\,\mathrm{G}$	2×10^{-6}	2×10^{-5}	2×10^{-4}	2×10^{-3}
$B = 10\,\mathrm{G}$	5×10^{-8}	5×10^{-7}	5×10^{-6}	5×10^{-5}
$B = 100\,\mathrm{G}$	2×10^{-9}	2×10^{-8}	2×10^{-7}	2×10^{-6}

where H_n are the Hermite polynomials. For the Ioffe-Pritchard field configuration the trap frequencies in X and Y are the same, $\omega_x = \omega_y =: \omega_\perp$, and we can equate

$$X_0 = Y_0 =: X_{0\perp} = \sqrt{\frac{\hbar}{\omega_\perp M}} \ . \tag{5.20}$$

The trap frequency for dominating Ioffe field can be approximated by the expression

$$\omega_\perp^2 = \frac{nG^2}{2BM} \ . \tag{5.21}$$

Energetically degenerate two-dimensional harmonic oscillator eigenstates have the same parity due to the parity of the Hermite polynomials, $PH_n = (-)^n$. Linear combinations of such degenerate states again have definite parity. Expectation values of odd operators in harmonic oscillator eigenstates therefore vanish. Eigenstates belonging to energetically neighboring eigenvalues on the other hand have different parity. If we concentrate on the dipole-dipole interaction induced excitations from the transversal center of mass ground state to the next higher state one can furthermore conclude that contributions to the off-diagonal elements of the interaction matrix coming from even operators vanish.

We analytically compute the couplings for the three states $|\psi_{2\mathrm{DHO},n_1,n_2}\rangle$ lowest in energy, $\{|\psi_{2\mathrm{DHO},0,0}\rangle, |\psi_{2\mathrm{DHO},1,0}\rangle, |\psi_{2\mathrm{DHO},1,1}\rangle\}$, using the electric dipole moment induced by the external electric field, $\boldsymbol{d}_F$, Eq. (5.10). If we exploit the smallness of the parameter

$$C = \left(\frac{X_{0\perp}G}{B}\right)^2 = \sqrt{\frac{2G^2}{nMB^3}} \ , \tag{5.22}$$

which is tabulated for a range of field parameters in Tab. 5.1, the analytic expressions for $\boldsymbol{D}_{KK'}$ simplify significantly as will be demonstrated in the following.

We write down the representation of the dipole-dipole interaction operator V_{dd} in the representation of the basis

$$\{|IJ\rangle\} = \{|11\rangle, |12\rangle, |11\rangle, |22\rangle\} \tag{5.23}$$

where 1 symbolizes the transversal center of mass ground state $|\psi_{2\mathrm{DHO},0,0}\rangle$ and 2 the one with the first excitation in X, $|\psi_{2\mathrm{DHO},1,0}\rangle$. Due to the form of the dependencies of the electric dipole moment (5.10) on X and Y, the corrections coming from the energetically degenerate center of mass state with the first excitation in Y, $|\psi_{2\mathrm{DHO},0,1}\rangle$, are even smaller

$(\sim C^2)$. We find the representation of the interaction to be

$$\langle IJ|V_{\mathrm{dd}}|I'J'\rangle \approx \frac{9}{2}n^2(n-1)F_x B \begin{pmatrix} 1 & 0 & 0 & -C \\ 0 & 1 & -C & 0 \\ 0 & -C & 1 & 0 \\ -C & 0 & 0 & 1 \end{pmatrix}. \qquad (5.24)$$

The parameter $C = \sqrt{2}G/\sqrt{nMB^3}$ quantifies the magnitude of the off-diagonal elements compared with the diagonal elements in (5.24). Since C is small for a vast range of field parameters (Tab. 5.1) we can neglect the dipole-dipole interaction induced coupling from the center of mass ground state to excited states that originate from the transversal center of mass dependence of the electric dipole moments.

5.5 Experimental realization

In order to observe the external dynamics of the gas of Rydberg atoms we need to consider their finite lifetime due to radiative decay which is discussed in detail in Ref. [96]. For moderate electric field strengths the circular character of the electronic wave function of the uppermost surface remains dominant resulting in one prevalent decay channel, $|\mathrm{circ}_n\rangle \rightarrow |\mathrm{circ}_{n-1}\rangle$, i.e. to the circular state of the adjacent manifold with the principal quantum number $n-1$. For an atom being confined to the energy surface which is shown in Fig. 5.2, we have calculated a lifetime of $\tau \approx 2.1\,\mathrm{ms}$ which is in good agreement with the corresponding field-free result $\tau(n, n-1) \approx 3n^5/(2c^2\alpha^5)$ [97]. Corrections to this bare decay rate are found to be of the order of $(F/B)^2 n^3$. Due to the scaling proportional to n^5, the lifetime can be significantly enhanced by exciting to a higher principal quantum number n. In addition, it can be further prolonged by establishing an adapted experimental setup which inhibits the electromagnetic field mode at the dominant transition frequency [98]. At the same time, a cryogenic environment will diminish the undesirable effect of stimulated (de-)excitation by blackbody radiation. We remark that the decay of one or several atoms into the circular state $|\mathrm{circ}_{n-1}\rangle$ does not immediately destroy the Rydberg gas since the properties of this state – and therewith those of the adiabatic surface and the electric dipole moment – are very similar.

The timescale of the dynamics of the Rydberg chain on the other hand depends on the inter-particle spacing and on the field strengths via the dipole moment: A harmonic approximation of the dipole-dipole interaction of one Rydberg atom with its next neighbors yields the longitudinal one-particle oscillator frequency

$$\omega_{\mathrm{dd}} = \sqrt{24\,\boldsymbol{d}^2(0)/(M_c a^5)}\,, \qquad (5.25)$$

where $\boldsymbol{d}(0)$ is the electric dipole moment at the origin and a is the inter-particle spacing that corresponds to the density $N_{1\mathrm{D}}$ in (5.14). As an example, the field configuration $B = 10\,\mathrm{G}$, $G = 100\,\mathrm{Tm}^{-1}$, and $F = 0.514\,\mathrm{Vm}^{-1}$ yields a timescale of less than one millisecond.

Let us now briefly comment on the experimental realization of such a Rydberg gas which is certainly a challenging experimental task. One could start from an extremely dilute ultracold atomic gas prepared in an elongated Ioffe-Pritchard trap. For transferring ground state atoms to high angular momentum Rydberg states, several techniques can be employed,

as we have described in Section 1.2. The excitation lasers have to be focused such that Rydberg atoms emerge only at positions separated by the inter-particle spacing a which is required to meet the criterion (5.14). Since a is in the order of several μm, which can be easily resolved optically, this should be feasible. Moreover, the large value of a ensures that the mutual ionization due to the overlap of the electronic clouds of two atoms does not occur. For our circular states with $n = 30$, the atomic extension can be estimated by $\langle r \rangle \approx n^2 = 48$ nm and is thus orders of magnitude smaller than the corresponding value of a for our field configuration. In order to probe the dynamics of the resultant Rydberg chain, one can field-ionize the atoms and subsequently detect the electrons: From the spatially resolved electron signal a direct mapping to the positions of the Rydberg atoms should be possible.

6 Longitudinal confinement

We show in Chapter 4 that a Ioffe-Pritchard magnetic field configuration can provide an extremely strong confinement for Rydberg atoms in transversal (ρ-)direction. In Chapter 4, as well as in the preceding Chapter 5, we consider the magnetic field configuration, and therewith the properties of the Rydberg atoms in it, as translationally symmetric in the longitudinal Z-direction. This can be achieved by choosing the right relation between the radius of the coils that generate the homogenous Ioffe field and their distance. The quadratic term in the magnetic field, $\boldsymbol{B}_q$ in Eq. (2.11), then vanishes and with it also the complicated contribution to the Rydberg Hamiltonian in Eq. (2.12) prefixed by the factor Q.

On atom chips, magnetic field configurations that resemble that of a macroscopic Ioffe-Pritchard trap are created by a current-carrying Z-shaped wire [52]. Due to the geometry a translational symmetry cannot be achieved. But also in macroscopic traps a translational symmetry is of limited use for our purpose since we want to excite Rydberg atoms from cold ground state atoms that have to be confined somehow.

These arguments alone are motivation enough to include the quadratic magnetic field term in our considerations. More interestingly, however, the longitudinal confinement can provide the missing ingredient to obtain a stable equilibrium state for atoms that repel each other like the Rydberg atoms described in the preceding chapter. By means of the adiabatic electronic potential energy surfaces derived in this chapter in cooperation with the dipolar repulsion discussed in Chapter 8 we can then describe such a stable configuration for two Rydberg atoms in the concluding Chapter 9.

In Section 6.1 we shortly present the magnetic field configuration on a chip and for a macroscopic setup. We then incorporate the additional terms in the Hamiltonian in Sec. 6.2. In Section 6.3 these terms are projected onto a single n-manifold which considerably simplifies their structure. We can then analytically find approximate expressions for the electronic energy surfaces in an adiabatic approach in the closing Section 6.4.

6.1 Magnetic trap geometries

Simple and versatile traps for neutral atoms can be built using the magnetic potentials created by a current-carrying wire and a homogeneous bias field [52]. In Fig. 6.1 we show different sections through the absolute value of the magnetic field of such a trap formed by a Z-shaped wire for an exemplary parameter set. The magnetic field generated by the individual segments of the wire is computed integrating Biot-Savarts law.

Like in case of the macroscopic Ioffe-Pritchard trap the absolute value of the magnetic field of the Z-trap is harmonic in all directions around its minimum (the trap center). The ratio of transversal and longitudinal confinement depends on $(B_{0,x}L/I)^4$ where $B_{0,x}$ is the homogeneous bias field, L is the length of the middle wire (which is located on the Z-axis) and I is the current through the wire [52]. The distance of the magnetic field minimum from
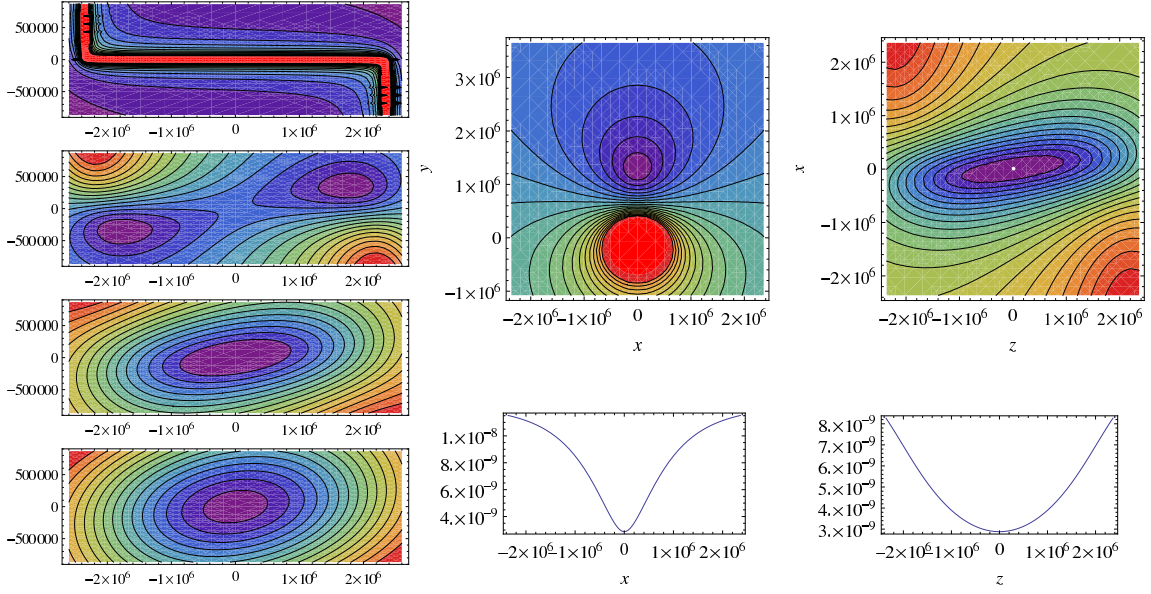
Figure 6.1: Absolute value of the magnetic field generated by a Z-shaped wire. The set of four plots on the left-hand side shows sections parallel to the chip surface (z-x-plane) with increasing distances from the surface in units of $y_{\min}$, the distance of the minimum from the chip, see text (0, 0.5, 1, 1.5, from top to bottom). The two plots in the middle show a x-y section through the center of the trap (top) and a one-dimensional profile in x through the center (bottom). In the x-z section through the minimum on the right-hand side the principal axis are indicated (top) and again a one-dimensional profile in z is plotted. Parameters: Length of middle wire $L = 250$ μm, bias field $B_{0,x} = 25$ G, current $I = 1$ A.

the wire plane (the chip surface) is reciprocal to the bias field, $y_{\min,\text{approx}} = 2I\alpha^2/B_{0,x}$ which for the parameters in Fig. 6.1 yields 80 μm. The trap frequencies along the principal axes are computed by diagonalizing the Hesse matrix at the potential minimum. With parameters from Fig. 6.1 we find 10.2 kHz, 10.0 kHz and 1.8 kHz for the trapping frequencies for the $5S_{1/2}$ $F = 2$ state ($m_F = 1/2$) of ^{87}Rb. We have to keep in mind that for high angular momentum Rydberg states the confinement is stronger by a factor $\frac{1}{2}(\frac{m_l}{2} + m_s)$, cf. Eq. (4.6). The advantage of wire traps are the high field gradients that can be created by bringing the atoms close to the sources of the field. The field gradients are limited for very small distances by surface effects due to chip imperfections or due to interactions of the atoms with the surface.

In the following we consider a non-Helmholtz configuration of a macroscopic Ioffe-Pritchard trap. The vector potential and the magnetic field around the center of a such a trap, cf. Eqs. (2.11) and (2.10), read

$$
\boldsymbol{A} = \frac{B}{2}\begin{pmatrix} -y \\ x \\ 0 \end{pmatrix} + G\begin{pmatrix} 0 \\ 0 \\ xy \end{pmatrix} + \frac{Q}{4}\begin{pmatrix} y(x^2 + y^2 - 4z^2) \\ -x(x^2 + y^2 - 4z^2) \\ 0 \end{pmatrix} =: \boldsymbol{A}_c + \boldsymbol{A}_l + \boldsymbol{A}_q \; ,
$$

$$
\boldsymbol{B} = B\begin{pmatrix} 0 \\ 0 \\ 1 \end{pmatrix} + G\begin{pmatrix} x \\ -y \\ 0 \end{pmatrix} + Q\begin{pmatrix} -2xz \\ -2yz \\ 2z^2 - x^2 - y^2 \end{pmatrix} =: \boldsymbol{B}_c + \boldsymbol{B}_l + \boldsymbol{B}_q \; , \qquad (6.1)
$$

where Q scales linearly with the Ioffe field strength B and depends on the radius R of the coils and their distance $2D$,

$$Q = B \cdot \frac{3}{2} \frac{4D^2 - R^2}{(D^2 + R^2)^2} =: B \cdot \tilde{Q}(D, R) \ . \tag{6.2}$$

The geometry factor $\tilde{Q}(D, R)$ vanishes for $2D = R$ (Helmholtz configuration). It is negative when $2D < R$ and in this case the absolute value of the magnetic field on the Z-axis, $|\boldsymbol{B}(0, 0, Z)| = B|1 + 2\tilde{Q}Z^2|$, decreases with $|Z|$ touching eventually zero outside the coils $(Z > D)$. $\tilde{Q}$ is positive when $2D > R$ and we then have a harmonic confinement in Z. We therefore assume $\tilde{Q}$ to be positive in the remaining chapters of this thesis. The geometry factor reaches its maximal value, $\tilde{Q}_{\max} = \frac{9}{10}D^{-2}$, when $2D = \sqrt{6}R$, that means the smaller the trap, the larger $\tilde{Q}$.

6.2 Ioffe-Pritchard Hamiltonian

In this section we analyze the coupling of the Rydberg atom to the quadratic magnetic field component $\boldsymbol{B}_q$ in (6.1) and include it into our considerations. We shortly recapitulate the procedure that leads to the two-body Hamiltonian (2.9) developed in Sec. 2.1 and give particular attention to the terms that involve the quadratic field: After introducing relative and center of mass coordinates, neglecting relativistic corrections and exploiting the large difference in the particles masses, we simplify the terms coupling relative and center of mass motion by applying the unitary transformation $U = \exp\left\{\frac{i}{2}\boldsymbol{B}_c \times \boldsymbol{r} \cdot \boldsymbol{R}\right\}$, Eq. (2.4). The transformation of the terms in the Hamiltonian (2.3) that include the quadratic magnetic field component $\boldsymbol{B}_q$ yields

$$U^\dagger \left(\boldsymbol{A}_q(\boldsymbol{R} + \boldsymbol{r}).\boldsymbol{p}\right) U = U^\dagger \left(\frac{1}{4}(\boldsymbol{L_r} + \boldsymbol{R} \times \boldsymbol{p}) \cdot \boldsymbol{B}_q(\boldsymbol{R} + \boldsymbol{r})\right) U$$
$$= \frac{1}{4}(\boldsymbol{L_r} + \boldsymbol{R} \times (\boldsymbol{p} - \frac{1}{2}(\boldsymbol{B}_c \times \boldsymbol{R}))) \cdot \boldsymbol{B}_q(\boldsymbol{R} + \boldsymbol{r}) \ . \tag{6.3}$$

The emerging extra term $\frac{1}{2}(\boldsymbol{R} \times (\boldsymbol{B}_c \times \boldsymbol{R})) \cdot \boldsymbol{B}_q(\boldsymbol{R} + \boldsymbol{r}) = \boldsymbol{A}_q(\boldsymbol{R} + \boldsymbol{r}).\boldsymbol{A}_c(\boldsymbol{R})$ is negligible compared with $(\boldsymbol{R} \times \boldsymbol{p}) \cdot \boldsymbol{B}_q(\boldsymbol{R} + \boldsymbol{r})$ as long as

$$|X|, |Y| \ll \frac{2}{Bn} \ . \tag{6.4}$$

This condition is the same as (2.7) except for a factor of 2. For a Ioffe field of 10 Gauss and $n = 50$, for example, it reads $|X|, |Y| \ll 10^7$. The transversal confinement in the Ioffe-Pritchard trap is strong, especially for Rydberg atoms, and this condition is hence easily fulfilled. We are thus going to assume that the conditions (2.7) and (6.4) can be met (which is always the case in the parameter regime of interest) and discard the transformation-induced terms emerging from magnetic field terms in the Hamiltonian (2.9) in the following. When we additionally omit the constant field-free Hamiltonian H_A (which is invariant under the transformation U) and the coupling of the nuclear spin to the field (since the core

magneton is around 2000 times smaller than the Bohr magneton), we find the Hamiltonian[1]

$$U^{\dagger}HU \;=\; \frac{\boldsymbol{P}^2}{2M} + \frac{1}{2}\boldsymbol{L_r} \cdot \boldsymbol{B_c} + \boldsymbol{A_l}(\boldsymbol{R}+\boldsymbol{r}) \cdot \boldsymbol{p} + \boldsymbol{A_q}(\boldsymbol{R}+\boldsymbol{r}) \cdot \boldsymbol{p} + \boldsymbol{S} \cdot \boldsymbol{B}(\boldsymbol{R}+\boldsymbol{r}) \;, \quad (6.5)$$

The magnetic field $\boldsymbol{B}$ in (6.5) now of course includes the quadratic term $\boldsymbol{B_q}$. We have also neglected[2] the terms that involve $\boldsymbol{A_q^2}$ or $\boldsymbol{B_q^2}$ in analogy to the discussion after Eq.(2.9).

6.3 Projection on a single hydrogenic manifold

In order to simplify the structure of the additional terms in the Hamiltonian that emerge due to a non-vanishing geometry factor $\tilde{Q}$ we exploit the fact that the field-free atomic Hamiltonian H_A dominates all other terms in the Hamiltonian of the system. We can therefore study the effect of the magnetic field within a single sub-manifold with a given principal quantum number n. To substantiate this claim the energetic separation of different n-manifolds $|E_A^n - E_A^{n\pm1}|$ has to be compared with the Zeeman energy, i.e. with the energy that comes from the coupling to the magnetic field. The dominant contribution to this energy is the effective coupling $\mu|\boldsymbol{B}|$ which is responsible for the confinement. We show in Section 2.3 that the inter-n-manifold couplings coming from the constant and the linear term in the magnetic field are negligible, cf. the discussion after Eq. (2.19). The quadratic term $|\boldsymbol{B_q}(\boldsymbol{R})|$ becomes comparable only for large displacements form the origin. Since the transversal confinement in a Ioffe-Pritchard trap is stronger than the longitudinal confinement for all reasonable parameter sets we consider $|\boldsymbol{B_q}(\boldsymbol{R})|$ for large $|Z|$ to estimate its influence,

$$|\boldsymbol{B_q}(\boldsymbol{R})| = |Q|\sqrt{\rho^4 + 4Z^4} \approx 2|Q|Z^2 \quad \text{for } Z \gg \rho = \sqrt{X^2 + Y^2} \,. \quad (6.6)$$

We compare the strength of the effective coupling $\mu|\boldsymbol{B_q}|$ with the distance of different n-manifolds, i.e. $2n|Q|Z^2 \ll n^{-3}$. For maximal Q, this results in $\frac{4}{5}B(\frac{Z}{D})^2 \ll n^{-4}$ which can be simplified to

$$B \ll n^{-4} \quad (6.7)$$

since $2|Z|$ must be smaller than the distance of the coils, $2D$, in order for the experiment to happen inside the trap. We hence find the same condition that we already required to hold (see page 19) to guarantee that the original Zeeman term $\frac{1}{2}BL_z$ does not couple different n-manifolds.

Given the argument above we can now represent the additional Hamiltonian due to the nonzero quadratic field $\boldsymbol{B_q}$, which can also formulated using the vector potential $\boldsymbol{A_q}$,

$$U^{\dagger}H_q U = \boldsymbol{A_q}(\boldsymbol{R}+\boldsymbol{r}) \cdot \boldsymbol{p} + \boldsymbol{S} \cdot \boldsymbol{B_q}(\boldsymbol{R}+\boldsymbol{r}) \;, \quad (6.8)$$

---

[1] In order to be able to physically classify the different terms in the Hamiltonian the formulation in magnetic field and angular momentum operators is instrumental. We, however, prefer to formulate the coupling to the quadratic field in terms of the vector potential here, since it proves advantageous for the simplification of the Hamiltonian in the following section.

[2] The neglect of the terms that are quadratic in the vector potential $\boldsymbol{A_q}$ or in the field $\boldsymbol{B_q}$ is legitimate when the conditions $Q \ll n^{-7}$ and $Qn \ll R^{-3}$ are fulfilled. With a macroscopic trap it is impossible to break the first condition with reasonable Ioffe field strengths. And in order to break the second condition, the distances to the trap center would have to be extremely large in comparison with the size of the trap.

in the hydrogen eigenfunctions $|\alpha\rangle$ for a given principal quantum number n. Within a single n-manifold we can then simplify it considerably using commutator relations involving the field-free Hamiltonian. We first examine the term

$$
\begin{aligned}
\boldsymbol{A}_q(\boldsymbol{R}+\boldsymbol{r})\boldsymbol{p} = (Q/4)[&(x^2 y - 4yz^2 + y^3 \\
&+ 2xyX + x^2 Y - 4z^2 Y + 3y^2 Y - 8yzZ \\
&+ yX^2 + 2xXY + 3yY^2 - 8zYZ - 4yZ^2)p_x \\
+(&-x^3 - xy^2 + 4xz^2 \\
&- 3x^2 X - y^2 X + 4z^2 X - 2xyY + 8xzZ \\
&- 2yXY - 3xX^2 - xY^2 + 8zXZ + 4xZ^2)p_y \\
+(&X^2 + Y^2 - 4Z^2)(Yp_x - Xp_y)] \,,
\end{aligned}
\tag{6.9}
$$

and use the fact that the eigenvalues of the field-free atomic Hamiltonian H_A are degenerate in a single n-manifold, i.e. $\forall \alpha : H_A|\alpha\rangle = E_n|\alpha\rangle$. Considering the commutator $\frac{i}{\hbar}[H_A, \boldsymbol{r}] = \boldsymbol{p}$ we can then discard all terms involving only p_i as a relative operator since $\langle\alpha'|\boldsymbol{p}|\alpha\rangle = \frac{i}{\hbar}\langle\alpha'|[H_A, \boldsymbol{r}]|\alpha\rangle = 0$. This cancels the last line in Eq. (6.9). The magnitude of the second-order contributions of these terms coupling different n-manifolds are estimated in footnote 2 on page 64. Furthermore, considering $xp_x = -\frac{i}{2\hbar}([x^2, H_A]-1)$ and $yp_y = -\frac{i}{2\hbar}([y^2, H_A]-1)$, we can make the term $(xp_x - yp_y)XY$ disappear. Similarly, the following relations can be deduced,

$$
\begin{aligned}
\langle\alpha'|xp_y|\alpha\rangle &= \langle\alpha'|L_z|\alpha\rangle/2 & \langle\alpha'|xp_z|\alpha\rangle &= -\langle\alpha'|L_y|\alpha\rangle/2 \\
\langle\alpha'|yp_z|\alpha\rangle &= \langle\alpha'|L_x|\alpha\rangle/2 & \langle\alpha'|yp_x|\alpha\rangle &= -\langle\alpha'|L_z|\alpha\rangle/2 \\
\langle\alpha'|zp_x|\alpha\rangle &= \langle\alpha'|L_y|\alpha\rangle/2 & \langle\alpha'|zp_y|\alpha\rangle &= -\langle\alpha'|L_x|\alpha\rangle/2 \,,
\end{aligned}
\tag{6.10}
$$

and we arrive at[3]

$$
\begin{aligned}
\boldsymbol{A}_q(\boldsymbol{R}+\boldsymbol{r})\boldsymbol{p} = (Q/4)[&(x^2 yp_x + y^3 p_x - 4yz^2)p_x + (-xy^2 - x^3 + 4xz^2)p_y \\
&+ (-y^2 p_y - 3x^2 p_y + 4z^2 p_y + 2xyp_x)X + (x^2 p_x + 3y^2 p_x - 4z^2 p_x - 2xyp_y)Y \\
&- 8(yzp_x + xzp_y)Z - 4XZL_x - 4YZL_y + \left(-2X^2 - 2Y^2 + 4Z^2\right)L_z] \,.
\end{aligned}
\tag{6.11}
$$

The terms linear in X and Y (second line in Eq. 6.11) are negligible compared to the corresponding field gradient terms that are linear in the center of mass coordinates (see the electronic Hamiltonian for vanishing Q, Eq. (2.19)) as soon as

$$
4\frac{|Q|}{G}n^2 \ll 1 \,.
\tag{6.12}
$$

For $B = 10\,\mathrm{G}$, $G = 1\,\mathrm{Tm}^{-1}$ and $n = 30$ the condition reads $\tilde{Q} \ll 1.5 \cdot 10^{-11}$. To reach geometric parameters $\tilde{Q}$ as high as 10^{-11} with a Ioffe-Pritchard configuration described in Sec. 6.1 the coils would have to be as close as $12\,\mu\mathrm{m}$ to each other! For a macroscopic trap the condition (6.12) hence cannot be broken with reasonable parameter sets.

---

[3]Instead of writing $\boldsymbol{A}_q(\boldsymbol{R}+\boldsymbol{r})\boldsymbol{p}$ we should in fact write $\langle\alpha'|\boldsymbol{A}_q(\boldsymbol{R}+\boldsymbol{r})\boldsymbol{p}|\alpha\rangle$ and we should also do so for all the operators on the right hand side of the equation. For the sake of readability we omit the brackets here and in the following.

Comparing the purely electronic terms in (6.11) with the purely electronic term coming from the gradient field, $Gxyp_z$, see Eq. (2.19), one finds essentially the same condition, $\frac{Q}{G}n^2 \ll 1$. Hence, if the terms in $\boldsymbol{A}_q(\boldsymbol{R}+\boldsymbol{r})\boldsymbol{p}$ that are linear in X and Y are negligible, so are the pure electronic terms. As long as the condition (6.12) holds we are therefore left with

$$\boldsymbol{A}_q(\boldsymbol{R}+\boldsymbol{r})\boldsymbol{p} \approx 2QZzL_z + \frac{Q}{2}(-2XZL_x - 2YZL_y + (-X^2 - Y^2 + 2Z^2)L_z) \,, \qquad (6.13)$$

where the notation of the term $2QZzL_z = 2QZ(xzp_y - yzp_x)$ should not mask that it is an off-diagonal operator in the hydrogen basis. Recalling the form of the quadratic term in the magnetic field configuration, Eq. (2.11), we can write

$$\boldsymbol{A}_q(\boldsymbol{R}+\boldsymbol{r})\boldsymbol{p} \approx 2QZzL_z + \frac{Q}{2}\boldsymbol{L_r} \cdot \begin{pmatrix} -2XZ \\ -2YZ \\ -X^2 - Y^2 + 2Z^2 \end{pmatrix} = 2QZzL_z + \frac{1}{2}\boldsymbol{L_r} \cdot \boldsymbol{B}_q(\boldsymbol{R}) \,. \quad (6.14)$$

Similar approximations can be made for the spin term in $U^\dagger H_q U$,

$$\boldsymbol{S} \cdot \boldsymbol{B}_q(\boldsymbol{R}+\boldsymbol{r}) = \boldsymbol{S} \cdot \boldsymbol{B}_q(\boldsymbol{R}) + \boldsymbol{S} \cdot \boldsymbol{B}_q(\boldsymbol{r}) + 2Q\boldsymbol{S} \cdot \begin{pmatrix} -xZ - Xz \\ -yZ - Yz \\ 2zZ - xX - yY \end{pmatrix} \,. \qquad (6.15)$$

The relative term $\boldsymbol{S} \cdot \boldsymbol{B}_q(\boldsymbol{r})$ is a lot smaller than $\boldsymbol{S} \cdot \boldsymbol{B}_l(\boldsymbol{r})$ as soon as, again, condition (6.12) holds . The same condition permits to discard the terms in the third summand of (6.15) that are linear in X and Y. We are then left with

$$\boldsymbol{S} \cdot \boldsymbol{B}_q(\boldsymbol{R}+\boldsymbol{r}) \approx \boldsymbol{S} \cdot \boldsymbol{B}_q(\boldsymbol{R}) - 2QZ(xS_x + yS_y - 2zS_z) \,. \qquad (6.16)$$

The additional Hamiltonian $U^\dagger H_q U$, Eq. (6.8), can then be approximated by

$$\boldsymbol{A}_q(\boldsymbol{R}+\boldsymbol{r})\boldsymbol{p} + \boldsymbol{S} \cdot \boldsymbol{B}_q(\boldsymbol{R}+\boldsymbol{r}) \approx \boldsymbol{\mu} \cdot \boldsymbol{B}_q(\boldsymbol{R}) + 2QZ(zL_z - xS_x - yS_y + 2zS_z) \,, \qquad (6.17)$$

where we have abbreviated $\frac{1}{2}\boldsymbol{L_r} \cdot \boldsymbol{B}_q(\boldsymbol{R}) + \boldsymbol{S} \cdot \boldsymbol{B}_q(\boldsymbol{R}) = \boldsymbol{\mu} \cdot \boldsymbol{B}_q(\boldsymbol{R})$. As long as the condition (6.12) holds the Ioffe-Pritchard Hamiltonian (6.5) in a single manifold can hence be brought into an advantageous form with a dominant Zeeman-like coupling to the field, cf. Eq. (2.25),

$$U^\dagger H U \approx \frac{\boldsymbol{P}^2}{2M} + \boldsymbol{\mu} \cdot \boldsymbol{B}(\boldsymbol{R}) + G(xyp_z + xS_x - yS_y) + \mathcal{H}_Q \,, \qquad (6.18)$$

where we use the projected expressions (2.19) and (2.23) developed in Sec. 2.3. Note that the Zeeman-like coupling term $\boldsymbol{\mu}\cdot\boldsymbol{B}(\boldsymbol{R})$ here includes the quadratic magnetic field $\boldsymbol{B}_q$ in contrast to the respective term in the working Hamiltonian (2.25) of the Chapters 2 and 4 that only includes the effective (and scaled) field $\boldsymbol{G}$, Eq. (2.24). In the above Hamiltonian (6.18) we omitted the field-free Hamiltonian H_A that only gives the constant energy offset E_A^n within an n-manifold. We also named the representation of the electronic terms originating from the longitudinal confinement

$$\mathcal{H}_Q \equiv (\langle\alpha'|H_Q|\alpha\rangle) := 2QZ(zL_z - xS_x - yS_y + 2zS_z) \,. \qquad (6.19)$$

In contrast to the finite-size term $\mathcal{H}_\gamma = G(xyp_z + xS_x - yS_y)$ that comes from the coupling to the linear magnetic field $\boldsymbol{B}_l$, the term $\mathcal{H}_Q$ that comes from the coupling to the quadratic magnetic field $\boldsymbol{B}_q$ does not only involve electronic coordinates but also depends on the center of mass position.

For an atom that is displaced on the Z-axis far enough from the origin, $|Z| \gg 2n^2$, the additional electronic Hamiltonian $\mathcal{H}_Q$ can be neglected. This is because the term $|2QZzL_z|$ is then negligible compared with $|QL_zZ^2|$, cf. Eq. (6.14), and the terms in $\mathcal{H}_Q$ involving spin operators are very small compared to term $|QS_zZ^2|$ from $\boldsymbol{S} \cdot \boldsymbol{B}_q(\boldsymbol{R})$ if $|Z| \gg 2n$. For this argument we simply estimated $\langle\alpha|x_i|\alpha\rangle \approx n^2$. A closer inspection shows, however, that the contribution of H_Q is even smaller: Since L_z is diagonal in the hydrogen basis, $\langle\alpha'|L_z|\alpha\rangle = m_l\delta_{\alpha'\alpha}$, the term in question is proportional to a dipole matrix element, $\mathcal{H}_Q \sim \langle\alpha'|zL_z|\alpha\rangle = \langle\alpha'|z|\alpha\rangle m_l$, and hence has only off-diagonal matrix elements. Comparing its second order energetic contribution with $|QL_zZ^2|$ (and assuming the energetic gap of adjacent surfaces to be $B/2$), we find the condition

$$4n^5\tilde{Q} \ll 1, \tag{6.20}$$

which in macroscopic traps can only be broken with principal quantum numbers n of the order of several hundreds. We do not even have to consider $\mathcal{H}_Q$ when the constraint coming from the spin terms, $|Z| \gg 2n$, is broken since $\mathcal{H}_Q$ is then negligible compared to the gradient term $Gxyp_z$. We will therefore omit $\mathcal{H}_Q$ and use

$$\mathcal{H}_{IP} = \frac{\boldsymbol{P}^2}{2M} + \mathcal{H}_e \tag{6.21}$$

as working Hamiltonian in the following where the electronic part reads

$$\begin{aligned}\mathcal{H}_e :&= \boldsymbol{\mu} \cdot \boldsymbol{B}(\boldsymbol{R}) + \mathcal{H}_\gamma \\ :&= \boldsymbol{\mu} \cdot \boldsymbol{B}(\boldsymbol{R}) + G(xyp_z + xS_x - yS_y) \ . \end{aligned} \tag{6.22}$$

6.4 Analytical diagonalization

Due to the large difference in the masses of electron and ionic core the timescales of the relative and the center of mass dynamics in the system are very different even for high principal quantum numbers n. This is especially true since we consider ultracold systems. We can assume that the slow change of the position of the ionic core allows the excited electron to instantaneously adapt to the local magnetic field. In analogy to Section 2.4 we can therefore adiabatically separate the relative and the center of mass motion. For this purpose we set the center of mass kinetic energy to zero and solve the remaining electronic Schrödinger equation

$$\mathcal{H}_e \, |\varphi_\kappa(\boldsymbol{r}; \boldsymbol{R})\rangle = E_\kappa(\boldsymbol{R}) \, |\varphi_\kappa(\boldsymbol{r}; \boldsymbol{R})\rangle \tag{6.23}$$

for the electronic potential energy surfaces $E_\kappa(\boldsymbol{R})$. The solutions of the internal problem $E_\kappa(\boldsymbol{R})$ depend only parametrically on the center of mass coordinates. Subject to the internal state of the atom, κ, the corresponding energy surface provides the potential for the center of mass dynamics, cf. Eq. (2.29). We provide expressions for the error that we make using the adiabatic approach, the so-called non-adiabatic couplings, in Section 2.4.

6 Longitudinal confinement

For large ratios of Ioffe field and magnetic field gradient, B/G, we can analytically find approximate expressions for the potential energy surfaces. The leading term in the electronic Hamiltonian in this case is $\boldsymbol{\mu} \cdot \boldsymbol{B}(\boldsymbol{R})$. We diagonalize it by applying the unitary transformation

$$U = \exp(-\imath\alpha(L_x + S_x)) \cdot \exp(-\imath\beta(L_y + S_y)) \tag{6.24}$$

with

$$\tan\alpha = \frac{-Y(G + 2QZ)}{\sqrt{(B - Q(X^2 + Y^2 - 2Z^2))^2 + (GX - 2QXZ)^2}} \ , \tag{6.25}$$

$$\tan\beta = \frac{X(G - 2QZ)}{Q(X^2 + Y^2 - 2Z^2) - B} \ . \tag{6.26}$$

We note that the field-free Hamiltonian H_A is invariant under the transformation U. Defining $\mathcal{R}_{x\alpha y\beta} := \mathcal{R}_x(\alpha)\mathcal{R}_y(\beta)$ we can write

$$U\boldsymbol{L_r}U^\dagger = \mathcal{R}_{x\alpha y\beta}^{-1}\boldsymbol{L_r} = \mathcal{R}_y(-\beta)\mathcal{R}_x(-\alpha)\boldsymbol{L_r} \ ,$$

$$U\boldsymbol{S}U^\dagger = \mathcal{R}_{x\alpha y\beta}^{-1}\boldsymbol{S} = \mathcal{R}_y(-\beta)\mathcal{R}_x(-\alpha)\boldsymbol{S} \ , \tag{6.27}$$

since $\boldsymbol{L_r}$ and $\boldsymbol{S}$ are axial vectors [87]. It is then

$$U\boldsymbol{\mu}U^\dagger\boldsymbol{B} = \frac{1}{2}(L_z + 2S_z)|\boldsymbol{B}| \ , \tag{6.28}$$

where L_z and S_z represent different operators than before; They are now defined with respect to the local quantization axis. The solutions of Eq. (6.23), the adiabatic energy surfaces E_κ, hence read

$$E_\kappa(\boldsymbol{R}) \approx (\frac{m_l}{2} + m_s)|\boldsymbol{B}| \tag{6.29}$$

$$= (\frac{m_l}{2} + m_s)\sqrt{(B - Q(X^2 + Y^2 - 2Z^2))^2 + X^2(G - 2QZ)^2 + Y^2(G + 2QZ)^2}.$$

For vanishing $\tilde{Q} = Q/B$ the expression (6.29) is identical with the potential surfaces found in Section 4.1, Eq. (4.6), as expected[4]. The procedure outlined above is equivalent to rotating the system into the local magnetic field direction.

It can be deduced from the analytic expression for the adiabatic surfaces, Eq. (6.29), that the energetically uppermost surface is constituted by the circular state since it is the state with the largest angular momentum projection quantum number m_l within the n-manifold. The crucial factor $(\frac{m_l}{2} + m_s)$ is the same as for the adiabatic surfaces computed for vanishing Q, Eq. (4.6), as could be expected.

On the Z-axis the absolute value of the magnetic field reads

$$|\boldsymbol{B}(0,0,Z)| = B + 2QZ^2 = B(1 + 2\tilde{Q}Z^2) \ . \tag{6.30}$$

The potential surfaces $E_\kappa(\boldsymbol{R})$, Eq. (6.29), hence approximately provide a harmonic confinement in z. For $Z = 0$ on the other hand it is

$$|\boldsymbol{B}(X,Y,0)| = \sqrt{B^2 + (G^2 - 2BQ)\rho^2 + Q^2\rho^4} = B + \left(\frac{G^2}{2B} - Q\right)\rho^2 + \mathcal{O}(\rho^4) \tag{6.31}$$

---

[4]The two expressions are formulated in different units; To compare them a scaling factor $\epsilon = \gamma^{\frac{2}{3}}/M$ has to be applied, see Section 2.3.

for small $\rho = \sqrt{X^2 + Y^2}$. The expression (6.31) unveils that $\tilde{Q}$ is not only responsible for the longitudinal confinement but can also leads to the loss of the transversal confinement for small gradients, more precisely as soon as

$$\left(\frac{G}{B}\right)^2 < 2\tilde{Q} \ . \tag{6.32}$$

(This is not only true for $Z = 0$. The confining property of $E_\kappa(\boldsymbol{R})$ in transversal direction is lost also for finite Z as soon as the condition (6.32) is met, see the corresponding expansion of $|\boldsymbol{B}|$ in Eq. (9.31).)

The part of the electronic Hamiltonian in Eq. (6.21) that we have neglected in this section, the finite-size term $G(xyp_z + xS_x - yS_y)$, not only constitutes a mere energy offset to the adiabatic electronic potentials. As has already been mentioned in Sec. 4.2, it is not intuitive at first view that the finite size term can provide any center of mass coordinate dependent contribution to the electronic wave function, since it lacks a dependence on $\boldsymbol{R}$. Due to the coupling of the relative and the center of mass dynamics, however, which is a major characteristic of the Rydberg Hamiltonian (6.21), even purely relative terms implicitly create an $\boldsymbol{R}$-dependent effect on the wave function. A convincing way to see this is to consider the approximate analytic solution in the Ioffe dominated regime. The transformation U, Eq. (6.24), that diagonalizes the approximate Hamiltonian $\boldsymbol{\mu}{\cdot}\boldsymbol{B}(\boldsymbol{R})$, depends parametrically on $\boldsymbol{R}$. It does not diagonalize the full electronic Hamiltonian including the finite size term. In a perturbative approach to include its effect on wave functions and energies, it has to be rotated into the diagonalized system. This rotation involving the unitary transformation U introduces the center of mass coordinate dependence to the finite size term. The finite size term is treated perturbatively in the following chapter.

7 Electric dipole moments

Neutral, isolated atoms exhibit no electric dipole moments due to the definite parity of their electronic wave functions. For Rydberg atoms in inhomogeneous fields this is no longer true. The electronic Hamiltonian for this situation reads, cf. Eq. (6.21),

$$\mathcal{H}_e = \boldsymbol{\mu} \cdot \boldsymbol{B}(\boldsymbol{R}) + \mathcal{H}_\gamma + \mathcal{H}_F \ , \tag{7.1}$$

where the term $\mathcal{H}_\gamma$ accounts for effects due to the finite size of Rydberg atoms and the additional term $\mathcal{H}_F$ accounts for an external electric field $\boldsymbol{F}$. The Zeeman term, $\boldsymbol{\mu} \cdot \boldsymbol{B}(\boldsymbol{R})$, is invariant under parity transformation and the solutions of its analytical diagonalization (Sec. 6.4) have definite parity and hence exhibit no electric dipole moment. The finite size term $\mathcal{H}_\gamma$ and the electric field term $\mathcal{H}_F$, however, gain a minus sign when the parity operator is applied. Due to the breaking of parity symmetry the eigenfunctions of the total electronic Hamiltonian are in general no parity eigenfunctions for finite magnetic field gradient g or finite electric field strength F. Non-zero electric dipole moments are then to be expected.

In this chapter we study the electric dipole moment in the uppermost adiabatic energy surface. This surface is constituted by the hydrogenic circular state $|\text{circ}\rangle$ with respect to the local magnetic field direction. We first address the finite size term $\mathcal{H}_\gamma$ in Section 7.1 that is neglected for analytically solving the internal Schrödinger equation in section Sec. 6.4. The contribution of the term is small for the parameter sets we are interested in and we can thus treat it perturbatively. In Section 7.2 we add an external electric field before we further investigate the properties of the resulting dipole moments in Sec. 7.3.

7.1 Permanent electric dipole moments as finite size effect

As soon as the finite size term $\mathcal{H}_\gamma = G(xyp_z + xS_x - yS_y)$ from (6.22) is considered we find a nonzero electric dipole moment expectation value in the uppermost surface even for zero electric field. As already mentioned this comes from the non-invariance of $\mathcal{H}_\gamma$ under parity transformation, mores specifically it is $\mathcal{H}_\gamma \to -\mathcal{H}_\gamma$ ($\boldsymbol{r} \to -\boldsymbol{r}$).

Doing perturbation theory with the term $\mathcal{H}_\gamma$ is meaningful only if it is small compared to $\boldsymbol{\mu} \cdot \boldsymbol{B}(\boldsymbol{R})$. This entails[1] the requirement

$$B/G \gg n^2 \ , \tag{7.2}$$

---

[1] We take the value of $\boldsymbol{\mu}\cdot\boldsymbol{B}$ at the origin for the comparison and do not consider the small contribution of the spin terms. We can therefore approximate $\boldsymbol{\mu} \cdot \boldsymbol{B}(O) \gg |Gxyp_z| \Rightarrow 3B \gg 2Gn^2$. With this requirement we guarantee that the matrix elements of the perturbing operator W are much smaller than those of the unperturbed Hamiltonian. More specifically, it must be required that the off-diagonal matrix elements of the perturbing operator W ($\sim G$) are much smaller than the corresponding non-perturbed energy differences ($\sim |\boldsymbol{B}|$). For a maximal estimation of the magnitude of $|Gxyp_z|$ this yields $3B \gg 2Gn^3$. The comparison with numerical results later in the chapter shows, however, that the less strict inequality (7.2) suffices.

which is easily satisfied for typical Ioffe field strengths (the very small Ioffe field strength $B = 0.1\,\mathrm{G}$ and the rather strong gradient $G = 10\,\mathrm{Tm^{-1}}$ still yield $21 \gg 1$ for $n = 30$).

We also have to make sure that all other terms that have been neglected in Section 6.3 are much smaller than $\mathcal{H}_\gamma$ and hence do not have to be taken into account for the perturbation theory. This is true as long as the coordinates of the atoms' position satisfy[2]

$$\rho^3 \ll \frac{n}{4}\frac{\sqrt{G}}{Q} \;, \quad Z^2 \ll \frac{n\sqrt{G}}{\rho Q} \;, \quad \text{and} \quad |Z| \ll \frac{G}{4Q} \;, \tag{7.3}$$

where $\rho^2 = X^2 + Y^2$. All restrictions in (7.3) loosen for decreasing Q and do not emerge at all for $Q = 0$. The maximally reachable geometry parameter $\tilde{Q} = Q/B$ in a macroscopic Ioffe-Pritchard trap depends on the size of the trap ($\tilde{Q}_\mathrm{max} \sim D^{-2}$, see Sec. 6.1). If we insert $\tilde{Q}_\mathrm{max}$ for a millimeter sized trap [99] and the field parameters $B = 10\,\mathrm{G}$ and $G = 0.1\,\mathrm{Tm^{-1}}$ the factor $n\sqrt{G}/Q$ is still as large as $6 \cdot 10^{16}$ and the restrictions in (7.3) become $\rho \ll 13\,\mu\mathrm{m}$, $|Z| \ll 3600\,\mu\mathrm{m}$ for $\rho = 13\,\mu\mathrm{m}$, and $|Z| \ll 117\,\mu\mathrm{m}$, respectively. For the region that we are interested in in Chapter 9, we can thus safely limit the perturbation theory to including the term $\mathcal{H}_\gamma$ only.

Perturbation theory with electronic finite size term $\mathcal{H}_\gamma$

In the analytically diagonalizable case of high Ioffe field the electronic state corresponding to the uppermost electronic adiabatic energy surface is the circular state with respect to the local field direction as quantization axis. For a finite gradient G the purely electronic finite-size term $\mathcal{H}_\gamma$ admixes states to the circular state that have opposite parity. The total wave function thus looses its definite parity and the matrix elements of the odd dipole operator $e\boldsymbol{r}$ no longer vanish identically due to symmetry. This can result in a permanent electric dipole moment.

Since the finite size term is suppressed by G ($= \gamma$ in scaled a.u.) we can treat it perturbatively as long as (7.2) holds. Because the unperturbed state vector is analytically given in the rotated system, i.e. with the local magnetic field axis as the quantization axis, the perturbing operator has to be rotated into this local frame, too. In a single n-manifold and in unscaled atomic units it reads:

$$W = UG(xyp_z + xS_x - yS_y)U^\dagger \;, \tag{7.4}$$

where U is the transformation (6.24) diagonalizing the electronic problem in the Ioffe-dominated regime. It is convenient to replace the momentum operator in W by angular momentum operators. This can be done exploiting the energetic degeneracy of an n-manifold

---

[2]Comparing $\mathcal{H}_\gamma$ with maximal estimates of the terms that can be neglected due to (6.12) yields the condition $\rho \ll \frac{1}{4}G/Q$. The comparison with the purely electronic terms in (6.11) yields $n^2 \ll \frac{1}{4}G/Q$ which is already required in (6.12) and which cannot be broken for practical parameter sets. Comparing $\mathcal{H}_\gamma$ with $\mathcal{H}_Q$ entails the condition $|Z| \ll \frac{1}{4}G/Q$. The terms involving only p_i as a relative operator have been discarded in Sec. 6.3 since they identically vanish within a *single n-manifold* due to the commutator $\frac{i}{\hbar}[H_A, \boldsymbol{r}] = \boldsymbol{p}$, see page 57. They can, however, still couple *different n-manifolds*. This second-order contribution to the energy is proportional to Q^2. Comparing it with the contribution of $\mathcal{H}_\gamma$ yields the condition $Z^2 \ll \frac{n}{\rho}\sqrt{G}/Q$ if $|Z| \gg \rho$, and it yields $\rho^3 \ll \frac{n}{4}\sqrt{G}/Q$ if $|Z| \ll \rho$. In summary, the restrictions formulated in Eq. (7.3) have to hold if we want to do perturbation theory with $\mathcal{H}_\gamma$ only.

in a field-free environment. The term xyp_z can be written as

$$xyp_z = \frac{1}{3i}[xyz, H_A] + \frac{1}{3}(xL_x - yL_y) \ . \tag{7.5}$$

The commutator vanishes within an n-manifold, $\langle\alpha|xyp_z|\alpha\rangle = \frac{1}{3}\langle\alpha|(xL_x - yL_y)|\alpha\rangle$, and W becomes

$$W = U\frac{G}{3}(xL_x - yLy + 3xS_x - 3yS_y)U^\dagger \ . \tag{7.6}$$

In the transformed frame $\mathcal{H}_\gamma$ then reads

$$
\begin{aligned}
W = U\mathcal{H}_\gamma U^\dagger =&\lambda\{(\mathcal{R}_{\alpha\beta}^{-1}\boldsymbol{r})_x \cdot (\mathcal{R}_{\alpha\beta}^{-1}\boldsymbol{L})_x - (\mathcal{R}_{\alpha\beta}^{-1}\boldsymbol{r})_y \cdot (\mathcal{R}_{\alpha\beta}^{-1}\boldsymbol{L})_y \\
&+ 3(\mathcal{R}_{\alpha\beta}^{-1}\boldsymbol{r})_x \cdot (\mathcal{R}_{\alpha\beta}^{-1}\boldsymbol{S})_x - 3(\mathcal{R}_{\alpha\beta}^{-1}\boldsymbol{r})_y \cdot (\mathcal{R}_{\alpha\beta}^{-1}\boldsymbol{S})_y\} \\
=:&\lambda \ c_{ij}(\boldsymbol{R}, B, G, Q) \ r_i(L_j + 3S_j) \ ,
\end{aligned}
\tag{7.7}
$$

where $\lambda = G/3$ a.u. ($= \gamma^{1/3}/3$ scaled a.u.) and $\mathcal{R}_{\alpha\beta}$ is the rotation associated with the transformation U. We write $\mathcal{R}_{\alpha\beta}^{-1}$ in Eq. (7.7) instead of $\mathcal{R}_{\alpha\beta}$ to recall the fact that the components of a *vector operator* transform in the rotation $\mathcal{R}$ like those of a vector in the rotation $\mathcal{R}^{-1}$ [100]. Both the coordinate vector $\boldsymbol{r}$ and the angular momentum operators $\boldsymbol{L}$ and $\boldsymbol{S}$ are vector operators.

We note that the perturbing operator $\mathcal{H}_\gamma$ that is of purely electronic nature in the laboratory frame now depends on the center of mass coordinates $\boldsymbol{R}$ through the coefficients $c_{ij}(\boldsymbol{R}, B, G, Q)$ in the rotated frame. This dependency is introduced by the transformation U that rotates the operator into the local direction of the magnetic field and is therefore $\boldsymbol{R}$-dependent itself.

The *first order energy correction* to the uppermost circular state $|\text{circ}\rangle$ vanishes,

$$\lambda\epsilon_1 = \langle\text{circ}|\lambda c_{ij}r_i(L_j + 3S_j)|\text{circ}\rangle = 0 \ , \tag{7.8}$$

since the operators L_i and S_i do not change the quantum number l when being applied on a hydrogen eigenstate (i.e. $L_i|l, m\rangle \sim |l, m'\rangle$) but they only change the quantum numbers m and m_s, respectively. The matrix element (7.8) is hence proportional to $\langle\text{circ}|r_i|\text{circ}\rangle$ which is zero since the dipole selection rule $\Delta l = \pm 1$ is violated.

The *first order correction in the wave function* reads

$$|\lambda\varphi_1^{(1)}\rangle = \sum_{p\neq 1}\frac{\langle\varphi_p|\lambda c_{ij} \ r_i(L_j + 3S_j)|\varphi_1\rangle}{E_1^0 - E_p^0}|\varphi_p\rangle =: \sum_{p\neq 1}\frac{W_{p1}}{E_{1p}}|\varphi_p\rangle =: \sum_{p\neq 1}f_p|\varphi_p\rangle \ . \tag{7.9}$$

Here we introduced the abbreviations $W_{pq} = \langle\varphi_p|\lambda c_{ij}r_i(L_j + 3S_j)|\varphi_q\rangle$ and $E_{pq} = E_p^0 - E_q^0$, and we use the symbols $|\varphi\rangle = |n, l, m, m_s\rangle$ for the unperturbed hydrogenic electronic states

in energetic order, starting with the circular state constituting the uppermost surface,

$$|\text{circ}\rangle = |\varphi_1\rangle = |n, n-1, n-1, 1/2\rangle \ ,$$
$$|\varphi_2\rangle = |n, n-1, n-2, 1/2\rangle \ ,$$
$$|\varphi_3\rangle = |n, n-2, n-2, 1/2\rangle \ ,$$
$$|\varphi_4\rangle = |n, n-1, n-3, 1/2\rangle \ ,$$
$$|\varphi_5\rangle = |n, n-2, n-3, 1/2\rangle \ ,$$
$$|\varphi_6\rangle = |n, n-3, n-3, 1/2\rangle \ ,$$
$$|\varphi_7\rangle = |n, n-1, n-1, -1/2\rangle \ ,$$
$$\vdots$$
$$|\varphi_{13}\rangle = |n, n-2, n-2, -1/2\rangle \ . \tag{7.10}$$

The states $\{|\varphi_2\rangle, |\varphi_3\rangle\}$, the states $\{|\varphi_4\rangle, \ldots, |\varphi_7\rangle\}$ and the states $\{|\varphi_8\rangle, \ldots, |\varphi_{13}\rangle\}$ are energetically degenerate in the limit $B/G \to \infty$. The quantum numbers are given with respect to the local quantization axis which is the direction of the magnetic field.

In order to compute the matrix elements $W_{p1} = W_{p,\text{circ}}$ defined in Eq. (7.9) we rewrite the angular momentum operators with ladder operators [101],

$$L_x|\text{circ}\rangle = \frac{1}{2}(L_+ + L_-)|\text{circ}\rangle = \frac{1}{2}L_-|\text{circ}\rangle, \tag{7.11}$$

$$L_y|\text{circ}\rangle = \frac{1}{2i}(L_+ - L_-)|\text{circ}\rangle = iL_x|\text{circ}\rangle, \tag{7.12}$$

where $L_-|l, m\rangle = \sqrt{l(l+1) - m(m-1)}\ |l, m-1\rangle$, ($\hbar = 1$ atomic unit). The only non-vanishing matrix elements in (7.9) are

$$\langle_{\varphi_5}^{\varphi_3}|c_{ix}r_iL_x|\text{circ}\rangle = \frac{1}{2}\sqrt{2n-3}\langle_{\varphi_5}^{\varphi_3}|c_{ix}r_i|\varphi_2\rangle \ , \tag{7.13}$$

$$\langle_{\varphi_5}^{\varphi_3}|c_{iy}r_iL_y|\text{circ}\rangle = i\frac{1}{2}\sqrt{2n-3}\langle_{\varphi_5}^{\varphi_3}|c_{iy}r_i|\varphi_2\rangle \ , \tag{7.14}$$

$$\langle\varphi_3|c_{iz}r_iL_z|\text{circ}\rangle = (n-1)\langle\varphi_3|c_{iz}r_i|\text{circ}\rangle \tag{7.15}$$

due to the dipole selection rules $\Delta l = \pm 1$, $\Delta m_l = 0, \pm 1$, and $\Delta m_s = 0$. We proceed similarly with the spin operators,

$$S_x|m_s = \pm\frac{1}{2}\rangle = \frac{1}{2}\ |m_s = \mp\frac{1}{2}\rangle \quad \text{and} \quad S_y|m_s = \pm\frac{1}{2}\rangle = \pm\frac{i}{2}\ |m_s = \mp\frac{1}{2}\rangle \ . \tag{7.16}$$

The only non-vanishing matrix elements involving the spin operators are

$$\langle\varphi_{13}|c_{ix}r_iS_x|\text{circ}\rangle = \frac{1}{2}\langle\varphi_{13}|c_{ix}r_i|\varphi_7\rangle \ , \tag{7.17}$$

$$\langle\varphi_{13}|c_{iy}r_iS_y|\text{circ}\rangle = \frac{i}{2}\langle\varphi_{13}|c_{iy}r_i|\varphi_7\rangle \ , \tag{7.18}$$

$$\langle\varphi_3|c_{iz}r_iS_z|\text{circ}\rangle = \frac{1}{2}\langle\varphi_3|c_{iz}r_i|\text{circ}\rangle \ . \tag{7.19}$$

Considering the following relations between the dipole matrix elements,

$$\langle l', m'|y|l, m\rangle = \pm i \langle l', m'|x|l, m\rangle \qquad\qquad \text{for } m' = m \mp 1$$
$$\langle l', m'|y|l, m\rangle = 0 = \langle l', m'|x|l, m\rangle \qquad\qquad \text{for } m' = m$$
$$\langle l', m'|z|l, m\rangle \sim \delta_{m,m'} \;, \qquad\qquad\qquad\qquad\qquad (7.20)$$

we find the first order correction to the wave function,

$$
\begin{aligned}
|\lambda\varphi_1^{(1)}\rangle &= \lambda\Big\{ \frac{|\varphi_3\rangle}{E_{13}}(c_{xz} + ic_{yz})\left((n - \tfrac{1}{2})x_{31} + \tfrac{1}{2}\sqrt{2n - 3}\,z_{32}\right) \\
&\quad + \frac{|\varphi_5\rangle}{E_{15}}(c_{xx} - c_{yy} + 2ic_{xy})\tfrac{1}{2}\sqrt{2n - 3}\,x_{52} \\
&\quad + \frac{|\varphi_{13}\rangle}{E_{13,5}}(c_{xx} - c_{yy} + 2ic_{xy})\tfrac{3}{2}x_{13,7}\Big\} \\
&= \lambda\Big\{ (c_{xz} + ic_{yz})\frac{|\varphi_3\rangle}{E_{13}}\left((n - \tfrac{1}{2})x_{31} + \tfrac{1}{2}\sqrt{2n - 3}\,z_{32}\right) \\
&\quad + (\tfrac{1}{2}c_{xx} - \tfrac{1}{2}c_{yy} + ic_{xy})\left(\frac{|\varphi_5\rangle}{E_{15}}\sqrt{2n - 3}\,x_{52} + \frac{|\varphi_{13}\rangle}{E_{13,5}}3x_{13,7}\right)\Big\} \;. \qquad (7.21)
\end{aligned}
$$

Here we introduced the notation $x_{ij} = \langle\varphi_i|x|\varphi_j\rangle$, $y_{ij} = \langle\varphi_i|y|\varphi_j\rangle$ and $z_{ij} = \langle\varphi_i|z|\varphi_j\rangle$. The following explicit expressions for the matrix elements can be deduced from the formulas for the radial and angular integrals involving hydrogenic wave functions in [102],

$$z_{32} = -\frac{3}{2}n \;, \qquad\qquad\qquad\qquad\qquad\qquad\qquad (7.22)$$

$$x_{13} = \frac{3}{2\sqrt{2}}n\sqrt{n - 1} \;, \qquad\qquad\qquad\qquad\qquad (7.23)$$

$$x_{52} = \frac{3}{2\sqrt{2}}n\sqrt{n - 2} \;, \qquad\qquad\qquad\qquad\qquad (7.24)$$

$$x_{13,7} = \frac{3}{2\sqrt{2}}n\sqrt{\frac{(n - 1/2)(n - 3/2)}{n - 2}} \;. \qquad\qquad (7.25)$$

Plugging these matrix elements into Eq. (7.21) yields

$$
\begin{aligned}
|\lambda\varphi_1^{(1)}\rangle &= \lambda\frac{3}{4}n\sqrt{2n - 3}\Big\{ (c_{xz} + ic_{yz})\frac{|\varphi_3\rangle}{E_{31}}\left(\left(n - \tfrac{1}{2}\right)\sqrt{\frac{n - 1}{n - 3/2}} - 1\right) \\
&\quad + \left(\frac{c_{xx}}{2} - \frac{c_{yy}}{2} + ic_{xy}\right)\left(\frac{|\varphi_5\rangle}{E_{51}}\sqrt{2}\sqrt{n - 2} + \frac{|\varphi_{13}\rangle}{E_{13,5}}3\sqrt{\frac{n - 1/2}{n - 2}}\right)\Big\} \\
&\approx \lambda\frac{3}{2\sqrt{2}}n\sqrt{n}\Big\{ (c_{xz} + ic_{yz})n\frac{|\varphi_3\rangle}{E_{31}} + \left(\frac{c_{xx}}{2} - \frac{c_{yy}}{2} + ic_{xy}\right)\left(\sqrt{2n}\frac{|\varphi_5\rangle}{E_{51}} + 3\frac{|\varphi_{13}\rangle}{E_{13,5}}\right)\Big\} \;, \quad (7.26)
\end{aligned}
$$

where the last line holds for large principal quantum numbers n. Note that the correction $|\lambda\varphi_1^{(1)}\rangle$ to the circular wave function $|\varphi_1\rangle = |\text{circ}\rangle$ has definite parity since $|\varphi_3\rangle$, $|\varphi_5\rangle$ and $|\varphi_{13}\rangle$ have the same l quantum number. It is opposite to the parity of $|\text{circ}\rangle$, however. The

involved coefficients $c_{ij}(\boldsymbol{R}, B, G, Q)$, defined in Eq. (7.7), come from the inverse rotation of $\boldsymbol{r}$, $\boldsymbol{L}$ and $\boldsymbol{S}$ with $\mathcal{R}_{\alpha\beta}$. $\mathcal{R}_{\alpha\beta}$ is the rotation associated with the unitary transformation U introduced in Sec. 2.4 that diagonalizes the internal problem, Eq. (2.28). Examples for such transformations are those in Eqs. (4.2) and (6.24). Expressed with the rotation angles α and β from the exponent of U, the coefficients read explicitly

$$
\begin{aligned}
c_{ix}r_i =&\, x\cos^2\beta + y\sin\alpha\sin\beta\cos\beta - z\cos\alpha\sin\beta\cos\beta \ , \\
c_{iy}r_i =&\, x\sin\alpha\sin\beta\cos\beta + y(\sin^2\alpha\sin^2\beta - \cos^2\alpha) - z\sin\alpha\cos\alpha(1+\sin^2\beta) \ , \\
c_{iz}r_i =&\, -x\cos\alpha\sin\beta\cos\beta - y\sin\alpha\cos\alpha(1+\sin^2\beta) + z(\cos^2\alpha\sin^2\beta - \sin^2\alpha) \ , \quad (7.27)
\end{aligned}
$$

where $c_{ij} = c_{ji}$. This is a general expression for the perturbing operator (7.7). The particular magnetic field configuration only enters via the explicit expressions for the angles α and β, Eqs. (4.4) or Eqs. (6.25). On the Z-axis ($\alpha = \beta = 0 \to U = \mathbf{1}$) all the coefficients but $c_{xx} = 1$ and $c_{yy} = -1$ vanish. The correction to the circular state in first order reduces to

$$
|\lambda\varphi_1^{(1)}\rangle(O) = \lambda\frac{3}{4}n\sqrt{2n-3}\left(\sqrt{2}\sqrt{n-2}\frac{|\varphi_5\rangle}{E_{51}} + 3\sqrt{\frac{n-1/2}{n-2}}\frac{|\varphi_{13}\rangle}{E_{13,5}} \right) \tag{7.28}
$$

$$
\approx \lambda\frac{3}{2}n\sqrt{n}\left(\sqrt{n}\frac{|\varphi_5\rangle}{E_{51}} + \frac{3}{\sqrt{2}}\frac{|\varphi_{13}\rangle}{E_{13,5}} \right) \ . \tag{7.29}
$$

The electric dipole moment expectation value therefore vanishes at the origin due to the dipole selection rules as will be described in the following.

The *electric dipole moment* of the electronic state to second order in perturbation theory is found computing the expectation value of the dipole operator rotated into the local direction of the magnetic field, $U^\dagger \boldsymbol{r} U$, in the perturbed state in the rotated frame, $|\varphi_1 + \lambda\varphi_1^{(1)}\rangle$,

$$
\begin{aligned}
\boldsymbol{d}_\gamma =&\, \langle\varphi_1 + \lambda\varphi_1^{(1)}|U^\dagger \boldsymbol{r} U|\varphi_1 + \lambda\varphi_1^{(1)}\rangle \\
=&\, \langle\varphi_1|U^\dagger \boldsymbol{r} U|\varphi_1\rangle + \langle\lambda\varphi_1^{(1)}|U^\dagger \boldsymbol{r} U|\lambda\varphi_1^{(1)}\rangle + 2\,\mathrm{Re}(\langle\varphi_1|U^\dagger \boldsymbol{r} U|\lambda\varphi_1^{(1)}\rangle) \ . \tag{7.30}
\end{aligned}
$$

The first two terms in (7.30) vanish due to definite parity of $|\varphi_1\rangle$ and $|\lambda\varphi_1^{(1)}\rangle$ and the matrix element in the third term simplifies due to the dipole selection rules (since $\Delta m = 2$ for $\langle\varphi_1|U\boldsymbol{r}U^\dagger|\varphi_5\rangle$ and $\Delta m_s = 1$ for $\langle\varphi_1|U\boldsymbol{r}U^\dagger|\varphi_{13}\rangle$),

$$
\langle\varphi_1|U^\dagger \boldsymbol{r} U|\lambda\varphi_1^{(1)}\rangle = f_3 U^\dagger\langle\varphi_1|\boldsymbol{r}|\varphi_3\rangle U = f_3 \mathcal{R}_{\alpha\beta}^{-1}\begin{pmatrix} x_{13} \\ -ix_{13} \\ 0 \end{pmatrix} \ , \tag{7.31}
$$

and it is

$$
\boldsymbol{d}_\gamma = 2 \, \mathrm{Re} \left(f_3 \mathcal{R}_{\alpha\beta}^{-1} \begin{pmatrix} x_{13} \\ -ix_{13} \\ 0 \end{pmatrix} \right)
$$

$$
= \mathcal{R}_{\alpha\beta}^{-1} (\mathrm{Re} \left(\frac{\lambda}{E_{31}} (c_{xz} + ic_{yz}) \left(2(n-1/2)x_{31}^2 + \sqrt{2n-3} \, x_{13} z_{32} \right) \begin{pmatrix} 1 \\ -i \\ 0 \end{pmatrix} \right))
$$

$$
= \lambda \underbrace{\left\{ \frac{1}{E_{31}} \left((2n-1)x_{31}^2 + \sqrt{2n-3} \, x_{13} z_{32} \right) \right\}}_{=:\chi} \mathcal{R}_{\alpha\beta}^{-1} \begin{pmatrix} c_{xz} \\ c_{yz} \\ 0 \end{pmatrix} . \tag{7.32}
$$

We can find the explicit spatial dependence of the electric dipole moment by expressing the angles α and β with the magnetic field components B_i,

$$
\boldsymbol{d}_\gamma = \lambda\chi \left\{ -\cos\alpha \sin\beta \cos\beta \begin{pmatrix} \cos\beta \\ 0 \\ \sin\beta \end{pmatrix} - \sin\alpha \cos\alpha (1 + \sin^2\beta) \begin{pmatrix} \sin\alpha \sin\beta \\ \cos\alpha \\ -\sin\alpha \cos\beta \end{pmatrix} \right\}
$$

$$
= \lambda \frac{9}{8} \frac{n^2}{E_{31}} \left(2n^2 - 3n - \sqrt{4n^2 - 10n + 6} + 1 \right) \frac{1}{|\boldsymbol{B}|^3} \begin{pmatrix} B_x(2B_y^2 + B_z^2) \\ -B_y(2B_x^2 + B_z^2) \\ (-B_x^2 + B_y^2)B_z \end{pmatrix} . \tag{7.33}
$$

The electric dipole moments hence depends on the ratio of the gradient and the absolute value of the magnetic field and strongly on the principal quantum number n. In leading order in n the dependency reads $\boldsymbol{d}_\gamma \sim n^4 G/|\boldsymbol{B}|$. For a Ioffe-Pritchard magnetic field configuration, Eq. (2.11), $\boldsymbol{d}_\gamma$ vanishes on the Z-axis because the magnetic field components B_x and B_y are zero there. This can be seen from the explicit expression for $\boldsymbol{d}_\gamma$,

$$
\boldsymbol{d}_\gamma = \frac{\lambda\chi}{|\boldsymbol{B}|^3} \begin{pmatrix} X(G - 2QZ)((B - Q(X^2 + Y^2 - 2Z^2))^2 + 2Y^2(G + 2QZ)^2) \\ Y(G + 2QZ)((B - Q(X^2 + Y^2 - 2Z^2))^2 + 2X^2(G - 2QZ)^2) \\ (B - Q(X^2 + Y^2 - 2Z^2))(Y^2(G + 2QZ)^2 - X^2(G - 2QZ)^2) \end{pmatrix} , \tag{7.34}
$$

where again $\lambda = G/3$ a.u. and $\chi = \frac{9}{8E_{31}} n^2 \left(2n^2 + \sqrt{4n^2 - 10n + 6} - 4n + 2 \right)$. It is convenient for the symmetry analysis to also write down the explicit form of $\boldsymbol{d}_\gamma$ for $Q = 0$,

$$
\boldsymbol{d}_\gamma(Q = 0) = \lambda\chi \frac{G^3}{|\boldsymbol{B}|^3} \begin{pmatrix} X(2Y^2 + B^2/G^2) \\ Y(2X^2 + B^2/G^2) \\ (Y^2 - X^2)(B/G) \end{pmatrix} \tag{7.35}
$$

As can be deduced from Eq. (7.32), the electric dipole moment expectation value is perpendicular to the local direction of the magnetic field,

$$
\boldsymbol{d}_\gamma \cdot \boldsymbol{B} \sim \mathcal{R}_{\alpha\beta}^{-1} \begin{pmatrix} c_{xz} \\ c_{yz} \\ 0 \end{pmatrix} \cdot \boldsymbol{B} = 0 . \tag{7.36}
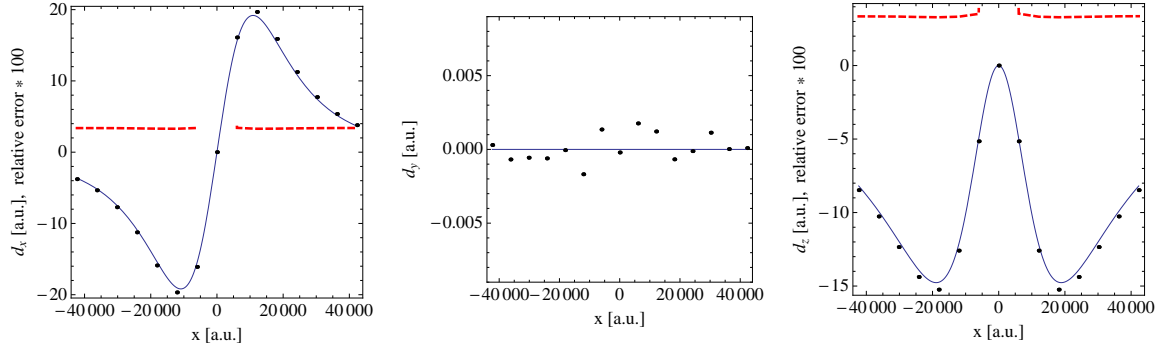$$

Figure 7.1: Comparison of perturbatively computed (continuous line) and numerically computed (dots) expectation values for the electric dipole moments $\boldsymbol{d}_\gamma$ for vanishing geometric parameter $\tilde{Q}$ and vanishing electric field strength F. The dashed lines show the relative error magnified by the factors 10^4 (left plot) and 10^2 (right plot) for visibility. The larger the ratio B/G, the better is the perturbative approximation, see Eq. 7.2. Even for the parameters in the shown plots, $B = 0.1\,\mathrm{G}$ and $G = 10\,\mathrm{Tm}^{-1}$, however, the relative error is still smaller than 0.04.

The electric dipole moment induced by the external electric field described in the following Section 7.2 has the same property. It has its reason in the symmetry of the electronic density of the perturbed state with respect to a plain perpendicular to the local magnetic field axis. This is elaborated in Section 7.3 and illustrated in Fig. 7.5.

A comparison with numerically calculated expectation values for the electric dipole moment can be found in Fig. 7.1.

7.2 Non-parallel moments in an electric field

As has been done for the finite size term $\mathcal{H}_\gamma$ already, we also have to determine the regime in which the effect of an external electric field can be treated perturbatively. The additional term in the Hamiltonian, $\mathcal{H}_F$, has to be compared with $\boldsymbol{\mu} \cdot \boldsymbol{B}(\boldsymbol{R})$. This can be done at the origin since for confining parameter sets the magnitude of the magnetic field is smallest at the origin and other quantities are approximated independently of $\boldsymbol{R}$. The resulting restriction is[3]

$$F_x \ll B/n \ . \tag{7.37}$$

Perturbation theory with electric field operator

The Hamiltonian for the additional external electric field is $H_F = q\phi = (xF_x + yF_y + zF_z)$ since $\boldsymbol{F} = -\mathrm{grad}\,\phi$ and $q = -e$ ($= -1$ in atomic units). According to the considerations in the preceeding chapter the perturbing operator therefore reads

$$W_F = U(\boldsymbol{r} \cdot \boldsymbol{F})U^\dagger = U\boldsymbol{r}U^\dagger \cdot \boldsymbol{F} =: c_{F,ij}F_i r_j \ , \tag{7.38}$$

---

[3]It suffices to fulfill $nF_x/(B + 2QZ^2) \ll 1$ which should be considered for extremely small B and large displacements

where the small parameter in the operator W_F is the modulus of the electric field, $\lambda_F = |\boldsymbol{F}|$. Considering the the Zeeman term dependence, $\boldsymbol{\mu B} \sim |\boldsymbol{B}|$, the perturbation parameter is the ratio of the field strengths, $\lambda_F = |\boldsymbol{F}|/|\boldsymbol{B}|$.

The *first order energy correction* due to W_F vanishes due to the dipole selection rules since $\Delta l = 0$,

$$\lambda_F \epsilon^{(1,F)} = \langle \mathrm{circ}|c_{F,ij}F_i r_j|\mathrm{circ}\rangle = 0 \ . \tag{7.39}$$

The *first order correction to the circular state* is

$$|\lambda_F \varphi_1^{(1,F)}\rangle = \sum_{p \neq 1} \frac{\langle \varphi_p|c_{F,ij}F_i r_j|\varphi_1\rangle}{E_1^0 - E_p^0}|\varphi_p\rangle =: \sum_{p \neq 1} \frac{W_{F,p1}}{E_{1p}}|\varphi_p\rangle = \frac{W_{F,31}}{E_{13}}|\varphi_3\rangle \ , \tag{7.40}$$

where we use the symbols $W_{F,pq} = \langle \varphi_p|c_{F,ij}F_i r_j|\varphi_q\rangle$ and $E_{pq} = E_p^0 - E_q^0$. For an electric field in arbitrary direction the numerator in (7.40) reads

$$W_{F,31} = ex_{31}\left[F_x(c_{F,xx} + ic_{F,xy}) + F_y ic_{F,yy} + F_z(c_{F,zx} + ic_{F,zy})\right] \tag{7.41}$$

and if we restrict our consideration to an electric field pointing in the X-axis we find

$$|\lambda_F \varphi_1^{(1,F_x)}\rangle = ex_{13}F_x(c_{F,xx} + ic_{F,xy})\frac{|\varphi_3\rangle}{E_{13}} \ , \tag{7.42}$$

where $c_{F,xx} = \cos\beta$ and $c_{F,xy} = \sin\alpha\sin\beta$.

The *second order energy correction* due to external electric field is

$$\begin{aligned}
\lambda_F^2 \epsilon^{(2,F_x)} &= F_x\langle \varphi_1 + \lambda_F \varphi_1^{(1,F_x)}|c_{F,xj}r_j|\varphi_1 + \lambda_F \varphi_1^{(1,F_x)}\rangle \\
&= 2\mathrm{Re}\left(F_x\langle \varphi_1|c_{F,xj}r_j|\lambda_F \varphi_1^{(1,F_x)}\rangle\right) \\
&= 2\frac{eF_x^2}{E_{13}}x_{13}^2(c_{F,xx}^2 + c_{F,xy}^2) \\
&= \frac{9}{4}\frac{F_x^2}{E_{13}}n^2(n-1)(\cos\beta^2 + \sin\alpha^2\sin\beta^2) \ . \tag{7.43}
\end{aligned}$$

For vanishing Q and with the approximate expression for the energetic separation between the coupling surfaces, $E_{13} \approx |\boldsymbol{B}|/2$, this reads

$$\lambda_F^2 \epsilon^{(2,F_x)} \approx \frac{9}{4}F_x^2 n^2(n-1)\frac{B^2 + G^2 Y^2}{B^2 + G^2 Y^2 + G^2 X^2} \ . \tag{7.44}$$

The perturbative contribution to the uppermost surface due to an external electric field $(F_x, 0, 0)$ is thus positive and it is maximal on the z axis.

Both the unperturbed wave function $|\varphi_1\rangle$ as well as the perturbation $|\lambda_F \varphi_1^{(1,F_x)}\rangle$ have definite parity. The *electric dipole moment expectation value* in the uppermost electronic

energy surface is therefore, analogously to (7.30),

$$
\begin{aligned}
\boldsymbol{d}_F =& 2\mathrm{Re}\left(\langle\varphi_1|U^\dagger \boldsymbol{r} U|\lambda_F\varphi_1^{(1,F_x)}\rangle\right)\\
=& \mathcal{R}_{\alpha\beta}^{-1}(2x_{31}\frac{F_x}{E_{13}}\mathrm{Re}(c_{F,x}\begin{pmatrix} x_{13} \\ -\imath x_{13} \\ 0 \end{pmatrix} + c_{F,y}\begin{pmatrix} \imath x_{13} \\ x_{13} \\ 0 \end{pmatrix}))\\
=& \frac{2F_x}{E_{13}}x_{13}^2\mathcal{R}_{\alpha\beta}^{-1}\begin{pmatrix} c_{F,x} \\ c_{F,y} \\ 0 \end{pmatrix}\\
=& \frac{2eF}{E_{13}}x_{13}^2\left(\cos\beta\begin{pmatrix} \cos\beta \\ 0 \\ \sin\beta \end{pmatrix} + \sin\alpha\sin\beta\begin{pmatrix} \sin\alpha\sin\beta \\ \cos\alpha \\ -\sin\alpha\cos\beta \end{pmatrix}\right)\\
=& \frac{9}{4}\frac{F_x}{E_{13}}n^2(n-1)\frac{1}{\boldsymbol{B}^2}\begin{pmatrix} B_y^2+B_z^2 \\ -B_xB_y \\ -B_xB_z \end{pmatrix}\;,
\end{aligned}
\tag{7.45}
$$

where we use $c_{F,x} = \cos\beta$, $c_{F,y} = \sin\alpha\sin\beta$, $x_{13} = \frac{3}{2\sqrt{2}}n\sqrt{n}$, and the relation (7.20). Recalling $E_{13} \approx |\boldsymbol{B}|/2$ one can see that the electric dipole moment induced by the electric field depends on the ratio of the field strengths, as expected, and on the cubed principal quantum number, $\boldsymbol{d}_F \sim n^3 F_x/|\boldsymbol{B}|$.

Inserting the magnetic Ioffe-Pritchard field configuration (6.1) into (7.45) yields

$$
\boldsymbol{d}_F = \frac{4F_x}{|\boldsymbol{B}|^3}x_{13}^2\begin{pmatrix} (B-Q(X^2+Y^2-2Z^2))^2 + Y^2(G+2QZ)^2 \\ XY(G^2-4Q^2Z^2) \\ X(G-2QZ)(Q(X^2+Y^2-2Z^2)-B) \end{pmatrix}\;,
\tag{7.46}
$$

which, in contrary to $\boldsymbol{d}_\gamma$, does not vanish on the Z-axis but points in the direction of the electric field with $d_{F,x} = 4x_{13}^2 F_x/|\boldsymbol{B}|$. This is not true away from the Z-axis. The dipole moment does not point in the electric field direction there but stays rather perpendicular to the local direction of the magnetic field (alike $\boldsymbol{d}_\gamma$, Eq. (7.36)). This can be deduced from the directional dependence in (7.45) for arbitrary magnetic field configurations,

$$
\boldsymbol{d}_F \cdot \boldsymbol{B} \sim \mathcal{R}_{\alpha\beta}^{-1}\begin{pmatrix} c_{F,x} \\ c_{F,y} \\ 0 \end{pmatrix}\cdot\boldsymbol{B} \sim \begin{pmatrix} B_y^2+B_z^2 \\ -B_xB_y \\ -B_xB_z \end{pmatrix}\cdot\boldsymbol{B} = 0\;.
\tag{7.47}
$$

An electric dipole moment that is induced by an external electric field but does not point in this very direction is not physically intuitive at first glance. A closer look on its origin reveals a simple explanation that is described in the next Section, 7.3. Before that, we shortly justify the additivity of $\boldsymbol{d}_\gamma$ and $\boldsymbol{d}_F$.

Addition of perturbatively calculated dipole moments

In this Section and in the previous Section 7.1 we considered the electric field term $\mathcal{H}_F$ and the finite size term $\mathcal{H}_\gamma$ as being separate perturbations to the non-perturbed Hamiltonian,

respectively. For a non-zero external field the right perturbation operator, however, is the sum of both,

$$W_{\text{tot}} = U\mathcal{H}_\gamma U^\dagger + U\mathcal{H}_F U^\dagger \ . \tag{7.48}$$

The total first order correction to the wave function hence reads

$$|\lambda 1\rangle = \sum_{p \neq 1} \frac{\langle \varphi_p | W_{\text{tot}} | \text{circ} \rangle}{E_1^0 - E_p^0} |\varphi_p\rangle =: |\lambda_\gamma 1\rangle_\gamma + |\lambda_F 1\rangle_F \ . \tag{7.49}$$

The question is now if the expectation values of the dipole operator computed in the respective perturbed wave function, $\boldsymbol{d}_\gamma$ and $\boldsymbol{d}_F$, can just be added to find the expectation value in the total perturbed wave function, $\boldsymbol{d} = \langle \text{circ} + \lambda 1 | \boldsymbol{r} | \text{circ} + \lambda 1 \rangle$. This is not in general correct since the calculation of the expectation value of the observable $\hat{O}$ in the perturbed state $|\text{circ} + \lambda 1\rangle$ yields mixed matrix elements,

$$\begin{aligned}
&\langle \text{circ} + \lambda 1 | \hat{O} | \text{circ} + \lambda 1 \rangle \\
&= \langle \text{circ} | \hat{O} | \text{circ} \rangle + 2\lambda \text{Re}(\langle \text{circ} | \hat{O} | 1 \rangle) + \lambda^2 \langle 1 | \hat{O} | 1 \rangle \\
&= \langle \text{circ} + \lambda_\gamma 1_\gamma | \hat{O} | \text{circ} + \lambda_\gamma 1_\gamma \rangle + \langle \text{circ} + \lambda_F 1_F | \hat{O} | \text{circ} + \lambda_F 1_F \rangle + 2\text{Re}(\langle \lambda_\gamma 1_\gamma | \hat{O} | \lambda_F 1_F \rangle) \\
&= \hat{O}_\gamma + \hat{O}_F + 2\text{Re}(\langle \lambda_\gamma 1_\gamma | \hat{O} | \lambda_F 1_F \rangle) \ . \tag{7.50}
\end{aligned}$$

The perturbations $|\lambda_\gamma 1\rangle_\gamma$ and $|\lambda_F 1\rangle_F$, Eqs. (7.21) and (7.40), involve the states $|\varphi_3\rangle$, $|\varphi_5\rangle$, $|\varphi_{13}\rangle$ which do not differ in their angular momentum quantum number l. They hence have the same definite parity since the parity of the spherical harmonics does not depend on the quantum number m. The mixed matrix element $\langle \lambda_\gamma 1_\gamma | \boldsymbol{d} | \lambda_F 1_F \rangle$ therefore vanishes (the dipole operator is an odd operator) and

$$\boldsymbol{d} = \langle \text{circ} + \lambda 1 | \boldsymbol{r} | \text{circ} + \lambda 1 \rangle = \boldsymbol{d}_\gamma + \boldsymbol{d}_F \ . \tag{7.51}$$

In other words, if taking into account the first order state vector perturbation only, then adding the different dipole moment expectation values $\boldsymbol{d}_\gamma$ and $\boldsymbol{d}_F$ is equivalent to calculating the expectation value with the combined perturbed state vector, Eq. (7.49).

A comparison with numerically calculated electric dipole moments for finite electric field strength can be found in Fig. 7.2.

7.3 Asymmetry for weak electric fields

In this section we investigate the properties of the electric dipole moments $\boldsymbol{d}_\gamma$ and $\boldsymbol{d}_F$ found in the preceeding sections. In particular we investigate their symmetry properties, their orientation to each other and we explain why they are perpendicular to the local magnetic field axis contrary to intuition.

We first study the symmetry properties of the electric dipole moments. For $\tilde{Q} = 0$ the Ioffe-Pritchard setup is translationally symmetric along the Z-axis. The electric dipole moment does therefore not depend on the Z-position of the atom in this case. For finite longitudinal confinement, $\tilde{Q} > 0$, we find that only an approximate symmetry in Z remains when $G/Q \gg 2|Z|$. This condition is already incorporated by the restriction (7.2) which is
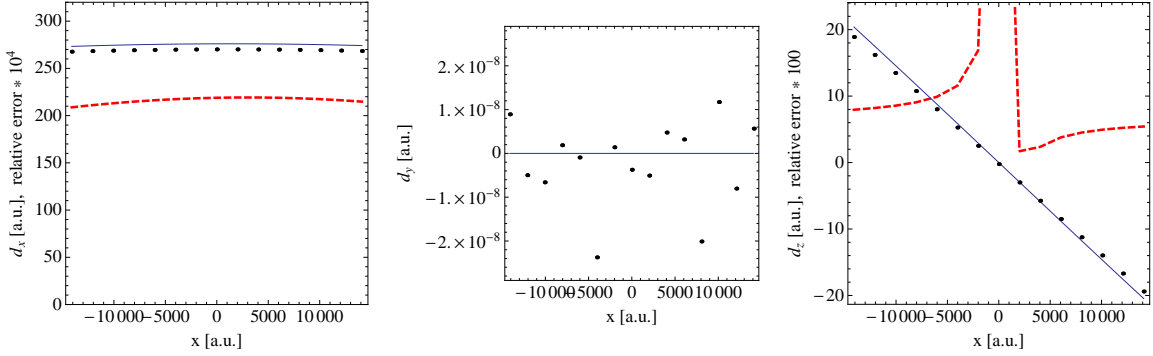
Figure 7.2: Comparison of perturbatively computed (continuous line) and numerically computed (dots) expectation values for the electric dipole moments for finite electric field strength F. The dashed lines show the relative error magnified by the factors 10^4 (left plot) and 10^2 (right) for visibility. Parameters: $B = 1\,\mathrm{G}$, $G = 10\,\mathrm{Tm}^{-1}$, $F = 10^{-12}$ a.u., $Q = 0$.

formulated in Section 7.1 to justify the perturbative treatment of $\mathcal{H}_\gamma$. If it holds the electric dipole moment is approximately symmetric to the x-y-plane,

$$\boldsymbol{d}(X, Y, Z) \approx -\boldsymbol{d}(X, Y, -Z) \ . \tag{7.52}$$

Much stronger than the dependence of the electric dipole moment on Z is its dependence on the transversal coordinates. As we will see, it is also more relevant for the following chapters. In a second step we therefore analyze the symmetry of the dipole moment with respect to the Z-axis without putting any restriction on the geometry parameter $\tilde{Q}$. If no electric field is present the only non-vanishing electric dipole moment is $\boldsymbol{d}_\gamma$, generated by the finite size term $\mathcal{H}_\gamma$. The symmetry properties of its components read

$$\begin{pmatrix} d_{\gamma x} \\ d_{\gamma y} \\ d_{\gamma z} \end{pmatrix} (X, Y) = \begin{pmatrix} d_{\gamma x} \\ -d_{\gamma y} \\ d_{\gamma z} \end{pmatrix} (X, -Y) = \begin{pmatrix} -d_{\gamma x} \\ d_{\gamma y} \\ d_{\gamma z} \end{pmatrix} (-X, Y) = \begin{pmatrix} -d_{\gamma x} \\ -d_{\gamma y} \\ d_{\gamma z} \end{pmatrix} (-X, -Y). \tag{7.53}$$

It is furthermore $d_{\gamma,z}(X, Y) = -d_{\gamma,z}(\pm Y, \pm X)$ and $d_{\gamma,x}(X, Y) = d_{\gamma,y}(Y, X)$. The dipole moment induced by the external electric field, $\boldsymbol{d}_F$, exhibits different symmetries. It is

$$\begin{pmatrix} d_{Fx} \\ d_{Fy} \\ d_{Fz} \end{pmatrix} (X, Y) = \begin{pmatrix} d_{Fx} \\ -d_{Fy} \\ d_{Fz} \end{pmatrix} (X, -Y) = \begin{pmatrix} d_{Fx} \\ -d_{Fy} \\ -d_{Fz} \end{pmatrix} (-X, Y) = \begin{pmatrix} d_{Fx} \\ d_{Fy} \\ -d_{Fz} \end{pmatrix} (-X, -Y). \tag{7.54}$$

The sum of the contributions, the electric dipole moment for finite electric field $\boldsymbol{d} = \boldsymbol{d}_\gamma + \boldsymbol{d}_F$, is hence only symmetric with respect to a reflection about the x-axis ($Y \to -Y$):

$$\boldsymbol{d} = \begin{pmatrix} d_x \\ d_y \\ d_z \end{pmatrix} (X, Y) = \begin{pmatrix} d_x \\ -d_y \\ d_z \end{pmatrix} (X, -Y) \ . \tag{7.55}$$

Already for moderate electric fields, however, $\boldsymbol{d}_\gamma$ is a mere perturbation to $\boldsymbol{d}$ and the symmetry properties of $\boldsymbol{d}$ are approximately those of $\boldsymbol{d}_F$, Eq. (7.54).

The components and the absolute value of $\boldsymbol{d}$ are depicted in Fig. 7.3. Both numerically and analytically computed data are plotted for different electric field strengths. It can be seen that when $\boldsymbol{d}_\gamma$ and $\boldsymbol{d}_F$ have the same order of magnitude (plot (d) in Fig. 7.3), all the symmetries but the one with respect to the x-axis are lost, see Eq. (7.55).
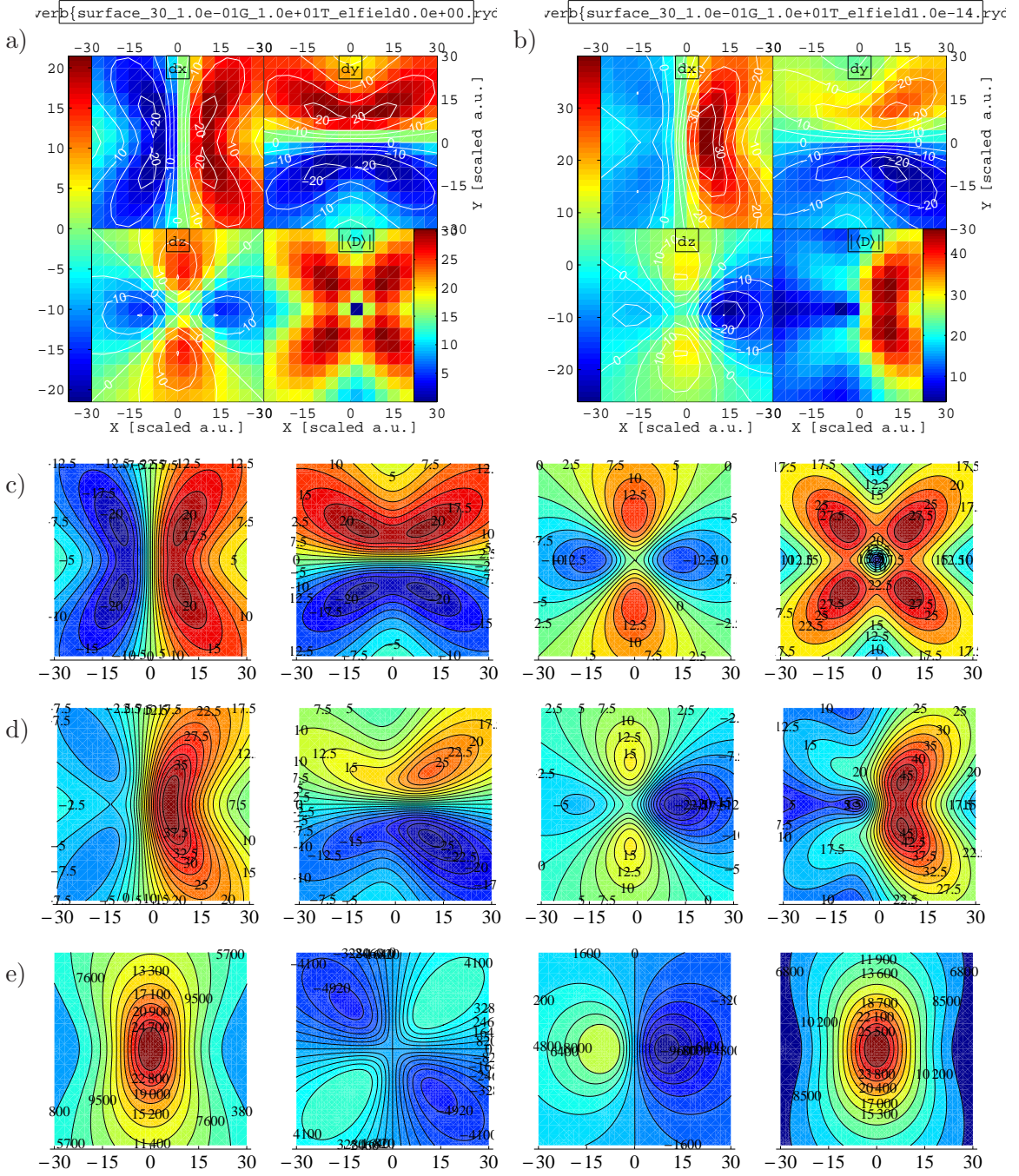
A more accessible depiction of the center of mass coordinate dependent direction of the induced dipole moments is shown in Fig. 7.4. The contributions to the electric dipole moment originating from the different perturbations, $\boldsymbol{d}_F$ and $\boldsymbol{d}_\gamma$ (blue and red arrows in the plots, respectively), are always perpendicular to the local magnetic field direction (yellow arrows). This is formulated in Eqs. (7.36) and (7.47). They are additionally perpendicular to each other on the y-axis and they are parallel on the positive x-axis and anti-parallel on the negative x-axis. This can be seen from the explicit expression for the angle that $\boldsymbol{d}_F$ and $\boldsymbol{d}_\gamma$ include,

$$
\begin{aligned}
\angle(\boldsymbol{d}_F, \boldsymbol{d}_\gamma) &= \arccos\left(\frac{B_x\left(2B_y^2 + B_z^2\right)}{\sqrt{\left(B_y^2 + B_z^2\right)\left(B_z^2\left(B_x^2 + B_y^2\right) + 4B_x^2 B_y^2\right)}}\right) \\
&= \arccos\left(\frac{X\left(B^2 + 2G^2 Y^2\right)}{\sqrt{\left(B^2 + G^2 Y^2\right)\left(B^2\left(X^2 + Y^2\right) + 4G^2 X^2 Y^2\right)}}\right) \,,
\end{aligned}
\tag{7.56}
$$

where we inserted the magnetic field of a Ioffe-Pritchard trap in Helmholtz configuration ($Q = 0$) to find the second line. On the X-axis it is $\angle(\boldsymbol{d}_F, \boldsymbol{d}_\gamma) = \arccos(\operatorname{sign}(X))$ which yields the angle π for negative values of X and zero for positive X.

The fact that the electric dipole moment induced by the external electric field does not point in the direction of this field but is rather perpendicular to the local quantization axis, which is set by the magnetic field direction $\boldsymbol{B}(\boldsymbol{R})$, is not intuitive. It can be easily explained, however, considering the symmetry of the perturbed electronic wave function. Since the radial part of the wave function is isotropic we are only interested in the angular part which is a superposition of spherical harmonics. More specifically we are interested in the absolute value of the wave function which is the square root of the probability density. The absolute value of some of the involved functions and their superpositions is visualized in spherical plots in Fig. 7.5 where the coordinate frame of the shown plots is not the laboratory frame but the z-axis rather points in the local magnetic field direction $\hat{\boldsymbol{B}}$. The admixture of $|\varphi_5\rangle$ and $|\varphi_{13}\rangle$ to the circular state does not yield a contribution to the dipole moment expectation values $\boldsymbol{d}_F$ and $\boldsymbol{d}_\gamma$ due to parity arguments, see the reasoning after Eq. (7.30). In order to explain why $\boldsymbol{d}_F$ and $\boldsymbol{d}_\gamma$ are perpendicular to $\boldsymbol{B}$ it therefore suffices to study the hybridized state $|\varphi_h\rangle = |\mathrm{circ}\rangle + f_3|\varphi_3\rangle$. We can set $f_3 = 1$ for simplicity without changing the symmetry. The corresponding superposition of spherical harmonics $|Y_{29}^{29} + Y_{28}^{28}|$ is shown in the bottom left plot of Fig. 7.5 where the z-axis points into the direction of the quantization axis, i.e. the local magnetic field direction. The superposition is symmetric under the reflection $z \to -z$ but it is not symmetric under the reflection $x \to -x$. We find that the center of the electronic charge density of the state $|\varphi_h\rangle$, $\rho_e = \varphi_h^* \varphi_h / \int \varphi_h^* \varphi_h$, is situated in the x-y-plane which is perpendicular to the local magnetic field direction and the electric dipole moment expectation value is hence also perpendicular to the latter. A small arrow indicates the position of the center of the electronic charge density in the respective plot.

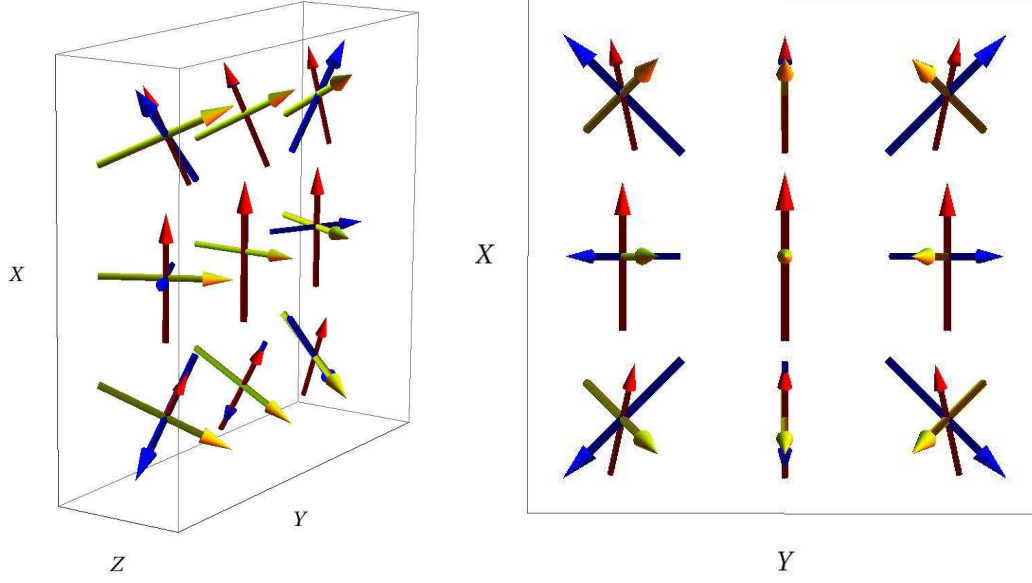**Figure 7.3:** Components d_i and absolute value $|\boldsymbol{d}|$ of the dipole moment expectation value for different electric field strengths F. Plots a) and b) show numerical data whereas plots c) to e) depict the perturbatively computed dipole moment, Eq. (7.51). The data plotted in a) and c) is computed for vanishing electric field F and therefore exhibits the symmetries (7.53). The only symmetry that survives when a small electric field is present (plots b) and d)) is the symmetry with respect to the x-axis, see Eq. 7.55. For larger electric field the symmetries of $\boldsymbol{d}_F$ are approximately valid (plot e)). Parameters: $B = 0.1\,\mathrm{G}$, $G = 10\,\mathrm{Tm}^{-1}$, $F = 0$ (a) and c)), $F = 10^{-14}$ a.u. (b) and d)) and $F = 10^{-11}$ a.u. (e)). All panels depict the x-y-plane within -30 and 30 scaled atomic units. Electric dipole moments are given in the atomic units $ea_0 = 2.54$ Debye.

Figure 7.4: Illustration of directions in the x-y-plane. The electric dipole moments $\boldsymbol{d}_\gamma$ and $\boldsymbol{d}_F$ whose directions are indicated by the blue and red arrows, respectively, are always perpendicular to the local magnetic field axis (yellow). On the y-axis they are additionally perpendicular to each other, whereas being (anti-)parallel on the positive (negative) x-axis.

We can conclude that an electric field in arbitrary direction, that satisfies the condition (7.37) allowing a perturbative treatment, can only perturb a circular state in a way that the electric dipole moment in the direction of the quantization axis z vanishes. In terms of the polarizability tensor α, defined via $d_i = \alpha_{ij}E_j$, this means that $\alpha_{zi} = 0$ for circular states. This is no longer true when the coupling of the Rydberg atoms to the electric field becomes comparable to the Zeeman coupling and can therefore no longer be treated perturbatively.

The rectangularity of the electric dipole moment expectation value $\boldsymbol{d}$ and the magnetic field direction $\boldsymbol{B}$ has been verified numerically. The normalized projection of $\boldsymbol{d}$ onto $\boldsymbol{B}$ is small as long as the electric field strength is small enough for the constraint (7.37) to be satisfied. The parameters $B = 1\,\mathrm{G}$, $F = 10^{-12}$ a.u., $n = 30$, for example, yield a maximal normalized projection of 0.01. As soon as the constraint is violated the electric dipole moment expectedly aligns with the external electric field.
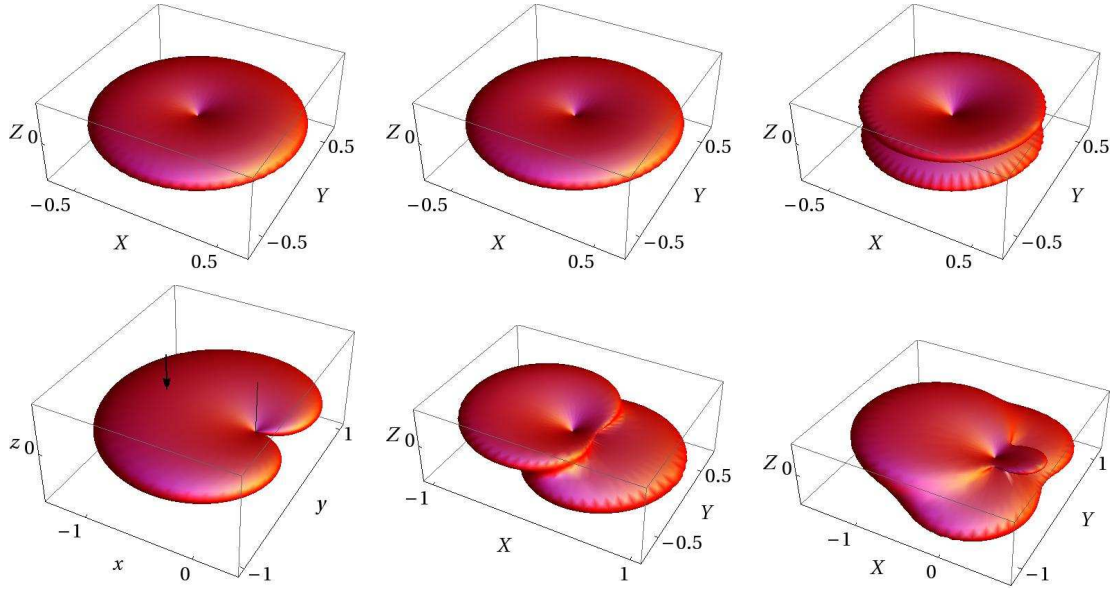
Figure 7.5: Illustration of the angular dependency of the perturbed electronic wave function exemplified for $n = 30$. The upper row of spherical plots shows the absolute value of the spherical harmonics Y_{29}^{29}, Y_{28}^{28} and Y_{27}^{27} that correspond to the hydrogenic eigenfunctions $|\varphi_1\rangle$, $|\varphi_3\rangle$ and $|\varphi_5\rangle$, respectively, as named in Eq. (7.10). The bottom row shows the absolute value of the superpositions $Y_{29}^{29} + Y_{28}^{28}$, $Y_{28}^{28} + Y_{28}^{27}$, and $Y_{29}^{29} + Y_{28}^{28} + Y_{28}^{27}$, only the second of which is invariant under parity transformation $\boldsymbol{r} \rightarrow -\boldsymbol{r}$ since the involved functions have the same l quantum number. This symmetry is used to justify the addition of the perturbatively computed dipole moments in Eq. (7.51). The asymmetry of the superposition $Y_{29}^{29} + Y_{28}^{28}$ in the bottom left plot, on the other hand, explains the existence of the electric dipole moments $\boldsymbol{d}_F$ and $\boldsymbol{d}_\gamma$ and their rectangularity to the local magnetic field direction which here coincides with the Z-axis. The arrow indicates the location of the first moment $\int d\tau \boldsymbol{r} \rho_e$ (where $\rho_e = \varphi_h^* \varphi_h / \int \varphi_h^* \varphi_h$, see text).

8 Rydberg-Rydberg interaction

In Chapter 5 we include the interaction of the Rydberg atoms among each other into our considerations via a simplified expression for the dipole-dipole interaction, see Sec. (5.3). This is a good approximation for atoms in the translationally symmetric setup with an external electric field in X-direction when their distance in Z, $|Z_A - Z_B|$, is large compared to the transversal oscillator length of the center of mass motion. However, this description does neither include the orientation of the electric dipole moments nor higher order multipole moment interactions.

In this chapter we derive expressions for the interaction energy of two Rydberg atoms – each modeled by a core and an electron – for inter-atomic distances that are large compared to the distance of the electrons to the respective core. To this end we first expand the Coulomb interaction of the charges of the different atoms in reciprocal powers of the distance of the atoms (Sec. 8.1). In a second step (Sec. 8.2) we determine for which conditions the derived interaction operators can be represented in the adiabatic electronic wave functions of the individual atoms found in Chapter 4 and Chapter 6. In Section 8.3 we examine the transition matrix elements of the dipole-dipole operator to other surfaces and the closely related second order contributions to the interaction of the atoms.

8.1 Multipole expansion of Coulomb interaction operators

Consider the interaction of two Rydberg atoms described by the coordinates of their cores $\boldsymbol{R}_A$ and $\boldsymbol{R}_B$ and of their valence electrons $\boldsymbol{R}_A + \boldsymbol{r}_A$ and $\boldsymbol{R}_B + \boldsymbol{r}_B$. The Coulomb interaction between charges of different atoms reads

$$\frac{V(\boldsymbol{r}_A, \boldsymbol{r}_B, \boldsymbol{R}_{AB})}{e^2/4\pi\epsilon_0} = \frac{1}{|\boldsymbol{R}_{AB}|} - \frac{1}{|\boldsymbol{R}_{AB} - \boldsymbol{r}_B|} - \frac{1}{|\boldsymbol{R}_{AB} + \boldsymbol{r}_A|} + \frac{1}{|\boldsymbol{R}_{AB} - (\boldsymbol{r}_B - \boldsymbol{r}_A)|} \quad (8.1)$$

where we abbreviate the vector connecting the cores by $\boldsymbol{R}_{AB} := \boldsymbol{R}_A - \boldsymbol{R}_B$. For large separations of the atoms – which is assumed in the following – the separation of the cores is much larger than the extension of the electronic wave functions, $\langle r_{A,B} \rangle \ll |\boldsymbol{R}_{AB}| =: R_{AB}$. In this case it is reasonable to write the interaction potential V as a multipole expansion in the small parameter $\langle r_{A,B} \rangle / R_{AB}$. This can be done taking into account that $\frac{1}{|\boldsymbol{r}-\boldsymbol{r}'|}$ is a generating function of the Legendre polynomials,

$$\frac{1}{|\boldsymbol{r} - \boldsymbol{r}'|} = \frac{1}{\sqrt{r^2 - r'^2 - 2rr'\cos\Theta}} = \sum_{l=0}^{\infty} \frac{r'^l}{r^{l+1}} \mathrm{P}_l(\cos\Theta) \quad \text{for} \quad r > r' . \quad (8.2)$$

Here Θ is the angle between the coordinates, $\cos\Theta = \boldsymbol{r}.\boldsymbol{r}'/(rr')$.

Due to the neutrality of the interacting constituents, the only non-vanishing term up to third order in the expansion of V is the dipole-dipole term. It reads

$$\frac{\boldsymbol{r}_A.\boldsymbol{r}_B - 3(\boldsymbol{r}_A.\hat{\boldsymbol{R}}_{AB})(\boldsymbol{r}_B.\hat{\boldsymbol{R}}_{AB})}{R_{AB}^3} , \quad (8.3)$$

where $\hat{\boldsymbol{R}}_{AB} = \boldsymbol{R}_{AB}/R_{AB}$ is the unit vector between the cores of the atoms. The fourth order term in the expansion (8.2) can be written as

$$
\frac{3}{2R_{AB}^4} \Big[r_B^2 (\boldsymbol{r}_B . \hat{\boldsymbol{R}}_{AB}) - r_A^2 (\boldsymbol{r}_A . \hat{\boldsymbol{R}}_{AB})
$$
$$
- \Big(5(\boldsymbol{r}_B . \hat{\boldsymbol{R}}_{AB})(\boldsymbol{r}_A . \hat{\boldsymbol{R}}_{AB}) + |\boldsymbol{r}_B - \boldsymbol{r}_A|^2 \Big) \Big((\boldsymbol{r}_B - \boldsymbol{r}_A) . \hat{\boldsymbol{R}}_{AB} \Big) \Big]
$$
$$
= \frac{3}{2R_{AB}^4} \Big[r_B^2 (\boldsymbol{r}_A . \hat{\boldsymbol{R}}_{AB}) - r_A^2 (\boldsymbol{r}_B . \hat{\boldsymbol{R}}_{AB})
$$
$$
- \Big(5(\boldsymbol{r}_B . \hat{\boldsymbol{R}}_{AB})(\boldsymbol{r}_A . \hat{\boldsymbol{R}}_{AB}) - 2(\boldsymbol{r}_A . \boldsymbol{r}_B) \Big) \Big((\boldsymbol{r}_B - \boldsymbol{r}_A) . \hat{\boldsymbol{R}}_{AB} \Big) \Big] . \tag{8.4}
$$

We abbreviate the projections of the electronic coordinates onto the vector connecting the cores as $r_i^P := \boldsymbol{r}_i . \hat{\boldsymbol{R}}_{AB}$ and $r_{AB}^P := (\boldsymbol{r}_A - \boldsymbol{r}_B) . \hat{\boldsymbol{R}}_{AB} = r_A^P - r_B^P$. The multipole terms up to the fourth order in the expansion of the potential

$$
V(\boldsymbol{r}_A, \boldsymbol{r}_B, \boldsymbol{R}_{AB}) = V_{\text{dd}} + V_{\text{dq}} + \mathcal{O}\Big(\Big(\frac{\langle r_{A,B} \rangle}{R_{AB}} \Big)^5 \Big) \tag{8.5}
$$

can then be rewritten as follows:

$$
\frac{V_{\text{dd}}}{e^2/4\pi\epsilon_0} = \frac{1}{R_{AB}^3} \Big(\boldsymbol{r}_A . \boldsymbol{r}_B - 3 r_A^P r_B^P \Big)
$$
$$
\frac{V_{\text{dq}}}{e^2/4\pi\epsilon_0} = \frac{1}{R_{AB}^4} \frac{3}{2} \Big(r_B^2 r_B^P - r_A^2 r_A^P + (5 r_B^P r_A^P + r_{AB}^2) r_{AB}^P \Big)
$$
$$
= \frac{1}{R_{AB}^4} \frac{3}{2} \Big(r_B^2 r_A^P - r_A^2 r_B^P + (5 r_B^P r_A^P - 2 \boldsymbol{r}_A . \boldsymbol{r}_B) r_{AB}^P \Big)
$$
$$
\approx \frac{1}{R_{AB}^4} \frac{3}{2} \Big((r^2 + 5 r_B^P r_A^P - 2 \boldsymbol{r}_A . \boldsymbol{r}_B) r_{AB}^P \Big) . \tag{8.6}
$$

The last line in (8.6) holds if $r_A^2 \approx r_B^2 =: r^2$, hence, e. g., for two circular Rydberg atoms in the same n-manifold. In this case the dipole-quadrupole interaction V_{dq} vanishes if r_{AB}^P vanishes, that is when the electric dipole moment expectation values for both atoms are the same.

If the Rydberg atoms line up on the Z-axis, i. e. $|X_i|, |Y_i| \ll |Z_{AB}|$, then the connecting vector $\hat{\boldsymbol{R}}_{AB}$ is approximately parallel to the Z-axis, $\hat{\boldsymbol{R}}_{AB} \approx (0, 0, 1)$[1], and we can write for the potential

$$
\frac{V(\boldsymbol{r}_A, \boldsymbol{r}_B, \boldsymbol{R}_{AB})}{e^2/4\pi\epsilon_0} \approx \frac{1}{R_{AB}^3} (\boldsymbol{r}_A . \boldsymbol{r}_B - 3 z_A z_B) + \frac{3}{2R_{AB}^4} \Big((r^2 + 5 z_A z_B - 2 \boldsymbol{r}_A . \boldsymbol{r}_B)(z_A - z_B) \Big) .
$$
$$
\tag{8.7}
$$

As soon as the dependence on $\boldsymbol{R}_{AB}$ is eliminated (consider the atoms distance R_{AB} as fixed here) the interaction could in principle be described by center of mass-wave-function-weighted multipole moments of the individual atoms that interact. It is crucial, however, to take into account the dependence on $\boldsymbol{R}_{AB}$ in order to study the stability of a two-atom configuration in a trap or to describe its collapse. This is evident form Figure 8.1 in which the dipole-dipole interaction is plotted assuming $\boldsymbol{R}_{AB}$ to be parallel to the Z-axis (left) and with the full angle dependence as it is written down in (8.3).

---

[1]depending on the naming of the atoms it could also be $\hat{\boldsymbol{R}}_{AB} \approx (0, 0, -1)$, but let us without loss of generality assume $Z_A > Z_B$
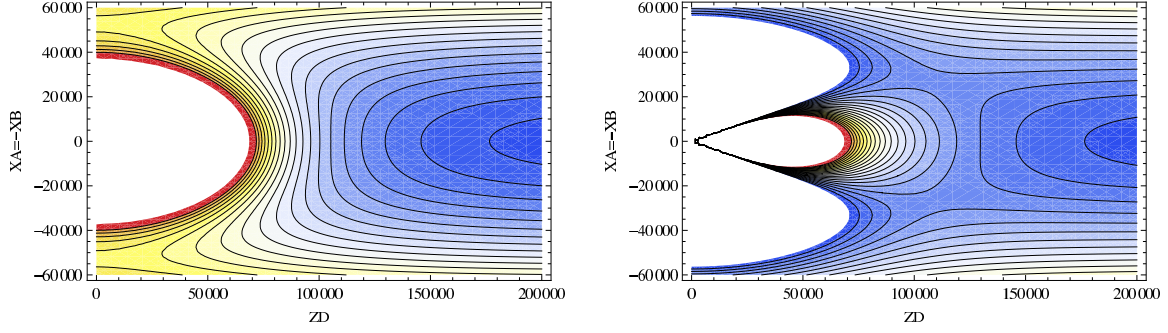
Figure 8.1: Sections through the two-atom potential including the dipole-dipole interaction and a trapping potential developed in the next chapter. For the *left* plot it is assumed that the vector connecting the atoms $\boldsymbol{R}_{AB}$ is parallel to the Z-axis. The plot on the *right* shows the full angle dependence of the dipole-dipole interaction, Eq. 8.1. The fundamental difference of the plots indicates that it is crucial to take into account the full angular dependence of the interaction when stepping out of the Z-axis, $\rho > 0$. The same color code is used in both plots. (The choice of coordinates will become clear in Sec. 9.)

8.2 Representation in single-atom electronic eigenstates

If the multipole-multipole interaction operator V is treated as a perturbation to the electronic Hamiltonians of the individual Rydberg atoms, H_A and H_B (to be quantified below), it is favorable to represent it in the two-electron basis

$$\{|\varphi_i^A; \varphi_j^B\rangle\} \equiv \{|ij\rangle\} \tag{8.8}$$

where i and j number the single-atom adiabatic electronic wave functions from above in energy. The total Hamiltonian reads $H = H_A + H_B + V$ and it is

$$(H_A + H_B)|\varphi_i^A; \varphi_j^B\rangle = (E_i + E_j)|\varphi_i^A; \varphi_j^B\rangle \ . \tag{8.9}$$

The leading order of the interaction is accounted for in the dipole-dipole interaction operator (cf. Eq. (8.6))

$$V_{dd}(\boldsymbol{r}_A, \boldsymbol{r}_B, \boldsymbol{R}_{AB}) = \frac{4\pi\epsilon_0}{e^2} \frac{1}{R_{AB}^3} (\boldsymbol{r}_A.\boldsymbol{r}_B - 3r_A^P r_B^P) \tag{8.10}$$

which can be represented in the above basis as

$$
\begin{aligned}
\frac{e^2 R_{AB}^3}{4\pi\epsilon_0} \langle i'j'|V_{dd}|ij\rangle &= \langle i'j'|\boldsymbol{r}_A.\boldsymbol{r}_B - 3r_A^P r_B^P|ij\rangle \\
&= \langle i'|\boldsymbol{r}|i\rangle.\langle j'|\boldsymbol{r}|j\rangle - 3\langle i'|r_A^P|i\rangle\langle j'|r_B^P|j\rangle \\
&= \boldsymbol{d}_{i'i}(\boldsymbol{R}_A).\boldsymbol{d}_{j'j}(\boldsymbol{R}_B) - 3d_{i'i}^P(\boldsymbol{R}_A, \boldsymbol{R}_{AB})d_{j'j}^P(\boldsymbol{R}_B, \boldsymbol{R}_{AB}) \ .
\end{aligned} \tag{8.11}
$$

Here we introduced the symbol $d_{ij}^P := \langle i|\boldsymbol{r}|j\rangle.\hat{\boldsymbol{R}}_{AB}$. For configurations close to the Z-axis, i. e. when $\hat{\boldsymbol{R}}_{AB} \approx (0,0,1)$, the last term can be approximately written involving the z-components of the electric dipole moments only, $d_{i'i}^P(\boldsymbol{R}_A, \boldsymbol{R}_{AB})d_{j'j}^P(\boldsymbol{R}_B, \boldsymbol{R}_{AB}) \approx d_{i'i,z}(\boldsymbol{R}_A)d_{j'j,z}(\boldsymbol{R}_B)$.

Considering two interacting Rydberg atoms with their valence electron in the uppermost electronic state, and assuming that the interaction does not induce transitions to other states, we only need to know $\boldsymbol{d}_{11}(\boldsymbol{R})$. In this case we treat the operator V_{dd} as a perturbation to the electronic Hamiltonians of the individual atoms as stated in the beginning of this section. In other words the dipole-dipole interaction energy between two atoms should be a lot smaller than the distance of adjacent single atom electronic surfaces,

$$E_{\mathrm{dd}}/\Delta E \ll 1 \ . \tag{8.12}$$

In order to show the dependencies of this ratio we consider the atoms to be on the Z-axis with a symmetric displacement, $Z_A = -Z_B =: Z$. It turns out in chapter 9 that the stable equilibrium for two atoms is reached for such a symmetrically displaced configuration (and intuition is proved correct). For a finite external electric field the relevant ratio (8.12) on the Z-axis is approximately

$$\frac{E_{\mathrm{dd}}(Z_A = -Z_B)}{\Delta E(0,0,Z)} \approx \frac{81}{16}(n-1)^2 n^4 \frac{F_x^2}{Z^3 (B + 2QZ^2)^3} \ , \tag{8.13}$$

where we discard finite size effects. We furthermore approximate $\Delta E(\boldsymbol{R}) \approx |\boldsymbol{B}(\boldsymbol{R})|/2$ and more specifically $\Delta E(0,0,Z) \approx (B + 2QZ^2)/2$ for $Q > 0$. The ratio (8.13) increases with increasing electric field strengths and with decreasing Ioffe field strengths. It does not depend on the magnetic field gradient G on the Z-axis, of course, and it always becomes small for large enough separations of the atoms. The single-atom-surfaces approximation thus only breaks down for the atoms coming very close to each other. The ratio (8.13) is shown in Fig. 9.6 in the next chapter for an exemplary parameter set accompanied by the overall two-atom potential.

In order to include the energetically neighboring electronic configurations $|ij\rangle$, $\boldsymbol{d}_{ij}(\boldsymbol{R})$ have to be computed. We discuss interaction-induced transitions to lower lying electronic surfaces in the following section.

8.3 Dipole-dipole interaction induced coupling to lower surfaces

In the preceding section we consider the interactions of two Rydberg atoms with their electrons in the energetically uppermost state which is constituted predominantly by the circular state $|\mathrm{circ}\rangle$ in the frame rotated into the local magnetic field direction. For $R_{AB} = \infty$ the two-atom electronic state can be written as a product of single atom electronic eigenstates $|\varphi_1^A; \varphi_1^B\rangle \equiv |11\rangle$, cf. Eq. (8.8). We have formulated an approximate requirement for the interaction strength (Eq. (8.13)) in order for this approach to be a good approximation also for finite atomic distances. This requirement is formulated for finite electric field and only considering the dipole-dipole interaction for atoms in the uppermost surface. Even for vanishing dipole-dipole interaction on the uppermost surface, however, the transition matrix elements of the dipole-dipole interaction matrix can be large. We now tackle this problem to find regimes where coupling to lower surfaces is negligible and to quantify the second order contributions to the interaction of the atoms.

For finite interaction between the atoms the two-atom basis states $|\varphi_i^A; \varphi_j^B\rangle \equiv |ij\rangle$ are no longer eigenstates of the system. The dipole-dipole interaction induces transitions from

$|\text{circ}; \text{circ}\rangle = |11\rangle$ to energetically lower lying two-atom states. On the one hand, admixtures of other states open new decay channels for the atoms and change the overall dipole-dipole potential that is experienced by the atoms. To prevent that, it has to be guaranteed that the off-diagonal dipole-dipole interaction matrix elements $\langle 11|V_{dd}|ij\rangle$ are a lot smaller than the energetic distance δ between the involved states. On the other hand these transition matrix elements are also responsible for the second order energy contributions to the long-range Rydberg-Rydberg interaction: The dipole-dipole interaction couples the state $|11\rangle$ to those two-atom states $|ij\rangle$ whose one-atom parts are dipole-connected to $|\varphi_1\rangle = |\text{circ}\rangle$, i.e. the quantum numbers of each electron have to meet the dipole selection rules $\Delta l = \pm 1$, $\Delta m = \pm 1, 0$ and $\Delta m_s = 0$. The dipole-dipole interaction is dominated by the energetically closest two-atom states of this type. If no external fields are present the states are degenerate in the orientational angular momentum quantum number m_l and for two-atom states with low angular momenta $l_{AB} = s, p, \ldots$ the closest connected two-atom states thus usually involve different principal quantum numbers n [103]. In case of an external magnetic field like in the Ioffe-Pritchard trap, the degeneracy in m is lifted. Keeping in mind that we deal with circular states, the energetically closest two-atom states that are connected to $|11\rangle$ are in the same n-manifold. The energy difference δ to these states is a lot smaller than the energy separation to dipole-connected states involving electronic states of different n-manifolds[2]. The involved matrix elements are of the same order of magnitude. We will therefore restrict our considerations to the energetically closest state in the same n-manifold.

In this two-state approximation the Hamiltonian describing the interaction is, cf. [103],

$$
\begin{pmatrix}
0 & \langle ij|V_{dd}|11\rangle \\
\langle 11|V_{dd}|ij\rangle & \delta
\end{pmatrix}
\tag{8.14}
$$

where δ is the energy difference $\delta = E(|\varphi_i\rangle) + E(|\varphi_j\rangle) - 2E(|\varphi_1\rangle) < 0$ and V_{dd} is the dipole-dipole operator (8.3) which is proportional to R_{AB}^{-3}. Solving for the so-called Förster energy eigenvalues Δ one finds

$$
\Delta_{|11\rangle} = \frac{\delta}{2} + \sqrt{\frac{\delta^2}{4} + \langle ij|V_{dd}|11\rangle\langle 11|V_{dd}|ij\rangle} \; .
\tag{8.15}
$$

The energetic correction $\Delta_{|11\rangle}$ to the two-atom electronic state $|11\rangle$ is zero for zero interaction, as expected (δ is negative). For large distances R_{AB} the energy shift is of classical van-der-Waals form

$$
\Delta_{|11\rangle} \approx \frac{|\langle 11|V_{dd}|ij\rangle|^2}{-\delta} \sim -\frac{1}{\delta R_{AB}^6} > 0 \; ,
\tag{8.16}
$$

---

[2]Due to the dipole selection rules $\Delta l = \pm 1$, $\Delta m_l = 0, \pm 1$, the circular state $|n, l, m_l\rangle = |n, n-1, n-1\rangle = |\text{circ}\rangle_n$ can only decay into the states $|n, n-2, n-2\rangle = |3\rangle$ and $|n-1, n-2, n-2\rangle = |\text{circ}\rangle_{n-1}$, the latter being the circular state in the adjacent n-manifold. The energetically closest dipole-connected state to $|\text{circ}\rangle_n \otimes |\text{circ}\rangle_n$ involving states from other n-manifolds is therefore $|\text{circ}\rangle_{n-1} \otimes |\text{circ}\rangle_{n+1}$ (bringing the second atom into a non-circular state in the (n+1)-manifold yields larger energetic distances). The energetic distance reads $\Delta E_{\text{inter}} = |2E(|\text{circ}\rangle_n) - (E(|\text{circ}\rangle_{n-1}) + E(|\text{circ}\rangle_{n+1}))| = 2/(n^2(n^2 + 1))$. It has to be compared with the energetic distance to the nearest dipole coupled state within the n-manifold which is $|33\rangle$ (see text), $\Delta E_{\text{intra}} = E(|11\rangle) - E(|33\rangle) \approx |\boldsymbol{B}|$. For ΔE_{inter} to be a lot larger than ΔE_{intra} the condition

$$
\Delta E_{\text{inter}} \gg \Delta E_{\text{intra}} \Leftrightarrow n^{-4} \gg |\boldsymbol{B}|/2
$$

must be satisfied. We already assumed this to be true in order to neglect inter-n-manifold couplings in Sec. 2.3. For $n = 30$ is explicitly reads $B \ll 2900$ Gauss, which is the case for any considered parameter set in this thesis.

Figure 8.2: Double-logarithmic diagram of the Förster energy $\Delta_{|11\rangle}$ from Eq. (8.15) for vanishing electric field on the Z-axis. The arrows indicate the cross-over distances R_c where the Förster energy transition happens from the resonant form ($\sim R_{AB}^{-3}$) to the van-der-Waals form ($\sim R_{AB}^{-6}$), see text. Parameters: $B = 10\,\mathrm{G}$ (solid lines), $B = 1\,\mathrm{G}$ (dashed lines), $Q = 0$, $F = 0$, $n = 30$.
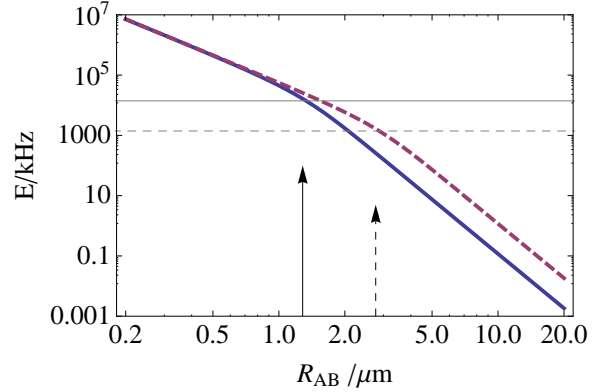
while for small R_{AB} the eigenvalue takes the resonant form

$$\Delta_{|11\rangle} \approx |\langle 11|V_{dd}|ij\rangle| \sim R_{AB}^{-3} \; . \tag{8.17}$$

To quantify what is meant by "large" and "small" a cross-over distance R_c can be defined via $\delta = |\langle 11|V_{dd}|ij\rangle|$, cf. Ref. [103]. In the cross-over region around R_c the interaction changes from the resonant to the van-der-Waals form.

For both concerns, quantifying the coupling to other surfaces and describing the Förster energy, we are thus interested in the absolute value of the matrix element $\langle 11|V_{dd}|ij\rangle$. Its explicit form reads

$$\langle 11|V_{dd}|ij\rangle = R_{AB}^{-3}\left(\boldsymbol{d}_{1i}(\boldsymbol{R}_A).\boldsymbol{d}_{1j}(\boldsymbol{R}_B) - 3d_{1i}^P(\boldsymbol{R}_A,\boldsymbol{R}_{AB})d_{1j}^P(\boldsymbol{R}_B,\boldsymbol{R}_{AB})\right) \; , \tag{8.18}$$

cf. Eq. (8.11). It involves the transition dipole matrix elements $\boldsymbol{d}_{1i} = \langle\varphi_1|\boldsymbol{r}|\varphi_i\rangle$, the only non-vanishing of which is

$$\boldsymbol{d}_{13}(\boldsymbol{R}) = x_{13}\mathcal{R}_{\alpha\beta}^{-1}\begin{pmatrix} 1 \\ -i \\ 0 \end{pmatrix} \; . \tag{8.19}$$

If we assume the atoms to be on the Z-axis, the rotation $\mathcal{R}_{\alpha\beta}$ is one, $\boldsymbol{d}_{13}$ does not depend on the position of the atom $\boldsymbol{R}$ and the projection of $\boldsymbol{d}_{13}$ onto $\boldsymbol{R}_{AB}$ vanish. On the Z-axis the only possibly finite transition matrix element in the dipole-dipole interaction therefore reads

$$\langle 11|V_{dd}|33\rangle = \frac{9}{4}\frac{n^2(n-1)}{R_{AB}^3} \; . \tag{8.20}$$

The resulting Förster energy eigenvalue $\Delta_{|11\rangle}$ (8.15) is plotted in Fig. 8.2 for the Ioffe field strengths $B = 10\,\mathrm{G}$ and $B = 1\,\mathrm{G}$. To quantify the coupling, this matrix element has to be compared with the energetic separation $\delta \approx |\boldsymbol{B}|$ of the surfaces. The coupling is small as long as

$$\langle 11|V_{dd}|33\rangle \ll \delta \quad \Leftrightarrow \quad R_{AB} \gg n\left(\frac{9}{4|\boldsymbol{B}|}\right)^{1/3} = R_c \; . \tag{8.21}$$

For the parameters $B = 10\,\mathrm{G}$ and $n = 30$ this yields $R_{AB} \gg 1.3\,\mu\mathrm{m}$, which is indicated by the arrow in Fig. 8.2.

9 Interaction-induced stabilization of two Rydberg atoms

We now understand how the large size of Rydberg atoms change their coupling to the inhomogeneous magnetic field (Ch. 4). We already know that the dipole moments induced by an external electric field can prevent them from ionizing each other (Ch. 5) and we also have analytical expressions for these dipole moments at hand (Ch. 7). We know the influence of the longitudinal confinement on the electronic adiabatic energy surfaces (Ch. 6) and we additionally understand the interaction between the Rydberg atoms (Ch. 8). Combining all these insights enables us to study two interacting Rydberg atoms confined in a Ioffe-Pritchard trap. If we model this interaction with the dipole-dipole interaction (8.10), which is the leading order in the expansion of the Coulomb interaction (8.1), the Schrödinger equation for the two-atom center of mass wave function, cf. Eq. (2.29), for this situation reads

$$(T_A + T_B + V_A(\boldsymbol{R}_A) + V_B(\boldsymbol{R}_B) + V_{dd}(\boldsymbol{R}_A, \boldsymbol{R}_B))|\Psi_{AB}\rangle = E|\Psi_{AB}\rangle \ . \qquad (9.1)$$

The one atom potential for the atoms A and B, $V_A = V_B$, can be approximated for high-Ioffe-configurations by the analytically diagonalized term (6.28). The interaction potential V_{dd}, Eq. (8.11), is formulated using the electric dipole moments of the individual atoms computed in the single-atom electronic adiabatic states. They depend on the positions of the atoms in the field and V_{dd} therefore does not only depend on the distance of the atoms and the relative orientation of their moments but on the absolute position of both atoms in the field. As long as V_{dd} is only a perturbation in (9.1) the electronic wave function of the two-atom system can be written to a good approximation as the product of the single-atom electronic states. The energetically uppermost electronic state of the system is then a product of the circular states of the atoms, each rotated into the local magnetic field direction. For the description of the dipole-dipole interaction between the atoms in this state it then suffices to know the electric dipole moment $\boldsymbol{d}$ calculated by perturbing the circular state in Chapter 7.

We begin this chapter with exploiting the potential of the Ioffe-Pritchard trap to reduce the dimensionality of the system. Due to the strong confinement in transversal direction we can restrict our considerations in a first step to the Z-axis in Section 9.1. In this simplified geometry we analytically find a stable configuration of the atoms in which their distance is easily tuneable without affecting neither stability nor trap frequencies. In Section 9.2 we extend our considerations into three dimensions and dwell on the question of stability. The last section is dedicated to experimental implementations suggesting different ways of realizing the system.

9.1 One-dimensional stable configuration

We have shown in chapter 4.3 that a Ioffe-Pritchard trap can provide an extremely strong confinement for Rydberg atoms in the transversal direction. We now want to take advantage of this peculiarity in order to restrict the study of the total potential $V_{tot}(\boldsymbol{R}_A, \boldsymbol{R}_B) = V_A(\boldsymbol{R}_A) + V_B(\boldsymbol{R}_B) + V_{dd}(\boldsymbol{R}_A, \boldsymbol{R}_B)$ to the Z-axis. In Section 9.2.2 we investigate the requirements on the magnetic field parameters to guarantee that this simplification is permitted. There we find that for large enough gradients G this is always the case since they entail strong transversal confinement. To simplify the situation even further we impose an external electric field pointing in the X-direction that keeps the atoms away from each other and prevents autoionization. This has led to the one-dimensional Rydberg gas in Chapter 5.

In particular we proceed as follows. In Section 9.1.1 we first consider a simplified expression for the total potential in which the one-atom potential is approximated by the analytically diagonalized term (6.28) and the electric dipole moment $\boldsymbol{d}$ is approximated by the contribution induced by the electric field, $\boldsymbol{d}_F$. We find an equilibrium position for the two atoms with an inter-atomic distance that is tuneable by the electric field strength. The analysis of small oscillations of the atoms around this equilibrium position yields analytical expressions for the trap frequencies that exhibit no dependency on the electric field strength and are hence independent from the distance of the atoms. In Section 9.1.2 we find the range of parameters where the applied approach is a good approximation. Finally in Section 9.1.3 we investigate the importance of higher order multipole interactions of the Rydberg atoms.

9.1.1 Small oscillations of generalized coordinates

In order to study the one-dimensional configuration we set the coordinates X and Y to zero and assume Q to be non-zero and positive[1] which generates the confining potential in the Z-direction. Please note that in this case $r_i^P \equiv \boldsymbol{r}_i.\hat{\boldsymbol{R}}_{AB} = z_i$ in Eq. (8.6), since the atomic separation vector coincides with the Z-axis and Eq. (8.7) is an exact equation. We insert the electric dipole moment of the single-atom eigenstate belonging to the uppermost potential energy surface, that has been computed in Chapter 7, into the dipole-dipole interaction, Eq. (8.11). Additionally inserting the trapping potential Eq. (6.30), naming the atoms so that $Z_A > Z_B$, and omitting the constant potential offset $2nB$, the two-atom potential represented in the single-atom electronic eigenfunctions reads[2]

$$V_{\text{tot,circ}}(Z_A, Z_B) := \langle \text{circ,circ} | V_{\text{tot}}(Z_A, Z_B) | \text{circ,circ} \rangle$$

$$= 2nQ(Z_A^2 + Z_B^2) + \frac{81 F_x^2 n^4 (n-1)^2}{4(B + 2QZ_A^2)(|Z_A - Z_B|)^3 (B + 2QZ_B^2)} \qquad (9.2)$$

With the approximation $B + 2QZ_{A,B}^2 \approx B$ that holds as long as

$$|Z_{A,B}| \ll \sqrt{B/(2Q)} \; , \qquad (9.3)$$

---

[1] We assume Q to be non-negative throughout this work except when stated otherwise.

[2] The electric constant $1/(4\pi\epsilon_0)$ and the electron charge e are both fundamental atomic units. We kept the expression $4\pi\epsilon_0/e^2$ in the last sections in order to avoid dimensional ambiguity. To simplify matters we now discard it.

the two-atom potential can be simplified to

$$V_{\text{tot,circ}}(Z_A, Z_B) \approx 2nQ(Z_A^2 + Z_B^2) + \frac{81}{4}n^4(n-1)^2\frac{F_x^2}{B^2}\frac{1}{(Z_A - Z_B)^3} . \tag{9.4}$$

The third term in (9.4) is the approximate version of the dipole-dipole interaction operator. It only depends on the distance of the atoms. Higher order terms originate in the quadratic Z-dependence of the interacting electric dipole moments. They become significant only for very large Z or exceptionally strong parameters Q reachable on atoms chips. It is reasonable to introduce generalized coordinates for the distance of the atoms and for their center of mass, $Z_D > 0$ and Z_S, respectively:

$$Z_D = Z_A - Z_B , \qquad\qquad Z_A = Z_S + Z_D/2 , \tag{9.5}$$
$$Z_S = (Z_A + Z_B)/2 , \qquad\qquad Z_B = Z_S - Z_D/2 . \tag{9.6}$$

With this new set of coordinates the condition (9.3) translates to

$$|Z_S| + Z_D/2 \ll \sqrt{B/(2Q)} . \tag{9.7}$$

If this condition holds, the total potential (9.2) reads

$$V_{\text{tot,circ}}(Z_D, Z_S) \approx \frac{81}{4}n^4(n-1)^2\frac{F_x^2}{B^2}Z_D^{-3} + nQ\left(Z_D^2 + 4Z_S^2\right) \tag{9.8}$$

The coordinate for the center of mass of both atoms, Z_S, appears as a quadratic shift $4nQZ_S^2$. An equilibrium configuration of the atoms is therefore bound to be symmetric around the origin, i.e. $Z_S = 0$. Minimizing the energy of the two-atom potential within this approximation we find the equilibrium position at

$$Z_{S,\text{min}} = 0 , \qquad\qquad Z_{D,\text{min}} = 3\sqrt[5]{\frac{F_x^2(n-1)^2n^3}{8B^2Q}} \approx \frac{3}{2^{3/5}}n\sqrt[5]{\frac{F_x^2}{B^2Q}} . \tag{9.9}$$

As can be seen from (9.9), the expression for the equilibrium distance $Z_{D,\text{min}}$ can be readily controlled by the electric field F_x when the Ioffe field is not varied at the same time. The condition of validity of our approximation (9.7) at the equilibrium position (9.9) reads

$$c_D := \frac{3}{2}\sqrt[5]{F_x^2(n-1)^2n^3}\sqrt[10]{\frac{Q^3}{2B^9}} \approx \frac{3n}{2}\sqrt[10]{\frac{F_x^4Q^3}{2B^9}} \ll 1 . \tag{9.10}$$

See Tab. 9.1 for explicit values.

Since we are interested in the motion of the system around a configuration of stable equilibrium, all functions can be expanded in Taylor series about that equilibrium. The expansion of the potential V around the equilibrium position lacks a linear term. This is because the generalized forces acting on the system, $\partial V/\partial Z_i$, vanish at equilibrium per definition. The constant offset term, i.e. the potential energy at equilibrium, can be made to disappear by adding an offset to the potential. The expressions' leading order reads [104]

$$V = \frac{1}{2}\sum_{i,j}\frac{\partial^2 V}{\partial Z_i \partial Z_j}\bigg|_{Z_i=0} Z_i Z_j =: \frac{1}{2}\sum_{i,j}V_{ij}Z_iZ_j . \tag{9.11}$$

Table 9.1: Explicit values for the condition $|Z_{A,B}| \ll \sqrt{B/(2Q)}$ at the approximate equilibrium position on the Z-axis, i.e. $Z_{D,\min}/2 \ll \sqrt{B/(2Q)} \Leftrightarrow c_D \ll 1$. The values are computed for the geometry parameter $\tilde{Q} = 6 \cdot 10^{-16}$ which is around the highest values reachable with macroscopic Ioffe-Pritchard traps [99]. The restriction $c_D \ll 1$ is broken only for very low Ioffe fields (given in Gauss) paired with relatively high electric fields (given in atomic units; 10^{-10} a.u. of el. charge$\approx$ 0.5 V/cm).

c_D	$F = 10^{-12}$ a.u.	$F = 10^{-11}$ a.u.	$F = 10^{-10}$ a.u.	$F = 10^{-9}$ a.u.
$B = 0.1$ G	0.0297	0.0747	0.1877	0.4714
$B = 1$ G	0.0075	0.0188	0.0471	0.1184
$B = 10$ G	0.0019	0.0047	0.0118	0.0297
$B = 100$ G	0.0005	0.0012	0.0030	0.0075

Similarly, the kinetic energy can be written approximately as a quadratic function of the velocities in the system,

$$T = \frac{m}{2}(\dot{Z}_A^2 + \dot{Z}_B^2) = \frac{m}{2}(\frac{1}{2}\dot{Z}_D^2 + 2\dot{Z}_S^2) =: \frac{1}{2}\sum_{i,j} T_{ij}\dot{Z}_i\dot{Z}_j \; , \tag{9.12}$$

where m here is the sum of the masses of both atoms. The Lagrangian is then given by $L = \frac{1}{2}(\dot{\boldsymbol{Z}}^T\mathcal{T}\boldsymbol{Z} - \dot{\boldsymbol{Z}}^T\mathcal{V}\boldsymbol{Z})$. Taking into account the symmetry of $\mathcal{T} = (T_{ij})$ and $\mathcal{V} = (V_{ij})$ the Euler-Lagrange equations yield the wave equation

$$\mathcal{T}\ddot{\boldsymbol{Z}} + \mathcal{V}\boldsymbol{Z} = 0 \; , \tag{9.13}$$

where $\boldsymbol{Z} = (Z_i)$. Provided that the above approximations hold, Eq. (9.3), we find

$$\mathcal{V} = 2nQ\begin{pmatrix} 5 & 0 \\ 0 & 4 \end{pmatrix} \quad \text{and} \quad \mathcal{T} = \begin{pmatrix} m/2 & 0 \\ 0 & 2m \end{pmatrix} \tag{9.14}$$

for the matrices of coefficients.

In order to solve the set of simultaneous linear differential equations (9.13) we use the oscillatory ansatz $Z_i = Ca_i e^{-i\omega t}$. Substituted into Eq. (9.13) it yields the generalized eigenvalue equation for the amplitudes $\boldsymbol{a} = (a_i)$,

$$\mathcal{V}\boldsymbol{a} = \omega^2\mathcal{T}\boldsymbol{a} \; . \tag{9.15}$$

The equations are already decoupled due to the approximation (9.3) and due to the appropriate choice of generalized coordinates. The frequencies read

$$\omega_D^2 = \frac{20nQ}{m}, \quad \omega_S^2 = \frac{4nQ}{m}, \tag{9.16}$$

and they belong to the eigenvalues $\boldsymbol{a}^{(D)} = \{\sqrt{2}, 0\}$ and $\boldsymbol{a}^{(S)} = \{0, \sqrt{2}\}$, respectively. It is most remarkable that within the approximation (9.3) *the eigenfrequencies are independent of the electric field strength F_x.* They indirectly depend on the Ioffe field strength since $Q = B\tilde{Q}$, where $\tilde{Q}$ is the parameter quantifying the geometry of the trap.

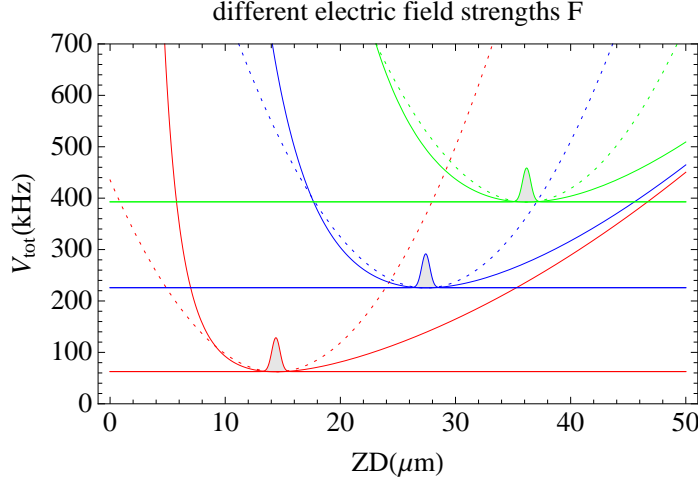The procedure does not yield such a nice analytic form if the condition (9.3) does not hold.

different electric field strengths F

Figure 9.1: Two-atom potential energy, Eq. (9.2) (continuous line), the harmonic approximation (dotted line) and the 1D ground state (not to scale) along Z_D for $Z_S = 0$ for different electric field strengths F. The trap frequency does not change when F is altered. Parameters: $B = 10\,\text{G}$, $Q = B \cdot 6 \cdot 10^{-16}$. $F = 1 \cdot 10^{-11}$ (red), $F = 5 \cdot 10^{-11}$ (blue), $F = 1 \cdot 10^{-10}$ (green), from smaller to larger equilibrium separations $Z_{D,\text{min}}$ of the atoms.

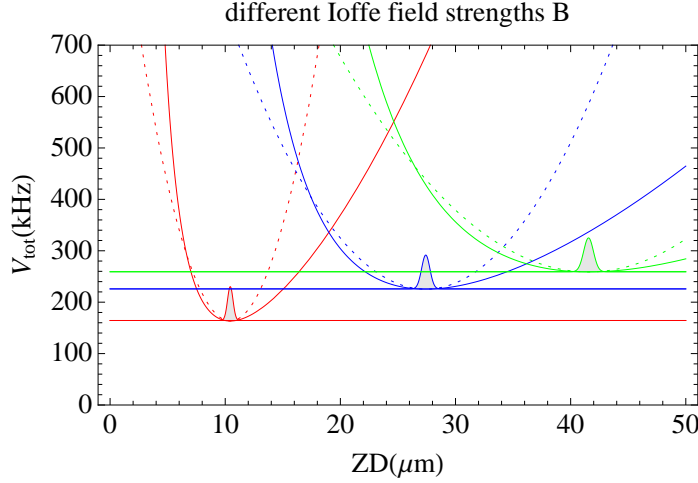### different Ioffe field strengths B

Figure 9.2: For different magnetic Ioffe field strengths B the trap frequencies are different. Shown are again the two-atom potential energy (continuous line), the harmonic approximation (dotted line) and the 1D ground state (not to scale) along Z_D for $Z_S = 0$. Parameters: $F = 5 \cdot 10^{-11}$, $Q = B \cdot 6 \cdot 10^{-16}$. $B = 50\,\text{G}$ (red), $B = 10\,\text{G}$ (blue), $B = 5\,\text{G}$ (green) from smaller to larger equilibrium separations $Z_{D,\text{min}}$ of the atoms.
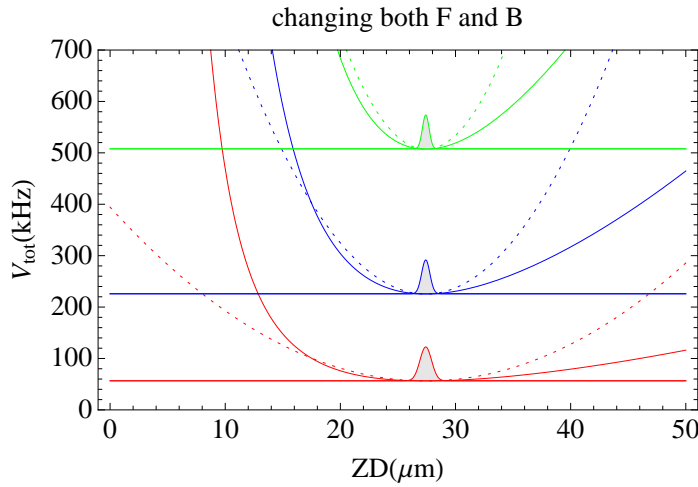
changing both F and B

Figure 9.3: The minimum position $Z_{D,\text{min}} \sim \sqrt[5]{F_x^2/(B^2 Q)}$ from Eq. (9.9) does not change as long as the electric field F and the bias field B are varied by a factor f^3 and by a factor f^2, respectively. $f = 0.5$ (red curve, lowest energy), $f = 1$ (blue curve, the same parameters as the blue curves in Figs. 9.1 and 9.2: $B = 10\,\text{G}$, $F = 5 \cdot 10^{-11}$, $Q = B \cdot 6 \cdot 10^{-16}$), $f = 1.5$ (green curve).

9.1.2 Tuning the distance of the atoms

In the last section we have found that the equilibrium distance $Z_{D,\text{min}}$ of the atoms, Eq. (9.9), can be increased without changing the trap frequency by just increasing the electric field strength F. This is depicted in Fig. 9.1 where the potential and its harmonic expansion around the equilibrium position are drawn for different electric field strengths. In order visualize the dependence of the distance on the electric field strength the scale of the plot is very large, both in V and in Z_D. The harmonic approximation of the potential around the minimum therefore seems to be very poor. This is not the case, however, as can be seen from a zoomed view around one of the minima in Fig. 9.5.

Lowering the bias field B also increases the distance of the atoms. This, however, affects the trap frequencies in all directions. Fig. 9.2 shows increasing trap frequencies in z for increasing atomic equilibrium distances. The trap frequency can, of course, also be changed leaving the equilibrium distance the same. The electric field strength and Ioffe field strength just have to be changed without altering the ratio F_x^2/B^3 which occurs in the expression for $Z_{D,\text{min}}$ in Eq. (9.9). This is exemplified with realistic parameters in Fig. 9.3.

In order for the just described mechanisms to be meaningful, two requirements have to be met. First, the quality of the approximation (9.3) has to be guaranteed that has led to the electric field independent expressions for the trap frequencies, Eq. (9.16). The requirement in question can be reduced to $1 \gg c_D \sim \sqrt[5]{F^2/B^3}$, Eq. (9.10), by inserting the approximate equilibrium position (9.9). Explicit numbers for different parameter pairs $\{B, F\}$ can be extracted from Table 9.1: For a Ioffe field of 10 Gauss the approximation becomes poor for electric field strengths larger than $\sim 10^{-9}$. For a Ioffe field of 10 Gauss this does not happen until $F \sim 10^{-8}$. The direct impact on the trap frequency ω_D can be seen in Figure 9.4 where we show the relative error of $\omega_{D,\text{approx}}$ from Eq. (9.16) with respect to the trap frequency at equilibrium that has been computed without assuming the approximation (9.10) to be valid. In the latter case no analytically closed form for the equilibrium position can be found. We therefore evaluate the trap frequency numerically assuming $Z_S = 0$. The figure shows that for a Ioffe field of 1 Gauss the relative error exceeds 10^{-3} for electric field strengths lager than $F = 4.5 \cdot 10^{10}$ a.u. ≈ 2.3 V/cm.

Second, it has to be assured that describing the potential as being harmonic is a good approximation at least in a region around the local minimum that is larger than the extension of the center of mass ground state. If this is the case the statement that the trap frequency stays the same while the distance of the atoms is changed implies that also the center of mass ground state for the different distances is the same. In Fig. 9.5 the two-atom potential is plotted accompanied by its harmonic approximation around the equilibrium position and by the center of mass ground state. The figure shows that we can safely assume the center of mass ground state to be a Gaussian with the corresponding trap frequency ω_D. With the parameter set in the left plot in Fig. 9.5 ($B = 1$ G) for instance the difference of the potential and its approximation is hardly visible in the depicted region. The plot on the right in the same figure furthermore shows expansion coefficients of the potential around the equilibrium position (also computed without using the approximation). It is evident from the plot that the description of the potential as a parabola around the equilibrium position is a good approximation for small Ioffe field strengths.

We have to keep in mind that we assume the dipole-dipole interaction not to induce couplings to lower electronic adiabatic energy surfaces. This is a good approximation as
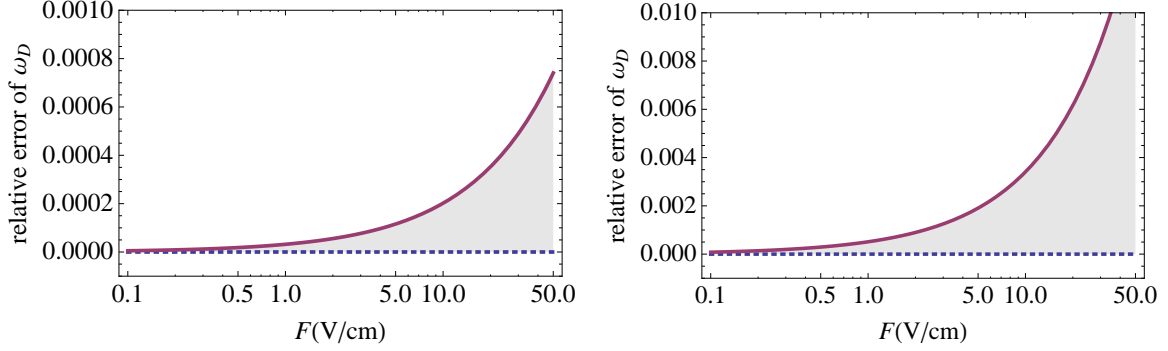
Figure 9.4: Relative error of the analytically computed approximate trap frequency $\omega_{D,\text{approx}}$ which does not depend on the electric field strength (solid line, Eq. (9.16)) with respect to the trap frequency computed without using the approximation (9.10). In spite of a nearly linear behavior of the relative error, a logarithmic scale is chosen in order to stretch the regime of relatively low electric field strengths we are primarily interested in ($F = 10^{10}$ a.u. ≈ 0.5 V/cm). Parameters: $Q = B \cdot 6 \cdot 10^{-16}$, $n = 30$, and $B = 10$ G $\rightarrow \omega_{D,\text{approx}} = 16.8$ kHz (left plot), $B = 1$ G $\rightarrow \omega_{D,\text{approx}} = 5.32$ kHz (right plot).
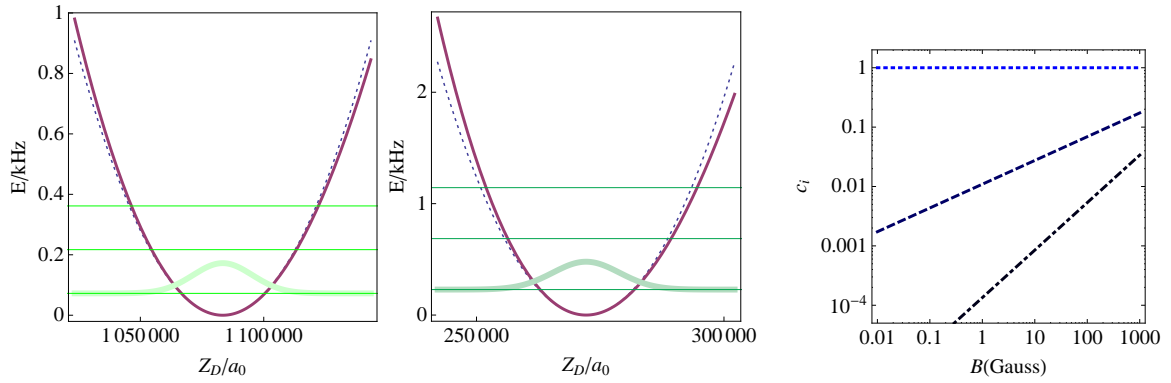

Figure 9.5: Quality of the harmonic approximation. The *left* and the *middle* plot depict the harmonic approximation (dotted line) of the two-atom potential $V_{\text{tot,circ}}$ (solid line) in a region around the local minimum comparable to the extension of the approximate center of mass ground state (thick Gaussian) for different Ioffe field strengths. The double-logarithmic plot on the *right* shows the quadratic (dotted), cubic (dashed) and the quartic (dot-dashed) coefficient of the expansion of the potential around the equilibrium position against the Ioffe field strength. It implies that approximating the potential by a parabola is a good approach for Ioffe field strengths up to 10 Gauss. Parameters: $B = 1$ G (left plot), $B = 10$ G (middle plot), $F = 10^{-11}$ a.u., $Q = B \cdot 6 \cdot 10^{-16}$, $n = 30$.

Figure 9.6: Ratio of dipole-dipole interaction energy and approximate energetic distance of the two uppermost electronic adiabatic surfaces, $E_{\mathrm{dd}}/\Delta E$, (blue line) accompanied by the two-atom potential (with subtracted offset, red line) with its minimum indicated with a vertical line. Parameters: $B = 10\,\mathrm{G}$, $Q = B \cdot 6 \cdot 10^{-16}$, $F = 1 \cdot 10^{-11}$, $n = 30$.
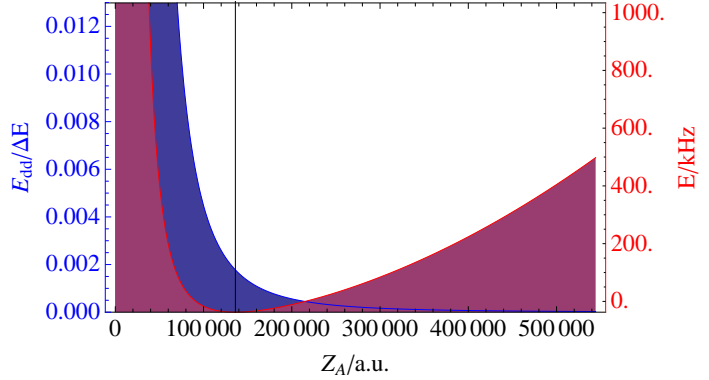
Table 9.2: As long as $c_{\mathrm{OSA}} \ll 1$ the dipole-dipole interaction energy of the two atoms in their equilibrium position is much smaller than the energetic distance of the electronic adiabatic surfaces of a single atom. There the single-atom-eigenstates approximation dealt with in Section 8.2 can be applied. Parameters: $n = 30$, $Q = B \cdot 6 \cdot 10^{-16}$ (maximum $\tilde{Q}$ for a macroscopic Ioffe-Pritchard trap [99]).

c_{OSA}	$F = 10^{-12}$ a.u.	$F = 10^{-11}$ a.u.	$F = 10^{-10}$ a.u.	$F = 10^{-9}$ a.u.
$B = 0.1\,\mathrm{G}$	1	7	46	289
$B = 1\,\mathrm{G}$	0.02	0.1	0.7	5
$B = 10\,\mathrm{G}$	0.0003	0.002	0.01	0.07
$B = 100\,\mathrm{G}$	0.000005	0.00003	0.0002	0.001

long as the dipole-dipole interaction operator V_{dd} can be treated as a perturbation to the electronic Hamiltonians of the individual atoms. This has been discussed in Section 8.2 already and it has been quantified into the restriction $E_{\mathrm{dd}}/\Delta E \ll 1$, cf. Eq. (8.13) and (8.12). This ratio is shown in Fig. 9.6 accompanied by the overall two-atom potential (9.2) for an exemplary parameter set.

The restriction (8.12) must hold in particular for the equilibrium configuration of the atoms in order for the latter to be stable. Approximating $B \gg 2QZ^2$ and inserting the approximate equilibrium position $\{Z_{S,\mathrm{min}}, Z_{D,\mathrm{min}}\}$ (analytically computed also using $B \gg 2QZ^2$, Eq. (9.9)), we find

$$c_{\mathrm{OSA}} = 3 \cdot 2^{4/5} n^3 \frac{F_x^{4/5} Q^{3/5}}{B^{9/5}} = 3 \cdot 2^{4/5} n^3 \frac{F_x^{4/5} \tilde{Q}^{3/5}}{B^{6/5}} \ll 1 \; . \tag{9.17}$$

The number c_{OSA} is tabulated for a range of parameters in Tab. 9.2. It shows that for $B = 10\,\mathrm{G}$ the condition (9.17) is still satisfied for $F = 10^{-9}$ a.u..

9.1.3 Quadrupole-quadrupole repulsion

Ever since the beginning of the chapter we did not account for terms of higher order than the dipole-dipole term in the expansion of the Coulomb interaction between the two atoms, Eq. (8.1). We now study the influence of higher order multipole interactions and answer the question in which situations can they change the behavior of the system as predicted by the simplified model Hamiltonian in Eq. (9.1).

We do this on the Z-axis for vanishing and for finite electric field. We also add estimates for the strengths of interaction terms when the atoms do not arrange on the Z-axis.

Vanishing electric field on the Z-axis

Isolated atoms in pure quantum states cannot have a permanent dipole moment [105]. This is due to the definite parity of their electronic states. As presented in Chapter 7.1 Rydberg atoms in a Ioffe-Pritchard trap feature a permanent electric dipole moment even for vanishing electric field. It originates from the finite size term $\mathcal{H}_\gamma$ in (6.22) that admixes quantum states to the circular state that have different parity and it is therefore suppressed by the perturbation parameter λ. On the Z-axis, however, the finite size term only admixes the states $|\varphi_5\rangle = |n-2, n-3, 1/2\rangle$ and $|\varphi_{13}\rangle = |n, n-2, n-2, -1/2\rangle$, see Eq. (7.28), which results in no electric dipole moment due to the dipole selection rules ($\Delta m = \pm 1, 0$, $\Delta m_s = 0$).

We can conclude that Rydberg atoms on the Z-axis of a Ioffe-Pritchard trap do not exhibit a permanent electric dipole moment when no electric field is present and are therefore neither subject to dipole-dipole interaction nor to dipole-quadrupole interaction.

However, Rydberg atoms in circular states feature a quadrupole moment since the circular electronic wave function is not spherically symmetric. As already the non-perturbed state has a quadrupole moment, it is not suppressed by a perturbation parameter as opposed to the dipole moments (only the corrections to the quadrupole moment due to the admixture of states with different parity is suppressed by λ). The leading order of the expansion in case of vanishing electric field on the Z-axis is hence the repulsive quadrupole-quadrupole interaction. For the special configuration it can be calculated using the simplified expression [106]

$$V_{qq} = \frac{3}{4Z_D^5} \{r_A^2 r_B^2 - 5(z_A^2 r_B^2 + r_A^2 z_B^2) - 15z_A^2 z_B^2 + 2(x_A x_B + y_A y_B - 4z_A z_B)^2\} \ . \quad (9.18)$$

With the matrix elements

$$\langle \text{circ}|r^2|\text{circ}\rangle = \frac{1}{4}n^2(n+1)(n+\frac{1}{2})$$
$$\langle \text{circ}|x^2|\text{circ}\rangle = \langle \text{circ}|y^2|\text{circ}\rangle = \frac{1}{2}n^3(n+1)$$
$$\langle \text{circ}|z^2|\text{circ}\rangle = \frac{1}{2}n^2(n+1) \quad (9.19)$$

we find

$$V_{qq} = \frac{1}{Z_D^5}\frac{3}{2}n^4(n+1)^2(n+\frac{1}{2})^2 \approx \frac{1}{Z_D^5}\frac{3}{2}n^8 \ . \quad (9.20)$$

For low enough center of mass kinetic energy the repulsion of the atoms due to the quadrupole-quadrupole interaction could in principle stabilize Rydberg atoms on the Z-axis against auto-ionization. In combination with the confinement in the Z-direction it could even permit a structured one-dimensional configuration similar to the atom chain in the magneto-electric trap discussed in Chapter 5.3. We must not forget, however, that the van-der-Waals interaction as a second order contribution to the multipole interaction can be large and attractive even though it is suppressed by an additional factor Z_D^{-1} compared to V_{qq}.
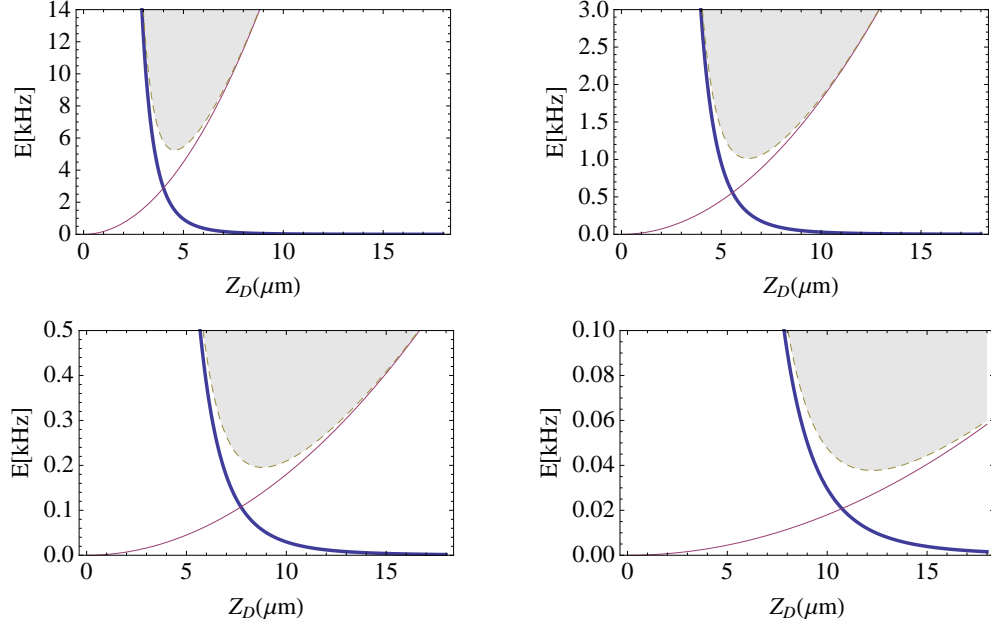
Figure 9.7: Quadrupole-quadrupole interaction energy of two Rydberg atoms on the Z-axis of a Ioffe-Pritchard trap for vanishing electric field strength against their distance Z_D (Eq. (9.18), thick line) accompanied by the longitudinal confinement due to the Ioffe-Pritchard configuration (see text, thin line). The sum of both is depicted as a dashed line and the corresponding trap frequencies are 19.9 kHz, 6.3 kHz, 2.0 kHz and 0.6 kHz (from top left to bottom right). Parameters: Different Ioffe field strengths $B = 10$ G (left column of plots), $B = 1$ G (right column), and different longitudinal confinement parameters $Q = B \cdot 6 \cdot 10^{-16}$ (upper row of plots), $Q = B \cdot 6 \cdot 10^{-18}$ (lower row), $n = 30$.

In Fig. 9.7 V_{qq} is plotted accompanied by the confining potential for different parameter sets. The confining potential for both atoms reads for symmetric displacement on the Z-axis

$$n\left(|\boldsymbol{B}(0,0,Z)| + |\boldsymbol{B}(0,0,-Z)|\right) = nQZ_D^2 \ , \tag{9.21}$$

cf. Eq.(6.28). The sum of confinement and quadrupole-quadrupole interaction (dashed grey lines in Fig. 9.7) has its minimum at $Z_{D,qq}$ with a trap frequency ω_{qq} there. For large n they read

$$Z_{D,qq} = n\left(\frac{15}{4Q}\right)^{1/7} \ , \quad \omega_{qq}^2 = 28nQ/M_{AB} \ , \tag{9.22}$$

where M_{AB} is the mass of both atoms. The trap frequencies that correspond to the parameters in Fig. 9.7 (from top left to bottom right) are 19.9 kHz, 6.3 kHz, 2.0 kHz and 0.6 kHz.

Finite electric field on the Z-axis

The situation changes completely when an electric field is applied. The induced dipole moments scale linearly with the field strength and the dipole-dipole interaction hence depends quadratically on F. Its magnitude can be estimated from the first term in Eq. (9.8) to be

$$V_{dd,Z\text{-axis}} \approx \frac{1}{Z_D^3}\left(\frac{9}{2}n^3\frac{F}{B}\right)^2 \tag{9.23}$$

The dipole-quadrupole interaction happens to be zero on the Z-axis even for finite electric field strength. This can be seen from Eq. (8.6) if one additionally bears in mind that the electric dipole moment of atoms on the Z-axis is perpendicular to it and all projections $\overset{P}{r}_i := \boldsymbol{r}_i . \hat{\boldsymbol{R}}_{AB}$ therefore vanish in the uppermost surface.

The atoms have an electric quadrupole moment even for zero electric field. The quadrupole-quadrupole interaction is thus a first order effect. The contributions to the quadrupole moment that come from an additional electric field (or from the finite size term $\mathcal{H}_\gamma$ in Eq. (6.22)) are of second order and do not significantly alter the quadrupole-quadrupole interaction for moderate field strengths. For an estimate of its magnitude it thus suffices to take the field-free expression (9.18). In order for the dipole-dipole interaction, $|V_{dd}| \sim |\boldsymbol{d}|^2/Z_D^3$, to dominate the quadrupole-quadrupole interaction, $|V_{qq}| \sim \frac{3}{2}n^8/Z_D^5$, the following condition must be fulfilled,

$$\left| \frac{V_{dd}}{V_{qq}} \right| = \frac{27}{2} \left(\frac{Z_D F}{nB} \right)^2 \gg 1 \Leftrightarrow Z_D \gg \frac{1}{3}\sqrt{\frac{2}{3}}n\frac{B}{F} \; . \tag{9.24}$$

For a Ioffe field strength $B = 10\,\mathrm{G}$ and an electric field strength as low as $F = 10^{-12}$ a.u. (and $n = 30$) this reads $Z_D \gg 35000$ a.u.$= 1.7\,\mu\mathrm{m}$. Increasing the electric field strength to $F = 2 \cdot 10^{-11}$ already yields $Z_D \gg 1700$ a.u.$= 90$ nm. We never consider such small atomic distances since the electronic wave functions would overlap when the atoms come this close to each other. For the examples above it is therefore legitimate to neglect the quadrupole-quadrupole interaction, as is done in the Hamiltonian (9.1) from the beginning of this chapter. Around the equilibrium configuration $Z_{D,\mathrm{min}}$ of the atoms, Eq. (9.9), the condition (9.24) is even easier to fulfill.

Finite electric field, three-dimensional case

To complete our considerations we estimate the magnitudes of the different multipole interactions for finite electric field when the atoms do not arrange on the Z-axis. The most simple approach is to compare the maximal possible value for a given distance of the atoms. This distance must then just be large enough in order for $|V_{dq}|_{\mathrm{max}} \sim r^2|\boldsymbol{d}|/R_{AB}^4$ to be dominated by $|V_{dd}|_{\mathrm{max}} \sim |\boldsymbol{d}|^2/R_{AB}^3$. Inserting the expression for the dipole moment from Chapter 7, $|\boldsymbol{d}_F| \approx \frac{9}{2}\frac{F}{B}n^3$, and also $r^2 \approx n^4/4$, the condition reduces to

$$\frac{|V_{dd}|_{\mathrm{max}}}{|V_{dq}|_{\mathrm{max}}} \gg 1 \Leftrightarrow R \gg \frac{n^4}{4|\boldsymbol{d}|} \approx \frac{n}{18}\frac{B}{F} \; . \tag{9.25}$$

For the parameters $B = 10\,\mathrm{G}$, $F = 10^{-12}$ a.u. and $n = 30$ this reads $R \gg 7090$ a.u.$= 0.35\,\mu\mathrm{m}$ (the extension of the electronic cloud of a circular Rydberg atom for $n = 30$ is around a thousand Bohr radii and the distance of two such atoms must in any case be a lot larger so that they do not ionize each other). If the electric dipole moment of at least one of the atoms vanishes, not only V_{dd} but also V_{dq} vanishes, too. The only situation in which V_{dq} can be the leading order of the interaction is thus when V_{dd} vanishes due to the relative arrangement of the finite electric dipole moments to each other. This happens when the V_{dd} changes character from a repulsive to an attractive interaction which can lead to instable configurations of two atoms in the trap even for a finite electric field in transversal direction. The stability of atomic configurations and their collapse is discussed in the next section.

9.2 Three-dimensional stable configuration and collapse

For a finite longitudinal confinement and a finite electric field there is a local minimum in the two-atom potential for a configuration where both atoms are located symmetrically on the longitudinal axis as long as the transversal confinement is sufficiently strong. Very strong translational confinement leads to the one-dimensional situation discussed in the preceding Chapter 9.1. Since the magnetic field gradient G only influences the transversal but not the longitudinal confinement the trap frequencies in the transversal and the longitudinal direction can be altered independently. If the transversal confinement is decreased and/or if the longitudinal confinement is increased the local minimum of the potential mentioned above turns into a saddle point: The tendency of the dipole-dipole interaction to force the atoms to step out of the Z-axis wins against the confining nature of the transversal magnetic field gradient. The atoms then attract each other and most probably eventually ionize.

In order to substantiate and refine the statements formulated above we proceed as follows. In Section 9.2.1 we first demonstrate that potential minima occur only at displacements of the atoms that are approximately symmetric in Z, i.e. $Z_S \approx 0$. We then generalize the findings from the one-dimensional treatment in Sec. 9.1 to three dimensions while keeping a strong transversal confinement and we analyze a characteristic example. In Section 9.2.2 we then investigate for which parameters the stability of the equilibrium configuration is lost, the responsible mechanisms for that loss and the way the collapse takes place.

9.2.1 Longitudinal symmetry and stable configuration

We first examine the longitudinal symmetry of the two-atom potential. We find that when easily satisfiable conditions are met (to be specified below) the potential exhibits an approximate longitudinal symmetry. We can exploit this symmetry to restrict our considerations to atomic configurations with symmetric displacements in Z, i.e. $Z_S = 0$.

This can be justified on account of the smallness of $\tilde{Q} = Q/B$. For the analytical solution of the one-dimensional problem we already require the condition

$$2\tilde{Q}Z^2 \ll 1 \tag{9.26}$$

to be true, see Eq. (9.3). For the perturbative derivation of the electric dipole moment in Section 7.1 we assume the requirement

$$4\tilde{Q}|Z| \ll G/B \tag{9.27}$$

to hold, see Eq. (7.3). If these two conditions (9.26) and (9.27) hold, one can show that the dipole-dipole interaction V_{dd} between two atoms in the circular state $|\mathrm{circ}\rangle$ only exhibits dependencies on Z_S that are negligible. The remaining part in the total potential V_{tot} that still depends on Z_S is the confinement due to the Ioffe-Pritchard magnetic field configuration. For typical parameters this magnetic confinement is harmonic around the origin in all directions. It therefore gives a positive contribution to the two-atom energy when the overall center of mass is displaced from the origin. In the one-dimensional case both arguments are apparent from the approximate expression for the total potential on the Z-axis, Eq. (9.8): The dipole-dipole interaction term does not depend on the two-atom-center-of-mass coordinate Z_S and the dependence in the magnetic confinement term is quadratic

and positive for positive Q, $4nQZ_S^2$. Within the range of validity of the approximations (9.26) and (9.27) we can thus conclude that minimizing the energy of the two atoms always leads to a symmetric configuration, $Z_S = 0$. We therefore set $Z_S = 0$ for the following considerations.

Stable configuration

The counteracting forces on the atoms, that come from the longitudinal confinement ($\sim B\tilde{Q}Z^2$) and from the dipole-dipole repulsion on the Z-axis ($\sim Z_D^{-3}(F/B)^2$), try to push the atoms out of the longitudinal axis of the trap. A stable configuration close to the equilibrium position (9.9) on the z-axis can be achieved as long as the transversal confinement ($\sim G/B$) is strong enough.

The one-dimensional approach to the description of two Rydberg atoms subject to dipole-dipole-interaction and magnetic confinement in Chapter 9.1 requires such a strong transversal confinement. Before we deal with the mechanisms in three dimensions that can destabilize the equilibrium configuration described in Chapter 9.1, we first generalize the findings for the stable configuration for three dimensions by keeping a relatively strong transversal confinement. Strong transversal confinement can for instance be obtained with small enough Ioffe field strengths B. In order to guarantee that the uppermost electronic adiabatic surface is well separated from others, however, and in order to achieve useful trap frequencies in the longitudinal direction, the Ioffe field strength should not be chosen too small. The transversal confinement is quantified by the trap frequencies in X- and Y-direction. For one atom in a Ioffe-Pritchard trap and for finite Q they read

$$\omega_X^2 = \frac{2n}{M}\frac{G^2 - 2Q(B + 2GZ)}{B + 2QZ^2} \ , \quad \omega_Y^2 = \frac{2n}{M}\frac{G^2 - 2Q(B - 2GZ)}{B + 2QZ^2} \ , \tag{9.28}$$

which for the parameters used in Fig. 9.8 yields $\omega_X = 15.71$ kHz and $\omega_Y = 15.73$ kHz for $Z = 5$ μm. The corrections due to the dipole-dipole interaction energy when two atoms are considered are proportional to $\frac{n^3}{M}\frac{F}{B}Z_D^{-5/2}$ for dominating Ioffe field and yield a reduction of the trap frequencies of 6% in the example from Fig. 9.8 ($Z_D = 10$ μm).

We are interested in the properties of the six-dimensional adiabatic two-atom potential around its local minimum. In Chapter 9.1 we studied the harmonicity of the potential around that minimum in the direction of the generalized coordinate for the distance of the atoms, Z_D, see Fig. 9.5. The generalized coordinate for the center of mass of both atoms, Z_S, only appears as the quadratic term $4nQZ_S^2$ in the approximate version of the potential (9.8). The harmonicity in this coordinate is thus granted. We also know from the discussion Section 6.4 that the transversal confinement is harmonic around the Z-axis, see Eq. (6.31). In view of the harmonic nature of the total potential around the equilibrium position, it is reasonable to diagonalize the Hesse matrix there in order to compute the trap frequencies and the principal axes of the potential. The six-dimensional center of mass ground state of the two atoms in this harmonic potential is a product of harmonic oscillator wave functions in every of the six generalized coordinates and the ground state energy is half the sum of all frequencies. We note that the center of mass dynamics of the individual atoms is strongly coupled via the generalized coordinates $R_{i,S}$ and $R_{i,D}$, each containing the respective atomic X-,Y- and Z-components of both atoms.
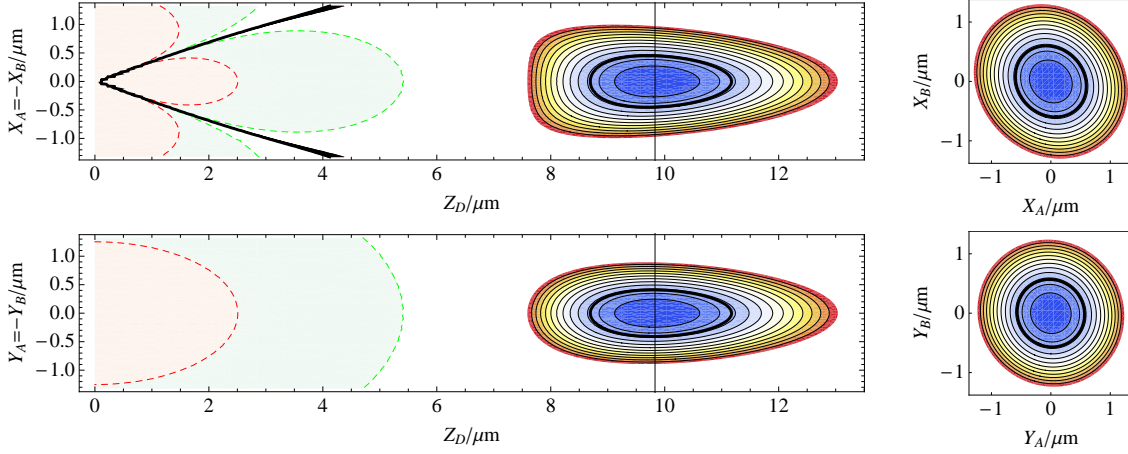
Figure 9.8: Sections through the six-dimensional two-atom potential around the local minimum. The Z_D-coordinate of the minimum is indicated by the vertical lines. The thick black contours are plotted at the energy of the two-atom harmonic center of mass ground state which corresponds to half the sum of all six trap frequencies, $E_0 = 4.1$ kHz. The contour plots are clipped at energies larger than 20 kHz (we offset the energy at the minimum to zero). The dashed lines in the plots on the left hand side guarantee the quality of the single-atom-surfaces-approximation introduced in Sec. 8.2. They are drawn where the ratio of dipole-dipole interaction energy and energetic distance of adjacent single-atom electronic surfaces, $E_{dd}/\Delta E$, Eq. (8.13), equals 0.1 (red) and 0.01 (green). Parameters: $B = 30$ G, $G = 10$ Tm^{-1}, $Q = B \cdot 6 \cdot 10^{-16}$, $F = 2 \cdot 10^{-11}$ a.u.$= 10.28$ V/m, $n = 30$.

We exemplify this by using the parameter set $B = 30$ G, $G = 10$ Tm^{-1}, $Q = B \cdot 6 \cdot 10^{-16}$, $F = 2 \cdot 10^{-11}$, and $n = 30$. For these parameters all the inequalities, that have been formulated up to now in order to measure the quality of the applied approximations, hold with a confidence factor of at least 10^2. The only exception is Eq. (7.37) describing the quality of the perturbative approach to determine the electric dipole moment. It explicitly reads $nF_x/B = 0.047 \ll 1$ for the chosen parameters which is still satisfactory. The numerically computed local minimum is the same (within numerical precision) as the analytically predicted minimum on the Z-axis, Eq. (9.9). Sections of the total potential around this minimum are plotted in Fig. 9.8.

We diagonalize the Hesse matrix $(\partial^2 V_{tot}/(\partial R_i \partial R_j))$ at the local minimum position of the total potential and extract the trap frequencies along the principal axes from the eigenvalues and its eigenvectors, respectively. They are

$$
\begin{aligned}
11.1 \text{kHz}, & \quad (Y_A = Y_B), \\
11.1 \text{kHz}, & \quad (X_A = X_B), \\
10.7 \text{kHz}, & \quad (Y_A = -Y_B), \\
9.7 \text{kHz}, & \quad (X_A = -X_B), \\
5.0 \text{kHz}, & \quad (Z_D), \\
4.5 \text{kHz}, & \quad (Z_S),
\end{aligned} \tag{9.29}
$$

where the equations in brackets define the directions of the principal axis. We will introduce appropriate generalized coordinates for X_i and Y_i analogous to Z_D and Z_S in Eq. (9.34). The trap frequencies in (9.29) have to be compared to the lifetime of the interacting atoms.

The field-free lifetime of the electronic state corresponding to the uppermost surface is $\tau(n, n-1) \approx \frac{3}{2c^2} \left(\frac{n}{\alpha}\right)^5 = 2.3\,\text{ms}$ [97]. The lifetime is reduced due to admixtures to the pure circular state originating from the finite size term and the coupling to the electric field. For the Rydberg atom chain discussed in Chapter 5, where we have both a strong transversal confinement and an external electric field, the lifetime is still 2.1 ms, which is close to field-free value. This means that with the trap frequencies in Z-direction in Eq. (9.29) we expect that more than 10 oscillations of the atomic motion in Z-direction may be observed within the lifetime of the Rydberg state. Since $\omega^2 \sim nQ = nB\tilde{Q}$ the trap frequencies ω can obviously be increased with higher principal quantum numbers n, with higher Ioffe field strengths B and by allowing for a stronger longitudinal confinement. The latter can be done by shrinking the trap onto an atom chip [50].

We again emphasize that the stable two-atom configuration is not immediately lost when one of the atoms decays to the circular state of the adjacent n-manifold since the electronic properties of that state are very similar and, therefore, so are the electric dipole moment and the adiabatic surface.

9.2.2 Loss of confinement and collapse

The discussion in the preceding sections is based on a strong transversal confinement. We now study mechanisms that endanger the stability of the equilibrium position on the Z-axis when the transversal confinement is relaxed. We identify two situations in which this happens. One of them is the loss of the confining property of the Ioffe-Pritchard field configuration for a single atom for large ratios B/G. Furthermore, the stability of the equilibrium configuration is also lost as soon as the transversal confinement becomes smaller than the transversal anti-confinement due to the dipole-dipole interaction. This anti-confinement comes from the reduction of the dipole-dipole interaction energy when the atoms step out of the Z-axis.

Breakdown of magnetic confinement

The confinement in the Z-direction is created by changing the Ioffe-Pritchard magnetic field configuration from being translationally symmetric in the longitudinal direction to being quadratically dependent on Z. This is done by changing the distance of the coils that generate the (Ioffe-) bias field. For a magnetic trap on a chip formed by a Z-shaped wire this quadratic dependence in Z around the position of minimal $|\boldsymbol{B}|$ is immanent. This dependence cannot be canceled completely like in case of a macroscopic trap and its strength depends on the length of the middle wire, see Sec. 6.1.

With the breaking of the translational symmetry of the Ioffe-Pritchard trap the parameter $\tilde{Q}$ is introduced which characterizes the geometry of the trap. It directly couples the Ioffe field strength B to the quadratic confinement in Z. On the Z-axis the absolute value of the magnetic field reads (cf. Eq. (6.1))

$$|\boldsymbol{B}(0, 0, Z)| = B + 2QZ^2 = B(1 + 2\tilde{Q}Z^2) \ . \tag{9.30}$$

The geometric parameter $\tilde{Q}$, however, also changes the transversal confinement. For small displacements from the longitudinal axis the absolute value of the magnetic field on the X-

and Y-axis reads

$$|\boldsymbol{B}(X,0,Z)| = \left(B + 2QZ^2\right) + \frac{G^2/2 - BQ - 4GQZ}{(B + 2QZ^2)}X^2 + \mathcal{O}\left(X^3\right) \; ,$$

$$|\boldsymbol{B}(0,Y,Z)| = \left(B + 2QZ^2\right) + \frac{G^2/2 - BQ + 4GQZ}{(B + 2QZ^2)}Y^2 + \mathcal{O}\left(Y^3\right) \; . \tag{9.31}$$

The absolute value $|\boldsymbol{B}|$ is directly coupled to the approximate adiabatic energy surfaces via the expression (6.29). The curvature of $|\boldsymbol{B}|$ in transversal direction, i.e. the factors that prefix X^2 and Y^2 in (9.31), can become negative and, hence, the transversal magnetic confinement for a single atom is only guaranteed as long as $G^2/2 - BQ - 4GQ|Z| > 0$, which is equivalent to

$$\frac{G^2}{B^2} > 2\tilde{Q}\left(1 + 4\frac{G}{B}|Z|\right) \; . \tag{9.32}$$

In order for this condition to be broken at the origin of the trap, $|Z| = 0$, the ratio G/B must be extremely small since the highest reachable values for the geometry parameter $\tilde{Q}$ in macroscopic Ioffe-Pritchard traps are around 10^{-15} (we use $\tilde{Q} = 6 \cdot 10^{-16}$ for all examples in this chapter [99]). For large enough displacements in Z-direction, however, the condition can always be broken. To give a sense of the numbers we insert the exemplary parameter set $B = 10\,\mathrm{G}$, $G = 2\,\mathrm{Tm}^{-1}$ and $\tilde{Q} = 6 \cdot 10^{-16}$ to find that the displacement $|Z|$ must be as large $2 \cdot 10^7 = 1$ mm to break the condition (9.32). We do not consider such large atomic distances from the trap center in any example we make.

Dipole-dipole interaction induced collapse

The second reason for the loss of the stable equilibrium configuration on the Z-axis is the dipole-dipole interaction between the two atoms. Besides being the interaction of longest range between neutral atoms, the major property of the dipole-dipole interaction is its anisotropic character. This comes into play when the atoms can step out of the Z-axis and the angles between the electric dipole moments and the connecting vector change.

If these angles are the same for both atoms, i.e. when the dipole moments are parallel, and assuming the strengths d of the electric dipole moments to be the same, the expression (8.3) for the dipole-dipole interaction operator simplifies to

$$V_{dd} = \frac{d^2}{R_{AB}^3}(1 - 3\cos^2\theta) \; , \tag{9.33}$$

where θ is the angle between the direction of the moments and the direction of the connecting vector $\boldsymbol{R}_{AB}$, $0 < \theta < \pi/2$. The dipole-dipole interaction has then the angular symmetry of the Legendre polynomial of second order $P_2(\cos\theta)$, i.e. d-wave [107], which can be deduced from the expansion (8.2). The expression in brackets in (9.33) yields one for parallel dipole moments next to each other ($\theta = \pi/2$). It becomes smaller when θ is reduced and eventually becomes negative for angles smaller than the so called magic angle $\theta^* = \arccos\left(3^{-1/2}\right) \approx 55°$. For the head-to-tail configuration, $\theta = 0$, it yields -2.

Analogously to the generalization of Z-coordinates in Eqs. (9.5) it is convenient to introduce generalized coordinates also for the displacement of the two atoms in the same

direction in X or Y, X_S and Y_S, and for the displacement in different directions in X or Y, X_D and Y_D:

$$X_S = \frac{1}{2}(X_A + X_B) \ , \qquad\qquad X_D = X_A - X_B,$$

$$Y_S = \frac{1}{2}(Y_A + Y_B) \ , \qquad\qquad Y_D = Y_A - Y_B \ . \qquad (9.34)$$

The advantage of these coordinates will become clear in the course of this section. Their introduction is also suggested by the results of the principal axes analysis in the example for a stable configuration in Section 9.2.1, see Eq. (9.29).

Polarized case: In order to simplify our considerations let us first assume that the external electric field $\boldsymbol{F} = (F_x, 0, 0)$ fully polarizes the atoms. This happens for relatively large electric field strengths as discussed in Sec. 7.2. Then all dipole moments point in the X-direction. For the sake of clearness we now additionally assume that the magnitude of the dipole moments does not depend on the position of the atom in the trap. Then a displacement of both atoms A and B from the Z-axis in the same direction, $X_S \neq 0$ and/or $Y_S \neq 0$, does not change the interaction energy since the angle θ does not change. The angle also stays the same for a displacement of the atoms in opposite y-directions, $Y_D \neq 0$. Here the interaction energy decreases only slightly due to the increase of the distance R_{AB} of the atoms. A displacement of the atoms in opposite X-directions, $X_D \neq 0$, however, changes θ and thereby decreases the interaction strength considerably. For a decreasing transversal confinement we therefore expect the stable configuration to collapse by a displacement of the atoms in opposite X-directions in the polarized case.

Tilted moments: The reasoning above is based on the assumption that the atoms are polarized, meaning that their dipole moments point in the direction of the electric field independent of the position of the atom. This is an oversimplification in case of Rydberg atoms in a strongly confining magnetic field configuration. We have seen in Chapter 7 that the application of a moderate electric field induces a dipole moment $\boldsymbol{d}_F$ that is perpendicular to the local direction of the magnetic field. In the Y-Z-plane $\boldsymbol{d}_F$ points in the X-direction[3]. For finite X, by contrast, it has a finite Z-component, see Sec. 7.2. The interesting physics thus again happens for displacements in X and we therefore set $Y_S = X_D = 0$ in the following. The non-polarized case is illustrated (for $Q = 0$) in Fig. 9.9.

In case of a displacement of the atoms in opposite directions, $X_D > 0$, the dipole moments of the two atoms include different angles with their connecting axis. They differ from the angles in the fully polarized case, θ_P, by the additional tilt due to the local magnetic field direction, $\pm\Delta\theta$. The interaction energy no longer depends on $(1 - \cos^2(\theta_P))$ but on $(1 - \cos(\theta_P + \Delta\theta)\cos(\theta_P - \Delta\theta))$ which is smaller than the former for $0 \leq \theta_P \pm \Delta\theta \leq \pi/2$. For electric dipole moments perpendicular to the local magnetic field axis, as considered here, the reduction of the dipole-dipole interaction energy for displacements in X_D is therefore smaller than in the fully polarized case discussed above. The curvature in that direction is thus expected to be still positive for shallower transversal confinements.

Symmetric displacements of the atoms in the same X direction, $X_S \neq 0$, do not change the dipole-dipole interaction energy in the fully polarized case as stated above. For tilted dipole

---

[3]The local direction of the magnetic field, and with it also the direction of the electric dipole moment, in fact also depends on Q. We do not consider this dependence at this point since its effect on the dipole-dipole interaction is small and does not considerably alter the effects we want to explain.
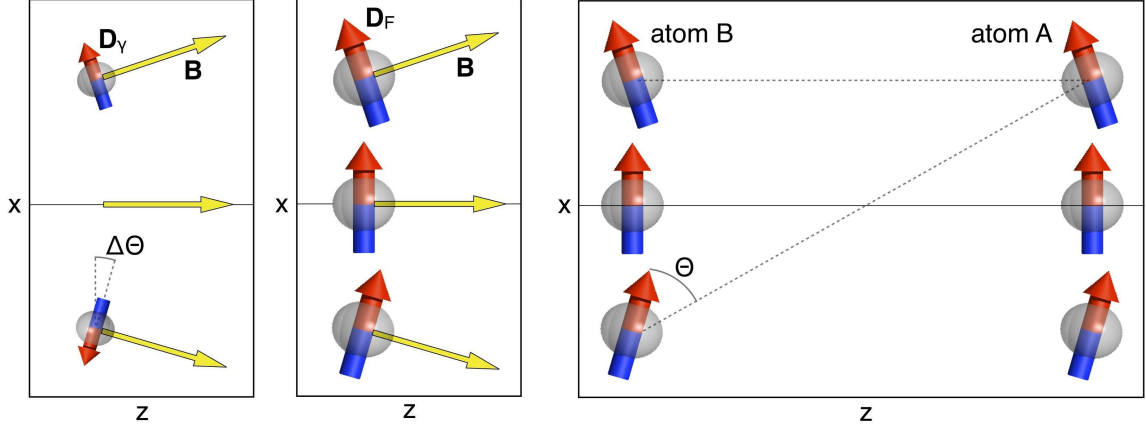
Figure 9.9: Spacial dependence of the direction of the electric dipole moments $\boldsymbol{d}_\gamma$ and $\boldsymbol{d}_F$. The *left plot* shows the electric dipole moment $\boldsymbol{d}_\gamma$ that originates from the finite size of the Rydberg atom. It is perpendicular to the local magnetic magnetic field direction (yellow arrows) and it vanishes on the Z-axis. On the positive (negative) X-axis it is parallel (anti-parallel) to the electric dipole moment $\boldsymbol{d}_F$ that is induced by the electric field and depicted in the *middle plot*. The plot on the *right-hand side* illustrates the orientation of $\boldsymbol{d}_F$ with respect to the vector $\boldsymbol{R}_{AB}$ connecting the interacting atoms A and B when they are displaced in the same X-direction, $X_S \neq 0$, or in different X-directions, $X_D \neq 0$, (dashed lines).

moments, however, the energy is reduced since the moments are no longer perpendicular to their connecting axis. This can be seen from the illustration in Fig. 9.9. The additional angle due to the orientation of the moments perpendicular to the local magnetic field axis (for $Q = 0$) explicitly reads

$$\Delta\theta = \arctan\left(\frac{G}{B}X\right) \ . \tag{9.35}$$

The effects due to $\Delta\theta$ described above are therefore weak for typical parameter sets since for typical parameters the ratio G/B is small. A strong effect on the dipole-dipole interaction energy is expected for large ratios G/B. In this case, however, the transversal confinement is strong and the curvature in X-direction is positive on the Z-axis nonetheless.

The situation would again complicate if we would additionally incorporate the electric dipole moment $\boldsymbol{d}_\gamma$ into the discussion. $\boldsymbol{d}_\gamma$ originates from the finite-size-term of the Rydberg Hamiltonian, see Section 7.1, and its X-dependence is illustrated in Fig. 9.9. It is small compared to the electric field induced moments $\boldsymbol{d}_F$ for all electric field strengths considered in this chapter and it is thus only responsible for small corrections to the loss mechanisms predicted above.

The loss of the stable local minimum for the two Rydberg atoms is depicted in the upper row of plots in Fig. 9.10 for an exemplary parameter set. Shown are sections through the total two-atom potential in X_S and X_D around the local minimum position on the Z-axis (cf. Eq. (9.9)). For decreasing magnetic field gradient G (from left to right in the figure) the curvature of the potential along X_D changes from positive to negative. This is not due to the loss of magnetic confinement of the single atoms but it is because of their interaction which is largest on the Z-axis. This is confirmed by the second row of plots in the same figure where we plotted the same sections only considering the magnetic confinement for
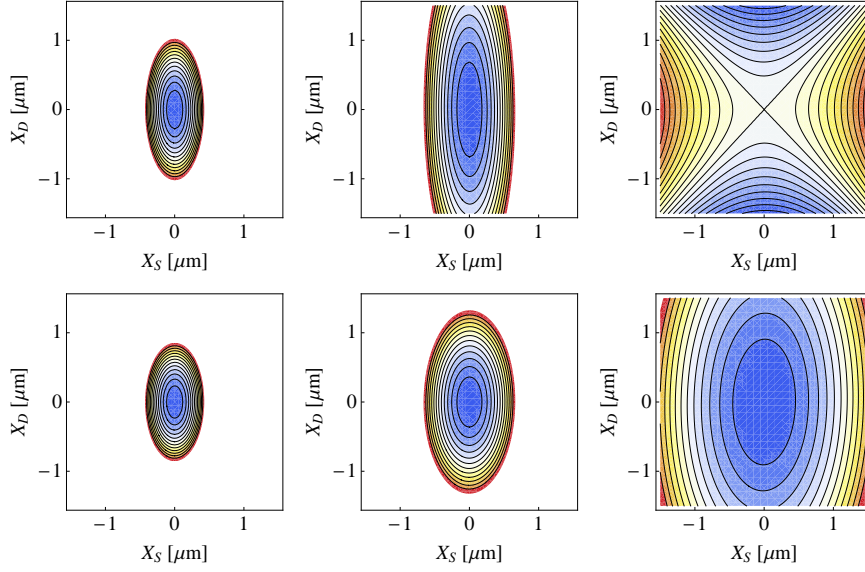
Figure 9.10: The series of transversal sections through the total two-atom potential (upper row of plots, $Y_S = Y_D = Z_S = 0$, $Z_D = Z_{D,\min}$ from Eq. (9.9)) shows the zero crossing of the curvature with respect to X_D for decreasing magnetic field gradient G. The second row of plots shows only the magnetic confinement for comparison. The colors represent the same energies in every plot. Parameters: $G = 3\,\mathrm{Tm}^{-1}$ (left column), $G = 2\,\mathrm{Tm}^{-1}$ (middle), $G = 1\,\mathrm{Tm}^{-1}$ (right), $B = 10\,\mathrm{G}$, $Q = B \cdot 6 \cdot 10^{-16}$, $F = 10^{-10}$, $n = 30$.

both atoms and omitting their interaction energy.

Verification of predictions: In order to verify the predictions above on how the stability of the equilibrium configuration of the atoms gets lost, and the predictions for the configuration the atoms take when they step out of the Z-axis, we minimize the total two-atom potential for the coordinates X_S, X_D, Y_S and Y_D for fixed symmetric displacements of the atoms in Z, $Z_D > 0$ and $Z_S = 0$. As discussed above we expect the atoms to align on the Z-axis as long as the transversal confinement dominates the interaction. When the longitudinal confinement increases and/or the transversal confinement decreases, the atoms are expected to step out of the Z-axis in different X-directions, i.e. $X_D \neq 0$, $X_S = Y_D = Y_S = 0$, since the negative transversal gradient at the equilibrium position due to the dipole-dipole interaction is largest in the X_D-direction.

This change of the atoms' configuration is depicted in Figs. 9.11 and 9.13 where we plot the computed X_D positions that yield minimal energy for fixed distances Z_D as black dots into the two-dimensional section through the two-atom potential for different parameter sets (left plots). The bar graphs on the right-hand side show the minimal energies computed for the fixed distances Z_D. The Figs. 9.12 and 9.14 complement the Figs. 9.11 and 9.13, respectively, by showing the results of the minimization for the other coordinates. The numbers for Y_i are many orders of magnitude smaller than those for X_D, as expected. The displacement of the center of mass of both atoms from the origin, X_S, is only one or two orders of magnitude smaller than X_D. This correction to the prediction $X_S = 0$ is a finite size effect as discussed below.

The parameter sets in Fig. 9.11 only differ in the magnetic field gradient G. The series
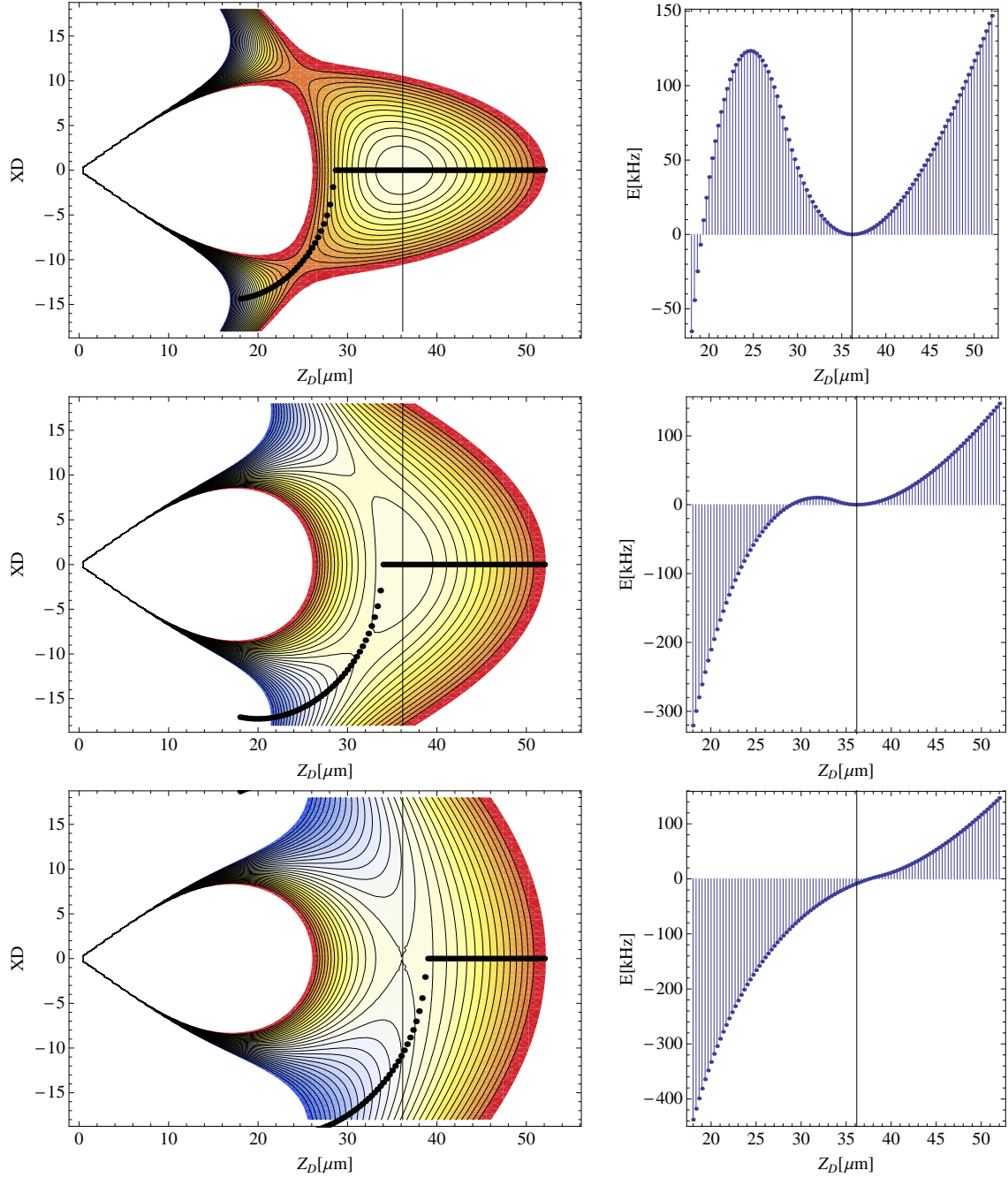
Figure 9.11: Loss of local minimum for decreasing magnetic field gradient G of the Ioffe-Pritchard trap. *Left column:* Two-dimensional sections of the six-dimensional two-atom potential through the X_D-Z_D plane, $X_S = Y_S = Y_D = Z_S = 0$. Red colors symbolize high energies and blue colors symbolize low energies. The plot range of all three contour plots is ± 150 kHz. *Right column:* Minimal energy of the two-atom potential against Z_D. Each point is computed minimizing the total potential for fixed Z_D with the other center of mass coordinates as parameters. The X_D positions are shown as black dots in the sections on the left. As expected, X_S, Y_S and Y_D are small, see Fig. 9.12. Parameters: $B = 10\,\mathrm{G}$, $Q = B \cdot 6 \cdot 10^{-16}$, $F = 10^{-10}$ a.u., $n = 30$, $G = 3\,\mathrm{Tm}^{-1}$ (first row), $G = 2\,\mathrm{Tm}^{-1}$ (second row), $G = 1.5\,\mathrm{Tm}^{-1}$ (third row).

Figure 9.12: Complement to Fig. 9.11. Coordinates X_S, Y_S and Y_D of the minimum position of the total potential for fixed Z_D given in μm. They are small compared to the values of X_D ($\mathcal{O}(10)$, see Fig. 9.11) due to the peculiarities of the dipole-dipole interaction described in the text. The parameters are the same as in Fig. 9.11: $B = 10\,$G, $Q = B \cdot 6 \cdot 10^{-16}$, $F = 10^{-10}$ a.u., $n = 30$, $G = 3\,\mathrm{Tm}^{-1}$ (first row), $G = 2\,\mathrm{Tm}^{-1}$ (second row), $G = 1.5\,\mathrm{Tm}^{-1}$ (third row).
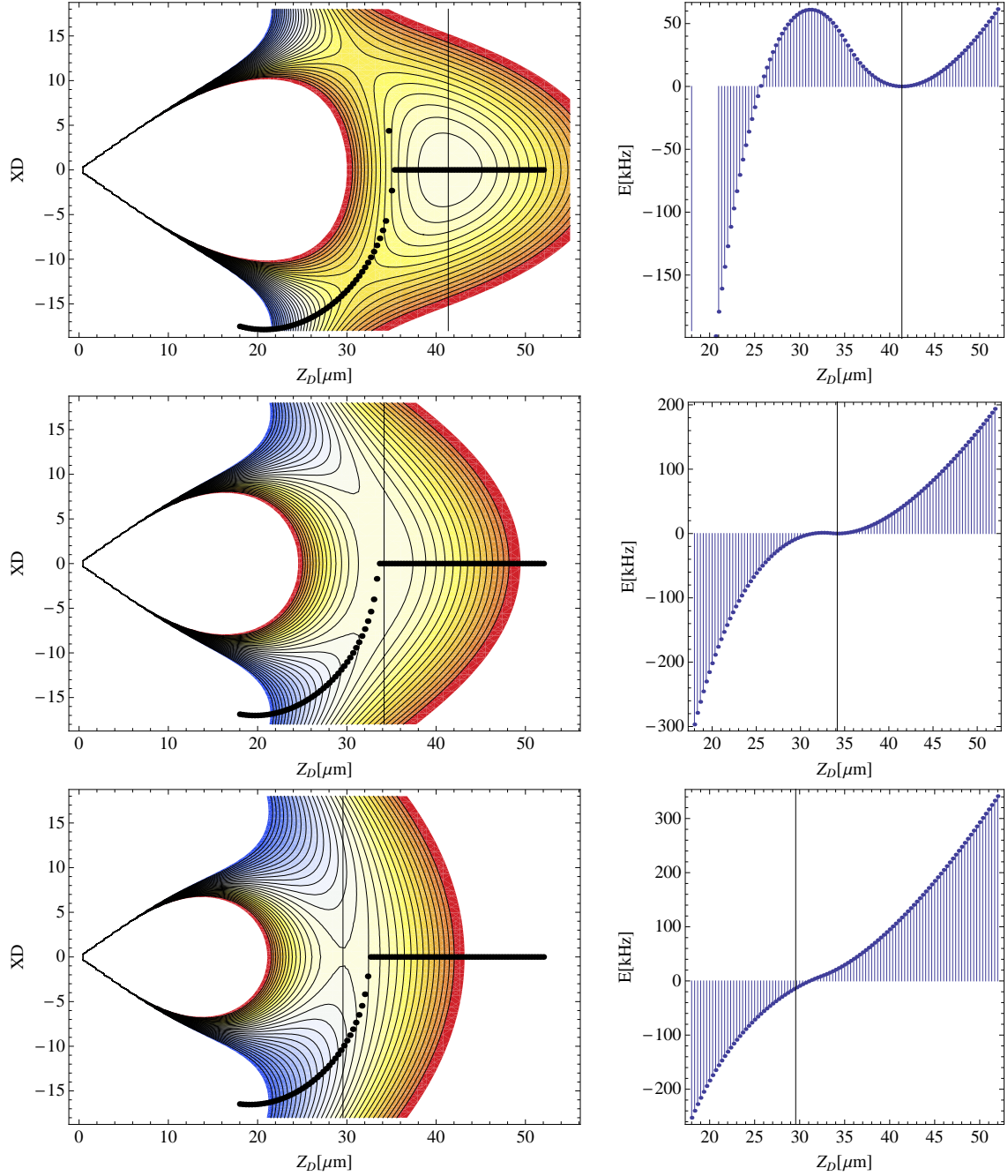
Figure 9.13: Loss of local minimum for increasing magnetic Ioffe field strength B of the Ioffe-Pritchard trap. *Left column:* Two-dimensional sections of the six-dimensional two-atom potential through the X_D-Z_D plane, $X_S = Y_S = Y_D = Z_S = 0$. Red colors symbolize high energies and blue colors symbolize low energies. The plot range of all three contour plots is ± 150 kHz. *Right column:* Minimal energy of the two-atom potential against Z_D. Each point is computed minimizing the total potential for fixed Z_D with the other center of mass coordinates as parameters. The X_D positions are shown as black dots in the sections on the left. As expected, X_S, Y_S and Y_D are small, see Fig. 9.14. Parameters: $G = 2 \, \mathrm{Tm}^{-1}$, $Q = B \cdot 6 \cdot 10^{-16}$, $F = 10^{-10}$ a.u., $n = 30$, $B = 8 \, \mathrm{G}$ (first row), $B = 11 \, \mathrm{G}$ (second row), $B = 14 \, \mathrm{G}$ (third row).
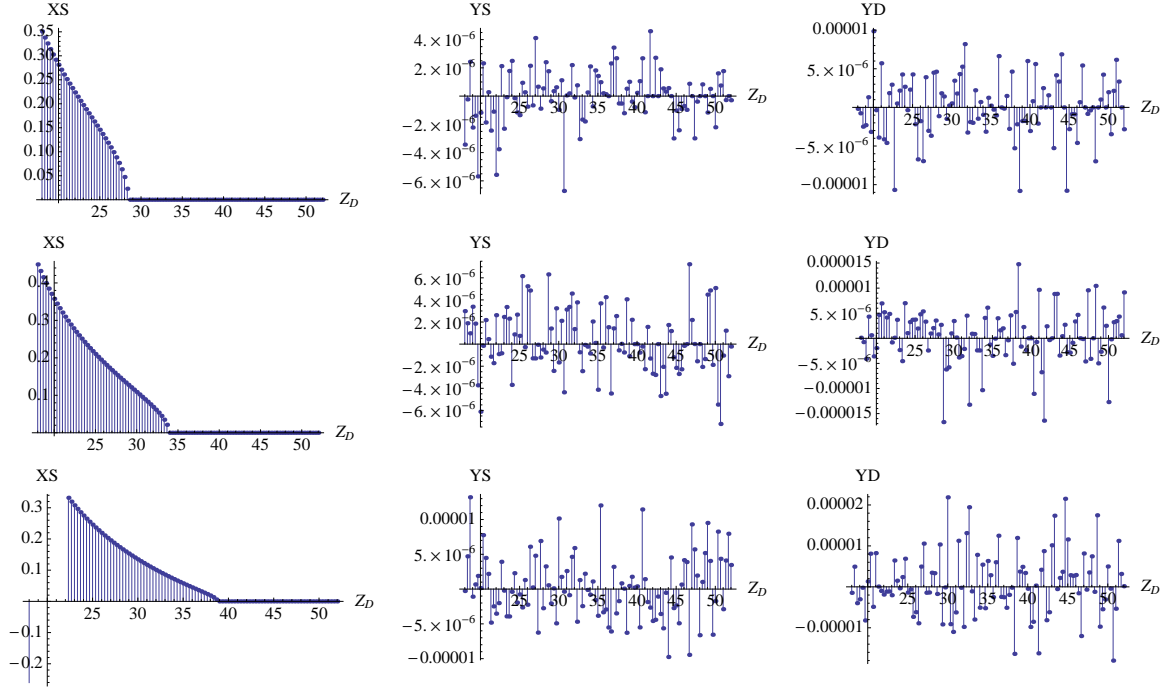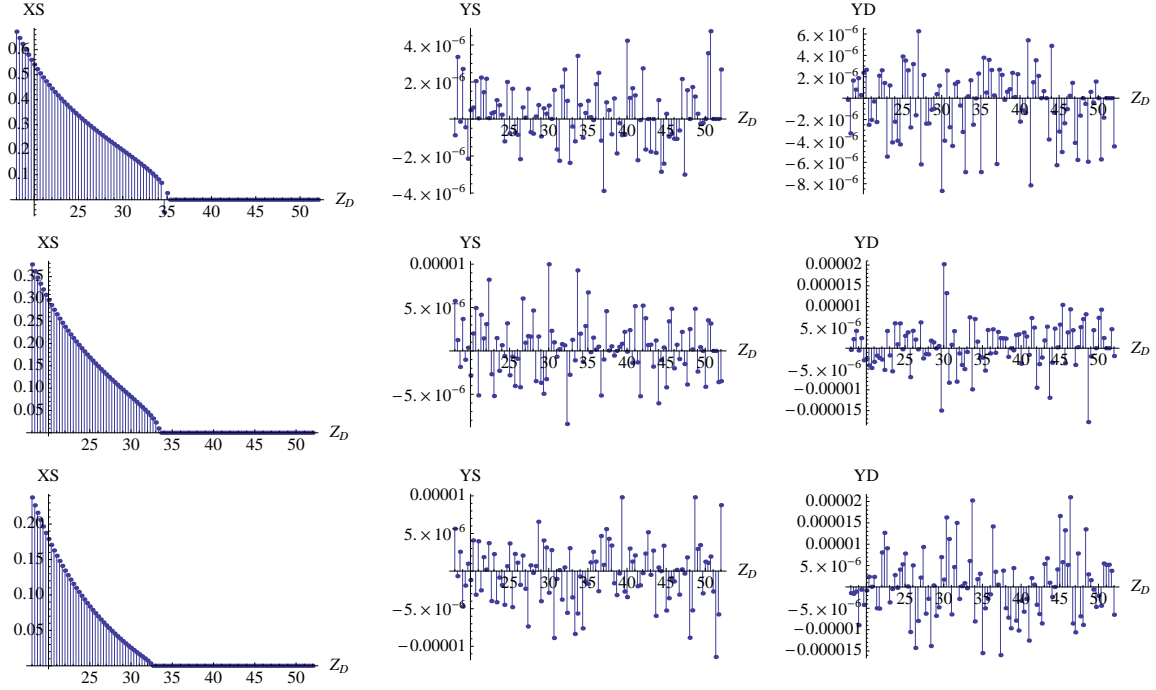
Figure 9.14: Complement to Fig. 9.13. Coordinates X_S, Y_S and Y_D of the minimum position of the total potential for fixed Z_D given in μm. They are small compared to the values of X_D ($\mathcal{O}(10)$, see Fig. 9.13) due to the peculiarities of the dipole-dipole interaction described in the text. The parameters are the same as in Fig. 9.13: $G = 2\,\mathrm{Tm}^{-1}$, $Q = B \cdot 6 \cdot 10^{-16}$, $F = 10^{-10}$ a.u., $n = 30$, $B = 8\,\mathrm{G}$ (first row), $B = 11\,\mathrm{G}$ (second row), $B = 14\,\mathrm{G}$ (third row).

of plots shows the loss of the local minimum position for relaxing transversal confinement due to decreasing field gradients G (from top to bottom). The vertical lines indicate the position of the equilibrium configuration on the Z-axis. Sections perpendicular to those in Fig. 9.11 that cross at these vertical lines have been described above and are depicted in the upper row of Fig. 9.10. The bar graphs on the right hand side show the minimal potential energy of the two atoms depending on the atomic distance in Z-direction, Z_D (we still assume symmetric displacements in Z, i.e. $Z_S = 0$). As long as the equilibrium position on the Z-axis is a local potential minimum, the minimal energy concordantly exhibits an energetic barrier towards smaller distances of the atoms. The peak of this energetic barrier is located at one of the two saddle points of the potential that are located symmetrically to the longitudinal axis. When the local potential minimum is lost, these saddle points collapse into one saddle point at the equilibrium position on the Z-axis where the local minimum simultaneously vanishes. This can be seen in the series of plots on the left hand side. The energy plots on the right hand side show that the energetic barrier also simultaneously vanishes.

The plots in Fig. 9.13 essentially show the same mechanism. The only difference is that not the magnetic field gradient G but the magnetic Ioffe field strength B is changed here. The transversal confinement also decreases for increasing B but in contrast to the situation in Fig. 9.11 the longitudinal confinement changes too: It increases for increasing B (top to bottom in Fig. 9.13). The local minimum then equally turns into a saddle point, the energetic barrier vanishes, and the stable configuration for two atoms is lost.

In contrast to the prediction above, where we argued assuming the magnitude of the dipole moments not to depend on the position of the atoms, we find the minimal value of the potential energy at $X_S \neq 0$. As can be seen from Figs. 9.11 to 9.14, X_S is around two orders of magnitude smaller than X_D, but nonzero. This is due to the permanent electric dipole moments $\boldsymbol{d}_\gamma$ for vanishing electric field, which in turn are a signature of the finite size of Rydberg atoms. The origin of these moments $\boldsymbol{d}_\gamma$ is described in Section 7.1 and their properties in the X-Z-plane are depicted in the left plot of Fig. 9.9. The illustration shows that they point in the same direction as the electric dipole moments induced by the electric field ($\boldsymbol{d}_F$, middle plot) for positive displacements of the atoms in X. They are anti-parallel for negative X and they vanish on the Z-axis. Since $\boldsymbol{d}_\gamma$ is a lot smaller than $\boldsymbol{d}_F$ for all considered electric fields in this chapter, $\boldsymbol{d}_\gamma$ can be considered a correction to $\boldsymbol{d}_F$ and their sum $\boldsymbol{d}$ is parallel to $\boldsymbol{d}_F$ but larger or smaller in magnitude than $\boldsymbol{d}_F$ for positive or negative X, respectively. This introduces an asymmetry in X_S and X_D into the dipole-dipole interaction energy and is hence responsible for the nonzero values of X_S for the position of minimal potential energy[4].

From Section 9.1.1 we know that it is possible in the one-dimensional case to increase the equilibrium distance of the two Rydberg atoms by just tuning the electric field strength F while neither changing the trap frequencies ω_{Z_S} and ω_{Z_D} nor changing the conditions for having a stable configuration. Fig 9.15 shows that this still holds in three dimensions. We start with a parameter set for which the local minimum on the Z-axis is close to being lost: A slight increase of B or a slight decrease of G would suffice to turn the local minimum

---

[4]This asymmetry is also responsible for the negative values of X_D for the positions of minimal potential energy plotted in Figs. 9.11 and 9.13 in spite of the fact that the slight asymmetry in the dipole-dipole interaction energy is not visible when the total potential is plotted.
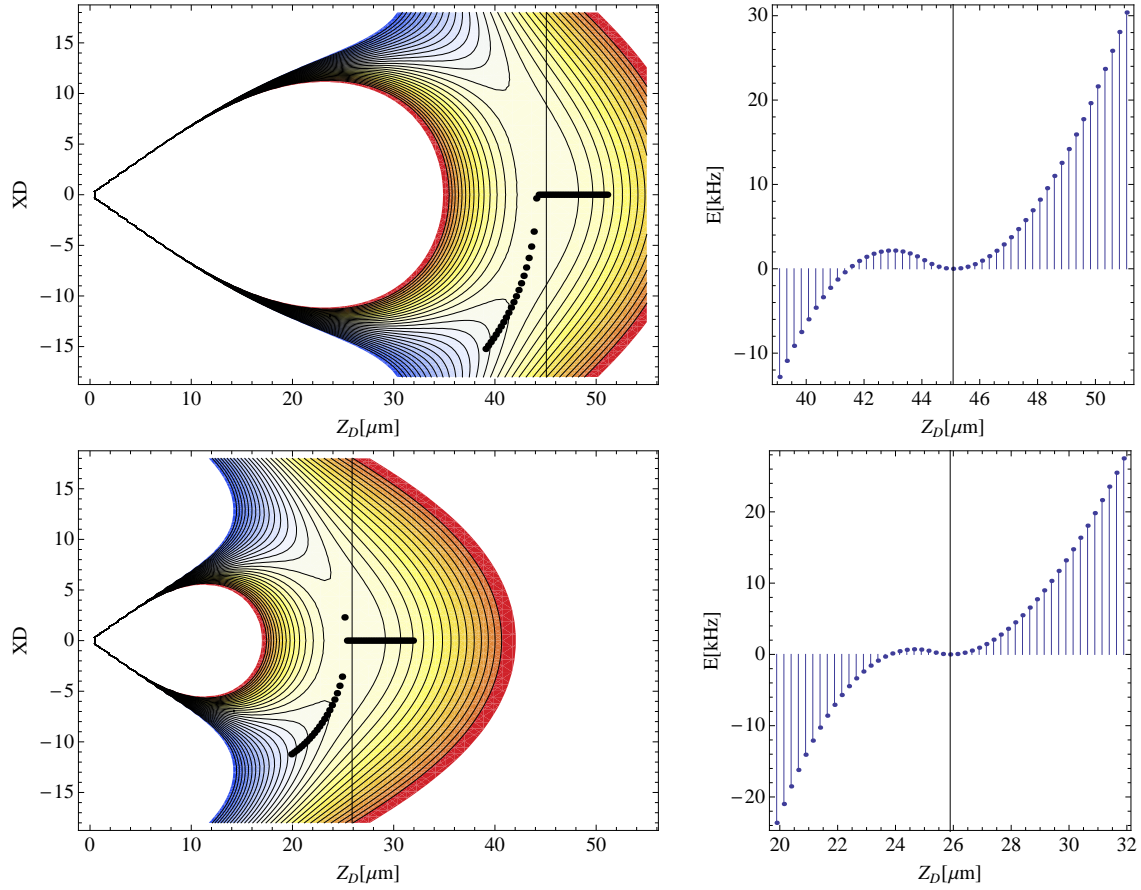
Figure 9.15: : Changes of the electric field strength hardly alter the stability of the equilibrium position. In the plotted example changing F by a factor of 10 alters the trap depth by less than 2 kHz (rows 1 and 2, $F = 5 \cdot 10^{-10}$ a.u., $F = 5 \cdot 10^{-11}$ a.u., respectively). Rows 3 and 4: Different principal quantum numbers ($n = 80$ line 4, $n = 30$ line 5). Parameters: $B = 11$ G, $G = 2$ Tm^{-1}, $Q = B \cdot 6 \cdot 10^{-16}$.

into a saddle point. Hence the height of the energetic barrier that prevents the atoms from ionizing is small (upper row of plots in Fig. 9.15). Changing the electric field strength by an order of magnitude hardly changes the height of this barrier (bottom row of plots in Fig 9.15). We conclude that the stability of the equilibrium configuration is insensitive to changes in the electric field strength and thereby also the transversal part of the center of mass wave function of the atoms.

We note that changing the principal quantum number n also has no considerable effect on the stability of the equilibrium position as long as the requirements involving n can be met.

Analytical stability condition

The stability of the equilibrium configuration of the two atoms hence depends essentially on the magnetic field parameters B, G and Q but not significantly on F and n. For a fixed trap geometry parameter $\tilde{Q}$ the ratio G/B has to be large enough to prevent a collapse of the system. When the ratio G/B decreases, the two saddle points of the potential in the X_D-Z_D-plane come closer to the Z-axis and eventually merge at the position where the local minimum simultaneously vanishes. This can be observed in the series of plots in Fig. 9.11.

In order to find an analytical stability condition involving the magnetic field parameters we examine the curvature of the potential in X_D-direction at the equilibrium position. It is the sum of the curvatures of the magnetic confinement and of the dipole-dipole interaction energy. The former reads

$$\left(\frac{\partial^2}{\partial X_D^2} n(|\boldsymbol{B}(\boldsymbol{R}_A)| + |\boldsymbol{B}(\boldsymbol{R}_B)|) \right) \Big|_{Z\text{-axis}} = \frac{n(G^2 - 2BQ)}{2B + QZ_D^2} \ . \tag{9.36}$$

For small ratios G/B (which is the case when the system is close to collapse), and assuming $F \gg nG$, we find the approximate expression for the curvature of the dipole-dipole interaction energy in X_D-direction

$$\left(\frac{\partial^2}{\partial X_D^2} V_{dd} \right) \Big|_{Z\text{-axis}} \approx \left(\frac{F_x}{B} \right)^2 \frac{n^6}{Z_D^5} \ , \tag{9.37}$$

which strongly depends on the distance of the atoms. Inserting the equilibrium distance $Z_{D,\text{min}}$ from Eq. (9.9), where the dipole-dipole repulsion and the longitudinal confinement add to zero, we find

$$\left(\frac{\partial^2}{\partial X_D^2} V_{dd} \right) \Big|_{\text{equilibrium}} \approx -6nQ \ . \tag{9.38}$$

For a stable configuration the curvature has to be positive at the equilibrium position. Hence the sum of the expressions (9.36) and (9.38) has to be larger than one there. This yields the condition

$$\frac{G^2}{B^2} > 14\tilde{Q} \ . \tag{9.39}$$

As soon as the right-hand side of this inequality becomes as large as the left-hand side the two saddle points at the potential barriers join on the Z-axis and the local minimum is lost.

Inserting the geometry parameter for the millimeter trap in Ref. [99] used throughout the chapter, $\tilde{Q} = 6 \cdot 10^{-16}$, the stability condition takes the explicit form $G/(\text{Tesla/meter}) > 0.17 \cdot B/\text{Gauss}$. As soon as this condition is broken the stability of the equilibrium position is lost as can be verified in Figs. 9.11 and 9.13.

In addition to the stability condition (9.39), the previously derived condition (9.32) has to hold that guarantees the magnetic confinement for each individual atom. In all the examples in this chapter, in particular for the examples in Figs. 9.11 to 9.14, the latter condition is less restrictive. This means that the collapse is interaction-induced and it is not due to the loss of magnetic confinement: Comparing the right hand sides of (9.39) and (9.32) we find this to be true as long as $|Z| < \frac{3}{2}\frac{B}{G}$. Inserting the minimum position $\frac{1}{2}Z_{D,\min}$ for $|Z|$ and the parameters used in the second row of Fig. 9.11 as an example, this inequality explicitly reads $6.8 \cdot 10^5 < 1.4 \cdot 10^7$.

Robustness

We have seen above that the equilibrium position on the Z-axis is a local minimum as long as the condition (9.39) holds. Then, the system has to overcome an energetic barrier in order to decrease the distance of the atoms.

For the existence of a stable configuration of the two atoms it does, in fact, not suffice to have a local minimum on the Z-axis, i.e. to meet the requirement (9.39). The potential well around the local minimum must additionally be deep enough to accommodate at least the two-atom center of mass ground state. The energy of this ground state is $\frac{1}{2}\sum_i \omega_i$ when the potential is harmonic in all directions around the local minimum position. ω_i are the trap frequencies in the different coordinate directions.

The minimal two-atom energy for a fixed distance of the atoms, Z_D, is plotted against Z_D in Fig. 9.16 for different transversal confinements. The depth of the potential well decreases from $1427\,\text{kHz}$ to $26.5\,\text{kHz}$ when the transversal confinement is relaxed by decreasing G from $G = 10\,\text{Tm}^{-1}$ to $G = 2.2\,\text{Tm}^{-1}$. The energy of the center of mass ground state is indicated by vertical lines. The potential barrier heights correspond to temperatures of the atoms ranging from $34.2\,\mu\text{K}$ (top left plot) to $640\,\text{nK}$ (bottom right plot).

In Fig. 9.17 the minimal energy is compared for two parameter sets that yield the same ratio B/G. Even though the condition for having a minimum, Eq. (9.38), only depends on this ratio when the geometry of the trap is not changed, the barrier height in the examples is not the same. In the left example it corresponds to $51.4\,\mu\text{K}$ which is as high as typical temperatures reached in a magneto-optical trap without further cooling.

9.3 Excitation schemes

Several techniques have been suggested and used to excite atoms into circular Rydberg states. We describe them in Section 1.2. Our concern in this section, however, is not the excitation of single atoms into circular states but the excitation of two atoms in a Ioffe-Pritchard trap with an additional electric field directly into the equilibrium configuration that is stabilized by the dipolar interaction of the atoms described in the preceding part of this chapter (see Sec. 9.2.1).

Ideally, the atoms should be excited into the single-atom states whose product approximately constitutes the two-atom state in stable equilibrium. This is complicated by several
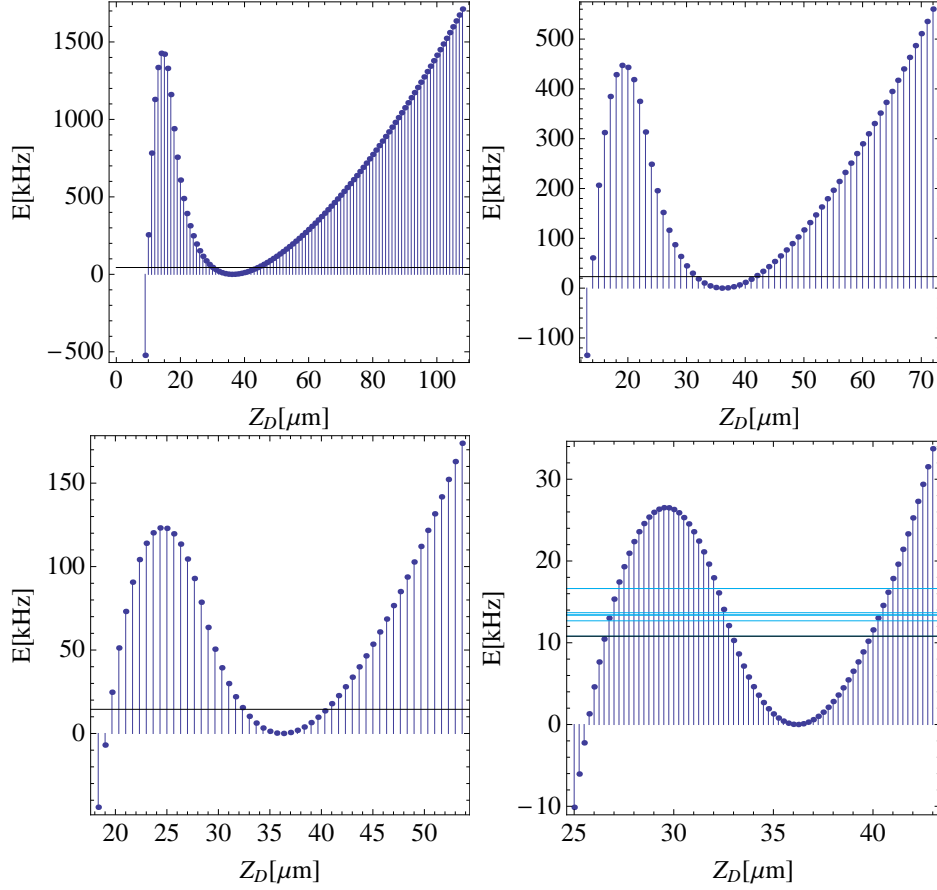
Figure 9.16: Minimal energy of the two-atom potential against Z_D for decreasing transversal confinement. Each point is computed minimizing the total potential for fixed Z_D with the other center of mass coordinates as parameters. The height of the potential barriers with respect to the local minima are $1427\,\text{kHz} \,\widehat{=}\, 34.2\,\mu\text{K}$, $448\,\text{kHz} \,\widehat{=}\, 10.8\,\mu\text{K}$, $123\,\text{kHz} \,\widehat{=}\, 3.0\,\mu\text{K}$, and $26.5\,\text{kHz} \,\widehat{=}\, 640\,\text{nK}$, from top left to bottom right. The energies of the two-atom center of mass ground states, indicated by the dark horizontal lines, are $44.2\,\text{kHz}$, $23.1\,\text{kHz}$, $14.5\,\text{kHz}$, and $10.8\,\text{kHz}$, respectively. Even though the trap frequencies in Z-direction do not change with G, the ground state energies are not the same because the trap frequencies in transversal direction decrease with decreasing G. The light horizontal lines in the plot on the right-hand side indicate the energies of the harmonic center of mass states with one excitation in any of the directions. Parameters: $B = 10\,\text{G}$, $G = 10\,\text{Tm}^{-1}$ (top left plot), $G = 5\,\text{Tm}^{-1}$ (top right), $G = 3\,\text{Tm}^{-1}$ (bottom left), $G = 2.2\,\text{Tm}^{-1}$ (bottom right), $F = 10^{-10}\,\text{a.u.}$, $Q = B \cdot 6 \cdot 10^{-16}$.
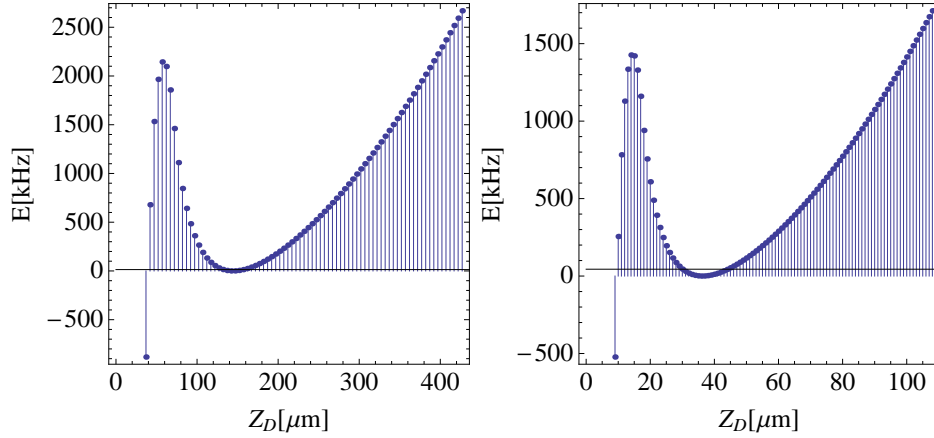
Figure 9.17: Same plots as in Fig. 9.16 for parameter sets that yield the same ratio B/G: $B = 1\,\mathrm{G}$, $G = 1\,\mathrm{Tm}^{-1}$, center of mass ground state energy $E_0 = 13.9\,\mathrm{kHz}$, barrier height $2144\,\mathrm{kHz} \cong 51.4\,\mu\mathrm{K}$ (*left plot*); $B = 10\,\mathrm{G}$, $G = 10\,\mathrm{Tm}^{-1}$, $E_0 = 44.2\,\mathrm{kHz}$, barrier height $1427\,\mathrm{kHz} \cong 34.2\,\mu\mathrm{K}$ (*right plot*); $F = 10^{-10}$ a.u., $Q = B \cdot 6 \cdot 10^{-16}$.

reasons that are all connected to the fact that the overall potential experienced by the two Rydberg atoms in the trap is composed of a single-atom part and an interaction part. The former is due to the coupling of a single Rydberg atom to the magnetic field generated by the Ioffe-Pritchard trap and it provides the confinement for the atoms. This confinement is harmonic around the origin and its strength depends linearly on the magnetic quantum number of the electronic state. It is thus stronger for Rydberg atoms in comparison to ground states atoms by a factor of $m_l/2 + m_s$, see Eq. (6.29). This part of the potential is the same (per atom) no matter how many Rydberg atoms are in the system. The second contribution to the two-atom potential, however, is the dipolar interaction energy that only appears when more than one atom is excited.

The minimum of the potential experienced by a single Rydberg atom is at the origin of the trap. If we want to excite into a localized state by applying a non-localized laser field we are bound to tune the laser such that it is resonant at only one point in space. This can only be the minimum at the origin. For two excited atoms in contrast, the equilibrium position is located on the Z-axis with a finite distance of the atoms, $Z_D \neq 0$. If the atoms are excited one after another, which we have to assume, we are facing the problem that an atom that is excited at the minimum of the one-atom potential is out of the equilibrium position of the two-atom potential that applies as soon as the second atom is excited.

If we assume one of the Rydberg atoms to sit at the origin of the trap, the two-Rydberg-atom potential has local minima with the same energy on either side of the origin on the Z-axis. This is due to the symmetry of the electric dipole moment expectation value to the origin on the Z-axis, see Eq. (7.46). The two-atom center of mass coordinate Z_S is non-zero for both configurations which entails a non-minimal kinetic energy of the system. Excited into these displaced configurations, the atoms would perform coupled oscillations in Z_S and Z_D around zero and $Z_{D,\mathrm{min}}$, respectively.

Solutions to the addressed complications include (*i*) externally forcing the excitation to happen at the desired positions only, or (*ii*) changing the single-atom potential such that its minima coincide with the two-atom potential minimum, or even (*iii*) adiabatically

transferring the system to the desired state by varying the detuning of the laser during the excitation process. A possible implementation of each of the options is described in the following. In principle all schemes are extendable to more than two atoms.

Optical tweezers

In equilibrium position both Rydberg atoms are located on the Z-axis. The only coordinates that have to be externally imposed are the Z-coordinates of the atoms since zero transversal displacement minimizes the energy for both the single-atom as well as the two-atom potential.

The cleanest way to do this is to trap individual ground state atoms in two optical dipole traps perpendicular to the longitudinal axis of the Ioffe-Pritchard trap at the desired Z-positions. The trapping volume of such optical tweezers [108] can be made so small (less than a μm in diameter) that only one atom can be captured in each trap [109]. These two atoms can then be excited using one of the methods described in Section 1.2.

Another way of forcing the Rydberg atoms to be produced at the desired Z-positions is to excite them from a cold ground state atom cloud by two laser beams perpendicular to the Z-axis that are focused next to each other to the desired equilibrium positions of the Rydberg atoms. This is possible if the equilibrium distance is considerably larger than the waist of the focused laser beams which can be as small as a μm. Due to the strong Rydberg-Rydberg interaction, which yields an energy shift within the excitation volume that is larger than the linewidth of the laser, only one atom can be excited within one of the laser beams. As the excitation can be located at any of the atoms in that region, however, the ensemble of atoms is excited collectively into a superposition state called *superatom* [110].

Modify the trap geometry – magnetic double wells

The second solution involves the modification of the single Rydberg atom potential. This can be done by adding an extra wire on the X-axis to the Z-trap on a chip or, correspondingly, by adding an extra coil between the coils of a macroscopic Ioffe-Pritchard trap that are responsible for the Ioffe field. Both setups yield a double well potential with a variable barrier height and a variable distance of the potential minima. For vanishing electric field two Rydberg atoms can be excited independently from each other, one in the bottom of each well, by tuning the laser just under the energy of the minimum. In order to keep heating as low as possible, the magnetic barrier can now be substituted by the dipolar repulsion between the atoms by decreasing the current through the extra coil or wire and simultaneously increasing the electric field strength.

The circularization of the Rydberg atoms with a modified adiabatic rapid passage method [64], for example, can be completed within $5\,\mu$s. The timescale of changing the magnetic field strongly depends on the configuration. If it is small enough the described excitation scheme is scalable to produce more than two excitations, i.e. a Rydberg atom chain. This can be done by applying a magnetic field gradient in Z-direction which tilts the trap and moves the stable Rydberg atom pair in Z-direction. The magnetic barrier can be ramped up again as to confine the pair in one of the wells. At the minimum of the other well an additional circular Rydberg atoms can be produced. The two atoms in the first well mutually tune themselves out of resonance of the exciting laser due to their interaction.

By ramping the magnetic barrier up and down, and exciting a Rydberg atom in the empty well every time as described, a stable chain of atoms can be produced in the trap. The procedure is restricted by the timescales of excitation, magnetic field switching and by the lifetime of the circular Rydberg atoms which is about $2\,\mathrm{ms}$ for $n = 30$ in the field-free case and scales with n^5.

Direct excitation into the stable configuration using the dipole blockade

With both schemes mentioned above, the atoms are excited into single-atom potential minima whose positions have to match the minimum of the two-atom potential that includes the interaction. Instead of artificially creating single-atom potential minima outside the origin, one can adiabatically transfer a cloud of ground state atoms from the state with no excitation via the state with one excited atom at the origin to the stable equilibrium state for two atoms relying on the structuring effect of the dipole-dipole repulsion. The electric field must thus be switched on at the beginning of the procedure.

The idea is based on the dynamical crystallization approach of Pohl et al. [20]. We start out from a cold gas of ground state atoms that can be modeled as consisting of two-level systems. This is legitimate[5] considering the rf-optical excitation technique described in Sec. 1.2. The coupling laser is detuned against the two-photon resonance. For large negative detunings the many-body ground state in the rotating frame of reference coincides with the initial state where all atoms are in the ground state. Increasing the detunings to positive values effectively lowers the energy levels of many-body states with one and two and more excitations. They cross at critical detunings Δ_1^0, Δ_2^1, ..., and states with 1, 2 and more Rydberg atoms are populated. The detuning is hence a control parameter that decreases the energy difference of adjacent number states $|0\rangle$, $|1\rangle$, $|2\rangle$,... with zero, one, two... excitations, respectively.

Since the laser couples the different number states, their energies undergo avoided crossings of separations δ_1^0, δ_2^1,... at the critical detunings. An adiabatic preparation of the states $|1\rangle$, $|2\rangle$,... is possible as long as the time in which the detuning of the laser changes is large compared to $1/\delta_1^0$, $1/\delta_2^1$,....

At the first crossing the initial state $|0\rangle$, with all atoms in the ground state, is directly coupled to the first excited state $|1\rangle$, with one Rydberg atom at the origin, which yields $\delta_1^0 \sim \Omega$. From $|1\rangle$ to $|2\rangle$, however, there is no direct laser coupling since the energetically lowest state with two Rydberg atoms, $|2\rangle$, is the stable equilibrium configuration described in Sec. 9.2.1 with two Rydberg atoms symmetrically displaced from the origin. To go from $|1\rangle$ to $|2\rangle$, two off-resonant intermediate steps are required. First the central atom is de-excited and subsequently the two Rydberg atoms at their equilibrium position are excited. A three-photon process is hence needed to come from $|1\rangle$ to $|2\rangle$. Assuming that $|1\rangle$ and $|2\rangle$

---

[5]The target of the two-photon excitation in this circularization approach is the rf-field-dressed state that adiabatically approaches the circular state when the rf-field is switched off. During the excitation process it hence exhibits admixtures of other $|l = m_l\rangle$-states (the radio field is σ^+-polarized) whose polarizability is smaller. In order to have the same dipolar repulsion the electric field must be stronger for compensation as long as the atoms are dressed by the rf-field.

are resonant at time t, then the intermediate states are detuned by $\Delta\Omega_i$ as defined below,

$$|0\rangle =$$

$$\downarrow \quad \Delta\Omega_a = -(\Delta\Omega_b + \Delta\Omega_c)$$

$$|1\rangle =$$

$$\downarrow \quad \Delta\Omega_b = V_{\boldsymbol{\mu B}}(0, 0, Z_{D,\mathrm{min}}/2)$$

$$\frac{1}{\sqrt{2}}(\qquad + \qquad)$$

$$\downarrow \quad \Delta\Omega_c = V_{\boldsymbol{\mu B}}(0, 0, Z_{D,\mathrm{min}}/2) + V_{dd}(Z_{D,\mathrm{min}})$$

$$|2\rangle = \qquad , \tag{9.40}$$

where the small spheres symbolize ground state atoms and the large spheres symbolize Rydberg atoms. For the parameters used in Section 9.2.1 (e.g. in Fig. 9.8; $B = 30\,\mathrm{G}$, $G = 10\,\mathrm{Tm}^{-1}$, $Q = B \cdot 6 \cdot 10^{-16}$, $F = 2 \cdot 10^{-11}$, $n = 30$) all detunings $\Delta\Omega_i$ are of the order of ~ 100 kHz. If the Rabi frequency is much smaller than the intermediate state detunings $\Delta\Omega_i$, then the intermediate states that couple $|1\rangle$ and $|2\rangle$ act as virtual levels for a resonant multi-photon transition. For larger Rabi frequencies, however, $\Omega(t) > \Delta\Omega_i$, power broadening exceeds the intermediate state detunings and the states are coupled by consecutive one photon transitions.

Conclusion and outlook

We have investigated the quantum nature of ultracold Rydberg atoms that couple to external fields and interact with each other. We have discovered how the large size alters the behavior of a Rydberg atom in a magnetic Ioffe-Pritchard trap. We have found extremely tight confinement for circular Rydberg atoms to be feasible without remarkably changing the electronic wave function of the atom and have exploited this result to constrain the system into a single dimension. In conjunction with the strong and long ranged dipolar interaction we have been able to form an ordered chain of Rydberg atoms with macroscopic interparticle distance that is stabilized against autoionization. We have seen that with an additional confinement in the longitudinal direction, two Rydberg atoms can stabilize each other via their dipolar repulsion. A thorough investigation of the strongly anisotropic Rydberg-Rydberg interaction, that exhibits an intricate dependence on the orientation of the electric dipole moments of the atoms, has led to the understanding of the mechanisms that destabilize this configuration which can thus be inhibited.

To arrive at that point we have first studied the quantum properties of ultracold Rydberg atoms in a Ioffe-Pritchard field configuration modeling the Rydberg atoms as a two-body system. Relativistic effects and deviations of the core potential from the Coulomb potential as well as diamagnetic interactions have not been taken into account, which is well justified a posteriori. Applying a spatially dependent unitary transformation and additionally exploiting the major mass difference of the electron and the core, we arrived at a two-particle Hamiltonian for highly excited atoms in an inhomogeneous field in which the appearance of the coupling of the relative and center of mass dynamics is simplified substantially. We have performed a symmetry analysis and we have justified that couplings of different n-manifolds can be neglected. The very different time scales of the relative and center of mass dynamics allows for an adiabatic separation which eliminates residual couplings. The solutions of the remaining internal problem for different center of mass positions constitute the adiabatic electronic energy surfaces that serve as potentials for the atomic motion. In the limit of large ratios of Ioffe field strength and field gradient, $B/(Gn^2)$, analytical expressions for the adiabatic surfaces have been provided. Even when this ratio is of the order of one, which entails tight transversal confinement, the shape of the uppermost surface and its energetic separation from others prove very robust. Non-adiabatic couplings are therefore small and we consider this surface the most appropriate to achieve confinement. Examining the compound quantized states we have found a regime where the extension of the center of mass wave function falls below the extension of the electronic cloud, i.e. the center of mass is stronger localized than the valence electron. Nevertheless, the electronic structure of the atom is barely changed compared to the field free case. Therefore, in this regime, Rydberg atoms in inhomogeneous magnetic fields cannot be considered as point-like particles.

As a natural enrichment of the system we have studied several Rydberg atoms confined to a magnetic guide by exploiting the extremely tight transversal confinement. We could show that an additional electric field renders it possible to stabilize the atoms against

autoionization and to create a one-dimensional Rydberg gas. This is possible by means of the repulsion between the field induced electric dipole moments which works towards a crystalline structure of the gas. Analytical expressions for the critical density, which is required to enter the one dimensional regime, have been calculated and we have found the lifetime of the Rydberg states to be sufficiently long to probe the dynamics of the interacting gas on ultracold timescales. This regime is complementary to the well-studied frozen Rydberg gases where atom-atom interaction induced motional effects can hardly be probed.

In order to deepen the understanding of the Rydberg-Rydberg interaction we have perturbatively calculated the electric dipole moment expectation values of Rydberg atoms in the strongly inhomogeneous magnetic field. Even for vanishing electric field we have found a permanent electric dipole moment outside the longitudinal axis that is perpendicular to the local magnetic field axis. This can be attributed to the finite size of the Rydberg atom. The corresponding term in the Hamiltonian admixes other basis states to the previously hydrogenic eigenstate. The electric dipole moment induced by an external electric field is likewise perpendicular to the local magnetic field axis but it exhibits different symmetries. When the permanent and the induced dipole moments have about the same magnitude (which happens already for very small electric fields), the total electric dipole moment becomes intriguingly asymmetric.

We have subsequently investigated how two Rydberg atoms, modeled as a two-particle system each, interact with each other when they are exposed to the electric and magnetic fields. For large enough inter-atomic distances we describe the interaction as a multipole expansion of the Coulomb interaction operators. Higher order multipole interactions are only significant if the dominant dipolar term is very small due to vanishing electric field or due to the geometry of the atomic configuration. We have furthermore identified the regime for which the interaction does not substantially change the electronic structure of the atom.

With this knowledge we have studied two interacting Rydberg atoms in the trap. Balancing the dipolar repulsion with an additional magnetic confinement in the longitudinal direction we have found a stable equilibrium configuration with an electrically tuneable inter-atomic distance. The six-dimensional adiabatic energy surface for the atoms' center of mass dynamics is harmonic around the stable configuration. The trap frequencies are independent of the inter-atomic distance and the two-atom ground state is therefore not expected to suffer from significant heating when the distance of the atoms is changed. We have shown these characteristics in the strongly confined one-dimensional case before we examined the robustness of the setup in three dimensions and described possible loss mechanisms. We suggest experimental implementations for the one-dimensional gas as well as for the stable two-atom configuration.

In order to be able to precisely control and manipulate ultracold Rydberg atoms, or even to exploit the electronic state dependent dipolar interaction to implement scalable quantum information schemes, a whole construction kit of electro-magnetic and optical tools is to be established. With creating long-lived tightly confined states exhibiting electric dipole moments of several hundred Debye and arranging them in versatile stable configurations with tuneable atoms distances, we have contributed a pivotal tool to this endeavor.

In spite of the presented results, the potential of the proposed magneto-electric trap is by far not exhausted. Promising ideas that could be pursued include the following: As

we have seen in Chapter 5, the degeneracy of the electronic surfaces below the uppermost surface is lifted by the external electric field. Their transversal minimum is shifted in opposite directions. The Rydberg atoms in the corresponding states are therefore confined in magnetic guides parallel to each other whose distance can be tuned electrically. One could envision two one-dimensional Rydberg chains next to each other whose interaction can be tuned by a multitude of field parameters and by the internal electronic states of the atoms.

Another question worth answering is whether for vanishing electric field the quadrupole-quadrupole repulsion can prevent the Rydberg atoms from ionizing each other or if the interaction between the permanent electric dipole moments impedes this stabilization or even actively brings the system to collapse. In case the quadrupole-quadrupole repulsion can stabilize the system: What are the temperatures that must not be exceeded? In any case the omission of an electric field decreases the atomic distances. For very small distances it may be advantageous to abandon the single atom electronic state approximation and to represent the interaction in a two-electron state basis set.

There are, undoubtedly, many exciting extensions of the discussed systems that still are to be discovered.

Atomic units

	atomic unit (a.u.)	SI units
mass	electron mass m_e	$9.10953 \cdot 10^{-31}$ kg
length	Bohr radius $a_0 = \frac{4\pi\epsilon_0 \hbar^2}{m_e e^2}$	$0.52918 \cdot 10^{-10}$ m
charge	electron charge e	$1.60219 \cdot 10^{-19}$ C
angular momentum	Planck constant $\hbar$	$1.05457 \cdot 10^{-34}$ Js
energy	$E_{\text{Ryd}} = \frac{1}{4\pi\epsilon_0} \frac{e^2}{a_0} = \alpha^2 m_e c^2 = 2$ Ry	$4.35974 \cdot 10^{-18}$ J
electric field	$2\times$ field at 1. Bohr orbit $\frac{E_{\text{Ryd}}}{e\, a_0}$	$5.14221 \cdot 10^{11}$ Vm^{-1}
magn. field strength	$\alpha^2 m_e^2 c^2/(e\hbar)$	$2.35051 \cdot 10^{5}$ T
magn. field gradient	$\alpha^2 m_e^2 c^2/(e\hbar a_0)$	$4.44181 \cdot 10^{15}$ Tm^{-1}
time	$\hbar/E_{\text{Ryd}}$	$2.41888 \cdot 10^{-17}$ s
momentum	$\hbar/a_0$	$1.99285 \cdot 10^{-24}$ kg m s^{-1}
el. dipole moment	$ea_0 = 2.54175$ Debye	$8.47835 \cdot 10^{-30}$ C m

Bibliography

[1] H. J. Metcalf and P. van der Straten, *Laser cooling and trapping of atoms*, J. Opt. Soc. Am. B **20**, 887 (2003).

[2] P. C. J. and S. H., *Bose-Einstein Condensation in Dilute Gases*, Cambridge University Press, 2002.

[3] S. Bose, *Plancks Gesetz und Lichtquantenhypothese*, Zeitschrift für Physik **26**, 178 (1924).

[4] A. Einstein, *Zur Quantentheorie des einatomigen Gases*, Sitzungsberichte der Preussischen Akademie der Wissenschaften, Mathematisch-Physikalische Klasse , 261 (1924).

[5] M. H. Anderson, J. R. Ensher, M. R. Matthews, C. E. Wieman, and E. A. Cornell, *Observation of Bose-Einstein Condensation in a Dilute Atomic Vapor*, Science **269**, 198 (1995).

[6] K. B. Davis, M. O. Mewes, M. R. Andrews, N. J. van Druten, D. S. Durfee, D. M. Kurn, and W. Ketterle, *Bose-Einstein Condensation in a Gas of Sodium Atoms*, Phys. Rev. Lett. **75**, 3969 (1995).

[7] R. Onofrio, C. Raman, J. M. Vogels, J. R. Abo-Shaeer, A. P. Chikkatur, and W. Ketterle, *Observation of Superfluid Flow in a Bose-Einstein Condensed Gas*, Phys. Rev. Lett. **85**, 2228 (2000).

[8] J. R. Abo-Shaeer, C. Raman, J. M. Vogels, and W. Ketterle, *Observation of Vortex Lattices in Bose-Einstein Condensates*, Science **292**, 476 (2001).

[9] M. R. Andrews, C. G. Townsend, H.-J. Miesner, D. S. Durfee, D. M. Kurn, and W. Ketterle, *Observation of Interference Between Two Bose Condensates*, Science **275**, 637 (1997).

[10] E. P. Gross, *Structure of a quantized vortex in boson systems*, Il Nuovo Cimento **20**, 454 (1961).

[11] E. P. Gross, *Hydrodynamics of a Superfluid Condensate*, J. Math. Phys. **4**, 195 (1963).

[12] L. P. Pitaevskii, Sov. Phys. JETP **13**, 451 (1961).

[13] L. P. Pitaevskii, Zh. Eksp. Teor. Fys. **40**, 646 (1961).

[14] D. Jaksch and P. Zoller, *The cold atom Hubbard toolbox*, Annals of Physics **315**, 52 (2005), Special Issue.

[15] R. P. Feynman, *Simulating physics with computers*, International Journal of Theoretical Physics **21**, 467 (1982).

[16] M. Greiner, O. Mandel, T. Esslinger, T. W. Hansch, and I. Bloch, *Quantum phase transition from a superfluid to a Mott insulator in a gas of ultracold atoms*, Nature **415**, 39 (2002).

[17] C. Chin, M. Bartenstein, A. Altmeyer, S. Riedl, S. Jochim, J. H. Denschlag, and R. Grimm, *Observation of the Pairing Gap in a Strongly Interacting Fermi Gas*, Science **305**, 1128 (2004).

[18] Z. Hadzibabic, P. Krüger, M. Cheneau, B. Battelier, and J. Dalibard, *Berezinskii-Kosterlitz-Thouless crossover in a trapped atomic gas*, Nature **441**, 1118 (2006).

[19] V. Bendkowsky, B. Butscher, J. Nipper, J. P. Shaffer, R. Low, and T. Pfau, *Observation of ultralong-range Rydberg molecules*, Nature **458**, 1005 (2009).

Bibliography

[20] T. Pohl, E. Demler, and M. D. Lukin, *Dynamical Crystallization in the Dipole Blockade of Ultracold Atoms*, Phys. Rev. Lett. **104**, 043002 (2010).

[21] H. Weimer, R. Löw, T. Pfau, and H. P. Büchler, *Quantum Critical Behavior in Strongly Interacting Rydberg Gases*, Physical Review Letters **101**, 250601 (2008).

[22] H. Weimer, M. Müller, I. Lesanovsky, P. Zoller, and H. P. Büchler, *A Rydberg quantum simulator*, Nat Phys **6**, 382 (2010).

[23] T. Pohl, T. Pattard, and J. Rost, *Plasma formation from ultracold Rydberg gases*, Phys. Rev. A **68**, 010703 (2003).

[24] I. Mourachko, D. Comparat, F. de Tomasi, A. Fioretti, P. Nosbaum, V. M. Akulin, and P. Pillet, *Many-body effects in a frozen Rydberg gas*, Phys. Rev. Lett. **80**, 253 (1998).

[25] K. Singer, M. Reetz-Lamour, T. Amthor, L. G. Marcassa, and M. Weidemüller, *Suppression of Excitation and Spectral Broadening Induced by Interactions in a Cold Gas of Rydberg Atoms*, Phys. Rev. Lett. **93**, 163001 (2004).

[26] D. Tong, S. M. Farooqi, J. Stanojevic, S. Krishnan, Y. P. Zhang, R. Côté, E. E. Eyler, and P. L. Gould, *Local Blockade of Rydberg Excitation in an Ultracold Gas*, Phys. Rev. Lett. **93**, 063001 (2004).

[27] T. Cubel Liebisch, A. Reinhard, P. R. Berman, and G. Raithel, *Atom Counting Statistics in Ensembles of Interacting Rydberg Atoms*, Phys. Rev. Lett. **95**, 253002 (2005).

[28] T. Vogt, M. Viteau, A. Chotia, J. Zhao, D. Comparat, and P. Pillet, *Electric-Field Induced Dipole Blockade with Rydberg Atoms*, Phys. Rev. Lett. **99**, 073002 (2007).

[29] C. S. E. van Ditzhuijzen, A. F. Koenderink, J. V. Hernández, F. Robicheaux, L. D. Noordam, and H. B. van Linden van den Heuvell, *Spatially Resolved Observation of Dipole-Dipole Interaction between Rydberg Atoms*, Phys. Rev. Lett. **100**, 243201 (2008).

[30] R. Heidemann, U. Raitzsch, V. Bendkowsky, B. Butscher, R. Löw, L. Santos, and T. Pfau, *Evidence for Coherent Collective Rydberg Excitation in the Strong Blockade Regime*, Phys. Rev. Lett. **99**, 163601 (2007).

[31] M. Reetz-Lamour, T. Amthor, J. Deiglmayr, and M. Weidemüller, *Rabi Oscillations and Excitation Trapping in the Coherent Excitation of a Mesoscopic Frozen Rydberg Gas*, Phys. Rev. Lett. **100**, 253001 (2008).

[32] T. A. Johnson, E. Urban, T. Henage, L. Isenhower, D. D. Yavuz, T. G. Walker, and M. Saffman, *Rabi Oscillations between Ground and Rydberg States with Dipole-Dipole Atomic Interactions*, Phys. Rev. Lett. **100**, 113003 (2008).

[33] D. Jaksch, J. I. Cirac, P. Zoller, S. L. Rolston, R. Côté, and M. D. Lukin, *Fast Quantum Gates for Neutral Atoms*, Phys. Rev. Lett. **85**, 2208 (2000).

[34] M. D. Lukin, M. Fleischhauer, R. Côté, L. M. Duan, D. Jaksch, J. I. Cirac, and P. Zoller, *Dipole Blockade and Quantum Information Processing in Mesoscopic Atomic Ensembles*, Phys. Rev. Lett. **87**, 037901 (2001).

[35] I. I. Ryabtsev, D. B. Tretyakov, and I. I. Beterov, *Applicability of Rydberg atoms to quantum computers*, J. Phys. B: At. Mol. Opt. Phys. **38**, S421 (2005).

[36] L. Isenhower, E. Urban, X. L. Zhang, A. T. Gill, T. Henage, T. A. Johnson, T. G. Walker, and M. Saffman, *Demonstration of a Neutral Atom Controlled-NOT Quantum Gate*, Phys. Rev. Lett. **104**, 010503 (2010).

124

[37] T. Wilk, A. Gaëtan, C. Evellin, J. Wolters, Y. Miroshnychenko, P. Grangier, and A. Browaeys, *Entanglement of Two Individual Neutral Atoms Using Rydberg Blockade*, Phys. Rev. Lett. **104**, 010502 (2010).

[38] C. Greene, A. Dickinson, and H. Sadeghpour, *Creation of polar and nonpolar ultralong-range Rydberg molecules*, Phys. Rev. Lett. **85**, 2458 (2000).

[39] E. L. Hamilton, C. H. Greene, and H. R. Sadeghpour, *Shape-resonance-induced long-range molecular Rydberg states*, J. Phys. B **35**, L199 (2002).

[40] A. A. Khuskivadze, M. I. Chibisov, and I. I. Fabrikant, *Adiabatic energy levels and electric dipole moments of Rydberg states of Rb_2 and Cs_2 dimers*, Phys. Rev. A **66**, 042709 (2002).

[41] I. Lesanovsky, P. Schmelcher, and H. R. Sadeghpour, *Ultra-long-range Rydberg molecules exposed to a magnetic field*, J. Phys. B **39**, L69 (2006).

[42] P. Hyafil, J. Mozley, A. Perrin, J. Tailleur, G. Nogues, M. Brune, J. M. Raimond, and S. Haroche, *Coherence-Preserving Trap Architecture for Long-Term Control of Giant Ryberg Atoms*, Phys. Rev. Lett. **93**, 103001 (2004).

[43] S. K. Dutta, J. R. Guest, D. Feldbaum, A. Walz-Flannigan, and G. Raithel, *Ponderomotive Optical Lattice for Rydberg Atoms*, Phys. Rev. Lett. **85**, 5551 (2000).

[44] J.-H. Choi, J. R. Guest, A. P. Povilus, E. Hansis, and G. Raithel, *Magnetic trapping of long-lived cold Rydberg atoms*, Phys. Rev. Lett. **95**, 243001 (2005).

[45] J.-H. Choi, J. R. Guest, and G. Raithel, *Magnetic trapping of strongly-magnetized Rydberg atoms*, Eur. Phys. J. D **40**, 19 (2006).

[46] I. Lesanovsky, J. Schmiedmayer, and P. Schmelcher, *Rydberg atoms in magnetic quadrupole traps*, Europhys. Lett. **65**, 478 (2004).

[47] I. Lesanovsky, J. Schmiedmayer, and P. Schmelcher, *Rydberg atoms in a magnetic quadrupole field*, J. Phys. B **38**, 151 (2005).

[48] I. Lesanovsky and P. Schmelcher, *Magnetic trapping of ultracold Rydberg atoms*, Phys. Rev. Lett. **95**, 053001 (2005).

[49] I. Lesanovsky and P. Schmelcher, *Quantum states of ultracold electronically excited atoms in a magnetic quadrupole trap*, Phys. Rev. A **72**, 53410 (2005).

[50] R. Folman, P. Krüger, J. Schmiedmayer, J. Denschlag, and C. Henkel, *Microscopic atom optics: From wires to an atomchip*, Adv. At. Mol. Opt. Phys. **48**, 263 (2002).

[51] J. Fortágh and C. Zimmermann, *Magnetic microtraps for ultracold atoms*, Rev. Mod. Phys. **79**, 235 (2007).

[52] A. Haase, D. Cassettari, B. Hessmo, and J. Schmiedmayer, *Trapping neutral atoms with a wire*, Phys. Rev. A **64**, 043405 (2001).

[53] N. Bohr, *On the constitution of atoms and molecules*, Philosophical Magazine Series 6 **26**, 1 (1913).

[54] P. Goy, J. M. Raimond, M. Gross, and S. Haroche, *Observation of Cavity-Enhanced Single-Atom Spontaneous Emission*, Phys. Rev. Lett. **50**, 1903 (1983).

[55] M. Brune, P. Nussenzveig, F. Schmidt-Kaler, F. Bernardot, A. Maali, J. M. Raimond, and S. Haroche, *From Lamb shift to light shifts: Vacuum and subphoton cavity fields measured by atomic phase sensitive detection*, Phys. Rev. Lett. **72**, 3339 (1994).

[56] R. F. Stebbings and F. B. Dunning, *Rydberg States of Atoms and Molecules*, 1983.

Bibliography

[57] D. G. Hummer and D. Mihalas, *The equation of state for stellar envelopes. I - an occupation probability formalism for the truncation of internal partition functions*, Astrophys. J. **331**, 794 (1988).

[58] V. L. Jacobs, J. Davis, and P. C. Kepple, *Enhancement of Dielectronic Recombination by Plasma Electric Microfields*, Phys. Rev. Lett. **37**, 1390 (1976).

[59] J. R. Rydberg, Philosophical Magazine 5th Ser. **29**, 331 (1890).

[60] T. F. Gallagher, *Rydberg atoms*, Reports on Progress in Physics **51**, 143 (1988).

[61] Y. Ralchenko, A. Kramida, J. Reader, and NIST ASD Team, NIST Atomic Spectra Database (version 3.1.5), http://physics.nist.gov/asd3 [2009, August 19]. National Institute of Standards and Technology, Gaithersburg, MD.

[62] E. de Prunelé, *Orientation effects in thermal collisions between "circular"–Rydberg-state atoms and ground-state helium*, Phys. Rev. A **31**, 3593 (1985).

[63] R. G. Hulet and D. Kleppner, *Rydberg Atoms in "Circular" States*, Phys. Rev. Lett. **51**, 1430 (1983).

[64] P. Nussenzveig, F. Bernardot, M. Brune, J. Hare, J. M. Raimond, S. Haroche, and W. Gawlik, *Preparation of high-principal-quantum-number "circular" states of rubidium*, Phys. Rev. A **48**, 3991 (1993).

[65] D. Delande and J. C. Gay, *A New Method for Producing Circular Rydberg States*, EPL (Europhysics Letters) **5**, 303 (1988).

[66] J. Hare, M. Gross, and P. Goy, *Circular Atoms Prepared by a New Method of Crossed Electric and Magnetic Fields*, Phys. Rev. Lett. **61**, 1938 (1988).

[67] R. Lutwak, J. Holley, P. P. Chang, S. Paine, D. Kleppner, and T. Ducas, *Circular states of atomic hydrogen*, Phys. Rev. A **56**, 1443 (1997).

[68] W. Pauli, *Über das Wasserstoffspektrum vom Standpunkt der neuen Quantenmechanik*, Zeitschrift für Physik **36**, 336 (1926).

[69] W. A. Molander, C. R. Stroud, and J. A. Yeazell, *Excitation of high angular momentum Rydberg states*, Journal of Physics B: Atomic and Molecular Physics **19**, L461 (1986).

[70] C. H. Cheng, C. Y. Lee, and T. F. Gallagher, *Production of Circular Rydberg States with Circularly Polarized Microwave Fields*, Phys. Rev. Lett. **73**, 3078 (1994).

[71] L. Chen, M. Cheret, F. Roussel, and G. Spiess, *New scheme for producing circular orbital states in combined RF and static fields*, Journal of Physics B: Atomic, Molecular and Optical Physics **26**, L437 (1993).

[72] B. Hezel, I. Lesanovsky, and P. Schmelcher, *Controlling Ultracold Rydberg Atoms in the Quantum Regime*, Phys. Rev. Lett. **97**, 223001 (2006).

[73] B. Hezel, I. Lesanovsky, and P. Schmelcher, *Ultracold Rydberg atoms in a Ioffe-Pritchard trap*, Phys. Rev. A **76**, 053417 (2007).

[74] H. A. Bethe and E. E. Salpeter, *Quantum Mechanics of One- and Two-Electron Atoms*, Springer, 1977.

[75] I. Lesanovsky, *Quantum dynamics of ultracold atoms in inhomogeneous magnetic fields. From ground state atoms to Rydberg atoms*, PhD thesis, 2006.

[76] P. Schmelcher and L. S. Cederbaum, *On chaos in unbounded phase space*, Phys. Lett. A **164**, 305 (1992).

[77] O. Dippel, P. Schmelcher, and L. S. Cederbaum, *The Charged Anisotropic Harmonic Oscillator and the Hydrogen Atom in Crossed Fields*, Phys. Rev. A **49**, 4415 (1994).

[78] J. E. Avron, I. W. Herbst, and B. Simon, *Separation of center of mass in homogeneous magnetic fields*, Annals of Physics **114**, 431 (1978).

[79] P. Schmelcher and L. S. Cederbaum, *Two-body Effects of the Hydrogen Atom in Crossed Electric and Magnetic Fields*, Chem. Phys. Lett. **208**, 548 (1993).

[80] P. Schmelcher, L. S. Cederbaum, and U. Kappes, *Molecules in Magnetic Fields: Fundamental Aspects*, pages 1–51, Conceptual Trends in Quantum Chemistry, Kluwer Academic Publishers, 1994.

[81] M.-O. Mewes, M. R. Andrews, N. J. van Druten, D. M. Kurn, D. S. Durfee, and W. Ketterle, *Bose-Einstein Condensation in a Tightly Confining dc Magnetic Trap*, Phys. Rev. Lett. **77**, 416 (1996).

[82] I. Lesanovsky, J. Schmiedmayer, and P. Schmelcher, *Rydberg atoms in a magnetic guide*, Phys. Rev. A **70**, 43409 (2004).

[83] P. Picasso, "Los ordenadores son inútiles. Sólo pueden darte respuestas.".

[84] A. Szabo and N. S. Ostlund, *Modern Quantum Chemistry: Introduction to Advanced Electronic Structure Theory*, Dover Publications, 1996.

[85] E. A. Hylleraas and B. Undheim, *Numerische Berechnung der 2S-Terme von Ortho- und Para-Helium*, Zeitschrift für Physik A Hadrons and Nuclei **65**, 759 (1930).

[86] H. Friedrich, *Theoretical Atomic Physics*, Springer, 1998.

[87] A. Messiah, *Quantum Mechanics*, Dover Publications, 2000.

[88] D. Sorensen, *Parallel numerical algorithms - Implicitly restarted Arnoldi/Lanczos methods for large scale eigenvalue calculations*, Kluwer Dordrecht, 1995.

[89] J. W. Demmel, S. C. Eisenstat, J. R. Gilbert, X. S. Li, and J. W. H. Liu, *A supernodal approach to sparse partial pivoting*, SIAM J. Matrix Analysis and Applications **20(3)**, 720 (1999).

[90] E. H. Lieb and W. Liniger, *Exact Analysis of an Interacting Bose Gas. I. The General Solution and the Ground State*, Phys. Rev. **130**, 1605 (1963).

[91] M. Girardeau, *Relationship between Systems of Impenetrable Bosons and Fermions in One Dimension*, Journal of Mathematical Physics **1**, 516 (1960).

[92] B. Paredes, A. Widera, V. Murg, O. Mandel, S. Folling, I. Cirac, G. V. Shlyapnikov, T. W. Hänsch, and I. Bloch, *Tonks-Girardeau gas of ultracold atoms in an optical lattice*, Nature **429**, 277 (2004).

[93] T. Bergeman, M. G. Moore, and M. Olshanii, *Atom-Atom Scattering under Cylindrical Harmonic Confinement: Numerical and Analytic Studies of the Confinement Induced Resonance*, Phys. Rev. Lett. **91**, 163201 (2003).

[94] E. Haller, M. J. Mark, R. Hart, J. G. Danzl, L. Reichsöllner, V. Melezhik, P. Schmelcher, and H.-C. Nägerl, *Confinement-Induced Resonances in Low-Dimensional Quantum Systems*, Phys. Rev. Lett. **104**, 153203 (2010).

[95] M. Mayle, B. Hezel, I. Lesanovsky, and P. Schmelcher, *One-Dimensional Rydberg Gas in a Magnetoelectric Trap*, Phys. Rev. Lett. **99**, 113004 (2007).

[96] M. Mayle, *Ultracold Rydberg atoms in a Ioffe-Pritchard trap*, PhD thesis, University of Heidelberg, 2009.

Bibliography

[97] U. D. Jentschura, E.-O. L. Bigot, J. Evers, P. J. Mohr, and C. H. Keitel, *Relativistic and radiative energy shifts for Rydberg states*, Journal of Physics B: Atomic, Molecular and Optical Physics **38**, S97 (2005).

[98] R. G. Hulet, E. S. Hilfer, and D. Kleppner, *Inhibited Spontaneous Emission by a Rydberg Atom*, Phys. Rev. Lett. **55**, 2137 (1985).

[99] K. L. Moore, T. P. Purdy, K. W. Murch, K. R. Brown, K. Dani, S. Gupta, and D. M. Stamper-Kurn, *Bose–Einstein condensation in a mm-scale Ioffe–Pritchard trap*, Applied Physics B: Lasers and Optics **82**, 533 (2006).

[100] A. Messiah, *Quantum Mechanics*, volume II, North-Holland Publishing Company, 1961.

[101] C. Cohen-Tannoudji, B. Diu, and F. Laloe, *Quantenmechanik, Tl.1*, Gruyter, 1999.

[102] M. L. Zimmerman, M. G. Littman, M. M. Kash, and D. Kleppner, *Stark structure of the Rydberg states of alkali-metal atoms*, Phys. Rev. A **20**, 2251 (1979).

[103] M. Saffman, T. G. Walker, and K. Molmer, *Quantum information with Rydberg atoms*, quant-ph/0909.4777 (2010).

[104] H. Goldstein, *Klassische Mechanik*, Addison-Wesley, 1983.

[105] J. O. Hirschfelder and W. J. Meath, *The Nature of Intermolecular Forces*, Advances in Chemical Physics **12** (1967).

[106] A. Dalgarno and W. D. Davison, *The calculation of van der waals interactions*, Advances in Atomic and Molecular Physics **2** (1966).

[107] T. Lahaye, C. Menotti, L. Santos, M. Lewenstein, and T. Pfau, *The physics of dipolar bosonic quantum gases*, Reports on Progress in Physics **72**, 126401 (2009).

[108] A. Ashkin, J. M. Dziedzic, J. E. Bjorkholm, and S. Chu, *Observation of a single-beam gradient force optical trap for dielectric particles*, Optics Letters **11**, 288 (1986).

[109] N. Schlosser, G. Reymond, I. Protsenko, and P. Grangier, *Sub-poissonian loading of single atoms in a microscopic dipole trap*, Nature **411**, 1024 (2001).

[110] V. Vuletic, *Quantum networks: When superatoms talk photons*, Nat Phys **2**, 801 (2006).

Danksagung

Bedanken möchte ich mich vor allem bei meinem Betreuer Peter Schmelcher, sowohl für die spannende Aufgabenstellung, die weit genug gefasst war, mir nicht die Freiheit bei der Ausgestaltung der Arbeit zu nehmen, als auch für sein Vertrauen.

Für die Erstellung des Zweitgutachtens möchte ich mich bei Thomas Gasenzer bedanken.

Ein spezieller Dank geht an Igor Lesanovsky der nicht nur profunde Vorarbeit geleistet hat, sondern mich auch später bei vielen Vorhaben unterstützt und durch Ideen und konkrete Vorschläge großen Anteil an der vorliegenden Arbeit hat. In diesem Zusammenhang möchte ich mich auch herzlich bei Michael Mayle für den Austausch und die Zusammenarbeit bedanken. Das eindimensionale Rydberggas haben wir gemeinsam stabilisiert.

Muchas gracias a Rosario González Férez. Las visitas en Granada me dieron la oportunidad de disfrutar de tu hospitalidad renombrada. Todavía no has canjeado el vale para la excursión a la Selva Negra.

Vielen Dank an Peter Krüger für die Einladung nach Nottingham und für die vielen kleinen Tipps die sich hier und da in dieser Arbeit niedergeschlagen haben.

Nun zu den *zwei glorreichen Halunken* in meinem Büro. Ich finde wir waren ein spannendes Zimmer. *The Good, the Bad and the Ugly* waren ja nie eindeutig zuzuordnen. Vielen Dank Florian für die politischen Streitgespräche die wir immer öfter *cool* geführt haben. Ein Stück Lebensqualität war auch Christophs Gebabbl von den Ethnien dieser Welt. Und danke für's Schmiere stehen beim Rüsselklau! Danke für Salat und gute Laune beim Endspurt, Nikolas. Ich möchte auch ausdrücklich der ganzen Arbeitsgruppe für die sehr angenehme (mediterrane) Atmosphäre danken.

Für erstklassige Kickerpartien, die mit internationaler Härte ausgetragen wurden, gilt mein Dank dem erweiterten Kader: Marc Deissendinho, Johannes Fester, Christoph Achkomm, Moppi Durchstecker, May Lee, Alex Gaucho, Hanna Onetouch, Nele Müller, Christoph Aihävid, Marc Chapuisat, Georg le Mure, und viele, viele Gäste.

Meinen Eltern und meinen Geschwistern möchte ich für den Rückhalt und die Zuneigung danken, die sie mir entgegenbringen. Sie sind bis nach Heidelberg spürbar, vielen Dank an euch! Ein kleines Zeichen dafür waren die care-Pakete, kleine Motivations- und Kalorienbomben, die zwar nicht von Flugzeugen abgeworfen wurden, aber doch meistens aus heiterem Himmel kamen.

Mest vill jag tacka min prinsessa, som omväxlande har bromsat och påskyndat framställandet av detta verk, men alltid med angenäma konsekvenser för mig. Det är en stor glädje för mig att vara med dig! Jag kommer alltid att vara det, d. ä. s. ä. d.

Heidelberg im Mai 2010